University of Tasmania

Upwelling dynamics in Southern Australia - Numerical Modelling and Observations

A thesis submitted in fulfilment of the requirements for the degree of Doctor of Philosophy in Quantitative Marine Science

Hugo Bastos de Oliveira, MSc, BSc(Hons)

Institute for Marine and Antarctic Studies
University of Tasmania

June 2018

University of Tasmania

Upwelling dynamics in Southern Australia - Numerical Modelling and Observations

A thesis submitted in fulfilment of the requirements for the degree of Doctor of Philosophy in Quantitative Marine Science

Hugo Bastos de Oliveira, MSc, BSc(Hons)

Institute for Marine and Antarctic Studies
University of Tasmania

June 2018

Declaration of Originality

This thesis contains no material which has been accepted for a degree or diploma by the University or any other institution, except by way of background information and duly acknowledged in the thesis, and to the best of my knowledge and belief no material previously published or written by another person except where due acknowledgement is made in the text of the thesis, nor does the thesis contain any material that infringes copyright.

This thesis contains my own work, with the assistance of my advisory team. The contribution from each advisor is explicitly stated, including project design, methods, style and linguistics in the statement of co-authorship.

29/06/2018

Hugo Bastos de Oliveira — Date

Copyright / Authority of Access

29/06/2018

Hugo Bastos de Oliveira — Date

Thesis Abstract

The ocean circulation along the Eastern Great Australian Bight (EGAB) is investigated using models and observations, with a focus on Australia's strongest upwelling region — the Bonney Coast (BC). A detailed analysis of the shelf circulation in this region has never been fully undertaken. The modelling studies examine how variations in shelf topography and Coastal Trapped Waves (CTWs) influence upwelling. The observations describe one of the most extreme upwelling seasons on record (Austral summer, 2016) with unprecedented coverage. The context for the intense observing program is provided by a detailed analysis of large-scale and local factors, quantifying their impacts.

The model used is a regional configuration that includes idealised forcing and initial conditions, and realistic topography and coastal geometry. A key finding from the modelling studies is the demonstration of the influence of alongshore variations in shelf topography - submerged headlands and valleys - on the upwelling circulation. This was the first demonstration of this phenomenon in the BC region. Upwelling is shown to be qualitatively consistent with vorticity dynamics. We show that alongshore baroclinic pressure gradients force a geostrophic onshore flow on the equatorward side of the submerged headlands. A second study also highlights the role of CTWs that act to shut-down the interior upwelling, with the strongest influence nearer the CTW source. The circulation driven by a periodic CTW is also studied as a proxy for wind-driven motions in the western Bight. The results show the mean characteristics of the flow and its adjustment to variable shelf-width and topography, with equatorward (poleward) alongshore velocities of the CTW driving intensified bottom upwelling (downwelling). As the remote forcing frequencies reduce (longer time-scales), local topography rectification and resonance with local winds clearly enhance upwelling in the main EGAB upwelling regions.

The observational coverage of the EGAB during Austral summer 2016 was unprecedented, with observations from gliders, moorings, coastal radar, tide gauges, and satellite measurements. The analysis exploited climate indices and reanalysis products to understand the broad scale context of the regional observations. Several factors made the EGAB pre-conditioned to extreme upwelling in 2016. Through the coastal wave guide, the 2015/16 El-Niño uplifted the isotherms over the slope, the South Australian Current was weaker than normal, and the Southern Annular Mode acted to enhance the upwelling favourable winds. Together, these factors meant that the shelf waters responded quickly and efficiently to strong wind-driven events in early 2016. The anomalies associated with this extreme upwelling season

included surface temperatures exceeding $2°C$ below average, winds in excess of 0.1Pa, and high Chlorophyll-A. Glider observations show that the upwelled waters were highly skewed (cold and fresh), with origins deeper than $350m$ (with Flinders Current origin), and with alongshore variations consistent with those implied by the modelling studies.

The analysis of climate indices showed significant lagged relationships between large-scale conditions and properties of the shelf circulation in the EGAB. We speculate that these lagged relationships could be used as a predictive tool, to identify when the EGAB is more prone to upwelling. Arguably, the results presented in this thesis represent the most comprehensive description of the shelf circulation in the EGAB. We show, for the first time, the importance of alongshore variations in topography, the impacts of CTWs, and the role of remote forcing on the shelf circulation. This research addresses some important knowledge-gaps of the oceanography of this region, and are particularly important for the management of fisheries and prediction of the EGAB upwelling system as a whole.

Dedication

To Camila and Andreas.
I'm truly thankful for having you both in my life.

Acknowledgements

I'm grateful to be part of the IMAS-CSIRO joint program and for the opportunity to be based in different institutions, including the SARDI, within the course of the Ph.D. The level of research is inspiring, and to be part of this scientific environment was a unique opportunity that shaped my scientific interest.

I wish to thank my supervisors, Prof. John Middleton, Prof. Richard Coleman, and Dr. Peter Oke for the main guidance. Their supervision, patience, and proofreading have lead to the completion of this thesis.

John always believed in this project and was ever enthusiastic about the model results. Thanks for your support during my time in Adelaide.

Richard also provided steady support in all aspects of the Ph.D, from my choices during the project to the comprehensive revisions. Thanks for the motivation.

Peter was always objective, with strong sound judgement, and a positive attitude towards my results. Thanks for your friendship.

I also thank Prof. Mauro Cirano, who helped bring this project to reality, and from the assist and encouragement from afar.

I would like to express my gratitude for the funding in my education and research by the Brazilian Research Council (CAPES - Ph.D Scholarship 1125/13-3), and the Quantitative Marine Science program.

I would like to acknowledge the IMOS network for the effort in providing free access to Australia's oceanographic data and the computational infrastructure provided by the Tasmanian Partnership for Advanced Computing (TPAC).

I'm thankful for the time spent in Hobart at the CSIRO Oceans and Atmosphere group, where I made new friends and crossed with old ones. Thanks to Gabriela Pilo, who became a great and helpful friend along this journey. And to Ana, Fabio, Leo, Leandro, Claudio & Sandra, Samantha & Matt, for making the time in the island more enjoyable.

I was also happy for being part of the SARDI Oceanography group, which

always provided a friendly work environment. My special thanks to John Luick and Lou, for helping me out in Adelaide, the several trips, and the family celebrations. Thank you Charles, Henry, Mark, Pauls, Ana, Nicole and Luciana for the friendship and assist.

A special thanks to Paula, for the supportive visit when Andreas was born. And to my friends Adrian and Lucy, who share the parenthood experience and became our family in Australia with their little ones.

Thank you, mum, dad, and brother for the absolute love and support of my decisions. And to my sister Ingrid, for sharing some time with us and made me feel back home again. All of you are part of this even from far away.

None of this could have been done without the endless love of my partner and friend Camila, and our dearest son Andreas. Thank you for all the support and happiness you gave me. I love you.

Finally, I would like thank everyone who encourage me.

Statement of Co-Authorship

The following people and institutions contributed to the publication of work undertaken as part of this thesis:

Candidate: Hugo Bastos de Oliveira, IMAS, CSIRO, SARDI

Author 1: John Middleton, SARDI
Author 2: Peter Oke, CSIRO
Author 3: Richard Coleman, IMAS

In the paper entitled "Upwelling along the shelves of the Greater Australian Bight. Part I: the role of submarine headlands and valleys" the candidate was the primary author contributing in all aspects of the work and author 1 contribute to the idea, formalisation and writing. Authors 2 and 3 contributed to final review.
In "Upwelling along the shelves of the Greater Australian Bight. Part II: set-up, geographical origins, the viscous limit and the role of Coastal Trapped Waves.", Author 1 is the primary author and main contribution within the manuscript rationalization and writing, while the candidate contribute in all analysis, idea, development and writing. Authors 2 and 3 contributed to final review.
Within "Interannual variability of upwelling in the Greater Australian Bight: Observations and the extreme event of 2016", the candidate was the main author and contribute to all aspects of the work. Author 2 contribute to ideas within the analysis and methods used, and writing. Author 3 contribute to methods used and writing. Author 1 contribute to observational funding and planning.

Prof. Richard Coleman
Supervisor
IMAS
University of Tasmania

	02/07/2018
Richard Coleman	Date

Supporting Publications

The results from chapters 4 and 5 will be published as:

de Oliveira, H.B. and Middleton, J.F. (2017). Upwelling along the shelves of the Greater Australian Bight. Part I: the role of submarine headlands and valleys. *Submitted to Journal of Geophysical Research: Oceans. under review*

Middleton, J.F. and de Oliveira, H.B. (2017). Upwelling along the shelves of the Greater Australian Bight - Part II: set-up, geographical origins, the viscous limit and role of Coastal Trapped Waves. *Submitted to Journal of Geophysical Research: Oceans. under review*

Some of the results from chapter 6 will appear as:

de Oliveira, H.B., Oke, P. R., Coleman, R., Middleton, J.F. (2018). Interannual variability of upwelling in the Great Australian Bight: Observations and the extreme event of 2015-2016. *in preparation for submission to Progress in Oceanography.*

Contents

List of Figures

List of Tables

Acronyms

ABSLMP	Australian Baseline Sea Level Monitoring Project
ACF	Autocorrelation function
AMSR	Advanced Microwave Scanning Radiometer
AVHRR	Advanced Very High Resolution Radiometer
BAS	British Antarctic Survey
BBL	bottom boundary layer
BC	Bonney Coast
BCLAKE	Bonney Coast Lake
BoM	Australian Bureau of Meteorology
BP	Bonney Plume
BRAN	BlueLink ReANalysis
BT	Bottom temperature
CARS	CSIRO Atlas of Regional Seas
CB	Coffin Bay
CCMP	Cross Calibrated Multi Platform Ocean Surface Wind Velocity
Chl-A	Chlorophyll-A
CSW	Continental Shelf Wave
CTD	Condutivity Temperature and Depth probe
CTW	Coastal Trapped Wave
DCM	Deep Chlorophyll Maximum
DJF	December, January and February
DMI	Dipole Mode Index of the Indian Ocean Dipole
DOF	degrees of freedom
ECMWF	European Centre for Medium-Range Weather Forecasts
EGAB	Eastern Great Australian Bight
ENSO	El-Niño-Southern Oscillation
EOF	Empirical Orthogonal Function
EP	Eyre Peninsula

ERAI	European Reanalysis Interim
FC	Flinders Current
FP	Fleurieu Peninsula
GAB	Great Australian Bight
ICW	Indian Central Water
IMOS	Integrated Marine Observing System
IOD	Indian Ocean Dipole
IPO	Tripole Index for the Interdecadal Pacific Oscillation
JAFFA	Cape Jaffa
JAMSTEC	Japan Agency for Marine-Earth Science and Technology
JFM	January,February,March
JPL	Jet Propulsion Laboratory
KI	Kangaroo Island
LC	Leeuwin Current
LS	Lacepede Shelf
MODOKI	El-Niño Modoki index
MPDATA	Multidimensional Positive Definite Advection Transport Algorithm
MSLP	mean sea level pressure
MUR	Multi-scale Ultra-high Resolution Sea Surface Temperature
NINO3.4	Nino3.4 Index
NOAA	National Ocean and Atmospheric Administration
OBC	Open Boundary Conditions

OGCM	Ocean General Circulation Model
OISST	Optimum Interpolation Sea Surface Temperture
OLS	Ordinary Least Squares
ONI	Oceanic Niño Index
OTWAY	Cape Otway
PORT	Portland
PSD	Physical Sciences Division
ROMS	Regional Ocean Modelling System
RSS	Remote Sensing Systems
SA	South Australia
SAC	South Australia Current
SAIMOS	Southern Australian Integrated Marine Observing System
SAM	Southern Annular Mode
SG	Spencer Gulf
SL	Sea Level
SLA	Sea Level Anomaly
SML	Surface Mixed Layer
SST	Sea Surface Temperature
STF	Sub Tropical Front
TG	Tide Gauge
THEV	Thevenard
ToA	Time of Arrival
WA	Western Australia
WBRY	western model boundary
WT	Western Tasmania
ZC	Zeehan Current

Chapter 1

Introduction

Upwelling is the process by which colder and deeper waters are uplifted towards the ocean surface. Upwelled waters are usually nutrient-rich, and so upwelling is important to marine industries, including fisheries. The most common type of upwelling is wind-driven upwelling, where, in coastal regions, an alongshore wind drives an offshore Ekman transport, which in turn draws a sub-surface upward return flow over the continental shelf. The eastern margins of the ocean basins are where upwelling is most pronounced (Richards 1981), but other regions and mechanisms for upwelling are also important, such as shelf-break and topographic upwelling (e.g., Gan et al. 2002b; Barth et al. 2005; Matano et al. 2008; Whitney et al. 2009a; Liu et al. 2015).

Around Australia, there are two regions that often experience upwelling favourable winds – off North-West WA, and the Great Australian Bight (GAB). Despite the occurrence of upwelling-favourable winds off WA, the dominance of the Leeuwin Current means that upwelling rarely occurs. This is atypical for eastern boundary currents (Cresswell et al. 1993; Gersbach et al. 1999; Pearce et al. 1999; Feng 2003; Rossi et al. 2013). By contrast, the Eastern Great Australian Bight (EGAB) - specifically the Bonney Coast (BC) (Figure 1.1a) - is Australia's strongest upwelling region (Foster et al. 2014), with strong upwelling typically in Austral summer.

In general, the spring-summer circulation in the GAB is influenced largely by upwelling-favourable winds, but still with a downwelling, weak and south-eastward shelf-break current — South Australia Current (SAC) — as well as a north-westward, deeper and upwelling favourable Flinders Current (FC) (Middleton et al. 2002; Cirano et al. 2004; Middleton et al. 2007b). During austral spring and summer, when high-pressure systems and mean anticyclonic winds are dominant (Fig. 1.1b), seasonally-permanent cold Sea Surface Temperature (SST) patches are found mainly between Thevenard and north-western Tasmania (Fig. 1.1c).

The coastal signal is also far from being homogeneous and occurs mainly between

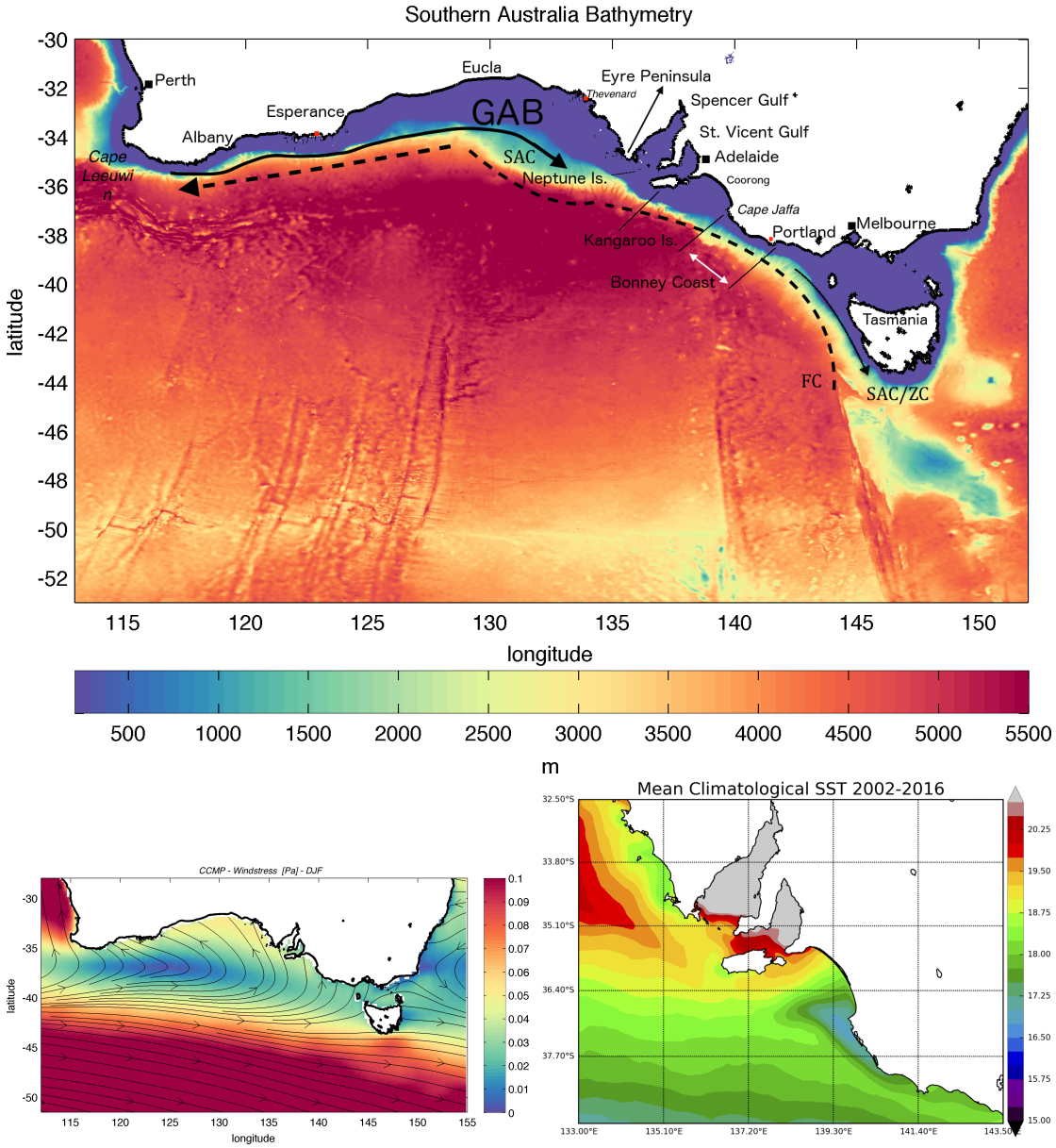

Figure 1.1: The Southern Australia Seas and the Great Australian Bight. (a) The Bathymetric chart. Topographic values are on a $250m$ grid resolution. The purple colour limit represents the $200m$ isobath. Data source: Geoscience Australia Bathymetric Chart $v2009$. (b) The 5–year (1997-2001) mean wind stress (streamlines) and magnitude (shading) during canonical austral summertime (December, January and February). Data source: Remotely sensed reanalysis Cross Calibrated Multi Platform Ocean Surface Wind Velocity (CCMP) $v01.1$–1997-2001. (c) Mean SST for canonical austral summer along the EGAB (DJF). Data Source: Remotely sensed reanalysis MUR/NASA $v4.1$ (2002-2016)

Thevenard and Kangaroo Island (KI) (Middleton et al. 2007b; Kämpf 2010), along the BC (Rochford 1977; Lewis 1981; Middleton et al. 2007a; Nieblas et al. 2009; Foster et al. 2014), and off north-western Tasmania (Evans et al. 1998; Kämpf 2015). The BC, between Cape Jaffa (South Australia) and Portland (Victoria), is regarded as Australia's strongest upwelling region (Foster et al. 2014). A common feature along the BC is the surface signature of the upwelling plume (south of $36.6°S$ in Fig. 1.1c), occurring throughout the upwelling season (spring–summer), and often enhanced between January–March (Nieblas et al. 2009). This plume is usually in phase with SST signals in the other EGAB sub-regions (Figure 1.2b,c), mainly along the KI region and north of the Eyre Peninsula (EP), but *not* with the western GAB regions. In the western GAB, despite the presence of upwelling-favourable winds, upwelling is mostly absent (e.g., Fig. 1.2a).

The GAB is a region characterised by Coastal Trapped Waves (CTWs) activity in the weather band (6–$25d$), with the most pronounced Sea Level (SL) variance occurring at Thevenard (Church et al. 1987; Maiwa et al. 2010). Other trapped waves are also prevalent in the GAB, including an annual wave (Ridgway et al. 2015) and others within the interannual variability (Clarke et al. 1994; Li et al. 2004; Middleton et al. 2007a).

The coastal wave guide effect allows the propagation of Pacific and tropical variability, El-Niño-Southern Oscillation (ENSO) signals (internal Kelvin waves or slope trapped waves), which are a considerable part of the SL interannual energy in the GAB (Clarke 1991; Li et al. 2004). Contrary to the eastern margins of the Pacific Ocean (Huyer et al. 1987; Shaffer et al. 1997; Jacox et al. 2015), during El-Niño (La-Niña) events, the tropical Australian region responds with negative (positive) sea level anomalies resulting from anomalous tropical westerlies. Hence, the north, west, and southern Australian coastline experiences lower (higher) sea level and thermocline uplift (downward), enhancing (reducing) the summertime upwelling during El-Niño (La-Niña) episodes (Li et al. 2004; Middleton et al. 2007a) .

While the SL response to ENSO is well-understood, recent and direct observations of upwelling during strong El-Niño events are limited. Also, the remote effects of ENSO along the southern end of the EGAB have not been fully explored. Middleton et al. (2007a) for example, noted that a seasonal asymmetry in SL anomalies in the EGAB that they attribute to ENSO. They also suggest that the weakening of shelf break alongshore transports associated with ENSO was less clear in summertime during ENSO events.

The upwelling regions in the EGAB are important. For example, the BC is a feeding ground for blue whales that abound during summer (Gill 2002). It is also a natural habitat of the most valuable fisheries in South Australia, rock

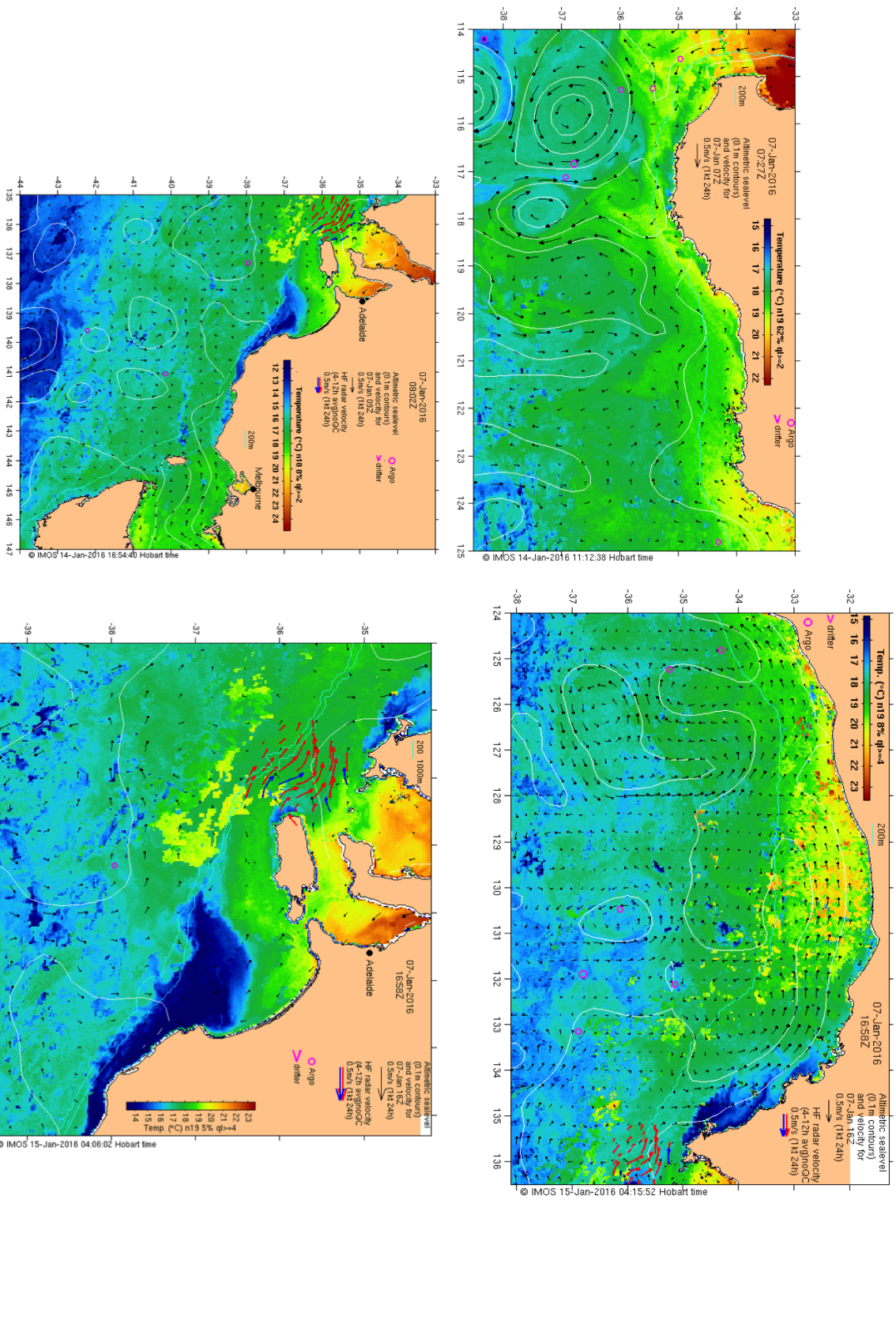

Figure 1.2: A Collage of the upwelling system in the GAB–January 2016 events. (a) The western limit of the GAB. (b) mid and northern EGAB. (c) southern EGAB. (d) The detail of the BC. Note the SST range is different within the figures. The contours and vectors represent dynamic topography (m) and geostrophic velocities (m/s) from altimetry, with other information. Courtesy of *oceancurrent.imos.org.au*

lobster (Linnane et al. 2010). The EGAB also sustains hot-spots of primary productivity and important national and state-wide fisheries (Ruth et al. 2010; Ward et al. 2006). The GAB is particularly important because it supports roughly 1/5 of the total Australian fisheries value (Savage 2015).

Despite its significance, very few regional and numerical studies have focused on the upwelling circulation of the EGAB (mostly limited to Cai 1992; Middleton et al. 2003; Middleton et al. 2007a; Kämpf 2010). From these studies, only two include numerical models of the BC upwelling (Cai 1992; Middleton et al. 2003), with only one study actually focused on the Bonney Coast (Cai 1992).

By contrast, more attention has been given to the northern EGAB. For example, it's known from both numerical models and observations that, despite the SST upwelling signal being smaller in the vicinity of KI, a strong sub-surface upwelling signal ('cold pool') is a permanent feature during summer (Middleton et al. 2003; McClatchie et al. 2006; Kämpf et al. 2004). Kämpf (2010) attributes the cold pool to canyon upwelling mechanisms.

1.1 Motivation

A key motivation for this study is to better understand the upwelling circulation in the EGAB and understand why upwelling is stronger in some locations compared to others. More specifically, we wish to better understand the role of alongshore topographic variations, the role of CTWs, the pathway of upwelling flows, and the relative roles of remote- and local forcing.

The BC upwelling is regarded as a classical case of two-dimensional wind-driven upwelling e.g., Middleton et al. 2003. However, this position seems somewhat inconsistent with the plume characteristics (Figure 1.2c). We wish to better understand what drives the alongshore variations of temperature - and to understand whether BC upwelling is indeed two-dimensional - or if its more complicated.

Also, much has been written recently about the impact of ENSO on the western and southern Australian shelves (Clarke et al. 1994; Li et al. 2004; Middleton et al. 2007a; Kataoka et al. 2014; Feng et al. 2014) – but some of the local impacts and timing of this influence remain unclear. We wish to re-examine this teleconnection in detail, understand the implications of tropical anomalies in influencing upwelling in the EGAB as well as other remote influences.

Additionally, new observational efforts in the region were made in the last decade. In particular, during one of the strongest El-Niño events of the last century, between 2015–2016, two autonomous underwater vehicles (gliders) sampled the BC region in an unprecedented observational effort. Together with other observations, including HF radar, moorings, tide gauges, and satellite measurements, the observational

coverage of the BC represents a unique opportunity to study and better understand this region.

1.2 Objectives

The main goal of this thesis is to study the dominant physical drivers of the summertime shelf circulation of the EGAB through numerical modelling and observations. More specifically, this thesis explore local and remote physical processes that control the development, localisation and modulation of the onshore flow and the upwelling conditions along the EGAB, with a particular focus on the BC region.

Several questions regarding the upwelling distribution in the GAB are still open:

1. How the vertical and horizontal upwelling distribution is affected by upwelling winds?
2. Is the alongshore topography important off the Bonney Coast?
3. What is the impact of the weather band CTWs signal in the EGAB upwelling regions?
4. How does the interannual variability in Sea level, Winds, and currents regulate the upwelling in the region?
5. Can we robustly detect and attribute El-Niño and/or other climate influences on the upwelling at the EGAB/Bonney Coast?

The overall aim of this thesis is to answer the above questions. The tools selected to answer these questions are a realistic Ocean General Circulation Model (OGCM) with idealised forcing and the observational analysis of several new independent observational datasets.

Hence, the specific objectives are to:

- Develop a numerical ocean model of the EGAB;
- Using an idealized surface forcing model, understand how the upwelling circulation over the shelf develop;
- Using a model with idealised boundary forcing, understand how the upwelling circulation over the shelf responds to the passage of CTWs;

- Study the interannual variability within the EGAB with new observations (gliders, sea level stations, local and satellite winds, SST, moorings);
- Provide an observational perspective of both wind-driven upwelling distribution and remote effects along the EGAB and the BC;

In the next Chapter, a brief review of the general circulation in the EGAB is presented, focused on the summertime upwelling, and the role of interannual variability. A short description of the OGCM used in this research is also provided in Chapter 3.

In Chapters 4 and 5, questions 1,2, and 3, above, are answered with a numerical model using idealised wind forcing and periodic but remotely generated CTW. Chapter 6 addresses the last questions, providing an interannual perspective of the upwelling variability, an updated view on the El-Niño role within the EGAB, and a synoptic view of the extreme upwelling season of 2016 along the BC. Moreover, the Chapter provides strong support of the results obtained with the numerical model used.

Finally, an overall summary and conclusions of the thesis are provided, along with an indication for future studies.

1.3 Summary of the thesis

As will be clear throughout the thesis, the topographic influence on the wind-driven upwelling circulation is remarkable. Numerical results with wind forcing suggest that valleys and submerged headlands/banks steer the bottom onshore flow, with bottom temperature fronts found locked to the topography. The overall net result, particularly along the BC, is downwelling on top of the headlands and upwelling on valleys. This circulation is found consistent with barotropic vorticity dynamics (Gill 1982). Upwelling is found to be stronger on the equatorward side of the headlands (here upstream in the CTW sense). This result derives from the alongshore baroclinic pressure gradient setup by the density field, which drives an onshore geostrophic flow.

The EGAB is suggested to be more prone to upwelling than the western sector, in accordance with barotropic CTW theory. This feature is a consequence of the fact that the time scale for viscous shut-down of interior upwelling is shorter than the arrival of the CTWs front generated in the west. The propagation phase within the numerical ocean model is highlighted, matched qualitatively with the theory, dissipating and redistributing energy along the isobaths. Particularly at KI, the bottom flow at the canyons is enhanced, while at the BC, the flow is again sensitive to the valley and headland distribution.

Furthermore, interannual analysis of observations confirmed the large influence of remote variability and El-Niño on upwelling, with a strong response associated with ENSO in sea level, bottom temperatures, and SST — the latter with statistically significant long time lags. An influence of the Southern Annular Mode (SAM) is found on alongshore winds in the GAB as well as a weakening of the SAC during summer at the BC. Recent observations support the existence of an almost one-to-one relationship exist between bottom temperatures in the GAB and SST anomalies in the central Pacific Ocean — a practical result.

Finally, high fidelity surveys along the BC highlight that one of the most extreme upwelling seasons in history occurred during 2016. ENSO effects in conjunction with strong anomalous winds led to record low SST, bottom temperatures, and large primary productivity. The observations confirmed the idealised model results — stronger upwelling is found on the equatorward side of the valleys and submerged headlands.

This study is important because it provides the most comprehensive description of the upwelling circulation along the BC, using both numerical tools and observations. The bottom pathway of the cold waters is evaluated, explained and shown to be highly sensitive to local topography and remote effects. The role of ENSO is robustly confirmed in the entire GAB and with another climate variability that needs to be constantly monitored — the SAM. The results found here are important for future observational efforts, management of fisheries and prediction of the EGAB upwelling system as a whole.

Chapter 2

A Brief Literature Review of the coastal circulation in Southern Australia

2.1 Geography and General Circulation in the Great Australian Bight

As shown in Figure 1.1, the shelf over the Southern Australia coastline varies spatially. The almost zonal region has a relatively narrow continental shelf in the west, close to Albany (Western Australia (WA)), widening after Esperance and with maximum shelf-width towards Eucla (South Australia (SA)). At about Thevenard in the Eastern Great Australian Bight (EGAB), the shelf width starts to reduce, and the orientation of the coastline becomes more northwest–southeast. A narrow shelf is located near Kangaroo Island (KI) region, close to the Gulfs. Continuing eastward, the shelf abruptly widens again in the Lacepede Shelf (LS) before narrowing at the Bonney Coast (BC). Towards the major cape to the south (Portland), the shelf widens again towards the Bass Strait. The EGAB shelf-break region has several canyons (yellow and red striped patterns in Figure 1.1), mainly in the vicinity of KI and BC. The canyons at KI are classified as shelf-incised canyons, following the classification of Huang et al. (2014), while those at the BC are confined to the slope, without a direct connection to the shelf – classified as blind canyons.

The general circulation is forced by seasonally-varying winds (Figure 2.1) that are predominantly zonal, with large wind-fetch (i.e., relatively spatially uniform). The circulation is characterised by low interannual sea surface height variability and slow ocean currents if compared to the other sub-tropical regions in Australia (Middleton et al. 2007b).

The seasonal migration of the subtropical atmospheric high-pressure systems over the region provides a stronger intraseasonal variability in the wind patterns. Between April and September (austral autumn–winter), Figure 2.1, the semi-permanent high-pressure system tilts to the north, reducing the wind stress curl over the ocean. Hence, stronger westerly/north-westerly winds are present over both the shelf and the open ocean — a stronger influence of the Southern Ocean westerlies. In spring–summer, the high-pressure system migrates meridionally to the south, increasing the wind stress curl over the ocean and providing marked upwelling favourable winds over the entire Greater Australian Bight (from Cape Leeuwin to Tasmania). This mechanism is clearly seen in the weak mean wind vector magnitude band during summertime (e.g. March in Figure 2.1), that shifts its position meridionally and forms a band of strong variability in zonal wind stress between $35°S$ and $40°S$. Most of the wind stress-curl during summer indicate downwelling conditions at the top of the surface Ekman layer for this region (see Risien et al. 2008). These seasonal wind patterns alone can explain a lot of the surface ocean circulation in the region, besides the oceanic currents being

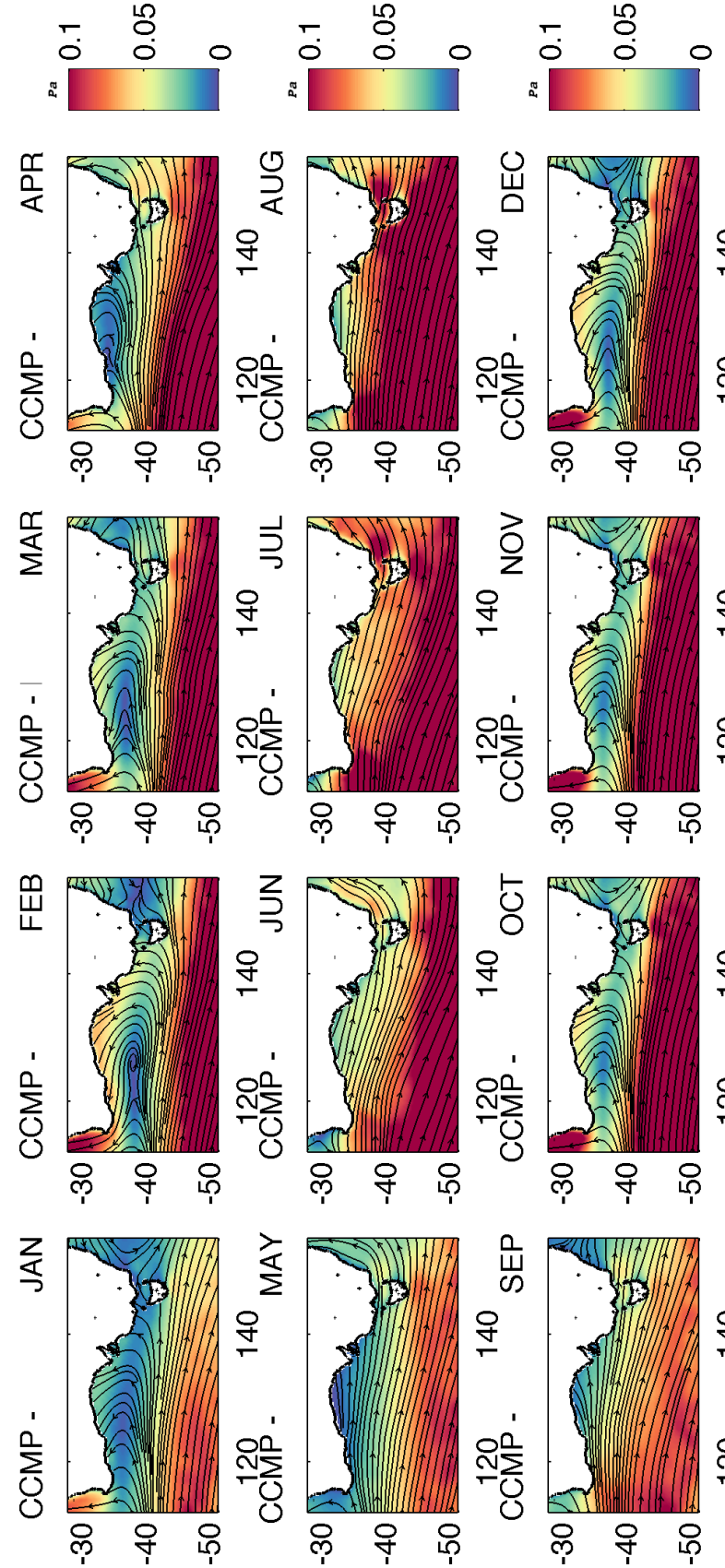

Figure 2.1: Monthly means of the wind stress magnitude (shading – Pa) and direction (streamlines) in Southern Australia. The period used is from 2005–2011. Data source: CCMP – Atlas et al. (2011).

maintained and affected by different processes.

The Leeuwin Current (LC) is a warm and relatively fresh ($26-18°C$,$34.9-35.7psu$) surface current located at the shelf-edge, flowing from the north-west coast of Australia, following the southern tip of WA and into the southern zonal shelves (see Fig. 2.2a,b). The alongshore pressure gradient driven by low density, tropical waters overwhelms the northward wind-stress forcing in WA, generating a narrow southward current with velocities in excess of $30cm/s$ in the upper $50m$ off the shelf-break that is strongest between autumn and winter (Cresswell et al. 1993; Feng 2003; Ridgway et al. 2004). After the namesake Cape, the flow continues towards the southern shelves with different names; the south-eastward current is called the South Australia Current (SAC) towards the east, while close to Tasmania it is termed the Zeehan Current (ZC) (Ridgway et al. 2004; Cirano et al. 2004; Middleton et al. 2007b). Despite the different names, the whole system is a poleward flow along the shelf-break that transports heat poleward, as shown in Figure 2.2b and e.g., in Ridgway et al. 2004.

The differences in the nomenclature of this flow are mainly due to the seasonality of the currents, wind forcing and different water mass characteristics. Following the current from the west, the LC-SAC boundary limit can be considered between $125°E$–$130°E$ — geographically located when the shelf starts to widen after Esperance. At these limits, the Great Australian Bight (GAB) outflow is characterised by warm and salty waters that are formed on the shelf and are entrained near the shelf-break (Ridgway et al. 2004). This entrainment affects the water mass signature to the east (see Fig. 2.3a,b and also Richardson et al. 2009). Here and below, we follow conventions, and we refer to the main surface flow over the shelf break along the eastern GAB as the SAC.

In wintertime, the winds drive a south-eastward flow, and the current system appears as a single, strong boundary current, while in summer, it is much weaker (Middleton et al. 2003; Middleton et al. 2007b). The enhancement by the westerly winds and cross-shore pressure gradients have already been proposed in studies with numerical models (Middleton et al. 2003; Cirano et al. 2004). A topographic Sverdrup transport generated by onshore Ekman flow in winter enhances the eastward flow, and over the EGAB, both wind-forcing and downwelling-generated pressure gradients are important in driving the bulk of the flow (Cirano et al. 2004).

During summertime, with the opposing winds, the cross-shore barotropic pressure gradient is relaxed and shelf-break (shelf) currents are reduced (reversed); e.g., compare the coastal sea level height in Fig. 2.2a and Fig. 2.4a. The summer is also when the positive wind stress curl within the Southern Australia Sea is maximum. The associated northward and oceanic Sverdrup transport of this

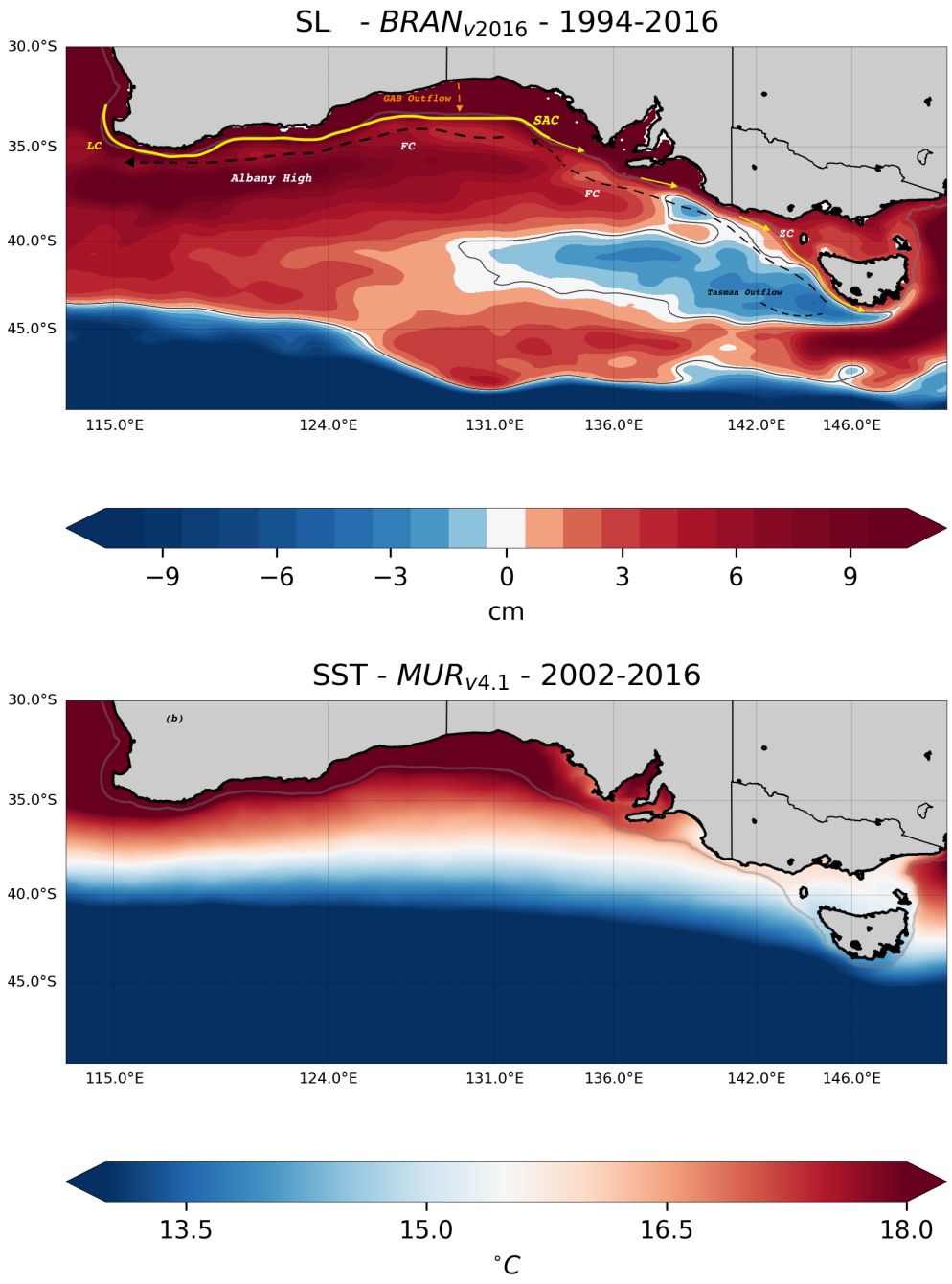

Figure 2.2: (Top) A schematic with the long-term mean Sea level height from the BlueLink ReANalysis (BRAN) (1994-2016) (Oke et al. 2013). (Bottom) The long term mean SST from Multi-scale Ultra-high Resolution Sea Surface Temperature (MUR) reanalysis product (2002-2016). The grey line represents the $200m$ isobath. Note the coastal pressure gradients and boundary signature of the LC-SAC signature, the deep north-westward Flinders Current (FC) flow signature (relative ridges along the slope region) and the Tasman Outflow (thin black contour). The heat transport is clearly seen through a narrow boundary current towards Tasmania. Within the EGAB, a weak signature of upwelling and winter cooling is present.

forcing, would then reach the slope and flow from east to west leading to the FC (Bye 1972; Bye 1983; Middleton et al. 2002; Middleton et al. 2003). This sub-surface flow is associated with interior upwelling at the shelf-break and thus defined as an upwelling favourable current Middleton et al. 2002.

One of the first measurements and findings of the FC was made by Bye (1972) and Bye (1983) — demonstrating that the Sverdrup flow is deflected by the topography, turning into a north-westward flux as the sum of the spatially variable Ekman and geostrophic transports. The FC is a year-round under-current, centred close to the permanent thermocline ($600 - 1000m$), with an upwelling favourable bottom boundary layer (BBL) (Middleton et al. 2002; Middleton et al. 2003; Cirano et al. 2004).

The Sverdrup transport signal of the FC is much narrower (wider) in the north-west (south-east) – see the relative ridges in Fig. 2.4a and/or Fig.1b of Middleton et al. (2002). The narrowing of Sea Level Anomaly (SLA) ridges between the coast and the "Albany high" (Fig. 2.2a) is where the FC is usually well defined, with higher transports (Cresswell et al. 1993; Middleton et al. 2003; Middleton et al. 2007b). The wider nature of the flow in the south-east, the role of the westward eddies and lack of direct observations complicates the definition of the FC there, given the current merges with the Tasman Outflow pattern (Middleton et al. 2003; Ridgway 2007a). The signature though is still clearly identifiable in both observations and models, by reduced SLAs offshore of the shelf-break, enhanced during summer (see Fig. 2.4a and also (Schiller et al. 2008)).

Of particular interest is the summer and upwelling circulation, modelled in Middleton et al. (2003). In the wider shelves in the north (Eucla), a positive wind stress curl over the shelf generates seaward transports and convergence with the oceanic Sverdrup transport (their Figure 9c). Hence, downwelling and an eastward flow over the $200m$ isobaths were found in general, with upwelling over the shelf. In general, the surface circulation in the model indicated wind-forced upwelling (offshore Ekman transport) with isotherm displacements up to $150m$ depth, north-westward currents (5–$10cm/s$) and an important advective flow over the bottom in the outer shelf off Kangaroo Island.

In the same study, the SAC warmer flow was also in clear contrast with the colder SSTs found over the shelf in the Eyre Peninsula (EP), KI and BC regions — all consistent with two-dimensional wind-forced upwelling (see also Fig. 2.4b). A narrower SAC was found poleward, indicating year-round downwelling conditions over the shelf-break. The minima in SST were found north of the BC, but with a plume attached to the coast instead of shifted to the west as is indicated in Fig. 2.4b. The model was clearly limited towards the south, with the resolution not permitting the BC to be properly resolved, both given by nominal resolution

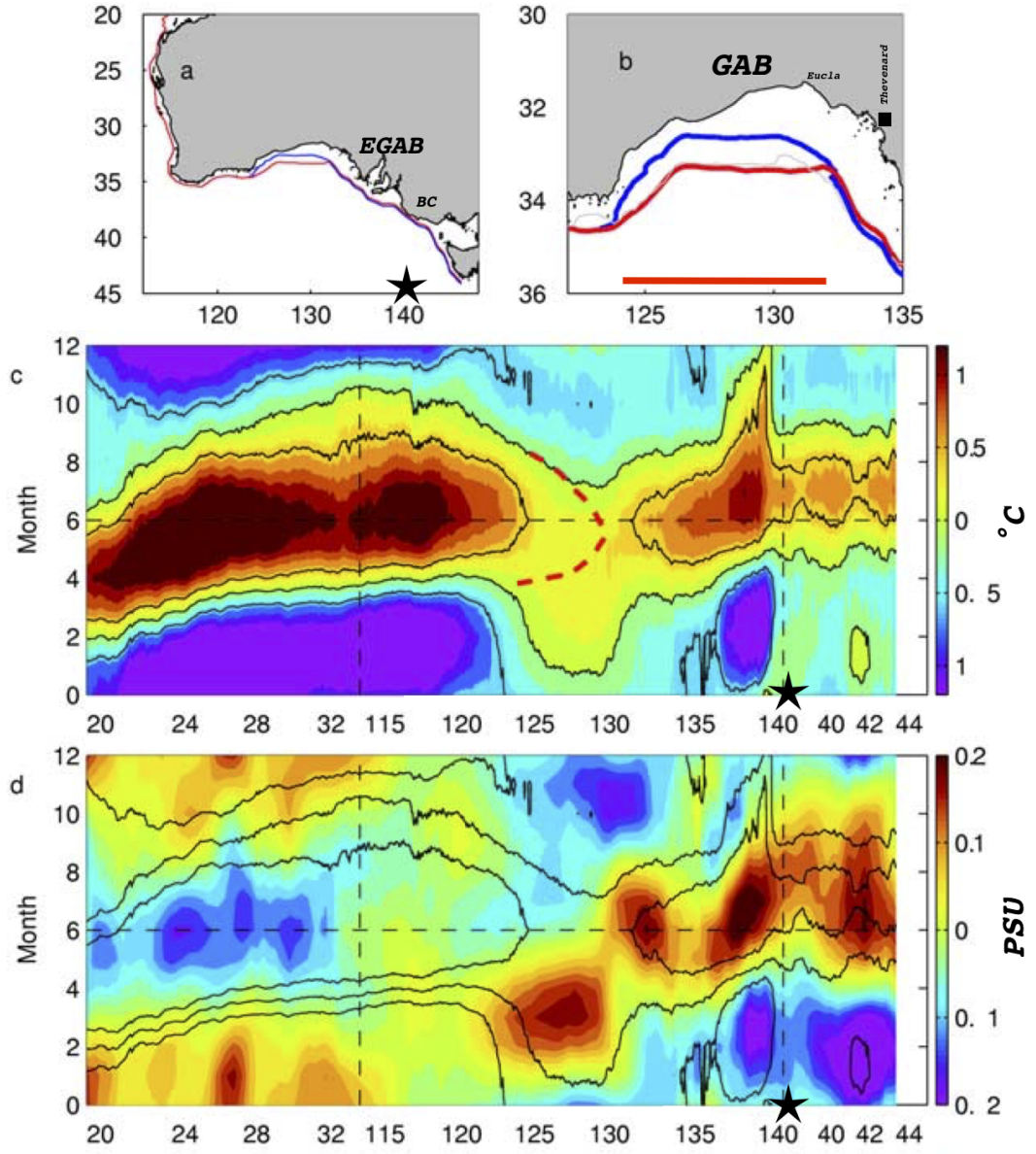

Figure 2.3: The mixing pathway along the LC-SAC system (adapted from Fig.10 in Ridgway et al. 2004). The alongshore red-line follow the shelf-break and the warm signal of the current system (a,b). Temperature (c) and Salinity (d) along the transect are anomalies from a spatial mean, and a spatial seasonal cycle between $112°E$ and $145°E$ and are representative of the first $300db$ following the shelf-break. Note the change in $x - axis$ values in (c,d) to match the shelf-break orientation and that in (d) black contours are Temperature ($°C$). The dashed curve red line is the 'limit' of the LC and the GAB outflow region (horizontal red line in (b)). The BC southern limit is located approximately at $141°E$ (black stars). Note the reduced temperature and salinity close to the BC during summertime.

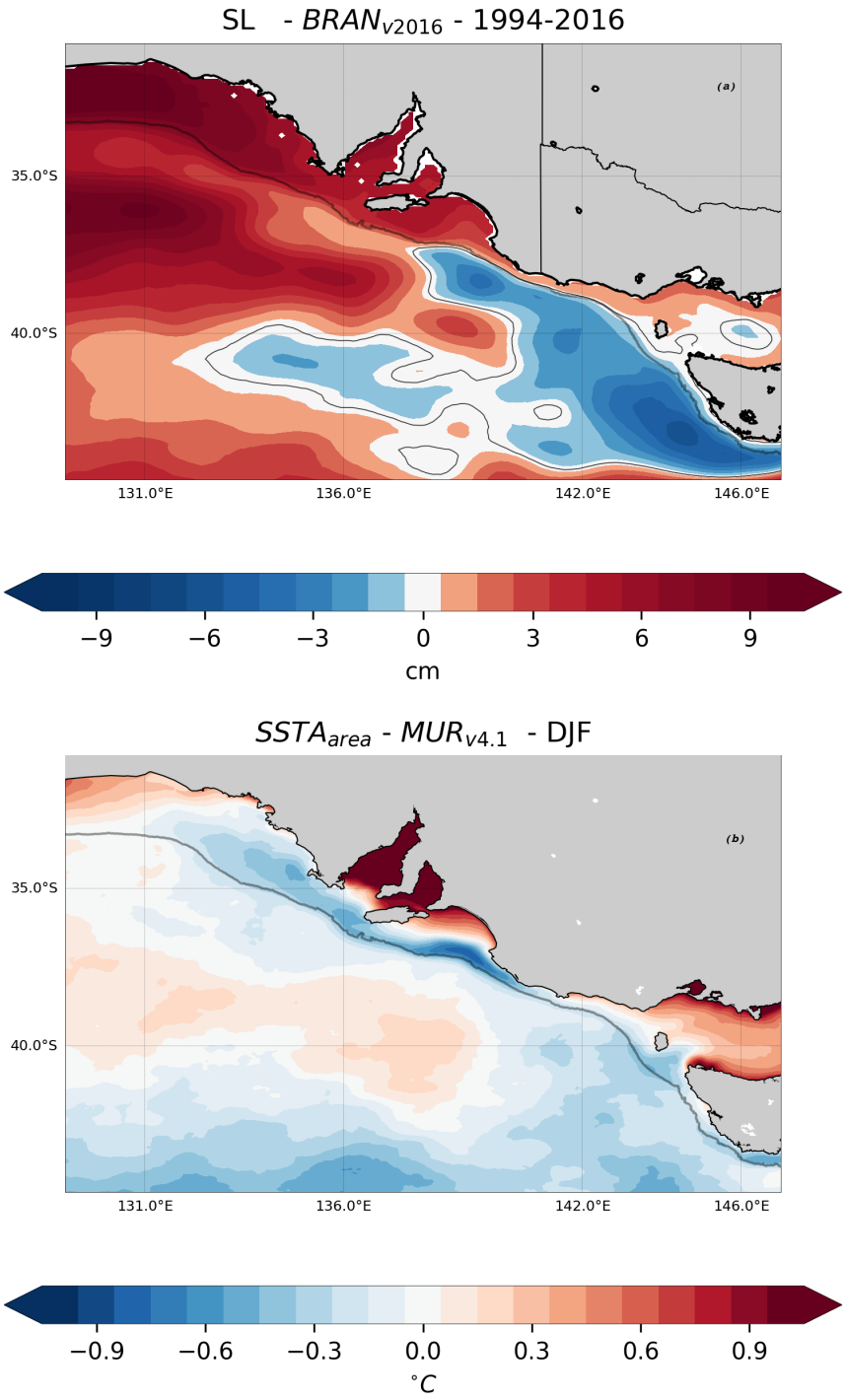

Figure 2.4: (Top) As in 2.2a, but for canonical summer (DJF) along the EGAB. (Bottom) The canonical summer (DJF) Sea Surface Temperature (SST) anomalies. The anomalies are relative to a normalised, regional and monthly cycle series ($SSTA_{area} = SST - SST_{regional}$) – as in Ridgway et al. (2004). Hence, the heating/cooling is relative to the white regions. The thick grey line delimits the $200m$ isobath. Note the increased signature of the FC in SLA in summer, strong heating (Gulfs and shallow areas) and general upwelling onshore of $200m$ (as well as a weaker SAC)

and by the lack of a shelf in the region ($z > 200m$ is over the entire BC region in their model).

Vertical mixing with FC waters over the shelf is confirmed in the isotope and water mass analysis of Richardson et al. (2009) but focused on the northern EGAB. Of interest here is the definition of a FC water mass: $T < 15.°C$ and $S < 35.5psu$ (see Table 2. in Richardson et al. 2009). The GAB plume/outflow water mass was also found to mix with FC waters ($35.9 < S < 36.2$), but the detection to the south was more limited due to lack of observations and strong mixing/upwelling. Nonetheless, their vertical profiles did indicate stronger upwelling in the KI and BC regions (their Fig.7).

In summary, the south-eastward, downwelling SAC is a year-round surface current, weaker (stronger) in summer (winter) and with a marked influence from shelf processes, particularly in the wider shelves within the mid-GAB. Below the upper ocean, the undercurrent associated with the FC has a deep upwelling signal, north-westward flow at about the permanent thermocline and is predominantly confined to the slope. In the mid-south EGAB, a large uncertainty still remains regarding both flows, mainly by the lack of direct and sustained observations. There, the surface signature of SAC is much narrower, while the FC is broad and merged with the Tasman Outflow region. Mixing with FC waters, however, is found over the slope and the shelf. The oceanic currents would then represent the variability in density distribution at the slope and thus regulate the source waters for upwelling.

2.2 Observations, shelf processes and interannual variability

The coastal upwelling fronts are regular features of the eastern GAB and have being reported in the literature in both modelling and observational studies (Rochford 1977; Lewis 1981; Schahinger 1987; Cai 1992; Middleton et al. 2003; Kämpf et al. 2004; McClatchie et al. 2006; Richardson et al. 2009; Kämpf 2010). The coastal upwelling signal in the northern limit of the EGAB is smaller, while towards the south, the signal is stronger to the west of the EP region, within the KI region and the strongest at the BC (see Figs. 1.1, 1.2, 2.4b).

Kämpf et al. (2004) reported a strong upwelling signal at the EP region, coherent with the SST at the BC, consistent with wind-forced upwelling and peak lag in Chlorophyll-A (Chl-A). The KI surface upwelling signature is in general weak and narrow, but at sub-surface, the region has a bottom trapped 'cold pool' signature, which is a predominant summer feature (Middleton et al. 2007b; McClatchie et al.

2006; Ruth et al. 2010).

McClatchie et al. (2006) presents an analysis of the water masses around the region and found that the cold pool waters remain nutrient rich, and are advected onshore and then westward along the EP region (see Figure 2.5). The pool is regarded as having waters as cold as $13.5°C$ and salinities ranging from $35.2 < S < 35.3$ psu. The shelf-break upwelling and the pool was found to be one of the reasons why the EP upwelling is so coherent with the BC — previous bottom upwelling and northward advection maintains the SST coherence. Although the Gulfs are an important source of dense water formation for the shelf, during summer a compensating density front is formed at the mouth of the Spencer Gulf and cross-shelf exchange is mostly arrested (Nunes Vaz et al. 1990).

Model results from Middleton et al. (2003) and Kämpf (2010) do indicate upwelling to be strong in the cold pool region, where the shelf-width changes over short distances and there are shelf-incisive canyons near the shelf-break. In particular, the model results reported by Kämpf (2010) indicated that a $0.02Pa$ alongshore wind-stress forced upwelling associated with the cold pool has a strong influence from the *du Couedic* canyon. Bottom velocities in excess of $0.4m/s$ filled the pool region, with waters as cold as $10°C$ and with a reduced response with the 'no-canyon' experiments (see his Figure 5.).

In the southern EGAB, upwelling is known to be stronger over the BC, as first observed by Rochford (1977). The upwelling was better characterised by Lewis (1981) and Schahinger (1987), where the horizontal structure was first observed, showing both a BBL and interior upwelling flow (see Figure 2.7). In the observations of Lewis (1981), the synoptic distribution of surface temperature and salinity provided the first clue that some regions in the BC could be more prone to upwelling. In the El-Niño year of 1983, up to $11 - 12°C$ waters reached the shelf break with strong alongshore currents developing during mid-March (Schahinger 1987). During the sampling, mean winds were $0.10Pa$, strong alongshore velocities developed (of up to $40cm/s$), but with stronger variability (standard deviation up to $20cm/s$). He also found a lag in Sea Level (SL) of 12–18hr between Portland and the pressure gauge in the north (black triangle in Fig. 2.7 top), for oscillations in the 2-10d band. Moreover, within the inner shelf, upwelling currents leading those offshore with good correlations between currents and SL.

The BC plume seasonal variations were studied by Nieblas et al. (2009) with a focus on primary productivity. They report a higher variability in SST during summer, more frequent days of upwelling winds up to April and a larger plume area in March. Alongshore winds, SST, and CHL-A were well correlated in the seasonal cycle. They also found marginal relationships between upwelling and El-Niño-Southern Oscillation (ENSO), but the time series were short and results

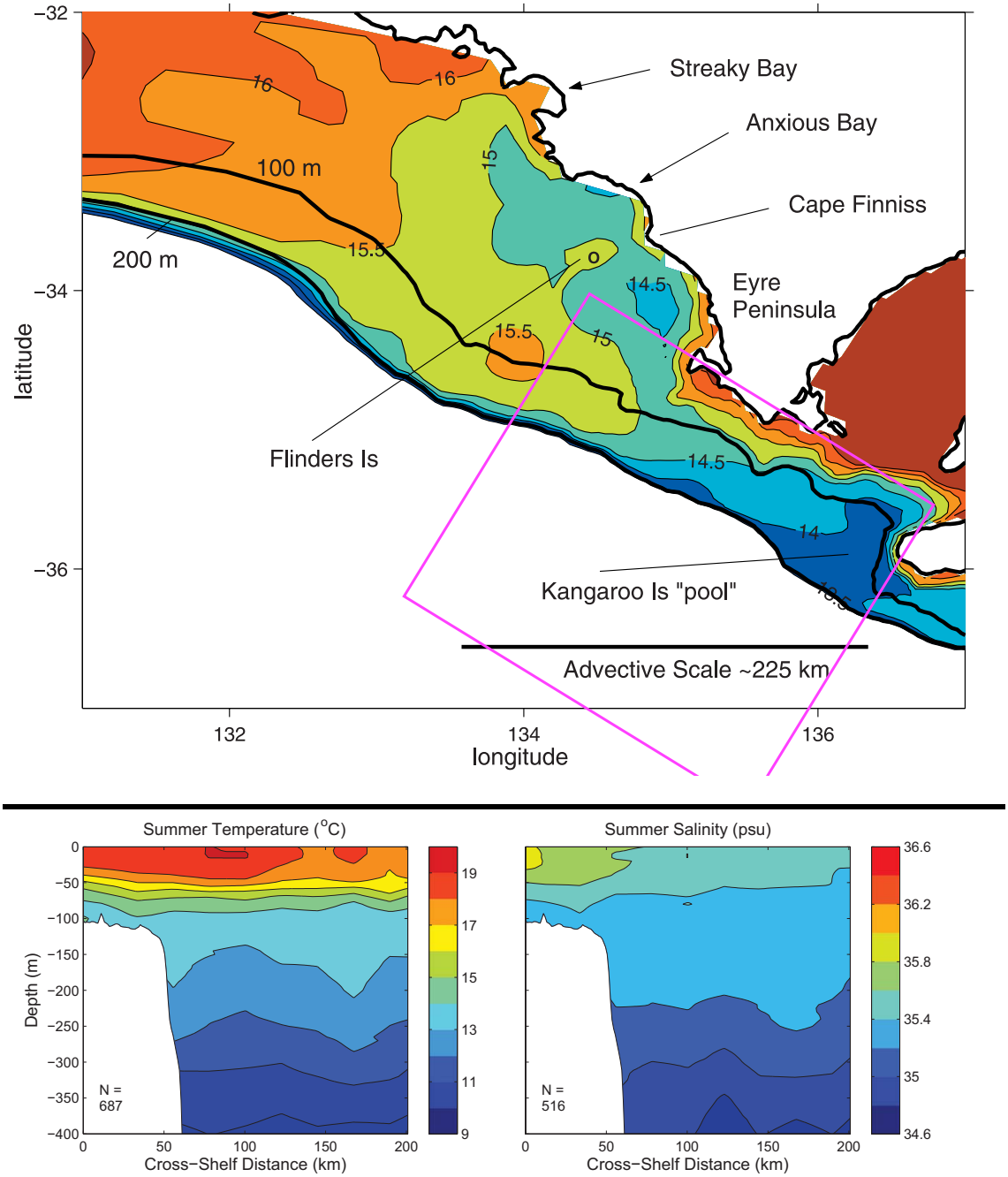

Figure 2.5: The KI cold pool (adapted from McClatchie et al. 2006; Middleton et al. 2014). (a) Horizontal distribution of Bottom Temperatures from the CARS2009 Atlas. (b) TS cross-shore profile from several casts obtained from the same atlas and augmented by recent cruises. The data in (b) is approximately contained in the magenta square in (a).

not conclusive in their analysis (1994-2007). The plume off the BC is particular; it flows into a westward jet into the wide LS, and, sometimes, a narrow and shallow jet attached to the coast (Figure 2.6). The upwelling front appears clearly related to the topographic features.

The only local numerical study focused on the BC is the one by Cai (1992). His results indicate the role of thermal relaxation — decoupling of the SST signal with SL and alongshore currents — as well as an offshore propagation of cold waters, with upwelling predominantly from Cape Jaffa to Portland. Also, the role of realistic shelf topography was shown to be important for amplifying the upwelling rate, compared to a flat shelf (as in e.g. Peffley et al. 1976).

Since the ground-breaking studies of Schahinger (1987) and Cai (1992), there has been little advance in our understanding of the role of shelf topography in this region. The southern margins of Australia are a particular region for generation and propagation of Coastal Trapped Waves (CTWs) (Church et al. 1987; Middleton et al. 1994; Maiwa et al. 2010). CTW (or hybrid waves) are a group of low-frequency oscillations that occur trapped to the coastal ocean. The generation of CTW is through changes in vorticity, with a cross-shore Ekman flux the most common method of generation (Gill et al. 1974; Clarke et al. 1985; Middleton et al. 1990). Trapped to the shelf and slope, they are the main source of variability in shelf-currents and sea level at sub-inertial time scales (Csanady 1978; Brink 1982).

For large-scale or idealised geometries with deep, vertical, coastal wall, the oscillations are trapped with a scale on the order of the Rossby radius of deformation — Kelvin waves. By the presence of a step or slopping shelf, motion becomes dependent (and trapped) on the shelf-slope and width. As well, the slope of isopycnals close to the boundary also acts to generate internal modes, such as internal Kelvin waves and baroclinic shelf waves. The CTW name convention usually applied when stratification is present, otherwise, Continental Shelf Wave (CSW) is used (when the Burger number is negligible). These waves, by conservation of vorticity, travel poleward along the GAB coastline (coast to the left in the Southern Hemisphere), with large spatial coherences. For the weather band between $8 - 15d$, they possess strong amplitude at Thevenard and coherence over the whole southern shelf (Church et al. 1987). Maiwa et al. (2010) through modelling studies provide some insight on the propagation nature on the southern shelves driven by wind patterns. Their results were consistent with observational data and dominance of the first CTW mode.

The role of these waves along the coastline is also not limited to the weather band and considerable advance was made within the seasonal and interannual variability in the form of much lower frequencies. The effect of the coastal wave guide is clear in the seasonal cycle variability (annual harmonic) of SL and currents

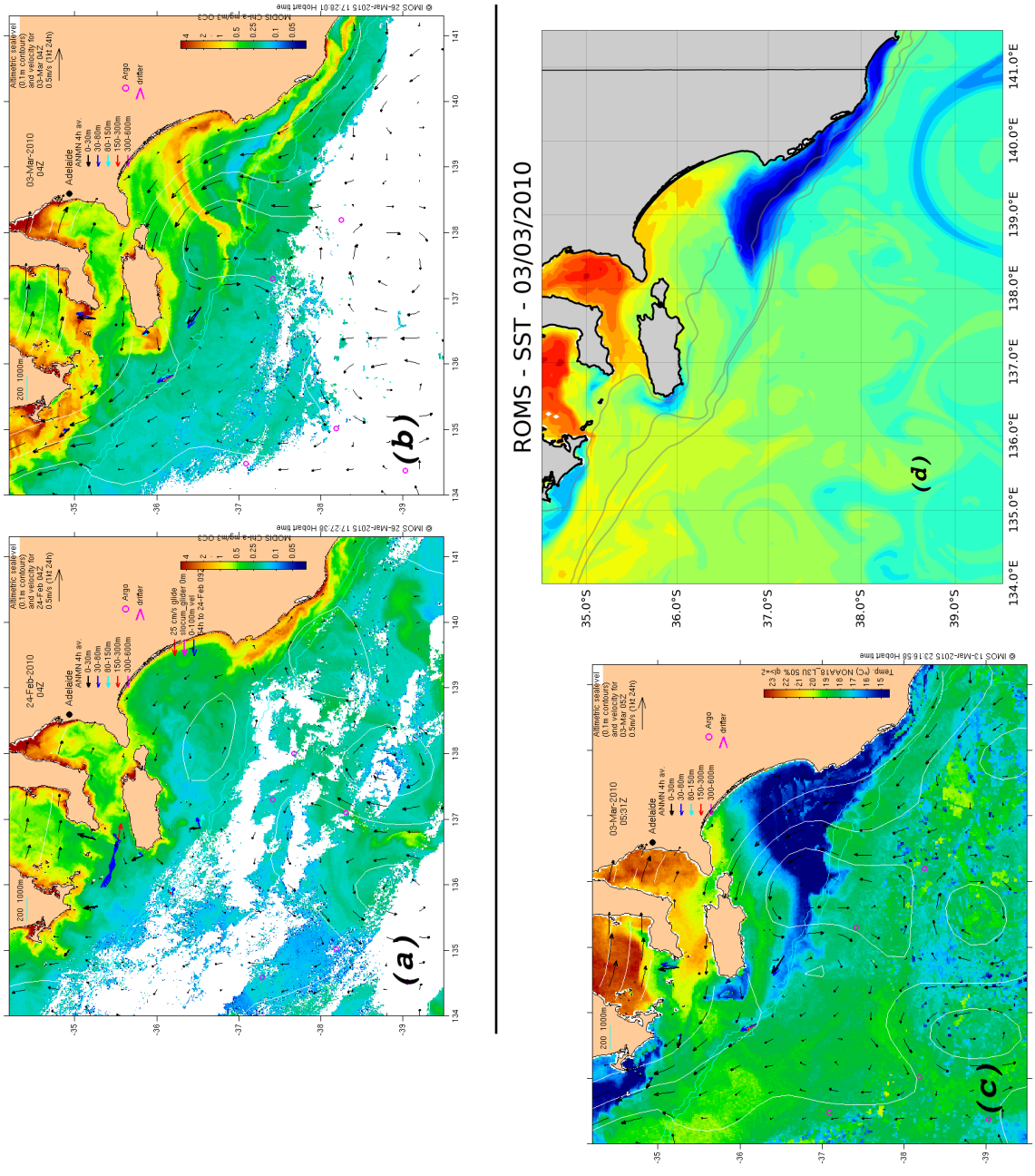

Figure 2.6: The BC upwelling plume in CHL-A and SST during an upwelling event in late February 2010. (a,b) CHL-A (MODIS) just before (a) the onset and after (b) sustained upwelling favourable winds. (c) the sustained SST signal of upwelling (values were also low in February). (d) SST from the same numerical model used this thesis, but with realistic atmospheric and oceanic forcing, but no tides (De Oliveira, unpublished results). (a,b,c) are remotely sensed CHL-A and SST from multiple sources (IMOS - *oceancurrents.imos.org.au*). Note the westward advection of cold waters, upwelling fronts in the fringe of the plume along the BC, and the upwelling of clear waters (low CHL-A) in a strip alongshore. The model is clearly warmer than in observations, but still with the upwelling and the same circulation features.

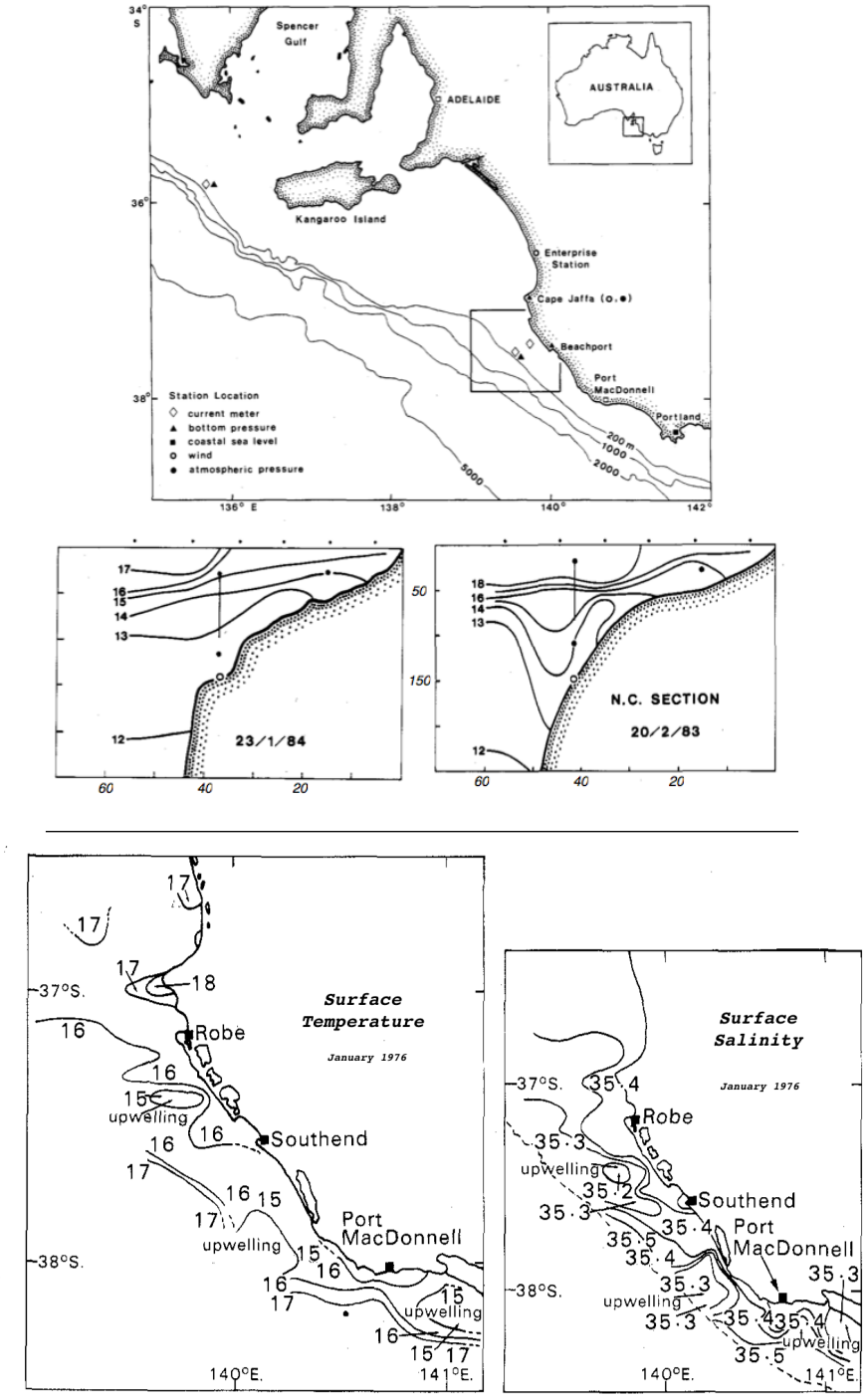

Figure 2.7: One of the first observations of upwelling in the BC (adapted from Lewis 1981; Schahinger 1987). (Top) location of the moored equipment (between Cape Jaffa and BeachPort). January (middle left) and February (middle right) cross-shore section of temperature. The circles atop of the upper x-axis are CTD stations, the vertical line the thermistor string, large black dots current meters, and white dots bottom pressure sensor. Depths are in meters and distance in km. (Bottom) Surface Temperature and Salinity in 1976 from Lewis (1981). Note the relatively sharp fronts in salinity close to the Bonney Lake (between Southend and Port MacDonnell), and the upwelling south of Robe.

along Australia's eastern margins (Ridgway et al. (2015) – see their figure 5.) — i.e., the coastal ocean is continuously connected from the tropics to western Tasmania in a very wide band of frequencies.

Over the southern shelves, Pariwono et al. (1986) was the first to identify a connection between sea level interannual variability and ENSO between the north, west and southern Australia. Contrary to the eastern margins of the Pacific Ocean (Huyer et al. 1987; Shaffer et al. 1997; Jacox et al. 2015), during El-Niño (La-Niña) events, tropical and southern Australian regions experience lower (higher) sea level and thermocline uplift (sinking), enhancing (reducing) the summertime upwelling (Li et al. 2004; Middleton et al. 2007a). The pattern of this oscillation is very clear in the correlations with an ENSO climate index, as shown in Fig. 2.8.

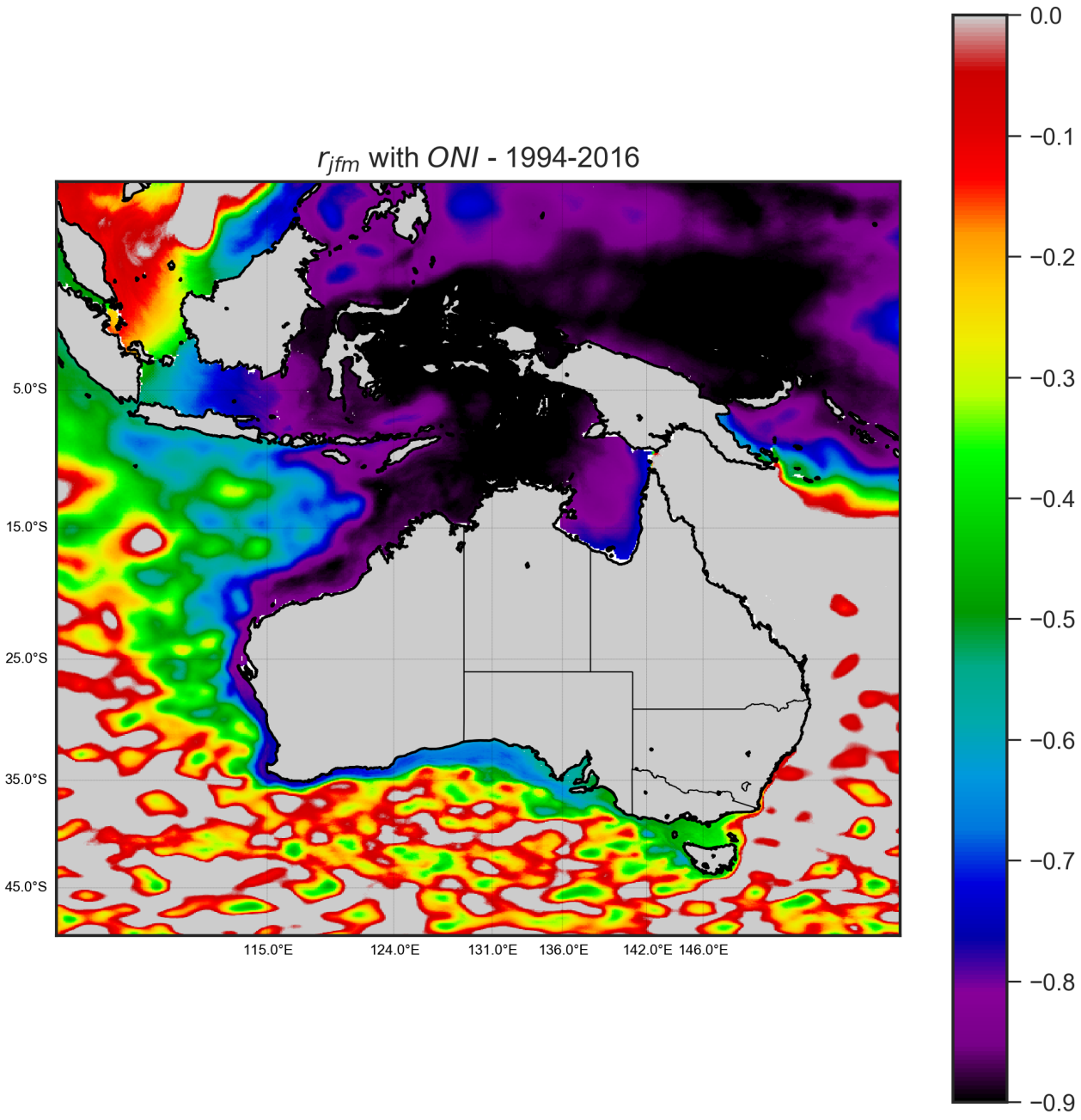

Figure 2.8: The correlation between the Oceanic Niño Index (ONI) index, an ENSO metric, and SL in the Australia eastern margins. The data is from $BRAN_{v2016}$ (Oke et al. 2013). Note the equatorial westward extension away from the shelf (equatorial rossby wave scattering - $r \approx 0.6$) and the trapped nature towards the south (Kelvin wave dynamics), mainly in the largely zonal southern shelves of Australia.

The reason for this is related to the propagation of long waves along the equator and the Australia coastline (Clarke 1991; Clarke et al. 1991; Clarke et al. 1994; Verschell et al. 1995; Meyers 1996; Li et al. 2004). Despite the complex topography and narrow straits, the Indonesian archipelagos still permit Pacific Ocean and tropical variability to leak towards the eastern margins of Australia (see Clarke (1991) and Clarke et al. (1994) for a theoretical perspective). The coastal wave guide nature permits these oscillations to propagate to the southern shelves, affecting SL, the thermocline depth and ocean transports, such as the LC system (Feng 2003; Li et al. 2004; Clarke et al. 2004; Feng et al. 2014).

Verschell et al. (1995) modelled the transmission nature of low-frequency energy (seasonal to interannual) of Pacific Ocean origin, and noted that SL variability and upper layer thickness changed dramatically when the gaps between the Pacific and Indian Oceans are completely closed. The dynamics of this leakage, follow a westward and poleward propagation of waves south of the Indonesian throughflow (Meyers 1996; Li et al. 2004). These waves became strongly coastally trapped south of $20°S$ when the coastline orientation changes over the WA region (Li et al. 2004). The signal propagates attached to the coast and slope over much of the GAB. The reason why this behaviour is the regime change and the dispersion relation of planetary waves — a dispersion into westward Rossby waves changing with coastline orientation, and zonal shelves are only permissive for Kelvin waves at these scales (Clarke et al. 1991).

The net result when ENSO is in a positive phase (El-Niño) over the west and southern shelves is a strong westward geostrophic flow in El-Niño years (as shown in results of (Li et al. 2004; Clarke et al. 2004)). In this phase, a positive shift of the permanent thermocline depth occurs, with positive density anomalies and considerable upwelling (Middleton et al. 2007a). Hence, ENSO is a larger component and coherent with SL in the GAB. Climate oscillations in the Indian and Southern Ocean also have impacts in the atmosphere in the vicinity of the GAB, like the Ningaloo Niño and the Southern Annular Mode (SAM) (Cai et al. 2005; Doi et al. 2013; Tozuka et al. 2014; Wang et al. 2013), but their role during summertime in the EGAB is not well understood.

In Middleton et al. (2007a), long-term observations were used to study the El-Niño impacts in the EGAB. Sea level was highly coherent with ENSO, but both SST and alongshore wind were incoherent with ENSO indices. Hence, ENSO events were considered driven by the propagation of the ENSO signal from the west without any direct effects on winds. The results from a global model failed to identify a consistent effect of ENSO in winter and summer, with El-Niño only notably reducing shelf-edge currents in winter. However, the signal was coherent with observations of SL (as in (Li et al. 2004)),temperature profiles and bottom

temperatures over the shelf in summer.

Hence, in previous studies, the upwelling in the Bonney Coast was considered to be a classical wind-driven upwelling region. Stronger winds, the weather band and the interannual low-frequency motions along the eastern margins affect the EGAB as a whole, through changes in the thermocline depth and SL. The BC often exhibits a strong and clearer signal in the SST compared to other regions. The SST pattern is very attached to the shelf, the flow appears dependent on the shelf topography, but the onshore pathway and the role of local topography and remote forcing are little explored. The efficiency of the upwelling would clearly be dictated jointly by winds, shelf-break conditions and the role of remote forcing.

Chapter 3

Methods

3.1 The numerical ocean model

The Regional Ocean Modelling System (ROMS) is a primitive equation model with a free-surface (Shchepetkin et al. 2005). The model uses the finite-volume technique with a staggered grid, both in the vertical and in horizontal curvilinear coordinates, all within a generalized topographic coordinate that follows the ocean bottom. A split-explicit time-stepping algorithm is used to separate the barotropic and baroclinic mode, with a specific filtering scheme to reduce misfits between the coupling of fast and slow motions. The model is written in Fortran 90/95 and is widely used in a diverse number of applications, including upwelling studies (e.g., Whitney et al. 2009a; Marchesiello et al. 2010; Connolly et al. 2014; Jacox et al. 2014; Liu et al. 2015).

For an in-depth description of the model, the reader is referred to the algorithms presented in Shchepetkin (2003) and Shchepetkin et al. (2005) and within the website *www.myroms.org*. Here we provide the general equations solved by the code, and detailed aspects in the model configuration related to the numerical experiments in Chapters 4 and 5.

The horizontal discretization is done in a staggered C-grid type with curvilinear coordinates, while in the vertical a terrain-following coordinate, called a s coordinate. This coordinate is more flexible than the classical 'sigma' coordinate (Shchepetkin et al. 2005). Figure 3.1 exemplifies a typical vertical distribution of these layers used in this study over the Bonney Coast (BC). The mode-splitting technique used to separate the fast waves modes is explicit and use a time-stepping numerical method of third-order (Leap-Frog) with an Adams–Moulton corrector. The version used in this thesis is the ROMS-Rutgers version 3.7.

The general equations of motion of the model are Hedström 2009:

$$\frac{\partial u}{\partial t} + \vec{v} \cdot \nabla u - fv = -\frac{\partial \phi}{\partial x} - \frac{\partial}{\partial z}(\overline{u'w'} - \upsilon \frac{\partial u}{\partial z}) + F_u + D_u \tag{3.1}$$

$$\frac{\partial v}{\partial t} + \vec{v} \cdot \nabla v + fu = -\frac{\partial \phi}{\partial y} - \frac{\partial}{\partial z}(\overline{v'w'} - \upsilon \frac{\partial v}{\partial z}) + \mathcal{F}_v + \mathcal{D}_v \tag{3.2}$$

$$\frac{\partial C}{\partial t} + \vec{v} \cdot \nabla C = -\frac{\partial}{\partial z}(\overline{C'w'} - \upsilon_\theta \frac{\partial C}{\partial z}) + \mathcal{F}_C + \mathcal{D}_C \tag{3.3}$$

$$\begin{aligned} \overline{u'w'} &= -K_M \frac{\partial u}{\partial z} \\ \overline{v'w'} &= -K_M \frac{\partial v}{\partial z} \\ \overline{C'w'} &= -K_C \frac{\partial C}{\partial z} \end{aligned} \tag{3.4}$$

$$\frac{\partial \phi}{\partial z} = -\frac{\rho g}{\rho_0} \tag{3.5}$$

$$\frac{\partial u}{\partial x} + \frac{\partial v}{\partial y} + \frac{\partial w}{\partial z} = 0 \tag{3.6}$$

$$\rho = \rho(T, S, P) \tag{3.7}$$

Where equations 3.1 and 3.2 are the momentum balance in the horizontal and eq. 3.5 is the Boussinesq vertical balance between vertical pressure gradient and buoyancy force. The tracer field is computed from eq. 3.3, mass conservation by eq. 3.6 and the parameterized Reynolds stresses by eq. 3.4. The parameterisation of turbulent fluxes can be selected by a variety of turbulence closure models, e.g., the Generalized Length Scale class of models (Umlauf et al. 2003; Warner et al. 2005). The Equation 3.7 can be a linear or non-linear function, computed according to Jackett et al. (1995).

The boundary conditions at the surface are imposed through eq. 3.4, with prescribed stresses, fluxes and a free surface ($z = \zeta(x, y, t)$):

$$w = \frac{\partial \zeta}{\partial t} \tag{3.8}$$

with w as the vertical velocity.

The bottom boundary conditions are ($z = -h(x, y)$):

$$K_m \frac{\partial u}{\partial z} = \tau_b^x(x, y, t) \tag{3.9a}$$

$$K_m \frac{\partial v}{\partial z} = \tau_b^y(x, y, t) \tag{3.9b}$$

$$K_C \frac{\partial C}{\partial z} = 0 \tag{3.9c}$$

$$w = \vec{v} \cdot \nabla h_b \tag{3.9d}$$

$$\tag{3.9e}$$

and h_b is the bottom depth.

In the interior, the default vertical coordinate z in the latest ROMS version is defined as:

$$z(x, y, \sigma, t) = \zeta(x, y, t) + S(x, y, \sigma)[\zeta(x, y, t) + h(x, y)] \tag{3.10}$$

where $S(x, y, \sigma)$ is a non-linear functional transformation:

$$S(x, y, \sigma) = \frac{h_c \sigma + h(x, y) C(\sigma)}{h_c + h(x, y)} \tag{3.11}$$

and $C(\sigma)$ is a vertical stretching function:

$$C(\sigma) = \frac{1 - cosh(\theta_s \sigma)}{cosh(\theta_s) - 1}, for \theta_s > 0$$

$$C(\sigma) = -\sigma^2, for\ \theta_s \leq 0 \tag{3.12}$$

$$C(\sigma) = \frac{exp(\theta_b C(\sigma)) - 1}{1 - exp(-\theta_b)}, for \theta_b \geq 0$$

The parameters $h_c, \theta_{s,b}$ are user-defined; They can be adjusted to provide maximum resolution at surface and/or bottom of the ocean. The choice of the vertical parameters is an important step towards configuring the model because it will influence the pressure gradient errors and representation of the boundary layers.

3.2 Model Setup

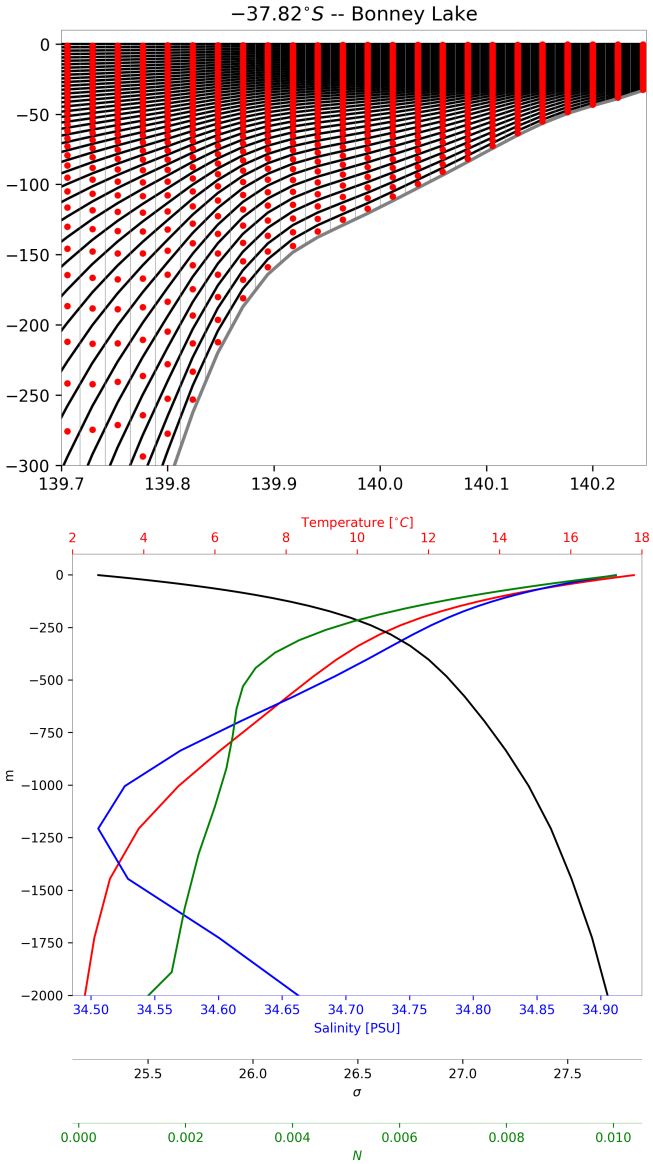

Figure 3.1: An example of the vertical coordinate setup used in ROMS and the stratified conditions used in the Eastern Great Australian Bight (EGAB) idealised numerical experiments. (a) zonal transect crossing the Bonney Lake. (b) vertical profiles of Temperature, Salinity, Density ($\sigma - Kg/m^3$) and Buoyancy frequency ($N - 1/s$). In (a,b), black lines delimit the layer thickness (vertical velocity) position, while red dots are the tracer position (TS) and shaved cells (light grey vertical lines) denote the staggered position of the U-component velocity faces.

Although described in Chapter 4, the model setup details are given here for a quick reference.

A numerical grid was created encompassing the region between the Mid Great Australian Bight, until the west of Tasmania, with boundary limits at $31.5-43.3^{\circ}$ S of latitude and $136.6-148.5^{\circ}$ E of longitude (Figure 3.2). These limits have been chosen to avoid the presence of the boundaries close to the study area and to ensure that boundaries lie in overall low ocean variance regions. Furthermore, the numerical grid is unrotated and positioned as to lie parallel to the shelf along the boundaries. This ensures the predominant flux at the boundaries is normal, avoiding limitations of open boundary conditions. The model resolution is telescopic: lower(higher) resolutions towards the boundaries (centre), with a higher resolution patch of 6° between Eyre Peninsula (EP) and BC. The northern boundary of the domain is closed by the mainland of the Australia Continent, while the model possesses open boundaries in the west, south, and east, with the latter only applied at the Bass Strait.

The nominal maximum (minimum) grid resolution in the zonal directions are $1.9km$ ($8.4km$) and $2.2km$ ($8km$) in the meridional direction, with the resolution in the telescopic region ranging from of $3.5-2.1km$ (Figure 3.2). The telescopic configuration is a parabolic increase in the BC direction with increments in the area of elements of less than 2% in both directions. The grid dimensions are $394x366x42$ (x, y, z).

The bathymetry was created using the Geoscience Australia bathymetric chart, version 2009, available at *www.ga.gov.au/marine/bathymetry.html* with a natural interpolation into the model domain from the Multi-beam $50m$ resolution dataset. The minimum and maximum bathymetric values used were $3m$ and $5000m$ For regional details of the bathymetry, the reader is directed to Chapter 4 and 5 and figures therein.

To ensure lower errors in the pressure gradient term and trace fluxes, the bathymetry was filtered to remove small grid noise and to ensure hydrostatic consistency. The noise reduction was achieved by application of a second order Shapiro filter into the log transformation of the bathymetry ($log(h)$), removing any feature that is not resolved by at least three grid points. The bathymetric values were also substituted by an Ocean General Circulation Model (OGCM) bathymetric values (BlueLink ReANalysis (BRAN) model) in all three open boundaries, given the same model is used in other studies not reported here. Finally a Linear Heuristic Method (Sikirić et al. 2009) was used to reduce the pressure gradient errors, i.e. the slopes numbers of Beckmann et al. (1993) and Haney (1991) to $rx0 = 0.25$ ($rx1 = 7$). This method was used with a stronger (weak) constraint in deep(shallow) water, with a maximum of $rx_0 = 0.15$ below $600m$ (the slope

Table 3.1: Table of model Parameters. The reader is referred to the ROMS model description and code for parameter descriptions.

Parameter	Value
Tracer Advection	MPDATA
Momentum Advection	3rd-order upstream
Tracer Mixing	∇_{geo}
Momentum Mixing	∇_s
Background hor. viscosity (diffusion) [i]	25 (5) $m^2 s^{-1}$
Sponge Layer	4–fold decreasing linear 60km away from the boundaries
Stability Function	Kantha-Clayson
Background vertical mixing coef.	10^{-7}
Bottom stress	Quadratic Law - $C_d = 2.5 \times 10^{-3}$
$V_{transform}$	2
$V_{stretching}$	4
θ_s	9
θ_b	1.5
h_c	$120m$
dt_e/dt_i	$3s/240s$
Momentum BC ($2d/3d$)	Flather/Orlansky Radiation
Sea level BC	Chapman Implicit
Tracers BC	Orlansky Radiation

[i] Equivalent of 7 (5) $m^2 s^{-1}$ at $60km$ off the boundary, with nominal value at the boundary 100 (20) $m^2 s^{-1}$

parameter).

The maximum slopes were at the southern boundary, close to the western Tasmania shelf, and offshore of Kangaroo Island (KI), in the canyons. There, the canyons were smoothed more by the heuristic method, while at the BC the shallow banks, valleys and headlands were mostly kept, being reduced in slope up to 50% from the $50m$ resolution data. In general, deeper regions were more affected, by one or more orders of magnitudes in the slope parameter. The pressure gradient errors were verified in several performance runs and no significant errors were found.

The general parameters used in all experiments are presented in Table 3.1.

The choices of the MPDATA advection scheme (Smolarkiewicz et al. 1998) here is remnant of previously selected options on realistic runs; they required this type of scheme given the stronger, high density and high salinity Spencer Gulf outflow in winter, that occurs close to KI (not shown). As well, sponge layers – the increase in horizontal mixing over the boundaries – are used to reduce noise and improve the functionality of the open boundary conditions, particularly in the Bass Strait (eastern) and Southern Tasmania (southern) boundaries. By filtering the momentum spectra close to the open boundaries, the internal solution

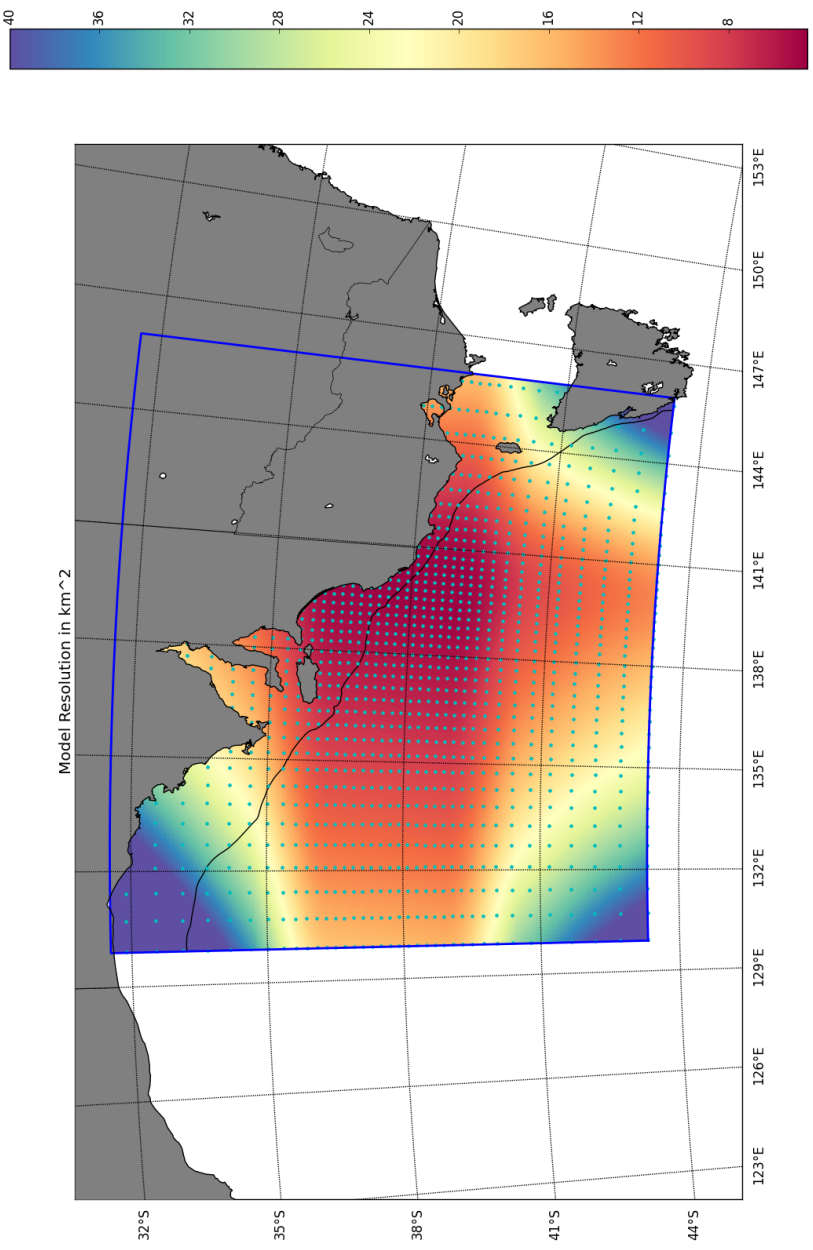

Figure 3.2: The Numerical grid resolution (km^2). The black line represent the $200m$ isobath, and the cyan dots are the numerical grid elements within a 10 points interval.

is matched more closely to the simplified physics condition imposed at the Flather Open Boundary Conditions (OBC) used (both with global/local solutions). This is applied together with a scale factor based on the minimum grid resolution, ensuring larger values are limited to low-resolution elements close to the boundaries. The nominal background viscosity/diffusivity at the upwelling regions (high resolution) is almost zero. The magnitude of viscosity/diffusivity used in the experiments was selected to remove small-scale noise by the Laplacian harmonic operator with time-scales less than the minimum local inertial period of the boundary (the northernmost water-point).

Experiments in Chapter 4 and 5 share common OBCs. For all boundaries, an implicit *Chapman* condition is used for η (GWI in Chapman (1985)). A Flather type of boundary condition is used in the normal barotropic momentum variables of each boundary (FRO condition in Palma et al. (2000)). Tangent to the boundaries, however, the conditions are a *Chapman* condition. Purely radiation conditions (Orlansky type) are applied for both tri-dimensional velocities and tracers. The assumption of no tri-dimensional flow/heat/salt flux at the boundary is appropriate, given the focus on the flow response to winds, topography and remote Coastal Trapped Wave (CTW) in these chapters (as in e.g. Gan et al. (2002b), Gan et al. (2002a), Liu et al. (2014), and Liu et al. (2015))..

In Chapter 4, the Flather condition in all boundaries have zero local solution (the FLA condition in Palma et al. 1998) since local boundary solutions are imposed as $V = U = 0$ – no momentum flux at and through the boundary. This is a subset of the FRO condition. In Chapter 5, subsection 5.3, only the western OBC is changed. There, an alongshore momentum flux at the shelf is imposed (using the FRO – local solution) through the use of a barotropic CTW analytical solution. These OBCs conditions are capable of representing the flow at the shelf,given that they use a radiative wave speed based on the shallow water wave speed. Although not perfect by any means, results with other OBCs (e.g. the characteristic Flather condition Mason et al. 2010) were mostly insensitive within the experiments presented in the thesis.

To reduce numerical problems with the OBC, the numerical domain used in the thesis was extended far beyond the upwelling regions. This *a priori* solution was put at place, together with approximately OBC located normal to the higher variance flow over the shelf/shelf-break. This ensures a more optimal behaviour of the OBCss. Although not perfect, some numerical errors along the boundaries were still present, mostly in the eastern and southern boundaries. These were irrelevant to the dynamics of the upwelling regions.

Finally, an idealized vertical profile of Temperature and Salinity is used for the entire domain in the experiments of Chapters 4 and 5 (see Fig. 3.1). As is explained

in the next chapter, these conditions are estimated from the CSIRO Atlas of Regional Seas (CARS) atlas (Ridgway et al. 2002) for the EGAB region during early summer (December). As will be shown in Chapter 6, these conditions are idealized, with a mean picture of the typical vertical variability in the region. Nonetheless, they are still quite representative in terms of the stratification parameter within the ocean interior during summer.

Chapter 4

Upwelling along the shelves of the Greater Australian Bight. Part I: The Role of submarine headlands and valleys

Abstract

A realistic numerical model with idealised forcing is used to analyse the summertime circulation along Australia's southern shelves. An impulsively started, constant alongshore wind stress and horizontally uniform stratification are used to study the two main upwelling areas – the Bonney Coast (BC) and the Kangaroo Island/Eyre Peninsula regions. For the BC, the coastline is reasonably uniform, but seven pairs of submarine headlands and valleys characterise the shelf topography to depths of $150m$. In agreement with studies of other regions, upwelling is found within the valleys and downwelling over the headlands. Here, the upwelling (downwelling) is shown to be qualitatively consistent with barotropic vorticity dynamics, where the bottom vertical velocity, w_b, is inferred from the acquisition of anti-cyclonic (cyclonic) vorticity as a fluid column moves equatorward across the headlands (valleys). Additionally, upwelling is most intense on the equatorward side of the submarine headlands: a feature long known for the Californian/Oregon shelves. A new explanation for this preferential upwelling is given and results from the alongshore baroclinic pressure gradient, set up by the up- and downwelled density field that in turn drives an onshore geostrophic flow. These dynamics are used to explain upwelling for both regions. The BC is known to have amongst the largest surface signatures of upwelling around Australia, even when the local winds are only weakly favourable.

4.1 Introduction

Summertime upwelling along Australia's southern shelves (Fig. 4.1) was first noted by Rochford (1977) and Lewis (1981) and has been the focus of several studies including those of the Bonney Coast (BC) and the regions of Kangaroo Island (KI) and the Eyre Peninsula (EP) (e.g., Schahinger 1987; Hahn 1986; Kämpf 2010; McClatchie et al. 2007; Middleton et al. 2014). The upwelling of nutrients is of great importance as it supports one of Australia's most productive planktonic ecosystems (Ruth et al. 2010), that in-turn underpins a diverse range of pelagic fish (e.g., sardines) and lobsters (Linnane et al. 2005) to apex predators including whales, sharks, Southern Blue Fin Tuna, sea lions and fur seals (Ward et al. 2006). Unusually, the upwelling region and ecosystem it supports occurs along a "zonal" shelf (Fig. 4.1), rather than a meridional shelf, as found for eastern boundary currents such as that of the United States.

The Eastern Great Australian Bight (EGAB) is here taken to include the shelf and slope regions from Eucla in the mid–Great Australian Bight (GAB) to the southern tip of Tasmania (Fig. 4.1). The topography of the region is quite complex with shelf widths of 200 km in the north-west to 30 km at the BC in the east. Between these extremes lie the widened shelf regions of the Gulfs, with narrows associated with the Eyre Peninsula and KI. In the far east lies the Bass Strait and the narrow shelves of Tasmania although the analysis here will focus on the shelves of the EGAB between the EP and Portland (BC). The shelf topography of the region is further complicated by the presence of deep canyons as well as submarine headlands and "valleys", notably in the region of the BC (see below).

During winter the shelf circulation is predominantly forced by westerly winds and the downwelling of cold, dense, salty waters formed in the coastal regions and gulfs (for further details see the review paper of Middleton et al. 2007b).

Of interest here are the studies of the summertime circulation and cross-shelf exchange (including upwelling). During summer, the average surface winds blow in an anti-cyclonic (anti-clockwise) sense and are generally upwelling favourable (along the curved coastline of the GAB). A typical example of upwelling conditions is presented in Fig. 4.2 where the mean sea level atmospheric pressure for the $7th$ February 2008 is presented.

Using such an anticyclonic wind field, Middleton et al. (2003) modelled the GAB circulation to show that coastal upwelling is most intense in the BC and KI regions but that shelf break downwelling should (on average) occur in the mid-GAB ($130°E$) all year round. Observational support for the summertime downwelling is given by Middleton et al. (2014) using data collected through the Southern Australian

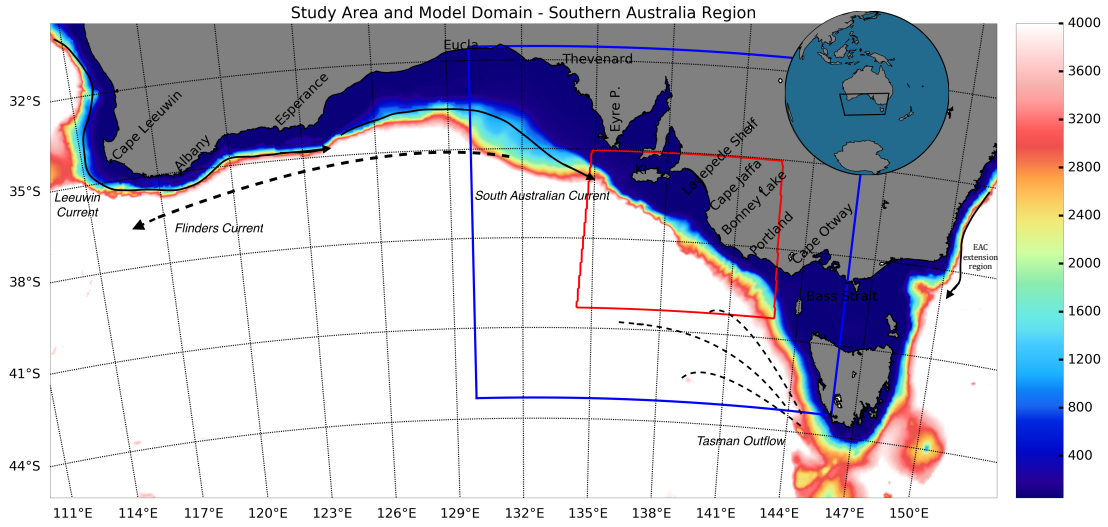

Figure 4.1: The study area, bathymetry (meters) and the model domain of the EGAB (outer blue rectangle) with the high-resolution region (3-4km) as the inner red rectangle. The 500, 1500 and 3000m isobaths are delimited by dark blue, green and red colours. Place names of interest are included, as well as an schematic including the main direction of Coastal Trapped Wave (CTW) propagation, the surface shelf-break current South Australia Current (SAC) (solid line) and the sub-surface flow of the Flinders Current (FC) and the westward Tasman Outflow (dotted line).

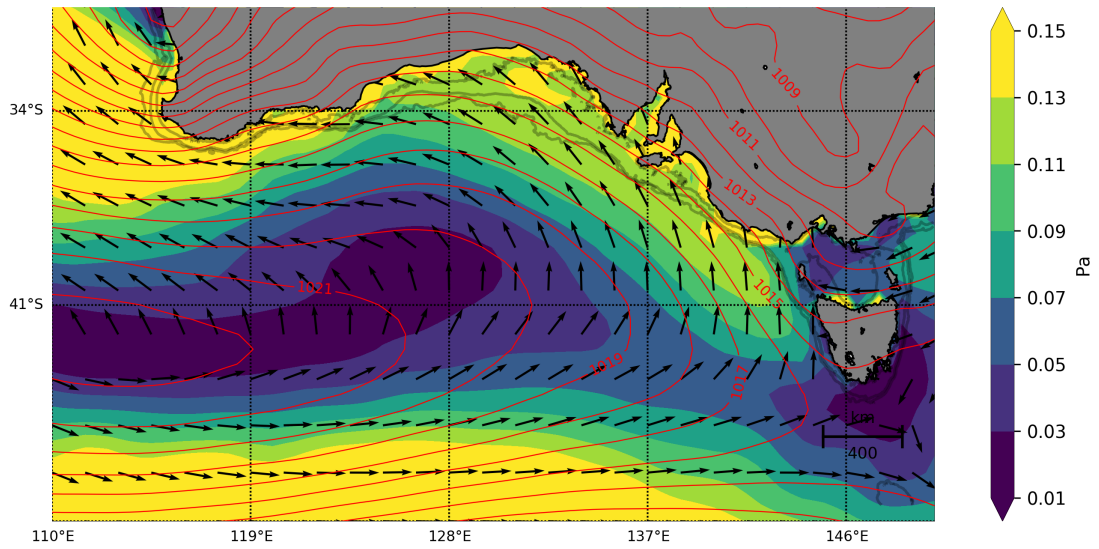

Figure 4.2: The mean surface wind stress magnitude (shading, units Pascals), surface wind stress direction (black arrows) and sea level atmospheric pressure (red contours, units hecto-Pascals) from $1-7$ of February 2008. Winds blow in an anticyclonic (anti-clockwise) sense and are upwelling favourable (source: European Centre for Medium-Range Weather Forecasts (ECMWF)).

Integrated Marine Observing System (SAIMOS) — *www.imos.org.au/saimos.html*.

Support for the summertime upwelling is given by Condutivity Temperature and Depth probe (CTD) and mooring data analysed by Lewis (1981), Hahn (1986), Schahinger (1987), Kämpf et al. (2004), and McClatchie et al. (2006), as well as Sea Surface Temperature (SST) data (Foster et al. 2014). An example of the latter SST fields is shown in Figure 4.3 and also for the $7th$ February 2008 when the atmospheric conditions (Fig. 4.2) were upwelling favourable for 5 days or so. The surface signature of the upwelling is most pronounced off the BC, which is the focus of the study here. This region has the coldest surface signature of upwelling in Australia (Foster et al. 2014). The upwelling off the KI/EP region appears weaker and is complicated by relatively wider shelves and the gulfs.

Several causes of the upwelling have also been addressed including wind-driven Ekman upwelling, through the studies noted above, and enhancement by El-Niño signal (Li et al. 2004; Middleton et al. 2007a). The latter signals propagate from the western Pacific Ocean past Papua New Guinea, southward along the coastal ocean over Western Australia, and into the GAB: these signals appear to raise the thermocline by up to $100m$ or so and enhance summertime Ekman upwelling. These signals also propagate in a "poleward" direction and in the same direction as CTWs with the coast on the left in the southern hemisphere. The notation of poleward and equatorward will be adopted here so that the southern hemisphere results presented are readily re-interpreted for northern hemisphere cases such as the Oregon/Californian coast. Here upwelling favourable winds and currents are

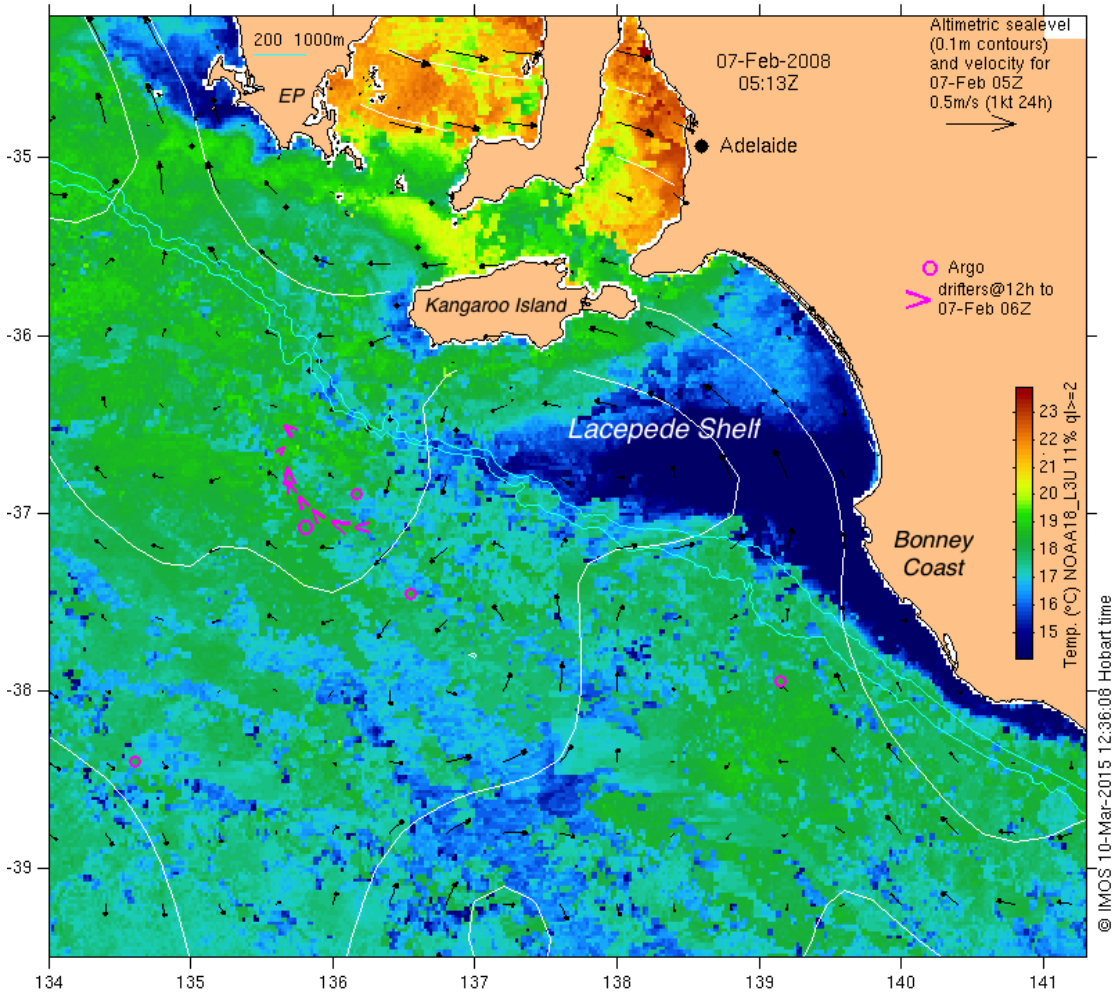

Figure 4.3: The satellite derived SST on the 7*th* February 2008. Black arrows denote surface currents and lines of constant (altimeter derived) sea level are shown in white (source IMOS OceanCurrents: *imos.org.au*) Note the strong surface signatures of upwelling along the BC, west coast of KI and the EP.

equatorward, which means directed to the north-west and west for the generally zonal shelves of the GAB shown in Fig. 4.1, and thus upstream of the CTW propagation (with the coast to the left).

A third mechanism may arise from upwelling in the deep canyons of the GAB, which can extend from depths of $1000m$ to that of the shelf break ($200m$). Such deep canyon upwelling has been examined in detail through many studies of other regions: the dynamics, observations, and previous research is well summarised by Allen et al. (2010). In the context of the GAB, Kämpf (2006) and Kämpf (2010) has examined the upwelling for the Cape du Couedic canyon off KI. Assuming zero gradient boundary conditions, he obtained a wind-forced, deep (200-$900m$) equatorward along-shelf slope flow of about $10cm/s$, with slope bottom currents above $25cm/s$, and significant deep upwelling results. This is much larger than found below (see Section 4.3.6), where flow speed of less than $5cm/s$ is found over depths greater than $120m$.

Finally, the fourth mechanism for upwelling to be explored in this study involves upwelling induced by the presence of submarine "valleys and headlands" over the shelf and extending from the coast to depths of $150m$ or so. As is shown in the detailed topography along section 4.3.2, there are several submarine valleys and headlands along the BC. The depth difference between the headlands and valleys is of order $50m$ and not large, but as will be shown is sufficient to drive substantial upwelling.

Upwelling associated with headlands along the Oregon and Californian shelves was recognised long ago to preferentially occur to the immediate south of submarine headlands/banks (Reid et al. 1958; Peffley et al. 1976). More recently, observational studies (e.g., Barth et al. 2005; Gan et al. 2002b) have confirmed that preferential upwelling should occur on the equatorward (southern) side of submarine headlands. A theory for such upwelling was advanced by Arthur (1965) based on conservation of vorticity in the case where (non-linear) curvature effects are important. Recently, numerical model studies have detailed the preferential upwelling on the equatorward side of headlands and downwelling over the submarine headlands (Whitney et al. 2009a; Whitney et al. 2009b). Arguments to explain the preferential upwelling have focused on the importance of non-linear effects including the gradient wind in enhancing the alongshore pressure gradient that in turn drives an (enhanced) onshore flow and upwelling (e.g., Gan et al. 2002a). Also,In the idealized studies of upwelling regimes over shallow shelf valleys (Zhang et al. 2017), the flow within a valley developed a stationary meandering upstream (in a coastal trapped wave sense), caused by coastal-trapped lee waves.

One unique aspect of this study is the focus on the upwelling induced by the presence of both submarine headlands and valleys. For the BC, seven pairs of

headlands and valleys exist, and analogue to many studies in the Oregon/Californian shelves, downwelling is found over the submarine headlands while upwelling in the valleys, being largest on the equatorward side of headlands. These remarkable results will here be largely explained using simple vorticity arguments and the enhanced alongshore baroclinic pressure gradients that arise from the upwelling and downwelling itself. The importance of the baroclinic pressure gradients should also apply to the Oregon/Californian shelf studies noted above although we have not been able to find in the literature an explicit statement of their importance.

In section 4.2, a brief outline of the numerical model (methods) is given. The response to an instantaneous, constant, upwelling favourable wind stress will be determined using an idealised numerical model of the EGAB (Fig. 4.1). While idealised, the model results will assist in the determination of the important dynamics of fully time-dependent, realistic simulations.

In section 4.3.1, a short description of results for the full model domain (Eucla to Tasmania) is given but without a dynamical explanation. Detailed model results and dynamical explanations are then given for the BC region in section 4.3.2. In section 4.3.6, results and analysis are briefly presented for the more complex KI region. A summary and discussion are made in the last section including comments on the sensitivity to the applied wind-forcing, experimental design, and possible ecosystem impacts.

In the companion study (Middleton and de Oliveira 2018 – part II – Chapter 5), an analysis is made of the transient set-up of upwelling over the first $2-6$ days and the implications of the western boundary condition used: the adoption here of Eucla (mid-GAB) as a 'geographical origin', where winds and currents vanish.

4.2 Methods – The numerical model

The Regional Ocean Modelling System (ROMS $v3.7$, Rutgers version, *SVN* revision 737) is adopted (see Shchepetkin et al. 2005). Important conditions used in the experiments are a quadratic bottom stress ($C_d = 2.5 \times 10^{-3}$), the advection of tracers via Multidimensional Positive Definite Advection Transport Algorithm (MPDATA) (Smolarkiewicz et al. 1998), while mixing is harmonic in geopotential surfaces. A *k-kl* turbulence closure and viscosity scaled by grid size with close to zero values over the high-resolution region is also used (see Table 3.1 in Chapter 3 for more details.). Boundary conditions adopted are purely radiation conditions for tracers and tri-dimensional velocities, and Flather/Chapman implicit (Flather 1976; Chapman 1985) for barotropic velocities and sea level respectively. The prescribed flux values that would otherwise be set by a parent model in realistic conditions are set to zero along the boundaries. This implies that the local solution under the Flather Open Boundary Conditions (OBC) condition is zero. A weak sponge layer is also used to improve radiation conditions along the open boundaries.

The domain (blue rectangle in Fig. 4.1) extends meridionally from the mid-GAB to the middle of Bass Strait, limited to the north by the GAB coastline and to the south by the southern tip of Tasmania. The boundaries generally lie in regions of low ocean variance/low eddy activity (except the southern region) and are normal to the mean shelf orientation (predominant normal flux). The grid is non-rotated, with lower resolution near the boundaries and higher resolution towards the centre, within an area of about 6° in longitude with maximum resolution region between the EP, KI and BC. The resolution in these areas is between 2–4km. The increase in horizontal resolution is done parabolically and limited to a 2% change for each step to ensure a smooth transition.

The topography and coastline are from the Geoscience Australia bathymetric chart (version 2009–available at *www.ga.gov.au/marine/bathymetry.html*), with 50m resolution. Since this grid is also used for realistic experiments, the topography is also blended with a low-resolution bathymetry from the BRAN model (Oke et al. 2008) at the boundaries, with a smooth transition towards the interior. The minimum (maximum) values adopted are 4m (5000m). The model is discretised with 42 sigma levels in the vertical with enhanced (boundary layer) resolution in the top 120m and close to the bottom. The steeper regions of the domain are the shelf break and continental rise off KI and BC. To ensure low errors in the pressure gradients, a Shapiro filter was applied to remove small-scale noise, followed by a slope/bathymetric dependent filter using the Sikirić et al. (2009) toolbox. The global maximum slopes adopted were 0.23 but given the bathymetric

dependence, values are closer to 0.15 in depths over $500m$. An outcome of the filtered bathymetry was to reduce to about an order of magnitude the shelf slopes from the original dataset.

A constant wind stress of magnitude $\tau_s = 0.05Pa$, north-westward (117° anticlockwise from the east) is used. This wind stress is adopted everywhere so that effects of Ekman pumping are zero and also approximates both the direction (upwelling favourable) and magnitude of the summer average: these winds approximate those of a $6-year$ average based on Atlas et al. (2011) Cross Calibrated Multi Platform Ocean Surface Wind Velocity (CCMP) reanalysis for the region. For simplicity, idealised initial profiles of temperature $T(z)$, and salinity $S(z)$, based on the CARS climatology (Ridgway et al. 2002) are adopted ($-z$ is depth) everywhere and which are representative of spring to summer conditions (December). The profiles were estimated from area averages of the region and fitted with a six- degree polynomial to ensure a smooth profile but still fit the purpose of representing the vertical distribution of temperature in the region. In our experiments, given the density profile is mostly dictated by temperature, we use this tracer as a direct proxy for density. We preclude atmospheric and tidal forcing and integrate the model for about sixty days, presenting results only for the first weeks, focusing mostly in the setup of the wind forced circulation at day 6 (mean values). This represents the duration of a typical upwelling event (e.g. Nieblas et al. 2009).

4.3 Results

4.3.1 The wind-driven upwelling circulation in the Eastern Great Australian Bight

The depth-averaged circulation and sea level field for the full model domain is illustrated in Fig. 4.4 for day 6. Nieblas et al. (2009) indicate that upwelling favourable winds persist for about 9 days and can occur up to 10 times each austral summer/autumn period (November to March). To underline some important processes, and representativeness of the typical upwelling signature at the BC results for $30 - day$ long periods of wind-forcing will also be presented. In a crude sense, these results might correspond to the cumulative effect of five events over the season.

As shown in Fig. 4.4, in the west the alongshore velocities (v) and sea level (η) are small as expected by the applied boundary condition: $v = \eta = 0$. Generally, sea level drops near the coast as expected for the offshore surface Ekman flux. The associated depth-averaged currents generally follow isobaths and are largest along the narrow BC and western Tasmanian shelf. Within the wide Lacepede Shelf, the currents bifurcate with flow along the $100m$ isobath and an in-shore core between the coast and the $50m$ isobath. Such bifurcation is seen in satellite images of SST for this region during strong upwelling events (Fig. 4.3).

Now consider the initial bottom temperatures (Fig. 4.5a). Since the vertical profiles of temperature and salinity are the same everywhere, the yellow band of $14°C$ water initially lies at a depth of $110m$ and the blue band of $12°C$ water lies at a depth of $150m$. As is evident, a cold pool of water ($12 - 14°C$) resides off the mouth of the Spencer Gulf and KI due to the relatively deep water ($> 100m$): this water was named the 'Kangaroo Island cold pool' based on observational data (McClatchie et al. 2007). In the far west, the shelf slope steepens, and the 'cold pool' becomes very narrow. Along both the KI and BC regions the yellow isotherm of $14°C$ water exhibits meanders that correspond to submarine valleys and headlands and not cross-shelf exchange.

By day 6, the wind forcing has changed the distribution of bottom temperature in some regions but not others (Fig. 4.5b). In the far west, the offshore Ekman transport changes bottom temperature little if only because the shelf is very wide. The interior return Ekman transport at that time is also largely shut-down by Continental Shelf Waves (CSWs) as is discussed in Chapter 5.

Off KI and the BC, the $12°C$ (blue) to $14°C$ (yellow) isotherms exhibit stronger

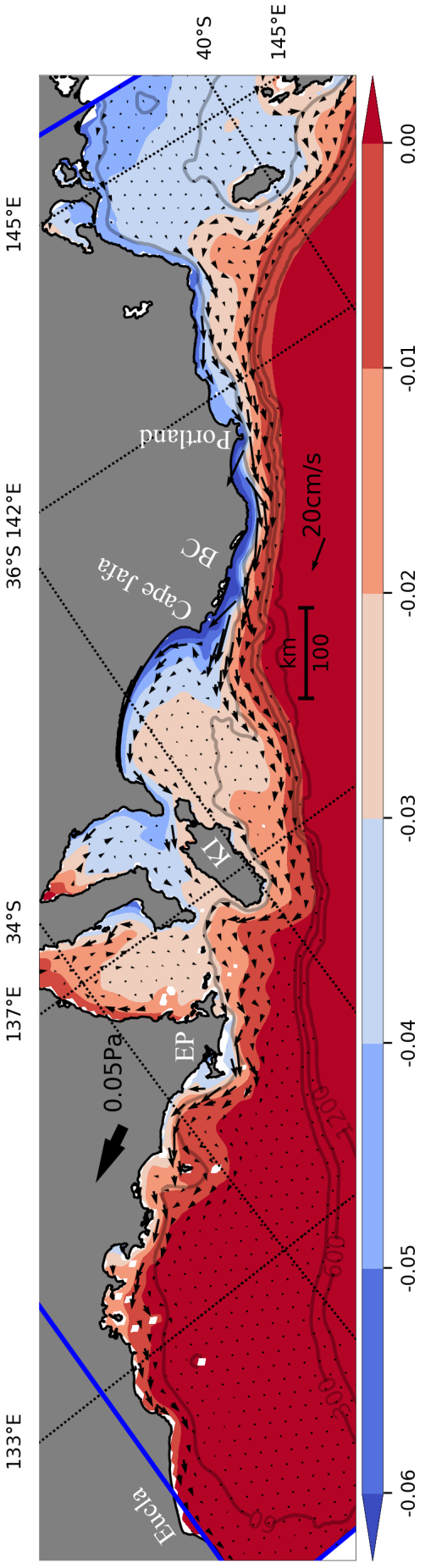

Figure 4.4: Sea level (shading – meters) and depth-averaged currents at day 6. A vector of A vector of length $20cm/s$ is indicated along with the $0.05Pa$ mean wind stress (thick black arrow). The 60, 300, 600 and $1200m$ isobaths are indicated by the light grey lines. Place name abbreviations are EP (Eyre Peninsula), KI (Kangaroo Island) and BC (Bonney Coast).

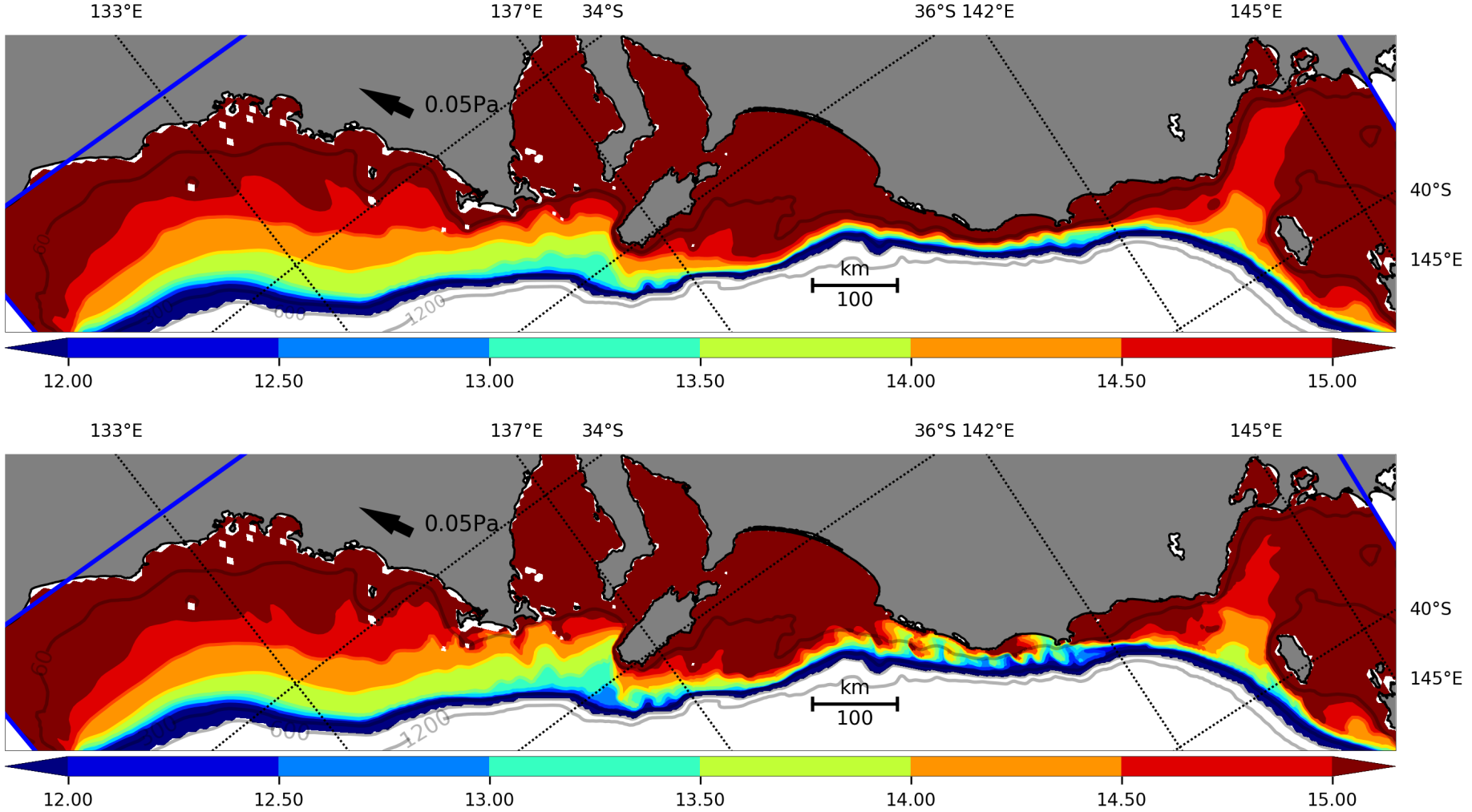

Figure 4.5: (a) Upper Panel: Initial Bottom temperature distribution (shading – $°C$). The yellow $14°C$ contour lies over the $110m$ isobath. (b) Lower Panel: As in upper panel (a), but for a mean value at day 6 – full domain. The isobaths are as in Fig. 4.4.

meanders indicating possible canyon and valley/headland upwelling outlined below. These meanders intensify along the BC such that the $14°C$ (yellow) isotherm has in places been drawn shoreward by $30-40km$ to now lie between the $20m$ isobath and coast: initially, the $14°C$ isotherm lay at the depth of the $110m$ isobath. Southwest of Portland, the upwelling is confined to be seaward of the $110m$ isobath since there is little change in the shelf location of the $14°C$ (yellow) isotherm.

4.3.2 The Bonney Coast region – description of model results

Details of the bottom temperature and velocity for the BC region are presented in Fig. 4.6. For the purpose of clarity, the fields are masked in the ocean region below $300m$. Again, at day zero the $14°C$ water lies near the depth of the $110m$ isobath and both meander due to the submarine valleys and headlands/banks. By day 6, Fig. 4.6b, the meanders in temperature intensify such that the $14°C$ (yellow) isotherm has, within the valleys, been drawn shoreward by $25km$ reaching the coast. The strongest upwelling is generally found in the valleys and on the equatorward side of the submarine headlands.

To further illustrate the upwelling, alongshore transects of temperature and vertical velocity (at day 6) are presented in Fig. 4.7. The transects are chosen to approximately lie over the $120m$ and $60m$ isobaths. Upwelling occurs within the valleys and is strongest on the equatorward side of the headlands with vertical velocities of $10-20m/day$. Downwelling is found over the headlands as found by Whitney et al. (2009a) (their Fig 9). Both up- and downwelling results in perturbations to the temperature field that extends to within $20m$ of the surface. The undulating temperature field looks similar to a set of stationary lee waves (Bell 1975). Results in Fig. 4.6 and below show that the temperature perturbations are horizontally associated (or locked) to the topography. Moreover, this pattern is not sensitive up to an order of magnitude increase in bottom drag values, being relatively constant over several days – see the animation for an experiment with $C_d = 0.02$ in *https://figshare.com/s/541a8b465cc3bc4e41cb*.

The upwelled vertical velocities are also consistent with the modelled onshore bottom flow and topographic slope. From Fig. 4.6b, the bottom velocity vectors at day 6 and within the valleys are typically around $5cm/s$ at $120m$.

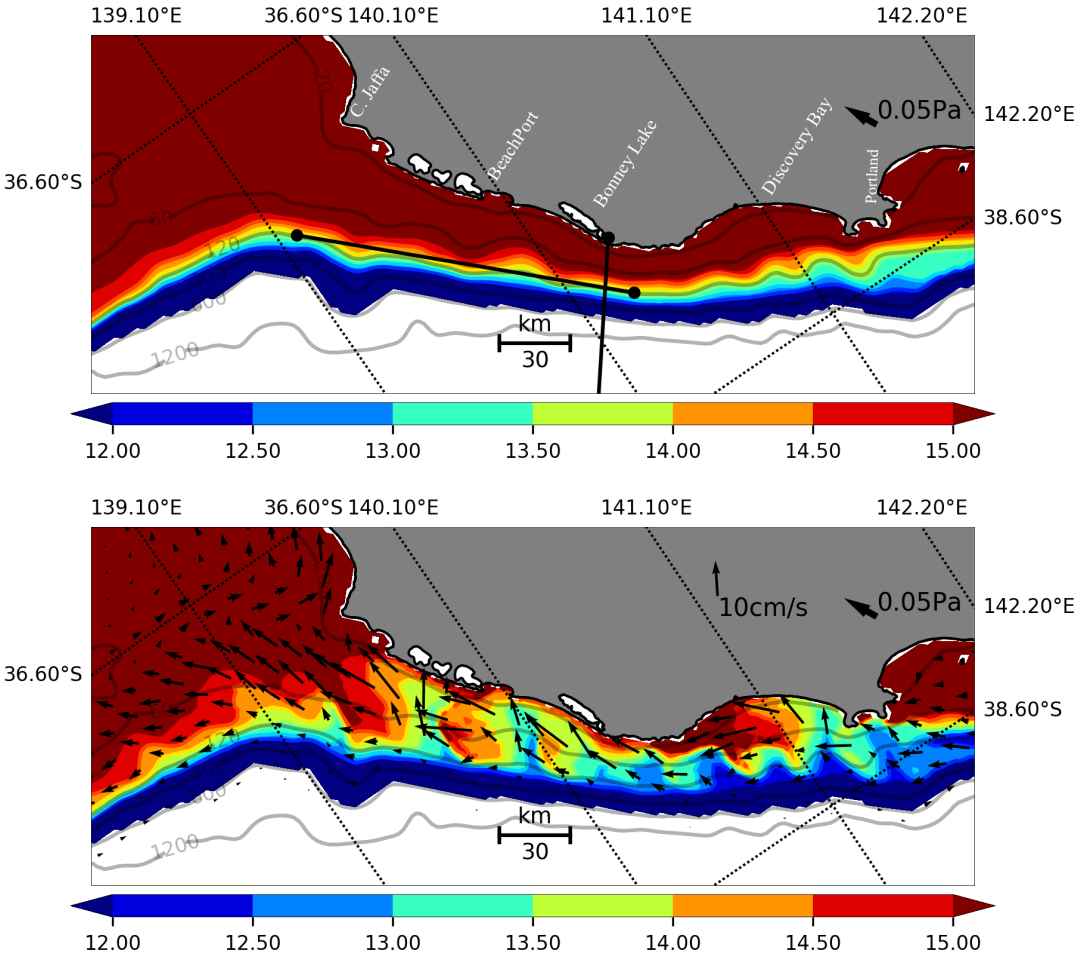

Figure 4.6: Details of the BC region. (a) Initial Bottom temperature (shading) with 20, 60, 120, 300, 600 and 1200m isobaths indicated. The thick black line denotes the Bonney Lake alongshore transect for which results are presented below (Fig. 4.6), as well as the cross-shelf transect presented in Fig. 4.8. Regional place names of interest are included. (b) As in upper panel but a mean for day 6 with black vectors of bottom velocity (scale of 10cm/s is indicated).

Close to the bottom the condition of no normal flow is (at $z = h_b = -h$):

$$\frac{D(z+h)}{Dt} = 0 \tag{4.1a}$$

$$w(x, y, -h, t) = w_b = -\frac{Dh}{Dt} \tag{4.1b}$$

Based on a typical topographic slope, $dh/dx = -0.006$ (see Fig. 4.8 below), and a cross-isobath bottom velocity of $u_b = 5cm/s$ $(4.3km/day)$ close to the Bonney Lake valley, the implied bottom vertical velocity from the kinematic boundary condition above:

$$u_b = \frac{\tau_b^x}{\rho_0 C_D \sqrt{u_b^2 + v_b^2}} \tag{4.2a}$$

$$w_b = -u_b \, dh/dx \tag{4.2b}$$

is about $25m/day$ and comparable to that found in the model (Fig. 4.7). Onshore values of $10cm/s$ for the $60m$ isobaths (see also Fig. 4.6b), implies values up to $40m/day$. Moreover, since day zero, these results are also consistent with the $20 - 30km$ shoreward displacement of $14°C$ water from the $110m$ isobath to the $20m$ isobath as illustrated in Fig. 4.6b.

4.3.3 Cross-shelf results – Interpretation using a 2-dimensional barotropic Ekman model

In contrast to the above alongshore up/downwelling systems linked to the submarine valleys and headlands, the cross-shelf structure of upwelling is illustrated in Fig. 4.8 and exhibits features of two-dimensional Ekman upwelling as outlined in the studies by Brink et al. (1978) and Allen et al. (1995) and Middleton et al. (2004). This cross-shelf transect was chosen as the alongshore topography here is reasonably uniform (Fig. 4.6a). The results at day 6 (Fig. 4.8) represent a "classical picture" of upwelling through the cross-shelf flow (u,w), alongshore velocity v, temperature and stress ratio ($r = \frac{\tau_b}{\tau_s}$) where τ_s (τ_b) are surface wind (bottom) stress. Note that vectors were rotated accordingly to the transect angle to match the alongshore (y-northwest) and onshore (x-positive onshore) definitions.

At day 0, the isotherms are flat and velocities are zero. By day 6 (Fig. 4.8), water less than $13.5°C$ has been upwelled from depths between $125m$ to about

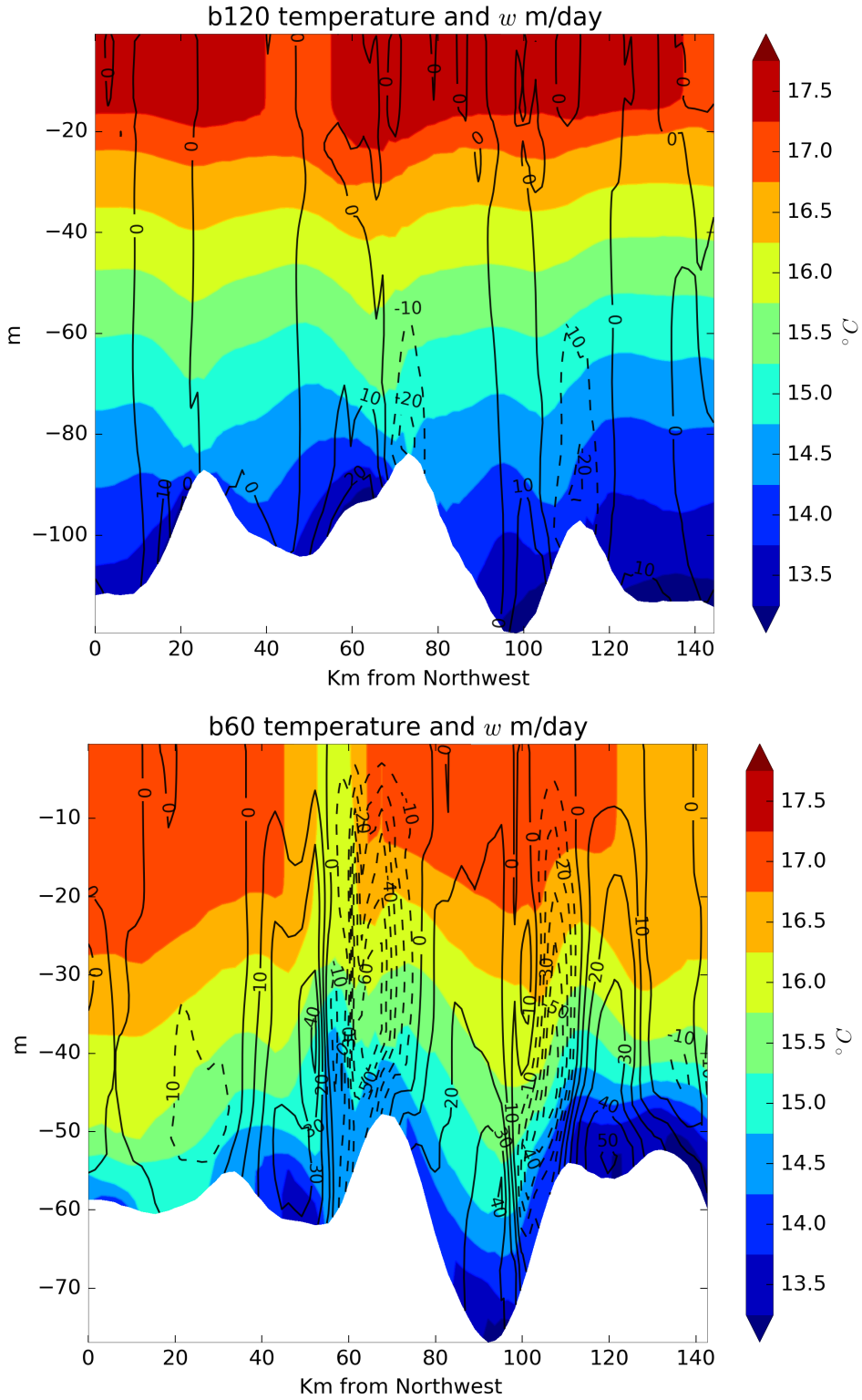

Figure 4.7: (a) An alongshore transect (units km) of temperature (shading – $°C$) and vertical velocity (m/day – contours) approximately centred over the $120m$ isobath and extent as shown in Fig. 4.6b. (b) As in (a) but for the $60m$ isobath. The results are for day 6 and the solid (dashed) black contours indicate upwelling (downwelling). The equatorward/downstream side of the transects are to the left. The white shaded regions illustrate the submerged headland and valley topography.

$40m$. Water nearer the surface ($> 15°C$) has been upwelled and draw offshore by the surface Ekman transport, evident in the top panels. The alongshore velocity (v; lower left panel) has accelerated to speeds of $45cm/s$ at the surface, and is reduced in magnitude towards the bottom, due to the thermal wind shear of the density the density (σ) field:

$$dv/dz = -(\frac{g}{\rho_0 f})d\sigma/dx \tag{4.3}$$

where g is the gravitational constant, f the Coriolis parameter, ρ_0 a constant density and again, the $y-axis$ is directed equatorward (north-west) and $x-axis$ is directed onshore.

At day 6, a significant component of the upwelling at coastal shelf depths of 20 to $50m$ occurs within the very narrow bottom boundary layer (BBL), as illustrated by the top panels of Fig. 4.8. A barotropic theory for upwelling provides a simple framework to discuss these stratified results (Brink et al. 1978; Allen et al. 1995; Lentz et al. 2004). In particular, for a barotropic ocean with no alongshore variations, Brink et al. 1978 show that the alongshore momentum equation may be written as:

$$\frac{dV}{dy} + fU = -h\frac{dP}{dy} + \frac{\tau_s - \tau_b}{\rho} \tag{4.4}$$

where $P = p/\rho$, $h(x)$ is shelf depth and U and V are depth-integrated currents. If no alongshore variations exist, and the rigid lid approximation is made, then $\frac{dP}{dy} = \frac{dV}{dy} = \frac{dU}{dx} = 0$. In addition, since $U = 0$ at the coast, and $\frac{dU}{dx} = 0$, then $U = 0$ everywhere and eq.(4.4) becomes:

$$\frac{dV}{dy} = \frac{\tau_s - \tau_b}{\rho} \tag{4.5}$$

Initially, τ_b is zero and the alongshore flow near the coast accelerates due to the wind stress τ_s and $\frac{dV}{dt}$ is positive. After some time, (and at depths less than $50m$), τ_b becomes larger until $r = 1$ and from eq.(4.5), $\frac{dV}{dt} = 0$. At this point, the coastal alongshore flow stops accelerating and since r is order 1, the onshore transport in the BBL balances the Ekman transport due to the surface wind stress: the interior upwelling is shut-down. Allen et al. (1995) also show that the balance of stress ($r \approx 1$), should occur later in deeper water and with a time scale proportional to water depth (h).

This barotropic analysis is broadly consistent with model results near the coast shown in Fig. 4.8 where r is of order one at depths less than $50m$. Middleton et al. 2004 identified this stress balance as a "viscous limit" of upwelling. In deeper water (e.g. $200m$), the results in Fig 4.3 show that r is near zero at both day 6 and much

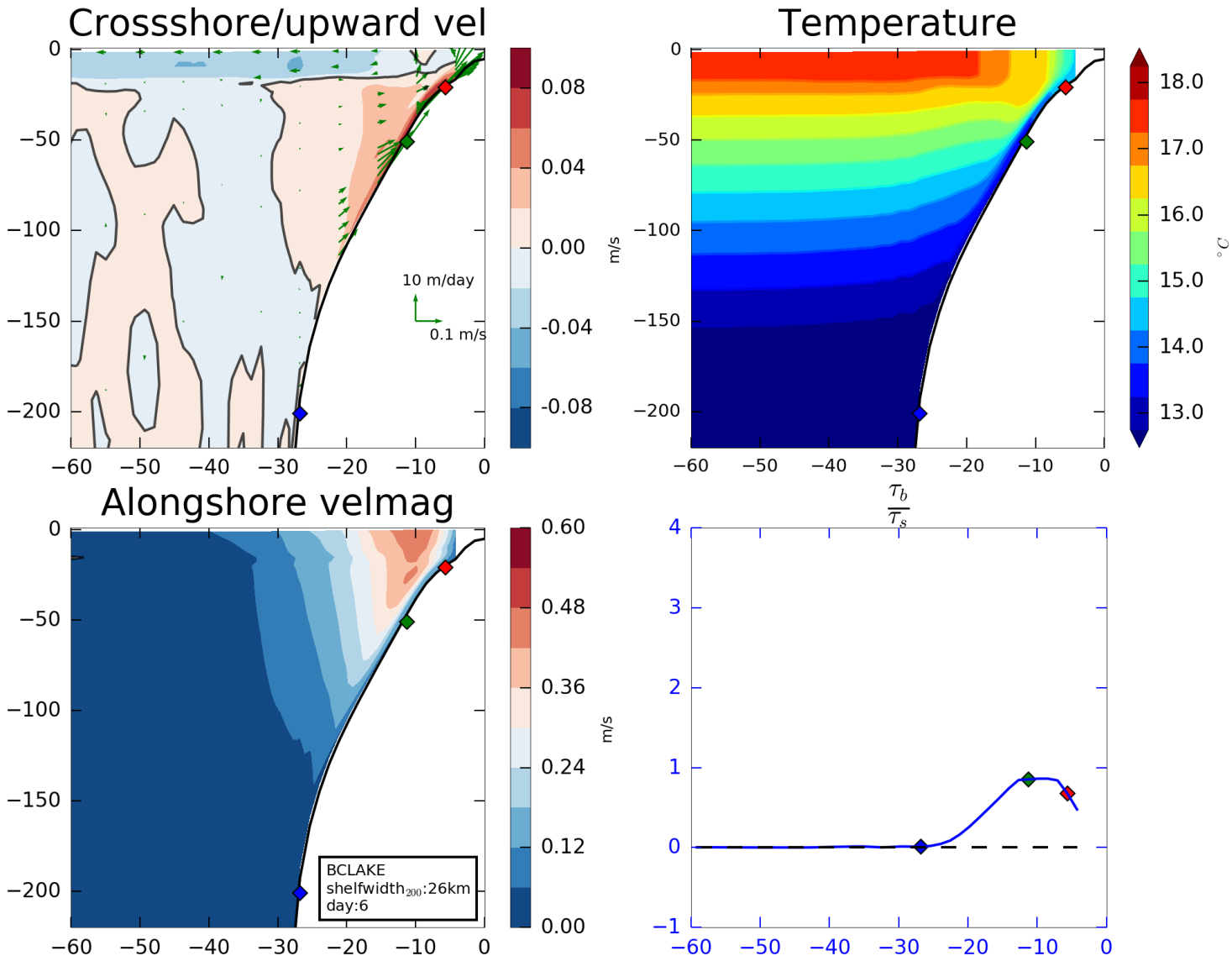

Figure 4.8: Cross section model output just to the south-east of Bonney Lake (see Fig. 4.6a) for day 6. Top left: cross-shelf velocity with the vertical velocity magnified: units m/s, m/day; Bottom Left: alongshore velocity v; units m/s. Top Right Temperature (units $°C$); Bottom right: ratio $r = \frac{\tau_b}{\tau_s}$ of wind to bottom stresses. In each panel, the diamonds indicate the location of the 20 (red), 50 (green) and 200m (blue) isobaths.

later at day 30 (not shown). The barotropic theory does not appear to hold at these depths since the thermal wind shear, eq.(4.3), leads to very small alongshore velocities and thus bottom stress (Fig 4.3, lower panels). More detail comparisons of barotropic and stratified model results are made in Middleton et al. 2004, while the CTW shut-down is highlighted in Chapter 5.

The flow does continue to evolve over time. Results for day 30 (not shown) the cross-shelf Bonney Lake transect showed the role of the offshore advection of cold waters: the alongshore jet shifted offshore and there is increased vertical shear, surface alongshore flow and interior upwelling (not shown). Bottom results from the model and for day 30 are shown in Fig. 4.9a (upper). A comparison with results of the day 6 (Fig. 4.6a) shows enhancement of upwelling in general, with overall colder waters north of the Bonney Lake/Portland. The marked signal of upwelling within the valleys and along the equatorward sides of the submarine headlands is still clearly visible. Overall, the bottom velocities were still onshore, with magnitudes decreased if compared to day 6 (black arrows), except within the vicinity of the topographic features (magenta arrows).

The depth-averaged alongshore velocities at day 30 are generally about 20% larger than at day 6 (Fig. 4.9b), indicating the alongshore flow has continued to accelerate. With the overall reduction in bottom velocities (and bottom stress), Fig. 4.9a, this indicates a surface (interior) intensification of the alongshore flow (upwelling) in the vicinity of the $60m$ isobath. This is consistent with the offshore advection of colder waters and the displacement of the mean upwelling jet.

4.3.4 The surface results

The surface upwelling by day 30 is evident on the SST plot in Fig. 4.9b. The coastal model SST has mixed from $17.6°C$ (initial conditions) to $13°C$. No evidence of the sub-surface up- or downwelling is evident in the SST (Fig. 4.9b) presumably due to horizontal mixing by winds. Instabilities and filaments are now evident in the SST (Fig. 4.9b) and a bifurcation of cold water is found over the LS: This SST bifurcation is typical of that seen in satellite data as illustrated in Fig. 4.3 above. Consistent with the weaker bottom onshore velocities at the Lacepede shelf, the origin of the plume is clearly from north/north-westward advection of colder waters from the BC region. The flow bifurcate into a westward flow off Cape Jaffa, and the bottom flow is veered alongshore since the equatorward side of the BeachPort Bank. The source of cold waters is them both the near-shore upwelled waters at the BC, as well as the advection by the jet within the BC (Figs. 4.6, 4.9).

Another notable feature of the SST data (Fig. 4.3) is that the surface signature of the upwelling appears as a plume beginning west off Portland. The model SST results in Fig. 4.9b show a similar result. The reason for this appears to be

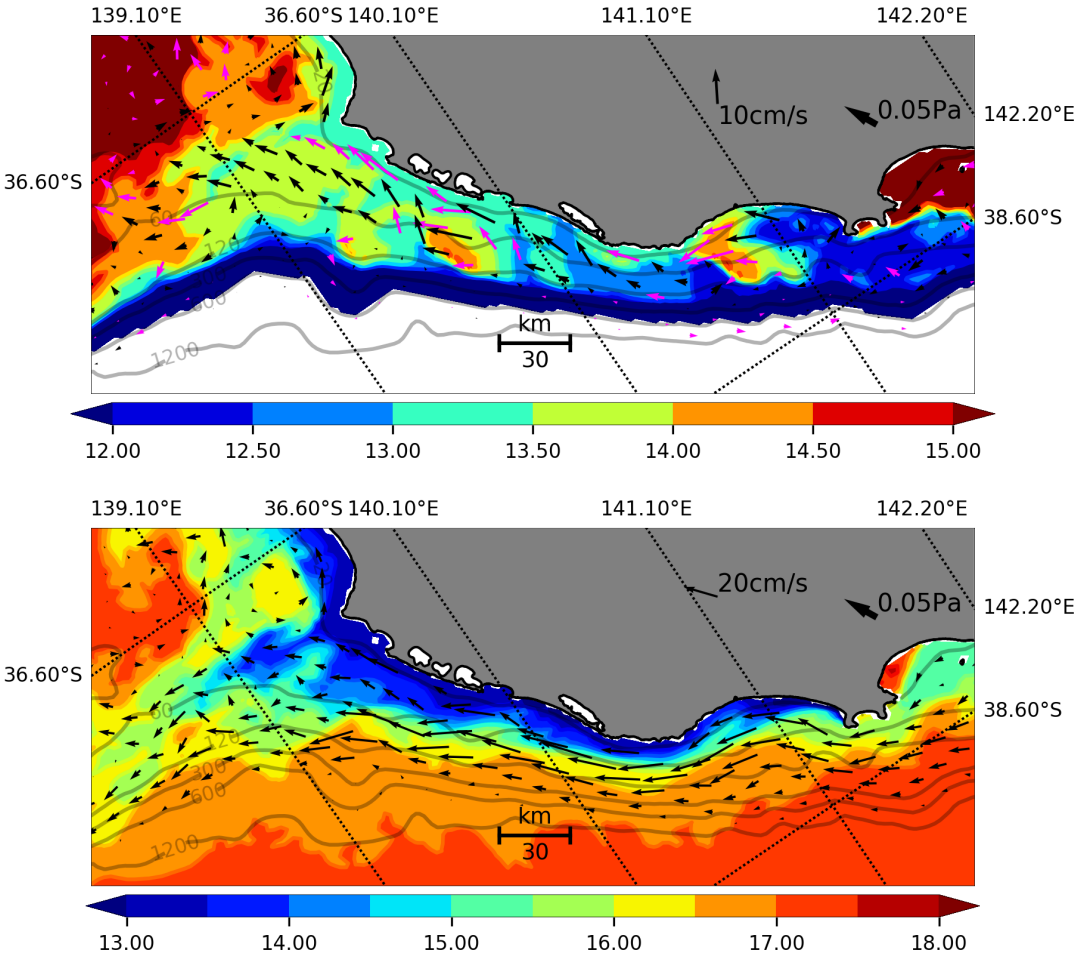

Figure 4.9: Details of the BC region at day 30. (a) Bottom temperatures averaged over day 30 (shading) with bottom velocity indicated by the vectors (legend of $10cm/s$ is indicated). Black (magenta) vector are ones where the magnitude of the flow decreased (increased) from day 6. (b) Sea surface temperature averaged over day 30 and with depth-averaged velocity vectors ($20cm/s$ legend indicated). Note the lack of different vector colours, the difference in colour shading and vector scale used in a). Isobaths as in Fig. 4.6.

related to the widening of the shelf to the east of Portland. There, onshore of the $60m$ isobath, bottom temperatures did not change significantly from the initial conditions. Colder bottom waters do not reach the Portland Bay region (compare the red, $15°C$ isotherm, Fig. 4.6 – Fig. 4.9a). Consistent with this, and to the south-east of Portland, the north-westward jet is situated over deeper isobaths (Fig. 4.9), and unable to bring shelf-edge upwelled water into the bay south off Portland.

4.3.5 Dynamics of submarine headland and valley upwelling: vortex stretching

The dynamics of the upwelling for the BC region appear to be strongly related to vortex stretching and squashing. This may be shown by considering the conservation of vorticity for an inviscid, barotropic ocean with no density variations. With $\zeta = v_x - u_y$ the relative vorticity, then following Gill (1982) (eqn. 7.10.7), and after invoking continuity, the equation for the total vorticity $(f + \zeta)$ may be written as eqn. 4.6:

$$w_z = D(1 + \zeta/f)/Dt(1/(1 + \zeta/f)) \tag{4.6}$$

where w is the vertical velocity (the subscript z denotes differentiation) and D/Dt the derivative following a fluid column. This may be integrated from the sea floor $(z = -h)$ to the surface $(z = 0)$ to obtain

$$w_b = w(x, y, -h, t) = -h(x, y)(1/(1 + \zeta/f))D(1 + \zeta/f)/Dt \tag{4.7}$$

where Ekman pumping at the surface is zero (constant winds) and the rigid lid approximation is made ($w = 0$ at $z = 0$): this can be shown to be a very good assumption using typical estimates for w at the surface $(d\eta/dt)$ and bottom (eq. 4.2 above). The contribution of the bottom stress curl was also determined and found to be about 25% of that due to the topographic slope (not shown). Equation (4.7) will prove useful in inferring the sign of the bottom velocity and thus upwelling. In addition, the equation for the conservation of potential vorticity (Gill 1982) may be written as

$$D[(\zeta + f)/h]/Dt = 0 \tag{4.8}$$

and will be used first to confirm the approximate locations of model estimates of ζ/f.

Now, consider Figure 4.10, which presents a detailed model view for the BC to assist in determining the causes of the upwelling. We note that the upwelling

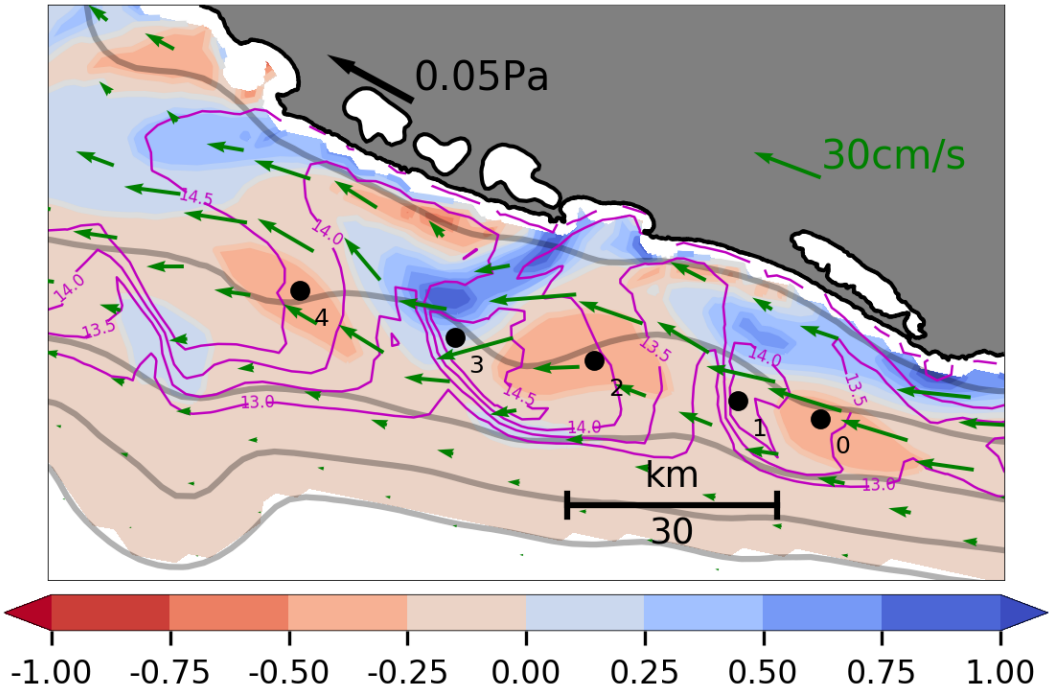

Figure 4.10: A detail for the BC at day 6 where ζ/f is indicated by the shading, with blue (orange) for cyclonic (anticyclonic) barotropic vorticity. Depth-averaged currents are presented as green vectors ($30cm/s$ vector indicated). Bottom temperature is indicated by the magenta lines (13, 13.5, 14 and $14.5°C$). Fluid column locations at points 0, 1, 2, 3, and 4 are labelled.

occurs within the valleys and is enhanced on the equatorward side of the headlands.

The regions of cyclonic (blue) and anticyclonic vorticity (red), determined from the model are shaded in Fig. 4.10 and are presented along with the direction of the depth-averaged flow (the green vectors). Between the points 0 and 1, the flow is directed into deeper water: to conserve potential vorticity $(\zeta + f)/h$, the relative vorticity ζ/f must increase and cyclonic vorticity results (blue shading). Between points 1 and 2, the flow becomes directed into shallower water, h is reduced and anti-cyclonic vorticity results (orange shading). Between points 2 and 3, the flow becomes directed into deeper water and the vorticity again becomes cyclonic (blue shading).

Now consider the use of eq. 4.7 to infer the bottom vertical velocity. First, it is noted that ζ/f varies from about -0.5 for anticyclonic regions to 0.5 for cyclonic regions and that $(1 + \zeta/f)$ is always positive. Thus, the magnitude of the bottom velocity w_b from eq. 4.7 will be smaller in cyclonic regions and larger in anticyclonic regions, but the sign of w_b only depends on $D(\zeta/f)/Dt$. The magnitude of w_b will also be larger in deeper regions due to the depth factor h in eq. 4.7.

Now consider the point 0 labelled in Fig. 4.10. Here the upwelling is relatively weak, as indicated by the isotherms, and the vorticity is anti-cyclonic. As a fluid column moves with the depth-averaged velocity towards point 1, it acquires cyclonic

vorticity and $D(\zeta/f)/Dt$ is positive and the bottom velocity is negative: this downwelling over the headland is consistent with the isotherms shown. Downwelling over a submarine headland was also found in the study of Gan et al. (2002b) and Gan et al. (2002a).

Moving from point 1 to 2 across the valley, the fluid column acquires anticyclonic vorticity, $D(\zeta/f)/Dt$ is negative and the vertical bottom velocity is positive (upwelling). In addition from eq. 4.2, the approximate kinematic boundary condition $w_b = -u_b\, dh/dx$, since dh/dx is negative, then u_b must be positive and directed onshore. This flow in part drives the upwelling apparent between points 1 and 2.

A similar result to those above is found following the flow from points 2 to 3, where cyclonic vorticity is acquired so $w_b < 0$ and headland downwelling occurs. Then between points 3 and 4 the column acquires anticyclonic vorticity so that $D(\zeta/f)/Dt$ is negative, w_b is positive and valley upwelling is again found.

To provide further confirmation of these results, the model was re-run for the northern hemisphere by reversing the sign of the Coriolis parameter and direction of the wind stress. With the implied change in the directions of poleward and equatorward, the preference for strongest upwelling over the equatorward side of headlands was again found and consistent with the observational and numerical modelling studies of the Oregon/Californian shelves noted above.

The arguments above relating barotropic vorticity to upwelling provide a simple qualitative explanation for the modelled upwelling (downwelling) over the valleys (headlands) both here and for the northern hemisphere case (Oregon/Californian shelves). In this context, it is noted that Whitney et al. (2009a) points out that while (barotropic) potential vorticity (eq.4.8) is not conserved, "the tendency for relative vorticity changes and depth changes partially counter each other " is helpful in understanding the dynamics of topographic induced upwelling.

For the case here (see Fig. 4.6b), typical values of $f = 1 \times 10^{-4}\,\mathrm{s}^{-1}$, $V = 0.15m/s$ and flow curvature $R = 15km$ give $R_o = V/(fR) = 0.1$ suggesting non-linear effects are small. For a larger $V = 0.4m/s$, R_o is still small (0.25) which implies that although not negligible, non-linear gradient effects in the context described by Arthur (1965) are of secondary importance.

In the studies of Whitney et al. (2009a) and Whitney et al. (2009b) they also concluded that gradient wind (non-linear) effects were small as quantified by the Rossby number above. Gan et al. (2002a) also suggest that the stronger onshore (geostrophic) flow and upwelling on the equatorward side of the Pt.Arena and Reyes headlands on the west coast of the United States are driven by an alongshore pressure intensified by the gradient wind so that non-linear effects are important.

The question then arises as to the physical cause of the preferential upwelling that is found on the equatorward (poleward) side of the submarine headlands

(valleys). With the exception of the analysis of Arthur (1965), we have been unable to obtain a direct (and simple) explanation of the cause of the preferential upwelling on the equatorward side of the submarine headlands or banks. Gan et al. (2002a) present momentum balances but we find it difficult to find a definitive explanation in their study for the enhanced alongshore pressure gradients that lead to the preferential upwelling.

Indeed, a simple hypothesis for the preferential upwelling found here (Figures 4.6b, 4.10) and elsewhere, is related to the alongshore pressure gradients set up by the upwelled dense and downwelled light water. Consider the point 3 labelled in Fig. 4.10 which is located on the equatorward side of the Beachport Bank submarine headland and where intense upwelled water is indicated by the onshore displacement of the magenta lines of $13 - 14°C$ water. To the immediate south-east, near point 2 (over and to the poleward side of the headland), the expected downwelling occurs as indicated by the offshore displacement of the $14°C$ isotherm. The upwelled dense and adjacent downwelled light waters will lead to an alongshore baroclinic pressure gradient largest near point 3 and directed to the south-east. This pressure force will, in turn, drive a geostrophic current that is itself directed onshore that will, as a positive feedback mechanism, enhance the upwelling of water near point 3. A similar result is obtained for the enhanced upwelling near point 1.

For downwelling, a similar argument holds: consider the pressure gradient between points 1 and 2. Towards the latter, the downwelling of mixed water leads to lighter water than found towards point 1 and the alongshore pressure gradient is now directed to the north-west. The geostrophic velocity will now be directed offshore leading to enhanced downwelling near point 2.

As indirect proof of the importance of this baroclinic mechanism, results are compared with those obtained without baroclinic gradients (constant temperature and salinity). Following Whitney et al. (2009a), the model vertical velocity w_{bbl} at a height $z1$ above the viscous BBL was determined: the height $z1$ is set to be the height at which the frictional terms become $1/10th$ of the bottom maximum value. The bottom vertical model velocities with baroclinic effects are presented in Fig. 4.11a (with amplitudes meters/day) and the approximate locations of the points 1, 2 and 3 are labelled by black dots as in Fig. 4.10. The upwelling and downwelling within the valleys and over the headlands are evident. The preferential upwelling (downwelling) on the equatorward (poleward) side of the headlands and valleys is also shown, although the precise regions are somewhat ill-defined due to the complex topography.

Now consider the barotropic results obtained for w_{bbl} by holding the temperature and salinity as constant everywhere (Fig. 4.11b). In this case, the results should

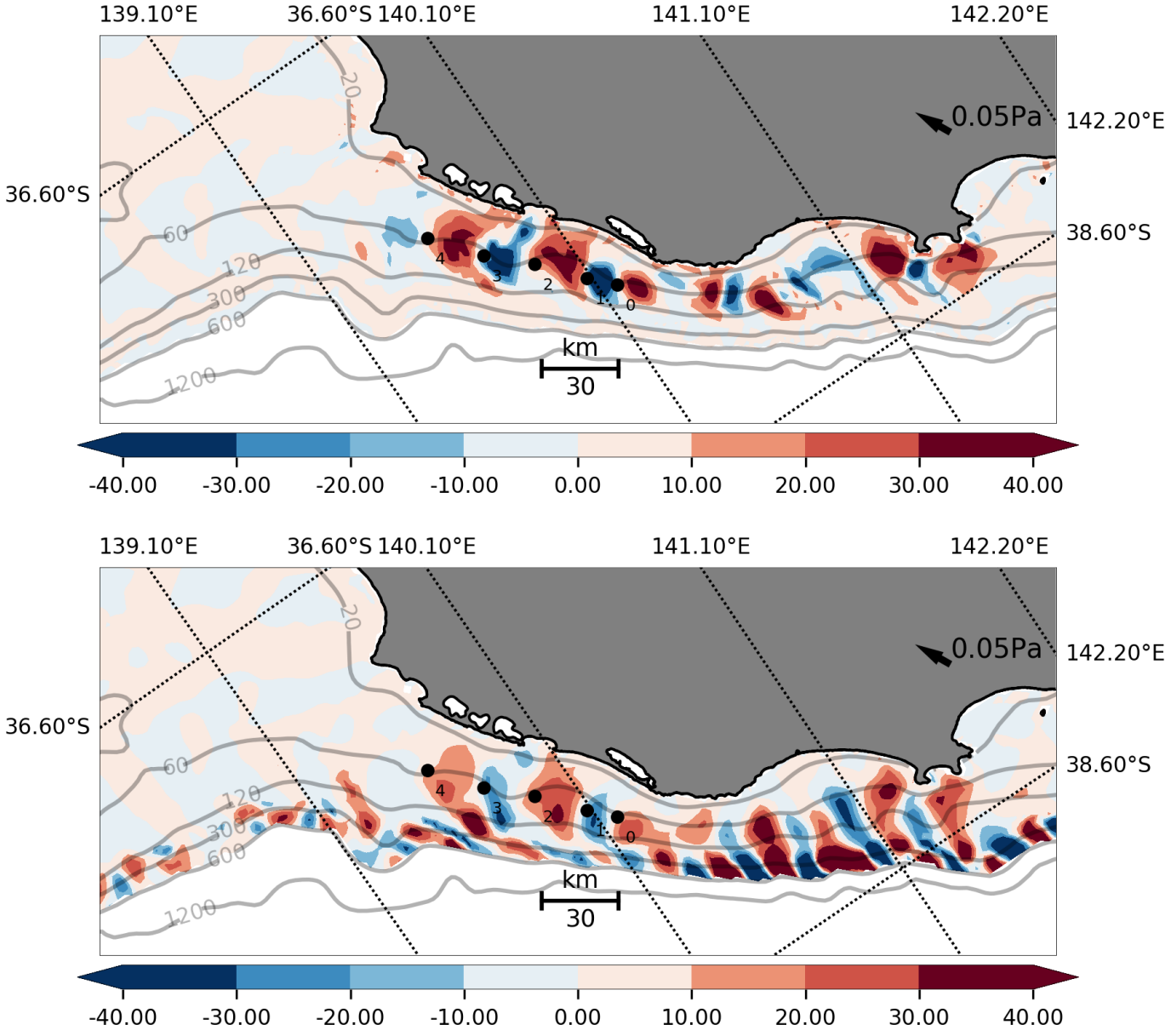

Figure 4.11: (a) The vertical model velocity (m/day – shading) at the "top" of the viscous BBL at day 6. Isobaths depths are 20, 60, 120, 300, 600, 1200m and indicated in black. Fluid column locations at points 0, 1, 2, 3, and 4 are in black circles (from South to North). (b) As in (a) but determined with temperature and salinity constant everywhere – no thermal wind shear.

mirror those obtained using the barotropic vorticity arguments above and again, downwelling is found over the headlands and upwelling within the valleys as illustrated in Fig. 4.11a. The vertical velocities shoreward of the $125 - 200m$ isobaths, that bound the valleys and headlands, are generally much weaker. Since $w_{bbl} = -u_{bbl}\, dh/dx$ and u_{bbl} is approximately geostrophically balanced, the results indicate that the alongshore baroclinic pressure gradients are very likely important. With temperature and salinity held constant, larger vertical velocities are also found to greater depths of $600m$ but this is an artefact of the lack of thermal wind shear, which would otherwise reduce these velocities from their near-surface values to near zero – see Fig. 4.8. Thus, the results of Liu et al. (2015) relating the bottom stress curl being an important player in the vorticity balance could not be extended towards deeper water: the stretching mechanism is more dominant in deeper water and under stratified conditions.

In summary, it has been shown that the vortex dynamics and enhanced alongshore pressure gradients due to upwelling and downwelling provide a simple qualitative explanation of cross-shelf exchange pumps that arise on the BC. The exchange and upwelling pumps arise from a sequence of gentle submarine headlands and valleys that characterize the shelf region at depths of $150m$ and less. A more definitive idealised modelling study is needed to extend these ideas but is beyond the scope of this study.

4.3.6 The Kangaroo Island region

The topography of the KI region is much more complex than the BC, with the two Gulfs, KI and the EP which act as both submarine and terrestrial headlands (Fig. 4.12a). In addition, a deep valley or "cold pool" (McClatchie et al. 2006) of water lies between these topographic features. Nonetheless, the results above for preferential upwelling into valleys, strongest intensification on the equatorward side of headlands and downwelling over headlands will find application here. Since the upwelling is not as pronounced as on the BC, results for days 0 and 30 will be presented: those for day 6 (not shown) are less pronounced than those at day 30 but otherwise qualitatively similar.

The surface elevation contours westward off Kangaroo Island, Figure 4.4,are clearly veered onshore, indicating a cyclonic jet that approximately follows deeper isobaths ($> 100m$) in the vicinity of the island. After passing the island, the flow is mostly alongshore, until the following coastal promontory EP, being again predominantly onshore.

This behaviour is similar to the barotropic and frictional dynamics in a coastal promontory studied in Liu et al. 2014. There, an alongshore increased in the

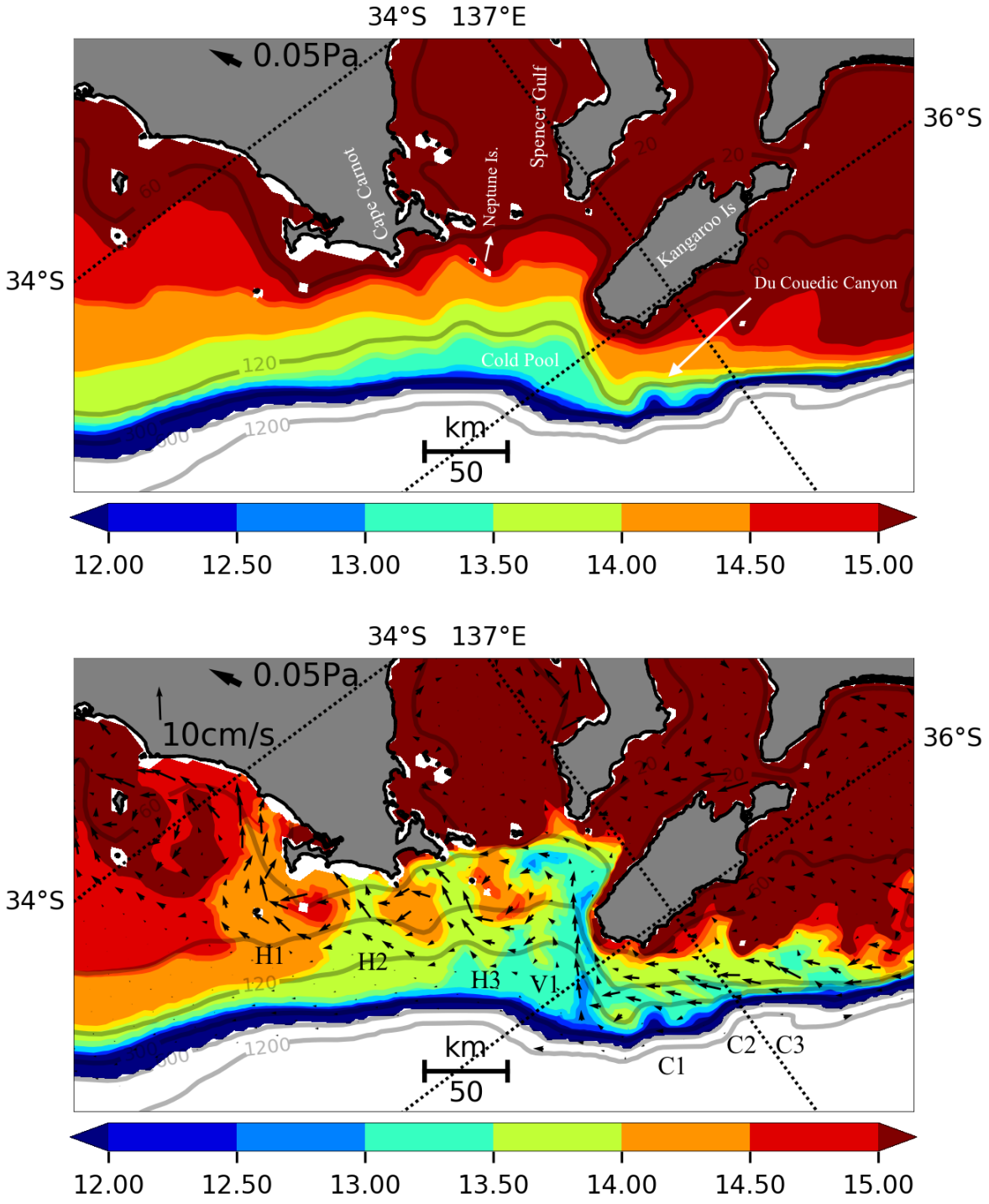

Figure 4.12: Detail of the Kangaroo Is region: (a) Initial Bottom temperatures. Place names are indicated, including the Du Couedic Canyon and Kangaroo Island Pool. Isobath as in Fig. 4.6. (b) As in (a) but for day 30 and with vectors of bottom velocity ($10cm/s$ legend indicated). The locations of submarine canyons ($C1$ – du Couedic and $C2/C3$ – Murray Canyons), headlands ($H1$ – Eyre Peninsula, $H2$ – Cape Carnot, $H3$ – Neptune Is.) and the valley $V1$ – Kangaroo Island cold pool, associated with upwelling are also labelled.

pressure gradient force is regarded as the origin of the intensified cross-shore flow downstream (in the current sense). Horizontal advection (and bottom stress) peaked in the vicinity of the promontory, with increased shoreward transports and stretching terms (see Figure 11. in Liu et al. (2014)). Although this balance will shift here, given the stratified conditions, the vortex stretching mechanism will also be stronger and dominant in deeper regions, such as in the vicinity of cold pool and deeper isobaths.

Details of bottom temperature for days 0 and 30 are presented in Fig. 4.12a,b. Bottom velocities are also presented for day 30 and are typically $10 - 20cm/s$. Again, for the initial state, the location of the yellow $14°C$ isotherm is illustrated in Fig. 4.12a and lies close to the $110m$ isobath. By day 30 (Fig. 4.12b), this water has been upwelled in between the three submerged headlands ($H1$,$H2$,$H3$) shown and to shallower depths of $50m$ or so. Over the submarine headlands ($H2$ and $H3$), the upwelling is much reduced which is consistent with both the directions of bottom velocity (Fig. 4.12b) as well as that expected from the above general analysis of the BC.

Upwelling is most intensified in valley $V1$ (the cold pool) and to the equatorward side of the Kangaroo Is (KI) headland. Here, a plume of very cold water ($12°C$; blue), is present by day 30, upwelled from depths of $150m$, towards the western end of KI and to depths close to the $60m$ isobath (Fig. 4.12b). The western (equatorward) flank of KI and the $120m$ isobath form a headland that draws the very cold $12°C$ (blue) plume from the south and to the equatorward side of it: that is to the north-west of KI. Indeed, the depth-averaged velocities (Fig. 4.13) at the southern extent of the plume ($150m$) turns to the north and along the $120m$ isobath and then meanders to the west seaward of the $60m$ isobath. In conjunction with the bottom velocities, this headland advection appears to be the likely cause of the extensive $12°C$ cold plume shown in Fig. 4.12b.

Along the southern coast of KI, upwelling of $14°C$ water (yellow contour) from the $110m$ to $50m$ isobaths is also evident (Fig. 4.12) and the depth-averaged alongshore velocities (Fig. 4.13) are relatively large with bottom velocities directed onshore (Fig. 4.12b). Presumably, the upwelling and alongshore velocities here result from 2-dimensional Ekman upwelling due to the presence of the southern coast of KI.

In deep water ($> 120m$), three possible canyon upwelling sources at day 30 are labelled in Fig. 4.12 as $C1$, $C2$ and $C3$. Surprisingly, none of these canyons indicate the local upwelling to be significant since the bottom temperatures are similar to those at day 0 and 30 (Fig. 4.12b). The depth-averaged alongshore flow at these canyons is, from Fig. 4.13, weak ($< 5cm/s$) and the onshore bottom velocities relatively small ($< 2cm/s$).

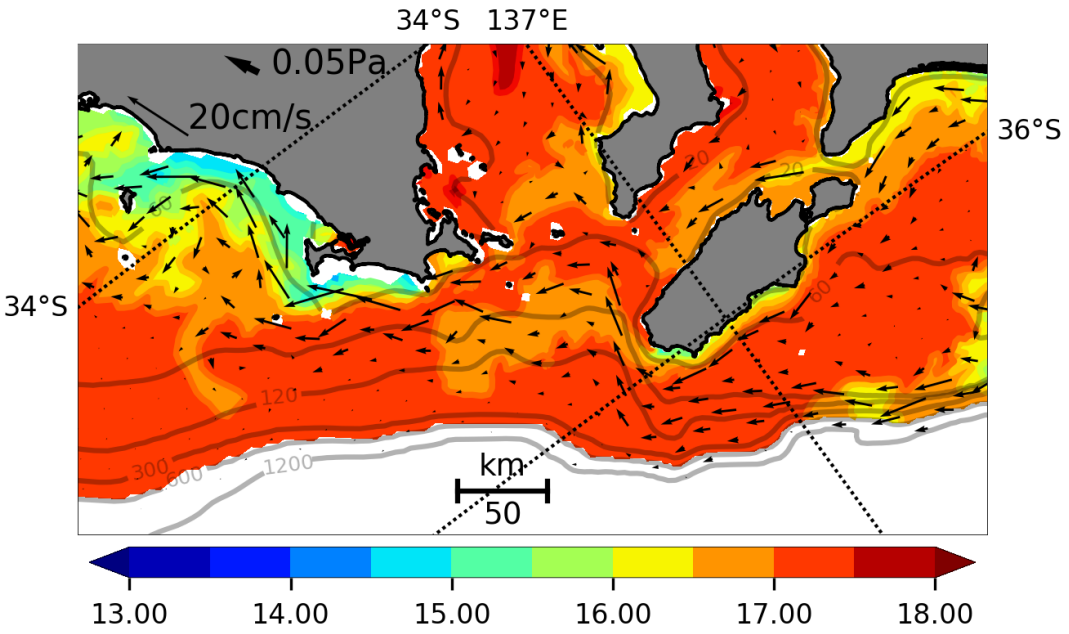

Figure 4.13: Detail of the Kangaroo Is region. Sea Surface Temperature ($°C$) at day 30 and with depth-averaged velocity vectors indicated ($20cm/s$ legend indicated). Note the change in the colour limits from Fig.4.12.

Additional regions of bottom upwelling are also associated with the EP headland $H1$, Cape Carnot headland $H2$ and Neptune Island headland $H3$. In each case, upwelling occurs near the equatorward side of these headlands (Fig. 4.12b). Advection by the north-westward bottom currents drive upwelled water from the cold pool to the north-west of the Eyre Peninsula leading to the SST cold water anomaly shown in Fig. 4.13.

Indeed, the general response of SST to the above bottom upwelling is shown in Fig. 4.13. Again, the initial SST was $17.6°C$. The coldest surface signature of upwelling occurs off the EP and south-west KI with temperatures of $14.5 - 15°C$. This upwelling plume is the strongest in the region, and driven by upwelling of $13.5 - 14°C$ water from the headlands $H1$ and $H2$ (Fig. 4.12b), along-isobath ($10cm/s$) advection and associated onshore BBL transport (Fig. 4.12b). Over 20–30 days, waters advected at $5cm/s$ would be moved a distance of around $85km$ which is sufficient to explain the resultant location of the cold EP plume. This result is consistent with the hypothesis (and results) raised by McClatchie et al. (2006) that the EP upwelling plume is influenced by cold pool waters from the south-east: our results here support this hypothesis but with the alongshore topographic features playing a significant role.

To the west of KI, the SST model results at day 30 are also consistent with the remotely sensed SST picture depicted in Fig. 4.3; the strongest signal is a coastal attached signature in the shallow shelf southwest of the KI. The surface signal at

the coast ($15°C$) is about the same off the EP ($15°C$), consistent with the above bottom flow (see Fig. 4.12b) but in a much-reduced area. Although the horizontal extent of the SST signal in the vicinity of KI is small, the upwelling through the bottom is relatively strong and the cold pool formation in spring/summer is an important reservoir of nutrient for the region (McClatchie et al. 2006; Ruth et al. 2010).

4.4 Summary and Conclusions

The southern shelves of Australia host two important upwelling systems off the BC and the region of KI/Eyre Peninsula. An idealised numerical model was developed to examine these upwelling systems and driven with an impulsively started $0.05Pa$ wind stress and initially horizontally uniform stratification. The wind stress was taken to be spatially uniform and to the north-west, so as to (a) approximate that found for summertime upwelling favourable winds, and, (b) to eliminate Ekman pumping as a source of upwelling.

The focus of the analysis was the remarkable upwelling induced by the seven pairs of gentle submarine valleys and headlands that characterise the BC shelf region. These valleys and headlands have alongshore scales of 20–30 km, depth differences of $10-40m$ and extend from the coast to depths of $120-150m$. Despite their gentle nature, the model results show that upwelling rates can exceed $30m/day$ with onshore velocities of order 4-8 km/day.

In agreement with studies (Whitney et al. 2009a; Whitney et al. 2009b) of other regions, such as the Californian/Oregon shelves, upwelling is found within the valleys and downwelling over the headlands. The results were well-illustrated by alongshore transects of temperature where the up- and downwelling appears as a standing wave locked to the topography.

However, the upwelling (downwelling) were shown to be qualitatively consistent with barotropic vorticity dynamics where the bottom vertical velocity w_b is inferred from the acquisition of anti-cyclonic (cyclonic) vorticity as a fluid column moves equatorward and across the headlands and valleys.

An additional feature of the solutions is that the upwelling was found to be intensified on the equatorward side of the submarine headlands. A similar result has long been known for the headlands off the Californian/Oregon shelves through the observational and modelling studies noted above. For the BC upwelling, non-linear curvature effects appear to be of secondary importance. Indeed, a new explanation for the preferential upwelling was given here and shown to result from the alongshore baroclinic pressure gradient set up by the up- and downwelled density field that in turn drives an onshore geostrophic flow: this intensifies the upwelling and acts as a positive feedback mechanism. Such a mechanism is simple and should find application to the dynamics of many other upwelling systems of the world. Indeed, by reversing the signs of the wind stress and Coriolis parameter, the "northern hemisphere" results here show that the preferential upwelling again occurs on the "southern" or equatorward side of the headlands as found for the Californian/Oregon shelves.

These results were also used to qualitatively explain the modelled upwelling

found for the topographically more complex regions of KI and the EP. The model results for surface temperature are also in qualitative agreement with satellite data. The cold upwelled plume off the BC is reproduced along with the bifurcation in the Lacepede Shelf. Cold upwelled waters are also found off the west coasts (equatorward sides) of the headlands of KI and the Eyre Peninsula.

A notable feature of the enhanced BC upwelling/downwelling is that it is driven by the alongshore velocity and associated vortex stretching. Winds are needed to bring upwelled water to the surface, but not for the bottom enhanced upwelling/downwelling itself.

This is important since SST observations show that upwelling off the BC can appear larger than that for the Kangaroo Is region, even though the alongshore upwelling favourable (geostrophic) surface winds are weaker for the BC (e.g., Figures 4.2, 4.3). A possible explanation here is that the wind-driven equatorward shelf currents for the Kangaroo Is. region are larger but extend poleward to the BC through CTW propagation (e.g., Middleton 2000). The enhanced alongshore currents on the BC in turn lead to vortex stretching and enhanced bottom upwelling even though local alongshore winds are relatively small.

Published observational evidence for the existence of the enhanced upwelling (downwelling) over valleys (headlands) is not available for the BC. However, the sites of enhanced up- and downwelling are well determined by the model results here and could be used to inform observational studies in the future.

The analysis here has not dealt with the set-up and shut-down of upwelling by Coastal Trapped Waves (CTWs) which arise from the 'geographical origin' located in the mid-GAB at Eucla; the backward western boundary of the numerical model at which winds and currents vanish. At this point upwelling also vanishes and a CTW front propagates poleward that acts to largely shut-down Ekman upwelling. Prior to the arrival of this front, (and assuming a uniform shelf), the upwelling would be 2-dimensional and Ekman-like in character and asymptotic to a maximum viscous limit (Middleton et al. 2004). An analysis of these effects is presented in Chapter 5, where it is shown that the results will be similar to those that would have been obtained if the western boundary was correctly chosen as Cape Leeuwin. An exception here is that the adoption of Eucla as the geographical origin means that upwelling for the KI region is likely shut-down before the viscous limit is reached. That is, upwelling at KI in the results above may underestimate that in reality. In addition, the effects on upwelling/downwelling of periodic remotely forced winds are examined through the use of a simple CTW paddle at the Eucla boundary.

Chapter 5

Upwelling along the shelves of the Greater Australian Bight. Part II: set-up, geographical origins, the viscous limit and role of Coastal Trapped Waves

Abstract

The transient set-up of coastal upwelling in the Greater Australian Bight (GAB) is examined using a hydrodynamic model driven by an impulsively applied, constant wind stress that vanishes in the mid-GAB (Eucla) which then acts as a geographical origin for upwelling set-up. Eucla is chosen as the backward model boundary due to computational constraints. The upwelling set-up is shown to be qualitatively explained by analytical theories that involve concepts of 2-dimensional Ekman upwelling, its maximal viscous limit, and shut-down by the Coastal Trapped Wave (CTW) front generated at the mid-bight geographical origin. The location of the geographical origin and associated CTW shut-down are often neglected in upwelling studies but can be important in regulating the degree of upwelling. In accord with observations, these theories show the upwelling to be largest in the east and weakest in the far west: the modelled upwelling off Kangaroo Island is likely underestimated. A second study involves the circulation driven by a 10 day periodic, CTW paddle at the mid-GAB boundary and is a proxy for wind-driven motions in the western bight. The results show that the equatorward (poleward) alongshore velocities of the CTWs drive bottom upwelling (downwelling). Periodic upwelling is found to occur in the valleys and is strongest on the equatorward side

of the submarine headlands: a result consistent with that found for forcing by a constant wind. The upwelling and downwelling were found to be quite asymmetric. When averaged over the CTW period, a weak but possibly significant rectification is found.

5.1 Introduction

The Greater Australian Bight (GAB) is here taken as the shelf and slope regions from Cape Leeuwin in the far west to the south-western tip of Tasmania (Fig. 4.1). The topography of the region is quite complex with shelf widths of $150km$ in the mid-west to $30km$ for the Bonney Coast (BC) in the east. Between these extremes, lie the widened shelf regions of the Gulfs with the narrow regions associated with the Eyre Peninsula and Kangaroo Island (KI). In the far east lies Bass Strait and the narrow shelves of Tasmania although the analysis here will deal only with the upwelling circulation between Cape Leeuwin and Portland on the BC.

The summertime atmospheric pressure in this region is characterised by a seasonal anticyclonic high-pressure system at approximately the centre of the Bight, generating winds that are upwelling favourable (e.g., Fig. 4.2 – Chapter 4). The upwelling generated by such winds was examined in a simplified framework in Chapter 4: a constant, impulsively started upwelling favourable wind was adopted with a focus on the upwelling regions of KI and the BC. Fluxes of heat and freshwater were set to zero. In that analysis, it was shown that the upwelling is modified by the presence of submarine headlands and valleys (particularly along the BC) that, through vortex stretching and squashing, (and the upwelling itself), leads to preferential upwelling on the equatorward side of submarine headlands. Such a result is consistent with studies of upwelling on the Californian/Oregon shelves, (e.g. Barth et al. 2005; Gan et al. 2002b; Gan et al. 2002a).

Note here and below, the notation of poleward and equatorward will be adopted so that the southern hemisphere results presented are readily re-interpreted for the northern hemisphere, western shelf cases such as those for Oregon and California. For both hemispheres, poleward denotes the direction in which CTWs propagate. For the southern hemisphere case here, that is with the coast on the left and from Cape Leeuwin towards the BC. Equatorward means in the opposite direction.

The results obtained in Chapter 4 adopted an idealised stratification and the western equatorward domain of the model ending at Eucla in the mid-Great Australian Bight (GAB) as shown in Fig 4.1: the later was chosen due to constraints in computational power. At and to the west of this boundary (as well as the others), winds, velocity and sea level variations were set to be zero in the Flather Open Boundary Conditions (OBC) ($\eta = V = U = 0$). As outlined next, these conditions imply that this boundary acts as a "geographical origin" for wind–forced CTW generation that affects the degree of upwelling poleward of the origin.

Indeed, theories for the important role of geographical origins in CTW generation were advanced almost 4 decades ago by Suginohara (1982), Crépon et al.

(1982), and Philander et al. (1982). Geographical origins correspond to regions where the alongshore component of wind either vanishes or where the coastal topography abruptly changes direction so that the cross-isobath component of Ekman transport vanishes. In both cases, the sea level and alongshore ocean velocities vanish at the origin and a CTW front is set up by the impulsively forced constant winds that propagate poleward along the shelf. Prior to the arrival of this CTW front, the wind-driven Ekman upwelling is 2-dimensional, time-dependent and continues toward a state of maximal upwelling (a viscous limit), where the surface wind stress and bottom stress approximately balance and the flow no longer accelerates (Brink et al. 1978; Middleton et al. 2004). Upon arrival of the CTW front, the associated alongshore velocity becomes quasi-steady and convergent and acts to "feed" the offshore surface Ekman transport. This partially shuts-down the need for an onshore interior transport that would otherwise contribute to upwelling. Such a theory was shown to be important in determining the correct degree of upwelling off the Chilean shelf (Middleton et al. 2004).

For the region of interest here, the predominantly zonal shelf of the GAB changes orientation at Cape Leeuwin (Fig. 4.1) to become meridional in orientation. To the immediate west of Cape Leeuwin, there is no zonal shelf and coast. The summer upwelling favourable winds (anti-clockwise winds of the GAB are typically associated with synoptic large high-pressure systems as illustrated in Fig. 4.2) off Cape Leeuwin are approximately directed offshore to the west and the associated surface Ekman transport (predominantly to the south) does not generate a return interior transport, CTWs or upwelling. Such a point acts as a geographical origin since to its immediate east; a zonal shelf does exist and serves as a site of CTW generation. Indeed, to the east of Cape Leeuwin the Sea Surface Temperature (SST) images for February $7th$ 2008 suggest that upwelling only occurs in the eastern regions of the GAB including KI and the BC (Fig 5.1 lower panel); little upwelling is apparent in the far western GAB (Fig 5.1 upper panel) that lies nearest to the geographical origin of Cape Leeuwin. In section 5.2, the solutions noted above for CTW generation and shut-down will be detailed to explain these observations as well as the numerical model results of Chapter 4 and the effect of (artificially) choosing Eucla in the mid-GAB as an effective geographical origin: the modelled upwelling off the BC correctly approximates that of the viscous limit (maximal), while that for the KI region likely under-estimates the maximal values expected in reality.

In addition, results will also be obtained in section 5.3 using a 10-day periodic CTW paddle at the Eucla boundary of the hydrodynamic model. This paddle drives a circulation that acts as a proxy for wind-driven energy generated on the equatorward side of the Eucla western boundary. Such periodic waves can,

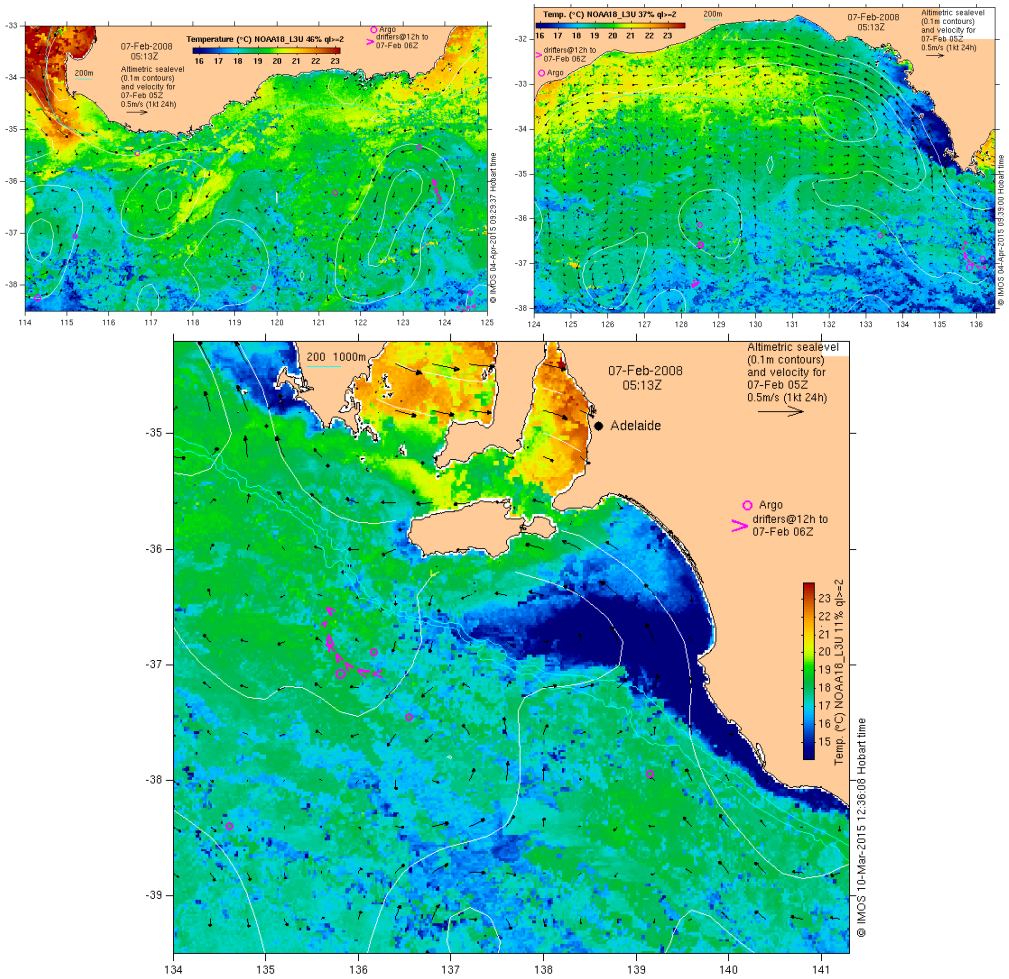

Figure 5.1: The satellite derived sea surface temperature (SST) on the 7*th* of February 2008. Upper left panel: Western GAB. Upper right pannel: Mid-GAB to northern Eastern Great Australian Bight (EGAB). Lower panel: Bonney Coast. Black arrows denote analysed surface currents and white lines of constant analysed sea level (both altimeter derived). Colour scales for temperature differ between panels. Note the lack of the upwelling in the west despite the strong signature in the east. Source: *imos.org.au*

through the bottom boundary layer (BBL), drive both upwelling and downwelling (Middleton et al. 1996; Austin et al. 2002). As will be shown, the alongshore currents of the CTWs drive upwelling (downwelling) within the valleys (headlands) and the mechanism are likely that due to vortex stretching as outlined in Chapter 4.

5.2 Classical Ekman Upwelling, the viscous limit and CTW shut-down: initial set-up 0-6 days.

Following Middleton et al. (2004), a brief summary is first given of classical Ekman upwelling, the viscous limit and its application to the modelling results for the BC, eastern GAB, obtained in Chapter 4. Then, the theory of CTW shut-down is outlined and a comparison with numerical model results made to determine the validity of the assumed geographical origin at Eucla in the mid-bight. These theories adopt a barotropic model with an idealised uniform shelf. Clearly, the shelf and upwelling of the GAB are far from uniform. Nonetheless, these idealised theories will provide explanations for dynamical aspects of the modelled upwelling. These are a) initial set up of upwelling and subsequent confinement largely to the BBL, b) the tendency for the bottom and surface stresses to balance — the 'viscous maximal limit', c) explanations based on CTW shut-down for the observed and modelled lack of upwelling in the western GAB.

5.2.1 Classical 2-Dimensional Ekman Upwelling: the viscous limit

Following Brink et al. (1978), the linear, barotropic equations of motion are

$$-fV = -hP_x \tag{5.1a}$$

$$V_t + fU = -hP_y + \frac{\tau_s - \tau_b}{\rho} \tag{5.1b}$$

where ρ is a constant density, $P = p/\rho$ is scaled pressure, $h(x)$ the shelf depth, τ_s the surface wind stress, τ_b the bottom stress, f the Coriolis parameter and U and V the depth-integrated velocities. The axes differ from the numerical model results of Chapter 4 and here the $y-$ direction is poleward and $x-$ direction offshore. Subscripts of x, y, and t denote partial derivatives.

Now, assume there are no alongshore variations. In this case, the alongshore surface wind stress τ_s and pressure field P are assumed to be independent of alongshore distance y so that the depth-integrated cross-shelf velocity U is zero. The surface offshore Ekman transport is thus exactly equal and opposite to the onshore interior transport associated with upwelling. The wind stress is also assumed constant and applied at $t = 0$. The alongshore depth-integrated velocity V is also assumed to be in geostrophic balance and the equation of motion may be

written as

$$V_t = (\tau_s - \tau_b)/\rho \tag{5.2a}$$

If the surface τ_s and bottom stresses τ_b balance, then the ratio $r = \tau_b/\tau_s$ is equal to one, the acceleration of V ceases and a 'viscous limit' occurs (Middleton et al. 2004). Now assuming the bottom stress can be modelling using a linear law $\tau_b = \rho C_d v_* V/h$ where v_* is some characteristic shelf bottom velocity and C_d a drag coefficient, then the solution for V is

$$V_t = \tau_s T_v[1 - exp(\frac{-t}{T_v})]/\rho \tag{5.2b}$$

$$\tag{5.2c}$$

where $T_v = \frac{h(x)}{C_D v_*}$ is a time-scale for the spin up towards a maximum alongshore transport V where the bottom and wind stress balance. From the numerical model results of Chapter 4, v_* is of order 0.1–0.3 ms^{-1}, $h = 50m$, and $C_d = 2.5 \times 10^{-3}$. The barotropic time scale T_v is then of order 1-2 days.

For a stratified ocean, the offshore surface Ekman transport must, therefore, be balanced by upwelling in the (thin) bottom boundary layer alone and the interior upwelling is largely shut-down. Since the time scale T_v increases with h and x, the quasi-steady viscous limit is achieved later in deeper water.

Middleton et al. (2004) present 2-dimensional numerical solutions that illustrate the above using an idealised stratification and shelf topography. Similar results were found in Chapter 4 as illustrated in Fig 5.2 for a shelf cross-transect just to the south of the Bonney Coast Lake (BCLAKE) (see Chapter 4, Fig. 4.6 for exact location). The upwelling is strong and already largely confined to the BBL with water upwelled from depths $150m$ to $50m$ or so. The stress ratio r at both the $20m$ and $50m$ isobaths have reduced and are close to one as expected for the viscous limit. In addition, the alongshore velocity has accelerated to a maximum value of about $43cm/s$.

It should be noted that the alongshore velocity v (in the $y-$direction) continues to accelerate beyond the barotropic time scale T_v (of order $1-2$ days) and the analogous plot to Fig 5.2 for day 30 (not shown) indicates magnitudes of $54cm/s$. This third stage (not explained by Middleton et al. 2004) results from the offshore (negative $x-$direction) advection in the SML of cold dense upwelled water, which acts to enhance the thermal wind shear:

$$dv/dz = -(\frac{g}{\rho_0 f})d\sigma/dx \tag{5.3}$$

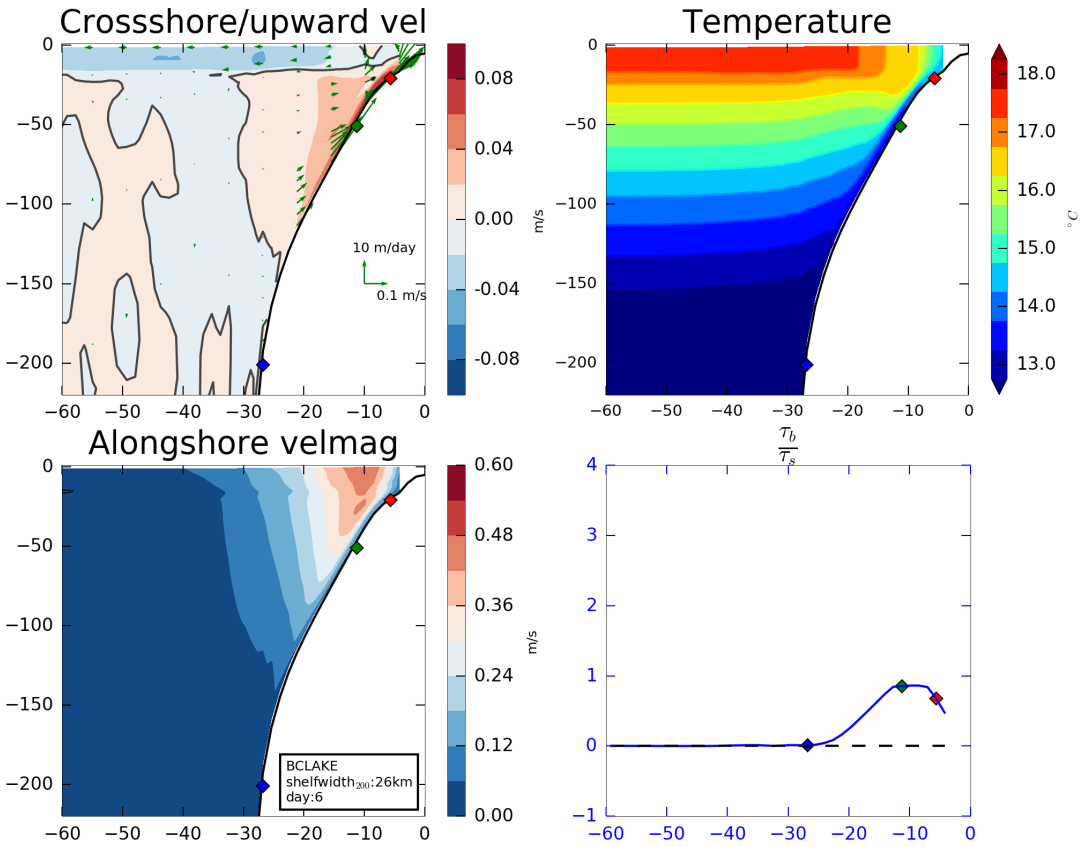

Figure 5.2: Cross section model output just to the south-east of Bonney Lake for day 6: the exact location in Figure 4.6a. Top left panel: cross-shelf velocity and vertical velocity magnified as indicated in the figure. Bottom left panel: alongshore velocity v (m/s). Top right panel: Temperature $(^{\circ}C)$. Bottom right panel: the ratio r $= \tau_s/\tau_b$ of alongshore component of wind stress τ_s to bottom stress τ_b. In each panel, the diamonds indicate the location of the 20 (red), 50 (green) and $200m$ (blue) isobaths. The horizontal axis is the offshore distance (km).

since the perturbation density σ increases towards the shore (positive $x-$direction) and f is negative (southern hemisphere). This enhanced shear would by itself reduce the near bottom alongshore currents and thus bottom stress. However, the bottom stress is not reduced since the current v accelerates and the ratio r is kept to be of order one. While noting this increased upwelling, the viscous limit of maximal upwelling described above will be adopted below and still provide a useful concept in the qualitative analysis of the upwelling.

5.2.2 CTW Shut-down

The model results of Chapter 4 was obtained by assuming that velocity and sea level vanish at Eucla in the mid-bight which lies about $1500km$ to the east of the actual geographical origin at Cape Leeuwin. Several questions arise. First, what is the effect of CTW shut-down on the upwelling within the GAB and notably why is upwelling not observed in the far western GAB (Albany) where the shelf is relatively narrow ($< 60km$) and the alongshore winds can be as large as off KI? Second, does the geographical origin at Eucla adopted previously adversely affect their modelled upwelling through CTW shut-down?

It is noted that the barotropic analysis below adopted formally applies to Continental Shelf Waves but as will be shown, is qualitatively applicable to the stratified model results of the previous chapter. For this reason, the analysis will be described using the term CTWs. To investigate CTW shut-down only, the solutions developed by Middleton et al. (2004) are presented since the application of these is only approximate. However, as will be seen, these solutions do describe the qualitative behaviour of the stratified, hydrodynamic solutions in Chapter 4.

As noted above, both the sea level and alongshore ocean velocities vanish at the adopted geographical origin and a CTW front is set up by the impulsively forced constant winds that propagate poleward along the shelf. Prior to the arrival of this CTW front, the wind-driven Ekman upwelling is 2-dimensional, time-dependent and continues toward a state of maximal upwelling (a viscous limit), where the surface wind stress and bottom stress approximately balance and the flow no longer accelerates (Brink et al. 1978; Middleton et al. 2004). Upon arrival of the CTW front, the associated alongshore velocity becomes quasi-steady and convergent and acts to "feed" the offshore surface Ekman transport.

Analytical solutions to this problem may be described by the stream function ψ where $U = \psi_y$ and $V = -\psi_x$ and

$$\psi = \sum_n \phi_n(y,t) F_n(x) \tag{5.4}$$

where $F_n(x)$ are the eigenfunctions or unforced solution and $\phi_n(y,t)$, the CTW

modal amplitudes.

It will prove useful to define the projection of the surface Ekman transport

$$U^E = \frac{\tau_s}{\rho f} \tag{5.5a}$$

onto the nth CTW mode by

$$U_n^E = b_n U^E \tag{5.5b}$$

where the b_n denote coupling coefficients that typically decrease with mode number n. The phase speed and frictional length scales are denoted by c_n and L_n respectively.

5.2.3 Two-dimensional, time-dependent response: Classical Ekman upwelling and approach to the viscous limit

Now, prior to the arrival of the nth CTW front at times $c_n t < y$, the solutions are two dimensional and $d\phi_n(y,t)/dy = 0$. The solution for the nth CTW amplitude transport V_n and amplitude $\phi_n(y,t)$ may then be written as

$$V_n = -\phi_n = -L_n U_n^E q(t) \tag{5.6a}$$

where the cross-shelf dependence on $dF_n(x)/dx$ is implicit here and below

$$q(t) = 1 - exp(-t/T_n) \tag{5.6b}$$

and $T_n = L_n/c_n$ is the frictional time scale over which the alongshore flow of the nth CTW mode grows exponentially towards the viscous limit:

$$V_n = -L_n U_n^E \tag{5.6c}$$

The solution (eq. 5.6) above for the nth CTW mode is similar to the exact solution (eq. 5.2b) in that both exhibit an exponential growth towards a (2-dimensional) steady viscous limit. It can be shown that the upwelling involves an on-shore interior transport due to the nth CTW model equal to

$$U_n^I = -U_n^E = -b_n U^E \tag{5.7}$$

Were there only a single mode, b_n would be equal to one and the total cross-shelf

transport would be zero: $U = U_n^I + b_n U^E = 0$ — total shut-down.

These solutions are derived under the assumption that the nth CTW mode front (generated at $y = 0$) has not yet arrived. A schematic of the non-dimensional solution for $\phi_n(y,t)$ above is shown in Fig. 5.3 with the red line $c_n t = y$ separating the solutions (eq. 5.6) from those described next that are affected by CTW propagation. For regions far from the geographical origin at $y = 0$, the results in Fig. 5.4 show the approach to the viscous limit is more complete.

5.2.4 The steady solutions and CTW Shut-down

The passage of the CTW modal front ($c_n t > y$) leaves behind a steady solution (Middleton et al. 2004) that is given by

$$V_n = -\phi_n = -L_n U_n^E q(y) \tag{5.8a}$$

where

$$q(y) = 1 - exp(-\frac{y}{L_n}) \tag{5.8b}$$

and

$$V_n = -L_n U_n^E \tag{5.8c}$$

These solutions for $\phi_n(y,t)$ are presented in the schematic Fig 5.3 and the abrupt transition from the two-dimensional Ekman upwelling to a steady-state is evident. The steady-state consists of an alongshore transport that increases in magnitude with y and is therefore convergent. The associated solution for the across-shelf interior transport is

$$U_n^I = -U_n^E[1 - exp(-\frac{y}{L_n})] \tag{5.9}$$

that in magnitude is smaller than that given by (eq. 5.7) prior to the arrival of the CTW modal front. That is, the arrival of the front sets up an alongshore convergence of the transport V which acts to "feed" the offshore surface Ekman transport and reduce the interior upwelling. For regions near the geographical origin ($y/Ln << 1$), both the alongshore transport (eq. 5.8a) and on-shore interior transport U_n^I (eq. 5.9) vanish and the upwelling associated with the nth CTW mode is shut-down. For regions far from the origin, the CTW front is frictionally

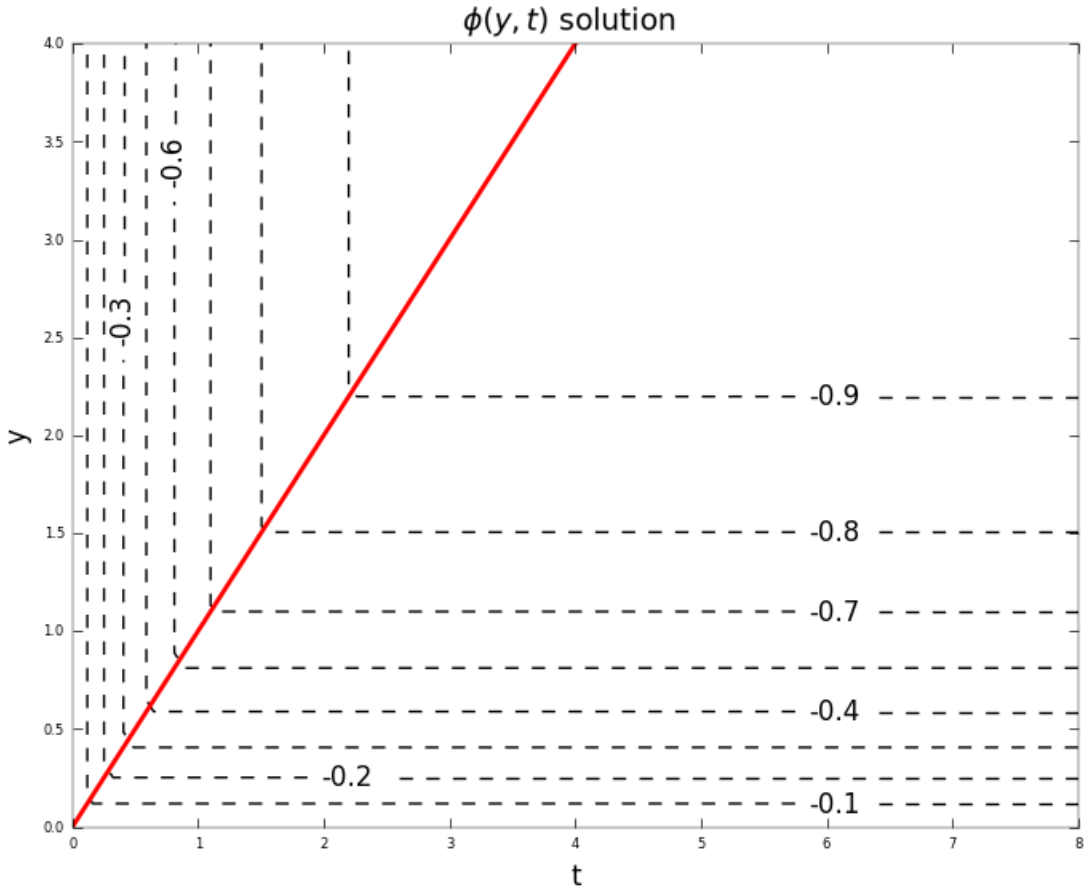

Figure 5.3: Schematic of non-dimensional solutions (2.6b) and (2.8b) for the nth CTW modal amplitude. The red line separates the solutions between a time-dependent and independent one.CTW shut-down occurs to the right of the red line.

dissipated, eq. 5.9 equals eq. 5.7 and the upwelling achieves the viscous limit.

These concepts may be applied to explain the hydrodynamic model results obtained in chapter 4. Since the real topography of the GAB is quite irregular the focus is on the qualitative effects of a first CTW mode with phase speed estimated simply by $c = -fL$: this value corresponds to the CTW speed for an inviscid, barotropic step shelf of width L.

Now, consider the hydrodynamic model results shown in Fig. 5.4 for the alongshore depth-averaged velocity along the $50m$ isobath and as a function of time since a constant wind stress was applied. The y-axis is defined as the distance along this isobath from the western boundary and extends to Cape Otway. The locations of several geographical and town names are shown and defined in the figure caption. In the right side panel, the estimate of the CTW phase speed is given as a function of y and is defined by $c = -fL$ where L is the distance from the coast to the $200m$ isobath. This estimate varies from $600 - 1300km/day$ for the widest sections of the shelf to $250km/day$ for the narrow KI and BC regions. To examine CTW phase propagation and shut-down, the location of the CTW

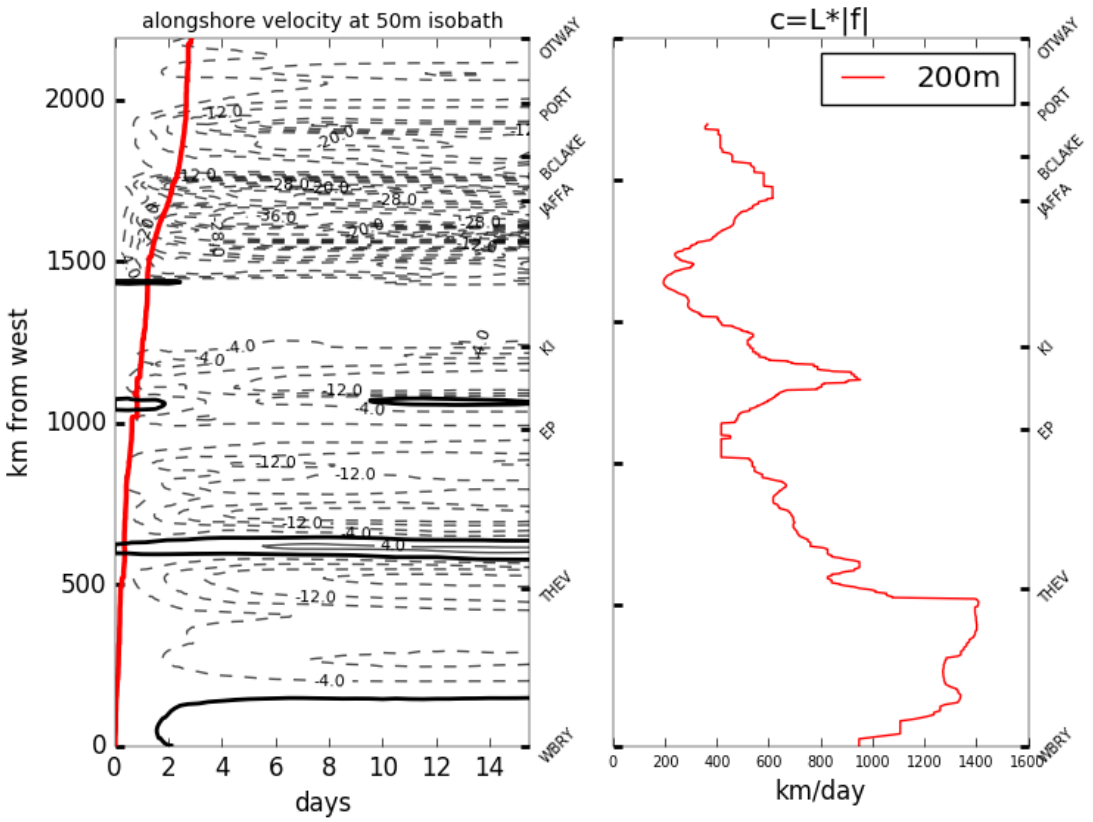

Figure 5.4: Left panel: Solutions for the depth-averaged model alongshore velocity v over the $50m$ isobath as a function of y for the constant wind-forcing in chapter 4 (constant winds and a geographical origin at Eucla). Black thick lines denote the zero contours and the red curve the position of the CTW front calculated with a simple step shelf with width at the $200m$ isobath. Right Panel: The CTW phase speed based on the shelf width. The locations of several sites of interest are labelled: western model boundary (WBRY), Thevenard (THEV), Eyre Peninsula (EP),KI, Cape Jaffa (JAFFA), BCLAKE, Portland (PORT), Cape Otway (OTWAY).

front was determined from

$$Y(t) = \int_0^t (c(Y(t'))dt' \tag{5.10}$$

and is presented as the thick red curve in Fig 5.4 (left panel).

According to the above idealised theory, summarised in Fig. 5.3, this curve should, if only one mode exists or is important, separate the region of time dependent Ekman upwelling (and viscous limit) from that of CTW shut-down where the alongshore velocity magnitude increases with y but not time. Surprisingly, given the evident non-uniform nature of the shelf, this is approximately the case. The velocity v is near zero at the mid-bight artificial geographical origin and between days 1 to 3, when the mode 1 CTW has passed, the velocities to the right of the curve $Y(t)$, are approximately independent of time and increase in magnitude with y. These results are also supported by the phase plot of model sea level (not presented) that more closely resembles the idealised solutions shown in Fig. 5.3. At Thevenard, the shut-down occurs within a day or less (Fig. 5.4) and a cross-shelf transect (not presented) shows that the upwelling here to be very weak. Of course, this may also be ascribed to the very wide shelf where the colder slope waters are some $150km$ offshore.

However, the results do indicate that CTW shut-down occurs somewhat later at KI (1 day) and the BC ($2-3$ days). The latter time scale is similar to that of 2 days given by the 2-dimensional limit (eq. 5.2b) so that the upwelling for the BC has had time to approach the "classical" two-dimensional viscous limit. Such a viscous limit would apply in reality since had the geographical origin been (correctly) chosen to be Cape Leeuwin, then the arrival of the CTW front would have occurred later than the above values. Indeed, Cape Leeuwin, lies some $1500km$ to the west of the Eucla origin assumed in Chapter 4 and using the shelf widths of the western GAB (a mean CTW phase speed of $400km/day$) implies an additional $3-4$ days of time to allow for 2-dimensional Ekman upwelling to reach the viscous state.

For the KI region, the viscous limit should also pertain in reality since the arrival time of the CTW mode from Cape Leeuwin is $4-5$ days and larger than the viscous limit time-scale of $1-2$ days. However, the adoption of Eucla as the geographical origin gives a CTW arrival time of only 1 day or so and the viscous limit may not be established in chapter 4: these estimates and conclusion are at best approximate since the shelf topography of the KI region is highly irregular compared to the BC or mid-bight.

However, the theory above also provides a likely explanation as to why there is little evidence for wind-forced upwelling in the far western GAB even when the

winds are alongshore, as indicated by Figure 4.2, and strong upwelling is found off KI and the BC (Fig 5.1). Simply, near the Cape Leeuwin geographical origin, the interior upwelling is from (eq. 5.9) equal to

$$U_n^I = -U_n^E y/Ln \tag{5.11}$$

and vanishes as y/Ln goes to zero. Albany lies some $250km$ from Cape Leeuwin and the frictional length scale might be estimated as $1000km$ (Middleton et al. 2004). In this case, the interior upwelling is about one-quarter of the maximum possible value that would be found at the BC were the shelf uniform and flow barotropic.

Archives of SST data (*oceancurrent.imos.org.au*) for the $1994-2016$ period were inspected and little evidence for upwelling in the far western GAB was found even when strong upwelling was found off the EGAB. For example, for the February 2008 upwelling event, the SST anomalies from this data were close to $-3°C$ for the eastern regions but only $-0.8°C$ for the western regions.

5.3 The effect of a periodic CTW on upwelling

To examine the effect of periodic CTWs on upwelling and circulation along the shelf, a mode 1 - barotropic CTW paddle was used to force the model adopted in the previous Chapter. The boundary conditions from the previous experiment are kept the same in all boundaries of the domain, except the western boundary. There, a Flather OBC condition is used with a local solution – the CTW paddle – to provide information of external/remote forcing. The paddle uses the cross-shelf structure of the first eigenfunction for sea level, $F_1(x)$. This eigenfunction was determined using the programs developed by Brink et al. (1987) and using the $160km$ wide, cross-shelf topography at the western Boundary of the domain — Eucla (Fig. 4.1). Such a paddle can be regarded as representative of wind-forced CTWs that are generated remotely, i.e. on the equatorward/western side of the boundary (e.g., Middleton et al. 1994, see also Middleton 2006). As such, a 10-day periodic wave was assumed with a maximum in coastal sea level of $10cm$ decreasing to zero at the shelf edge (at about the $100m$ depth). The alongshore (geostrophic) velocity was close to $10cm/s$. For the 10 day period wave, the implied phase speed and wavelength are $14m/s$ and $12,200km$, using the western boundary estimates ($L = 160km$, $f = -7.7 \times 10^{-5}\,\mathrm{s}^{-1}$).

This paddle was applied as boundary conditions to both sea level η and barotropic alongshore velocity v at the mid-GAB (Eucla) of the same stratified model in Chapter 4. No wind-stress or other forcing was used. Thus, numerically, a shelf limited energy source is imposed in the zonal momentum component (local solution at the boundary), while η is imposed with a consistent implicit Chapman OBC. As expected, given the barotropic nature of the forcing, the 3d-momentum equation OBCs were unchanged.

For sea level, the paddle may be written as

$$\eta = A[F1(x)/F1(0)]sin(\omega t) \tag{5.12}$$

where $A = 10cm$ is the CTW amplitude and ω a frequency for the 10 day wave period. This choice was not arbitrary. Church et al. (1987) found that the Thevenard spectra of sub-surface pressure had maximum variance at the $8-12$ day periods, with an amplitude of about $8cm$ (see their Fig. 2). In the lieu of this fact, the model results represent a monochromatic view of the strongest harmonic of the sub-inertial flow that would influence the shelf circulation poleward/eastward of the boundary.

The phase plot for depth-averaged alongshore velocity v over the $50m$ isobath of the model is shown for the alongshore model domain in Fig 5.5 and over 21

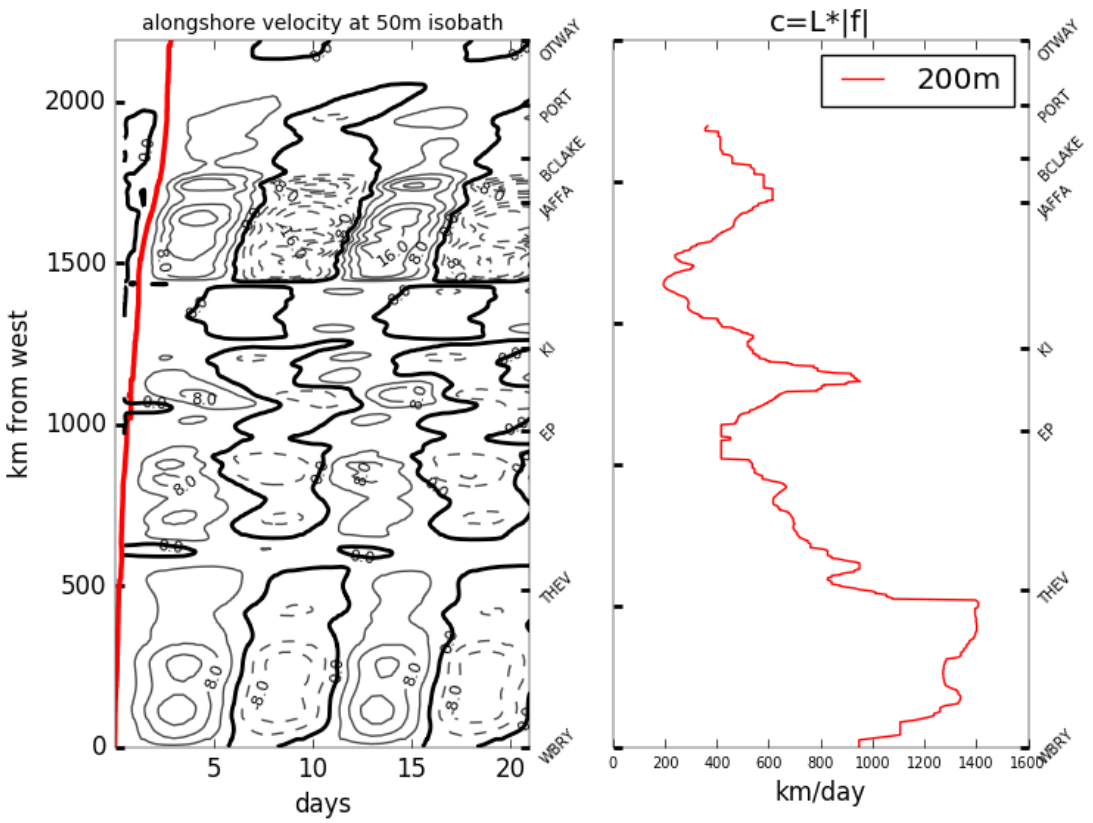

Figure 5.5: as in Figure 5.4 but for the $10d$ periodic CTW paddle experiment.

days. The results are, after the first 5 days or so, strongly periodic in time and the adjustment to the stratified, viscous model near the western boundary is smooth and leads to a reduction in the maximum in velocity by about $1cm/s$. The location of the free-wave is again estimated by the displacement $Y(t)$ given by eq. 5.10, where the phase speed is estimated by $c = -fL$ where L is the distance from the coast to the $200m$ isobath. Positive (negative) velocities shown are directed poleward in Fig 5.5 and for a uniform shelf would have a BBL that is downwelling (upwelling) favourable.

Results show that the CTW energy over the $50m$ isobath and for the wide mid-GAB is directed into deeper water for the narrow shelf region between Spencer Gulf (SG) and the Fleurieu Peninsula (FP) (not shown). The CTW velocity energy is then reduced as it is redistributed over the wide Lacepede Shelf (LS) until Cape Jaffa. Along the narrow BC, between Jaffa and Portland, the energy is then redirected back into shallower water with amplitudes of up to $12cm/s$ over the $50m$ isobath (Fig 5.5) – larger than at the paddle itself. Results for the $20m$ isobath show current speeds of $8cm/s$ for the BC but near zero elsewhere along the shelf indicating energy to be focused between the coast and $50m$ isobaths: a result consistent with the cross-shelf transect results in Fig 5.2.

Beyond Portland, the shelf again widens but little energy is found over the 20,

50 or 200m isobaths indicating the CTW generated at the mid-bight boundary has been frictionally and/or topographically scattered.

The first implication of these results is that the CTW front generated by a remote forcing does, as suggested by the above analysis, propagate as far as Portland and is important to CTW shut-down. As noted, the alongshore currents of the CTW paddle can be either equatorward or poleward and, for a uniform shelf, the BBLs can be quite asymmetric. Moreover, during the equatorward current phase of the CTW paddle, the alongshore currents should act to drive upwelling within the submarine valleys and downwelling over the headlands as found in Chapter 4: strongest upwelling should also be found on the equatorward side of the headlands. Such complexity in response also suggests some rectification may exist over the 10 day period of the CTW.

The Time of Arrival (ToA) of this wave is also important, and is presented in Fig. 5.6 based on the maximum cross-correlation of sea level at Eucla with sea level over the shelf. Again, consistent with the previous analysis, the time of arrival (phase) and shut-down occurs later to the east and the signal arrives at the KI region in less than a day. To the south-east of KI and in the broad LS, the CTW sea level signal travels faster over the outer LS, reaching Cape Jaffa and the BC at 2–2.5 days.

Moreover, the contour lines of the ToA can also be considered a stream function of the CTW signal (phase lines). Clearly, the CTW propagation characteristics generate alongshore pressure gradients and the same bifurcation pattern within the Lacepede Shelf. There is also a convergence of streamlines at the BC. Thus, the plume characteristics appear related to the mean flow dictated by the CTW adjustment. This is expected, given that the CTW have to adjust to the shelf-width and topography, whit an earlier (later) adjustment in shallow (deep) waters Csanady 1978; Brink et al. 1978. Pringle (2002) study this shelf narrowing adjustment of the CTW signal in idealized conditions, which indicate excessive energy (and upwelling) downstream of a narrowing shelf if compared to a straight one. The case here, however, appears to be more abrupt than his study.

Although with a different methodology, the results here (and in Chapter 4) are similar to the Gan et al. 2009 study, where a narrow shelf-width region is the source of the upwelling waters. However, the origin of the large-scale pressure gradient here is clear within the CTW energy propagation characteristics.

To investigate further the effect on upwelling, animations were made of model bottom temperature for the KI and BC regions: *https://figshare.com/s/7565165f965ce2fa2217*. Surprisingly, these results indicate that the displacement of isotherms to be strongly periodic. An analysis of the periodic components of bottom temperature indicates ToA's of the CTW to be about 0.5 days (for KI)

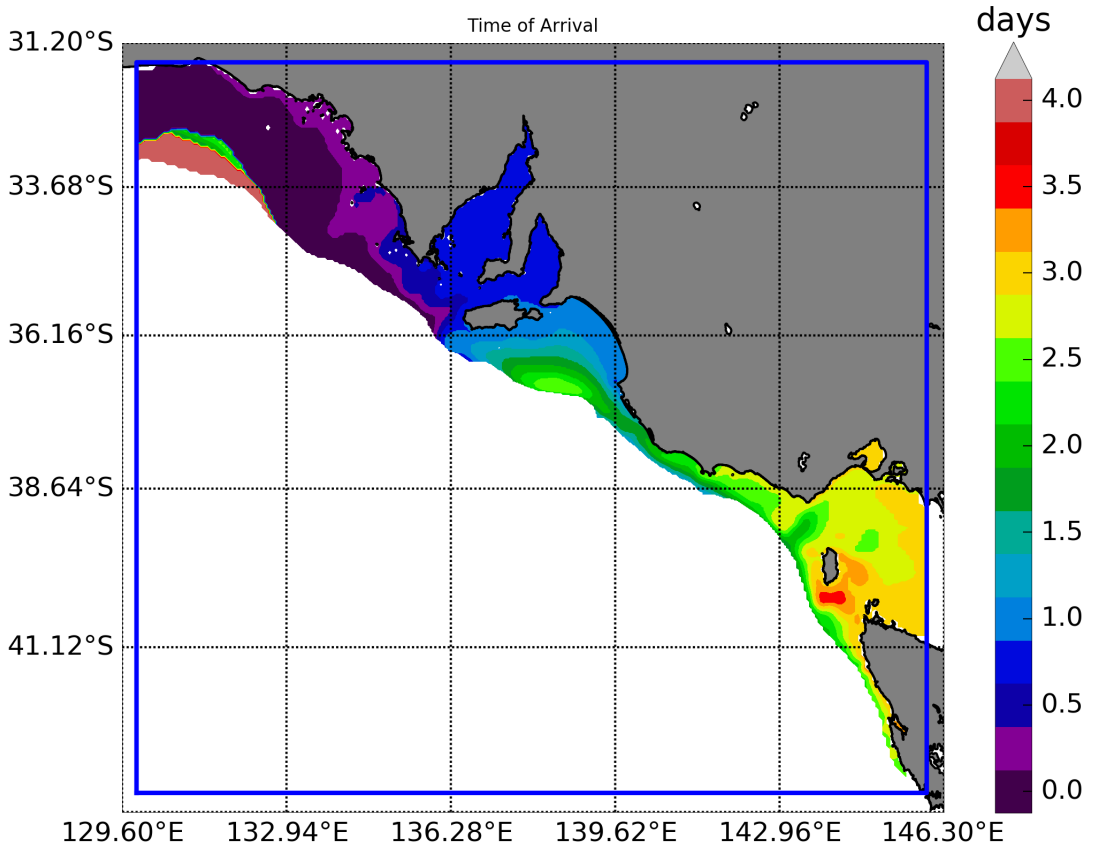

Figure 5.6: The Time of Arrival of the 10 day CTW sea level harmonic based on the maximum cross correlation with the western boundary (Eucla). Time is in days and results are only presented to depths of $300m$.

and 1.5 days (for the BC) and shorter than those indicated for sea level. These differences may be related to the effects of bottom friction.

For the BC region, results for bottom temperature are presented in Figures 5.7 and 5.8 based on a ToA lag of 1.5 days. In Figure 5.7, the results (upper panel) are for the initial state at day 0 when the forcing is zero. The $14°C$ (yellow) isotherm is located very close to a depth of $110m$.

The results in Fig. 5.7 show the changes from the initial field of bottom temperature to that at day 6.5, which corresponds to the end of the downwelling state on the BC. Careful inspection shows that the poleward velocities of the paddle have led to downwelling of $20 - 30m$ of the yellow $14°C$ isotherm. The results obtained at the end of the next downwelling phase (at day 16.5) are almost identical to those at day 6.5. Results at the end of two upwelling phases of the CTW paddle are shown in Fig 5.8. Upwelling in both cases is nearly identical and largest within the submarine valleys and on the equatorward side of the submarine headlands. Over the top of the headlands, downwelling is found and both results mimic that obtained previously for constant wind forcing. The maximum (vertical) upwelling excursion of the yellow $14°C$ isotherm is about $60m$.

As noted the solutions are strongly periodic although some weak rectification was found. An analysis was made to determine the magnitude of rectification and estimated to be largest at about $-0.015°C/day$ and on the equatorward side of headlands. The rectification then is about $-0.15°C$ over 10 days (net upwelling) and small compared to the periodic peak to peak amplitude of $2°C$ that is associated with the up/downwelling phases. This rectification was not spatially homogeneous but associated with topography. This again indicates flow-topography interaction as shown in Chapter 4. The role of horizontal advection is important (see Figure 4.10 in Chapter 4) as well as vertical mixing. However, the rectification may arise from numerical model errors or unresolved physics in the closure schemes adopted. Nonetheless, the role of longer period CTW, for example, will lead to more important and larger rectifications with stronger bottom flows. Further (idealised) studies of the mechanisms for this rectification are needed.

Strongly periodic results were also obtained for the KI region, as shown in Fig. 5.9 for the downwelling phase (upper panel) and upwelling phase (lower panel), although the vertical displacements were smaller than for the BC and about $40m$. The smaller displacements might be expected since the shelf is much wider than for the BC region and the alongshore bottom velocities are of order $4cm/s$ and half those off the BC: as noted in Chapter 4, the alongshore velocities drive upwelling through vortex stretching that occurs following a fluid column.

Nonetheless, the upwelling from the initial state is not small ($20m$) and notably larger in the deepwater canyons off the south-east tip of KI: here water is upwelled

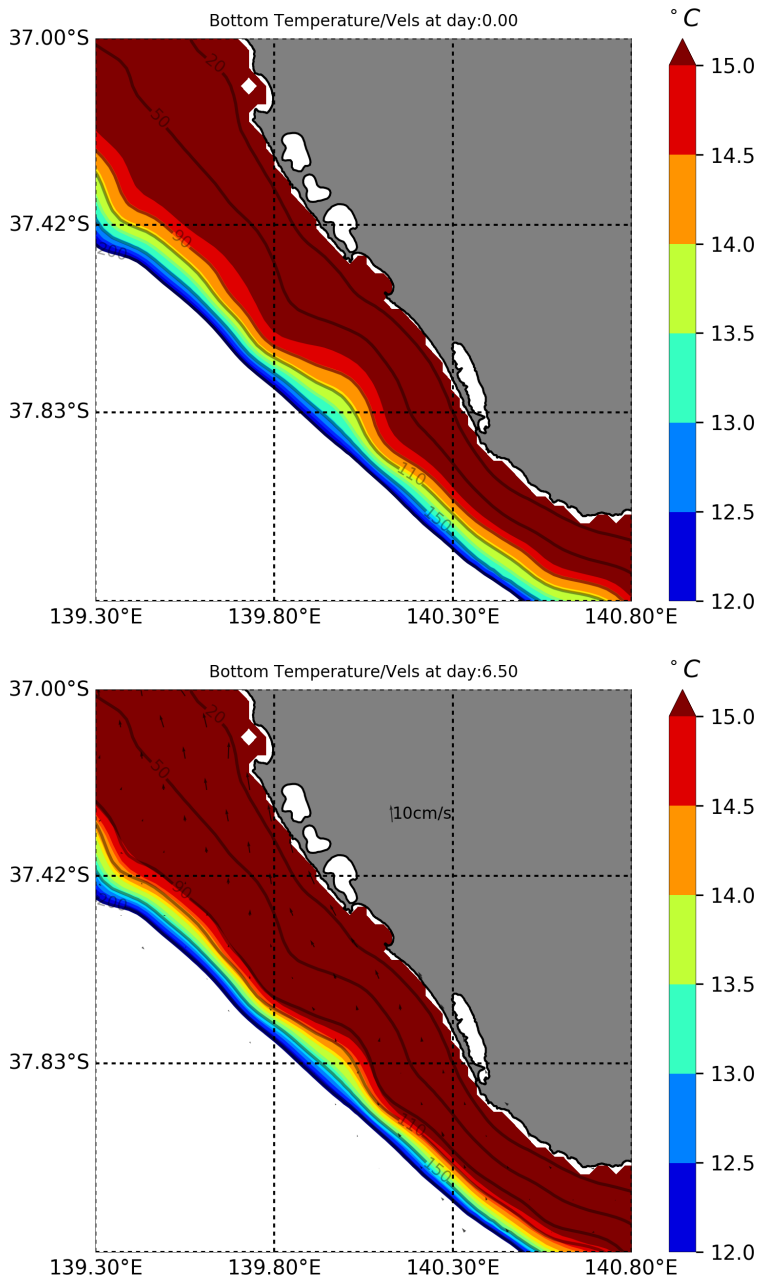

Figure 5.7: Bottom temperatures ($°C$) of the CTW periodic paddle experiment for the BC region. Upper panel: Initial state (day zero). Bottom panel: at the first maximum downwelling phase (day 6.5). Vectors are averaged in a regular grid and plotted approximately at every ten grid points. Unit is cm/s and a vector scale is provided. The 20, 60, 90, 110, 150 and $200m$ isobaths are indicated

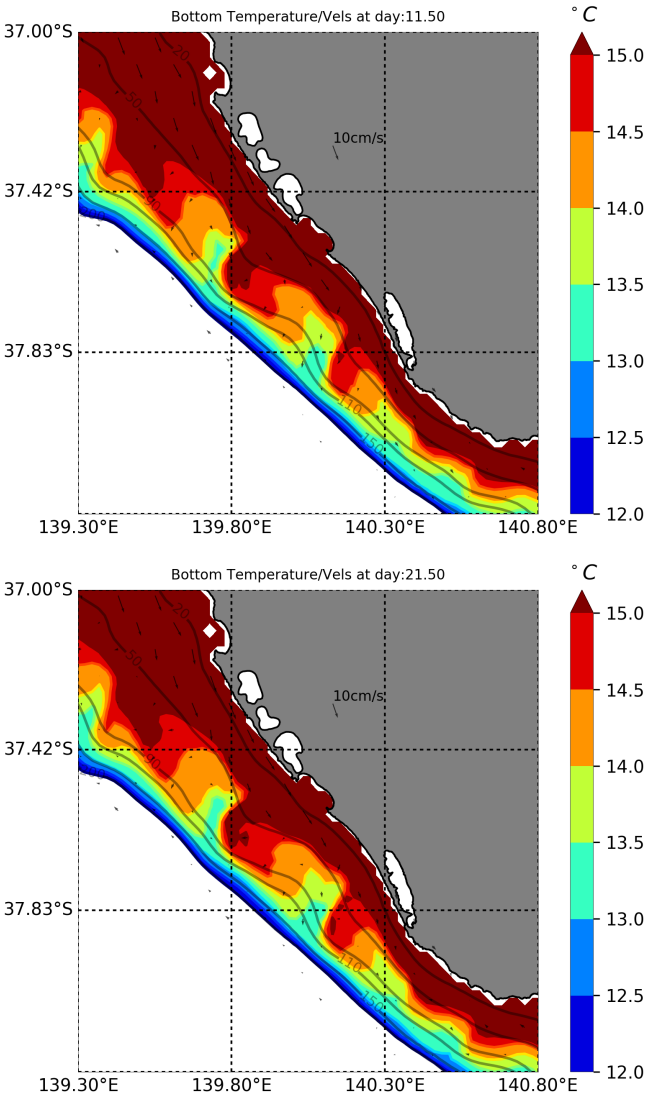

Figure 5.8: As in 5.7 but for the upwelling phases. Upper panel: after the first maximum upwelling (day 11.5). Bottom panel: after the second maximum upwelling phase (day 21.5).

from depths of $300m$ to nearly $100m$.

In summary, relative to the initial state, the upwelling over the shelf driven by the CTW paddle is of order $10 - 60m$ off the BC and $10 - 40m$ off KI. These results are smaller to those obtained in the previous chapter, where an impulsive wind was applied: after 6 days and for the BC, upwelling of the $14°C$ isotherm is of order $110m$ were found (reaching the coast), while for KI, the displacements were about $20 - 40m$.

One exception here is that the CTW forced upwelling for the deep canyons were of order $150m$ and much larger than that of about $30m$ for the constant wind forcing case.

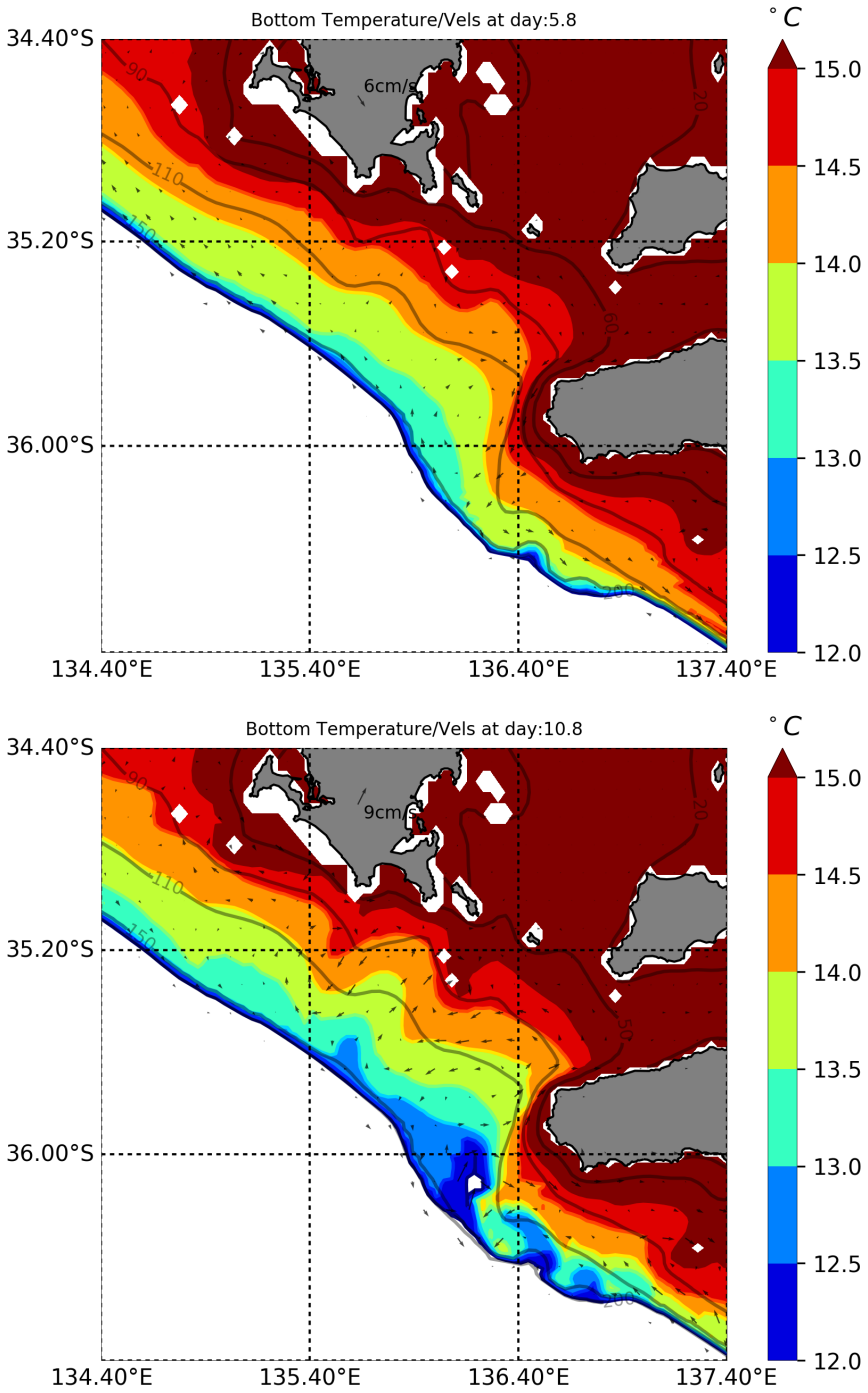

Figure 5.9: As in Figures 5.8, but for the KI region. Top panel: after the first maximum downwelling (day 5.8). Bottom panel: after the first upwelling phase (day 10.8)

5.4 Summary and Discussion

In Chapter 4, the response of the eastern GAB to an impulsively started constant wind was examined: no other forcing was applied in the hydrodynamic model and the equatorward boundary chosen to be in the mid-bight at Eucla where velocity was set to zero: a geographical origin for the model response. The results show that bottom upwelling (downwelling) is found to occur within the submarine valleys (headlands) of the BC that are driven by vortex stretching and squashing.

The purpose of this Chapter 5 was to evaluate some of the assumptions made in the previous Chapter that can impact on the degree of upwelling. These were:

- The role of 2-dimensional Ekman upwelling and associated viscous limit of maximum upwelling.
- The role of CTW shut-down of Ekman upwelling.
- The validity or otherwise, of the adopted western boundary at Eucla rather than Cape Leeuwin (some $1500km$ to the west).
- The importance to cross-shelf exchange of periodic CTWs that are driven as a "paddle" at the western boundary and travel poleward into the model domain: such CTWs act as a proxy for time-varying wind forcing in the western GAB.

The barotropic theory of 2-dimensional Ekman maximal upwelling was here found to qualitatively explain the stratified model results for the BC and over the first few days when the alongshore wind-driven shelf currents accelerate until the bottom stress balances the surface wind stress. At this stage, achieved after $1-2$ days, the model upwelling is driven largely within the thin upwelled BBL and the interior upwelling is small.

The theory (Middleton et al. 2004) also shows that the impulsive applied winds should also drive a CTW front poleward from the adopted geographical origin at Eucla. Upon arrival of the CTW front, the associated alongshore velocity becomes steady and convergent and acts to "feed" the offshore surface Ekman transport. This partially shuts-down the need for an onshore interior transport that would otherwise contribute to upwelling.

The shelves of the GAB are highly irregular in width L and slope. However, adopting a simple (step shelf) estimate for the CTW front phase speed ($c = -fL$), the location of the front was estimated and plotted over a phase diagram of the (depth-averaged) alongshore velocity over the $50m$ isobath. Surprisingly, given the assumptions made in the theory, the location of the front does approximately separate the hydrodynamic model initial phase of 2-dimensional Ekman upwelling

(independent of alongshore distance), from the quasi-steady solutions associated with CTW shut-down. At KI, shut-down occurs within a day, while at the BC, between 1.5 and 2.5 days so the maximal viscous limit in the model of Chapter 4 is more closely approached for the BC than for the KI region.

This is important as Cape Leeuwin (rather than Eucla) is the actual geographical origin for the southern shelves of the GAB and CTW shut-down would in reality occur some $3-4$ days later off KI and the BC: i.e., the viscous maximal limit for upwelling should occur in reality at both the BC and KI regions. The above timescales and analysis suggest that this does occur in the experiment of Chapter 4 (constant winds) for the BC region, but to a lesser extent at KI. That is, the upwelling off KI may be under-estimated.

The theory of Middleton et al. (2004) also provides a likely explanation as to why there is little evidence for wind-forced upwelling in the far western GAB even when the winds are alongshore, (Fig. 4.2), and strong upwelling is found off KI and the BC (Fig. 5.1). Near the geographical origin at Cape Leeuwin, the interior upwelling is described by eq. 5.11 and vanishes as y/Ln goes to zero. Such a result is consistent with SST data which indicates little or no significant upwelling despite the alongshore winds and relatively narrow shelf (Figures 4.2, 5.1). Canyon upwelling may occur in the far west (Esperance/Albany) due to the likely existence of the equatorward flowing Flinders Current (depths $500-300m$) with speeds of order $20cm/s$, (Middleton et al. 2007b).

Results were also obtained using a $10cm/s$ amplitude CTW 10 day period paddle at the western domain, without *local* wind forcing. The results show that the periodic CTW propagates as far as Portland on the BC and the associated equatorward (poleward) alongshore velocities drive bottom upwelling (downwelling). During the upwelling phase, the important dynamics are presumably as for upwelling driven by steady winds, since the bottom upwelling again occurs in the valleys and is strongest on the equatorward side of the submarine headlands. Alongshore pressure gradients associated with the flow adjustment over variable shelf-width are also clear. The origin of the bifurcation pattern found in the wind experiments appears related to the shelf widening and narrowing downstream, and the characteristics of the CTW adjustment. This downstream shelf narrowing also can enhance the upwelling Pringle 2002.

As expected from idealised studies of the BBL (e.g., Trowbridge et al. 1991; Middleton et al. 1996) the upwelling and downwelling are quite asymmetric. When averaged over the 10 day period of the CTW paddle, the strongest rectification was found to be about $-0.15°C$ over 10 days (net upwelling) and small compared to the periodic peak to peak amplitude of $2°C$ that is associated with the up/downwelling phases. Over longer times, the rectification will lead to relatively larger values and

be more important. However, as noted, the rectification may arise from numerical model errors or unresolved physics in the closure schemes adopted. High resolution, idealised studies of the mechanisms for this rectification are needed but beyond the scope of this thesis.

Moreover, the periodic CTW driven cross-shelf exchange is not insignificant compared with that forced by constant winds (see Chapter 4). Relative to the initial state, the shelf upwelling (and downwelling) driven by the CTW paddle is of order $10-60m$ off the BC and $10-40m$ off KI. These results may be compared to those obtained previously where an impulsive wind was applied: after 6 days, upwelling of order $90m$ and $30m$ was found for the BC and KI regions respectively. One exception here is that the CTW forced upwelling for the deep canyons off KI is of order $150m$ and much larger than that obtained for constant winds.

While it is not possible to simply add the CTW paddle and steady results for upwelling, the results here do show that CTWs can lead to additional (and significant) upwelling and should be incorporated into models of upwelling by winds. Additionally, it is important to note that the CTW propagation implies a resonance mechanism: a remote signal could provide enhanced upwelling during summertime, such as the El-Niño signal or stronger westward winds at the western side of the GAB.

The CTW periodic upwelling in combination with steady wind-forced upwelling may also lead to rectification of the upwelling of nutrients since these can be available to phytoplankton over scales of several days and in the near-surface euphotic zone. As noted, both forcing mechanisms lead to stronger upwelling on the equatorward side of submarine headlands and these sites may also lead to ecosystem hot-spots. They might also serve as sites for long-term monitoring of upwelling and ecosystem response.

Chapter 6

Upwelling along the shelves of the Great Australian Bight: Observations of remote and local influences in the extreme upwelling during the 2016 El-Niño

Abstract

The Bonney Coast (BC), in Southern Australia, is the region of strongest wind-driven upwelling around Australia. In this research, through an extensive analysis of data from different sources – including gliders, HF radar, moorings, coastal tide gauges, satellite remote sensing, and ocean reanalysis – we provide a comprehensive description of the upwelling season off the BC and its interannual variability. We show that the summertime of 2016 was extreme and the strongest in the last 15 years. Two main factors, stronger wind stress (τ_w) and long trapped waves (coastal trapped waves and El-Niño effects), explain the intensity of the 2016 upwelling. Interannual analysis indicates that Eastern Great Australian Bight (EGAB) summer sea-level variability is indeed highly coherent with El-Niño-Southern Oscillation (ENSO) but with other tropical and non-local components. We show that El-Niño is coherent with Sea Level (SL), isotherm uplift, setup of Bottom temperature (BT) anomalies over the shelf and weakening of the South Australia Current — an almost one-to-one relationship exists between BT and central Pacific Sea Surface Temperature (SST) within the last decade. Regional alongshore winds (and upwelling) are also found to be influenced by the Southern Annular Mode (SAM), and a lagged effect in SST is indeed implied under ENSO

persistent effects as the onset time of the thermocline displacements. These effects act to precondition the region to quickly and efficiently respond to the wind-driven circulation in summer, which acted in phase with high amplitude SL oscillations within the bi-monthly to the weather band. Persistent ENSO effects are found related to the thermocline, reduction of the South Australia Current (SAC) and overall cooling in the upper ocean. Extreme SST anomalies up to $-2°C$, τ_w in excess of $0.1Pa$ and high Chlorophyll-A (CHL-A) values were found at the upwelling peak. Glider observations in the region show highly skewed waters (cold and fresh) over the shelf, source depths up to $350m$ and of Flinders Current origin. The alongshore variability of upwelling is significant, and the distribution is found sensitive to the alongshore topography – coldest and fresher waters are found within the valleys and on the equatorward side of the headlands – consistent with previous numerical results.

6.1 Introduction

Forty years ago, one of the first reports of upwelling observations during summertime off the southern shelves of Australia was published (Rochford 1977), providing evidence of what is known today as the strongest upwelling region in Australia: the BC (Middleton et al. 2007b; Foster et al. 2014). This region, here defined between Robe and Portland (the coastline in the magenta polygon in Fig. 6.1), is the location of a large coherent upwelling signal that occurs along the EGAB, between late spring and late summer.

The upwelling occurs during favourable alongshore wind stress within the Bight (Middleton et al. 2003; Kämpf et al. 2004; Ridgway et al. 2004; Ridgway et al. 2015). The summertime climatological surface winds blow in an anti-cyclonic sense along the coastline of the Great Australian Bight (GAB), driving offshore surface waters (Ekman transport), divergence and, by consequence, a compensating sub-surface flow that uplifts cold and nutrient-rich sub-surface waters. On seasonal time-scales, this process is particularly important to maintain the marine ecosystem in the GAB, generating hot spots of productivity where upwelling is the strongest along the highly variable coastline (e.g, Ward et al. 2006; Ruth et al. 2010).

Several recent observational studies (Kämpf et al. 2004; McClatchie et al. 2006; Middleton et al. 2007a; Middleton et al. 2012), including studies using remotely sensed SST and CHL-A estimates (Ridgway et al. 2004; Nieblas et al. 2009), and ocean models (Middleton et al. 2002; Middleton et al. 2003; Schiller et al. 2008; Kämpf 2010) have provided some significant understanding of the oceanography of the Southern shelves. However, very few direct observations have been collected at the BC, with the majority of observations limited to single point measurements such as bottom temperatures as in Middleton (2006) and Middleton et al. (2012), short cruises (Paterson et al. 2012) or within the northern EGAB (Richardson et al. 2009).

It is well-known that coastal Sea Level of southern and western Australia is highly (negatively) correlated with the ENSO phase (Pariwono et al. 1986; Clarke 1991; Clarke et al. 1994; Verschell et al. 1995; Meyers 1996; Li et al. 2004; Clarke et al. 2004; Tozuka et al. 2014); this feature results from the low-frequency transmission nature of anomalies from the tropics through the Indonesian seas. So, during El-Niño (La-Niña), the SL signal in the seasonal to interannual time-scales is consistently lower (higher) off the north-west-southern Australia coast, with a poleward signal that is trapped near the coast and slope. The effect of ENSO in the GAB was studied in Li et al. (2004) and Middleton et al. (2007a), and it is mostly perceivable in sea level and bottom temperature changes. In

particular, Li et al. (2004) provide observational evidence that the ENSO signal influences the low-frequency currents in the zonal sections of Australian southern shelves year-round. On the other hand, Middleton et al. (2007a) indicated that during La-Niña conditions the shelf-edge currents are substantially reduced in winter, but not during summer. The direct relationship with SST, was reportedly smaller (Middleton et al. 2007a), but still consistent with an ENSO influence in SL and BT.

Furthermore, ENSO and winds are not directly related in the region (Middleton et al. 2007a), which imposes a natural question of what control do the regional winds and the shelf currents have during upwelling events at the BC? The behaviour of the SAC at this location is mostly unknown, but observations have already shown that under El-Niño conditions, the seasonal thermocline depth in the region is uplifted and upwelling is stronger. So, if the shelf-break current, which is a downwelling current (on the bottom boundary layer (BBL)) is not weakened in summer, how can strong upwelling occur within the BC? Should it be generated only by interior Ekman transport? Or does the current only change its position ?

Finally, previous studies suggest that a persistence effect occurs in the EGAB in winter, after the onset of an El-Niño event, as well as the following summer – El-Niño upwelling enhancement (Middleton et al. 2007b). Can this persistence be detected with recent observations? In which conditions does this condition appear to hold and for how long?

The primary objective of this chapter is to provide a new observational insight of the upwelling season in the EGAB, particularly along the BC region. From interannual to synoptic scales, new and independent observations are used to provide a comprehensive view of the BC variability and the peak upwelling season of 2016. The majority of the previous results in the region are revisited and extended, mainly relative to winds and the role of El-Niño during summer. As will be shown, the interannual variability of upwelling in the region is largely influenced by El-Niño and its propagation nature; the summertime of 2016 was then marked by extremes (Subsection 6.3.1). Besides the effect of ENSO in SL, we show that during summertime along the EGAB, a considerable variability in SL has its origin close to Cape Leeuwin. Surprisingly, mean alongshore wind anomalies are also found related to SAM, despite their smallness magnitude. Hence, the EGAB upwelling circulation is particularly sensitive to remote forcing.

Consistent with previous studies, ENSO is not directly coherent with coastal SST and we suggest two reasons; the presence of summertime heating anomalies that are incoherent with ENSO, and ENSO persistence effects that create a delayed response from the central Pacific that is related to the onset of the seasonal thermocline. The spatial analysis of SST also shows that the BC upwelling plume

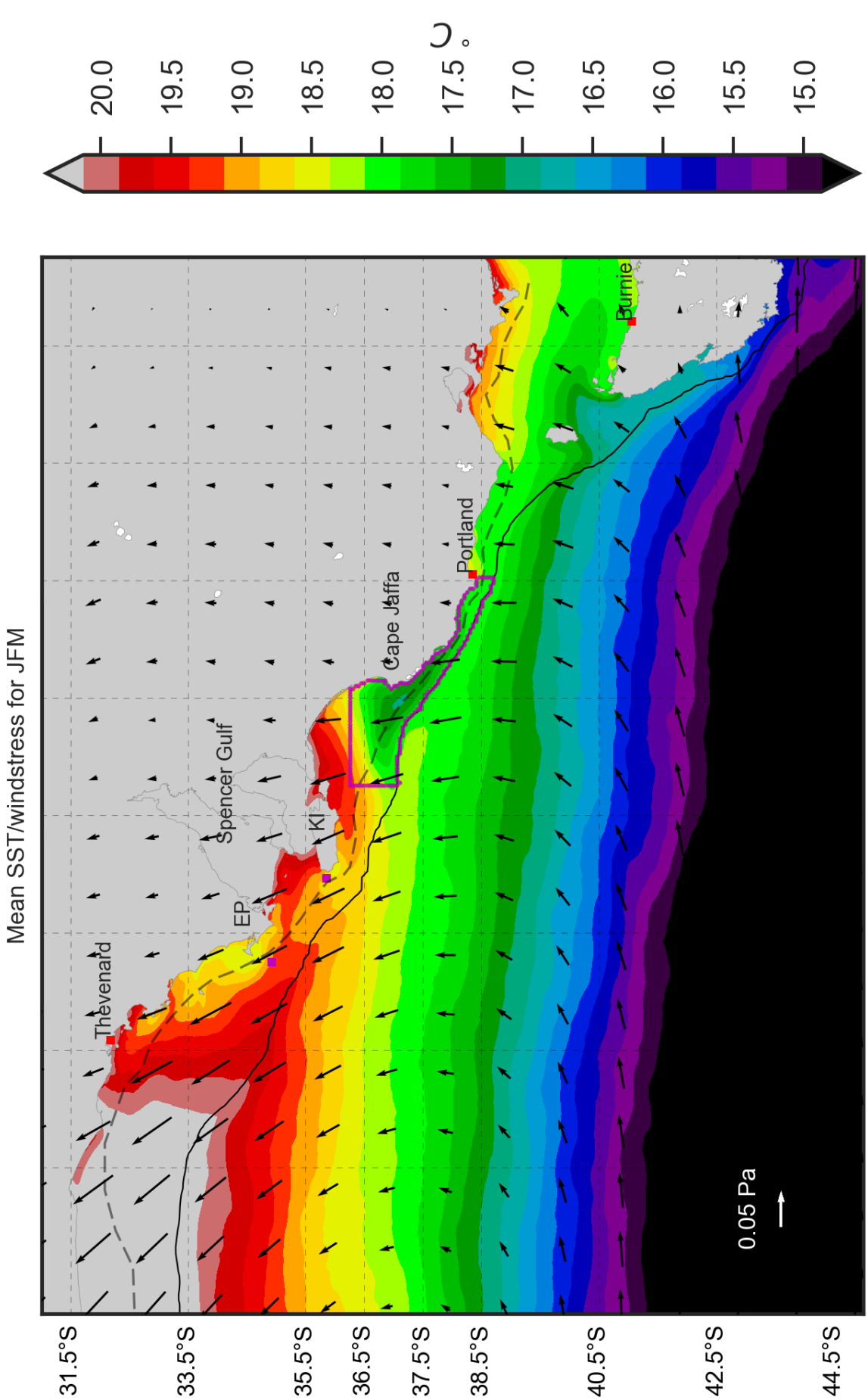

Figure 6.1: The study region: Southern Shelves of Australia. Shading: Seasonal SST ($°C$) for January,February,March (JFM) from Multi-scale Ultra-high Resolution Sea Surface Temperature (MUR) for the 2002 – 2016 period. Arrows: Seasonal vector mean of wind stress (Pa) for JFM from Cross Calibrated Multi Platform Ocean Surface Wind Velocity (CCMP). Black (dashed) lines delimit the 200m (60m) isobaths.

is the most prone to extreme events and a good proxy for upwelling (as is SL) from Thevenard to Portland (Subsection 6.3.2).).

The relationship between SL and vertical distribution of temperature over the EGAB is further explored, as well as with the shelf and shelf-break currents. SL and BT are strongly coupled, as well as BT with SST in the Pacific (ENSO). The latter relationship, in the last 10 years, is found the strongest of all variables and locked to summertime (Subsection 6.3.3). The mechanism of why this relationship is so strong is explored in a reanalysis transect along the BC. El-Niño conditions affect the summer SL cross-shore gradients, enhanced the northward shelf flow, reduce the SAC south-eastward flow and reduce the downwelling at the shelf-break. This consolidates previous hypothesis and results for the EGAB region. The net effect of the El-Niño conditions is shown to be an uplift of the permanent and seasonal thermocline depths, upwelling of isotherms close to the slope and a more efficient interior Ekman and BBL upwelling generated by the wind-driven circulation. Although a widespread cooling in the upper ocean was found in 2016, the strongest anomalies were trapped to the coast and slope, providing important preconditions for upwelling at the shelf and consistent with long waves trapped to the coastal ocean.

Finally, a synoptic view of the upwelling is provided in subsection 6.3.4, with the aid of the first summertime glider observations off the BC. During the peak, wind stresses were very strong for the region, SST anomalies were within the $10th$ percentile of all historical observations (up to $-2°C$) with anomalous large primary production. The waters were highly skewed towards cold and fresh over the shelf, with source depths up to $350m$ and of Flinders Current origin. The distribution of upwelling is found to be particular sensitive to the alongshore topography – the coldest and fresher waters ($\theta_{min} = 11°C$,$S_{A_{min}} = 35.1g/kg$) are located within the valleys and on the equatorward side of the headlands – consistent with previous results.

6.2 Data and Methods

6.2.1 General description of the datasets

All the data used in this chapter is summarised in Table 6.1. Several datasets are used and briefly described below, as well as the analysis and techniques used.

For SL, we use 2 different products, the gridded sea level (SL) estimates from the BlueLink ReANalysis (BRAN) project (Oke et al. 2008), starting in January 1994

to August 2016 (extended version-BRAN2016), and the coastal Tide Gauge (TG) stations from the Australian Baseline Sea Level Monitoring Project (ABSLMP) provided by the Australian Bureau of Meteorology (BoM), from January 1992 to December 2016. Although the BRAN2016 SL field was saved in lower precision by an operational error, in the lower frequencies (month to interannual), the two SL datasets are equivalent (see below). The higher correlations between model SL and TG observations is expected since BRAN analysis uses the TG data in its Ensemble Optimal Interpolation assimilation scheme (Oke et al. 2008; Oke et al. 2012). Nonetheless, the re-analysed SL is used just for spatial distribution ($\approx 10km$ resolution) and to fill gaps in the monthly TG stations. Months with less than $15d$ of data were marked as missing and filled using a hierarchical linear model (a linear fit for grouped months of the year – see below). The biggest data gap is for Hillarys, Western Australia (WA), between April and July 2002. As is commonly done in SL studies, the inverse barometer effect is estimated using linear regression onto the SL anomalies for the TG data. The adjusted SL is the residual of regression of pressure onto SL. For the BRAN model, this step was not necessary since BRAN did not include atmospheric pressure forcing.

Following Church et al. (1987), estimates of the daily adjusted SL are presented in Table 6.2 below and correspond to their Table 1, even though the time series differs considerably. However, it's known that the response to atmospheric pressure holds only for sub-inertial oscillations (Ponte 1994; Mathers et al. 2004). Given that some TG stations are located within the tropics, a correction over longer times scales is more appropriate. SL anomalies corrected at monthly scales are reported in Table 6.3. They are consistent with Table 6.2, sharing an increase in barometric factors (and coefficients) in the tropics, a mild increase in the GAB, and maintenance of the isostatic value in the South (Burnie). Although the reduced variance is stronger for monthly time-scales, 30% (50%) for daily (monthly) data, the corrections are generally small for the GAB stations, with deviations from the daily barometric factors within the confidence intervals. Moreover, these pressure-independent SL values also reduce the variance explained by winds at all stations, given the implicit correlation between pressure and winds (not shown). In other words, the adjusted SL at monthly timescales are more representative of the steric effects, i.e., internal dynamics. Here, and below, we refer to the adjusted monthly anomalies as the adjusted SL (SL_{adj}). The adjusted SL data were also used within an EOF analysis of the stations, to provide insights of the wave-guide effect and equivalence of our results to other studies in the region (Li et al. 2004; Middleton et al. 2007b).

Temperature (T) and Salinity (S) climatology were obtained from the CSIRO Atlas of Regional Seas (CARS) 2009 dataset (Ridgway et al. 2002). We also

Table 6.1: Observations and data providers used in the analysis. SL – sea level; τ_w – surface wind stress; P_{atm} – mean sea level pressure; T – temperature ; S – salinity ; $U/V(U_{surf}/V_{surf})$ – zonal/meridional velocity component (surface); $\nabla \times \tau_w$ – wind stress curl; Q_{net} – surface net heat flux ; SST – Sea surface Temperature; $Chl-A$ – Chlorophyll-A; T_{bot} – Bottom temperatures; RA – Reanalysis

Product name	source	base version	type	time resolution	horizontal resolution	Period	variable	variable type	url
BoM Tide Gauges	BoM	–	sparse obs.	hourly	–	09/1992–12/2016	SL, τ_w, P_{atm}	point	*http://www.bom.gov.au/oceanography/projects/abslmp/abslmp.shtml*
BRAN	CSIRO	Extended-2016	model RA	daily	0.08°	1994– 08/2016	SL, T, S, U, V	grid	*http://wp.csiro.au/bluelink/global/bran/*
CARS Obs	CSIRO	Atlas/Extended-2016	obs.RA/sparse obs.	daily	–	1965– 05/2016	T, S	profile	*http://www.marine.csiro.au/~dunn/cars2009/*
CCMP	RSS	*v*02.0	obs. RA	6hr	0.25°	1990–05/2016	τ_w, $\nabla \times \tau_w$	grid	*http://www.remss.com/measurements/ccmp.html*
ERA-I	ECMWF	Interim reanalysis	model RA	3hr	0.5°	1980–05/2016	τ_w, Q_{net}	grid	*https://www.ECMWF.int/en/research/climate-reanalysis/era-interim*
Climate Indices	NOAA/JAMSTEC/	ERSSTv4,HadSSTI	obs. RA, obs.	monthly	–	1980–12/2016	SST, P_{atm}	index	
MUR	NASA/JPL	V4.1	obs. RA	daily	0.01°	06/2002–06/2016	SST	grid	*https://mur.jpl.nasa.gov/*
AVHRR-OI	NASA/JPL	V1.0-rev1.7	obs. RA	daily	0.25°	1982–06/2016	SST	grid	*https://www.ncdc.noaa.gov/oisst/*
MODIS-A OCI	NASA/JPL	2014.0	obs. RA	daily	0.04°	2003–03/2016	Chl-A	grid	*https://oceancolor.gsfc.nasa.gov/reprocessing/r2014/*
IMOS Network	IMOS	–	sparse obs.	1hr,$< 1hr$	6km,-	02/2002–09/2016	U_{surf}, V_{surf}, T_{bot}, U, V, T, S, Chl-A	point,profile	*http://www.imos.org.au*

analysed the original individual profiles used to generate the gridded estimates of CARS and recent profiles not used in the Atlas. These profiles are more recent (2011 onwards), and used for model comparison and assimilation under the BRAN project. Here, we call this dataset as the Extended–CARS, to differentiate from the CARS 2009. From the extended-CARS dataset, we identified approximately 2000 TS pairs for a region within a bounding box ($137°E$–$141.8°E$,$-39°S$–$-36.3°S$). This includes Argo profiles, World Ocean Atlas historical data, and CTD casts from research vessels. These observations are used as our benchmark for the expected mean state of the ocean and upwelling at the BC.

Atmospheric data is also provided by the same BoM TG stations, such as surface wind components ($10m$ height) and mean sea level pressure. Additionally, to provide a spatial view of the atmospheric circulation, we use reanalysis data from the Remote Sensing Systems (RSS)/CCMP gridded surface vector winds product, from January 1990 to May 2016, as well as mean winds and sea level pressures from the ECMWF-European Reanalysis Interim (ERAI) from January 1980 to May 2016 (Dee et al. 2011). Wind data from the ECMWF reanalysis are consistent with CCMP, but the latter provided smaller errors when compared to the EGAB TG stations (not shown), mostly because CCMP uses ECMWF data as a first guess to project the microwave wind measurements (Atlas et al. 2011). We also used the ECMWF mean sea level pressure (MSLP) to fill the gaps, as done for SL. The weather station at Thevenard appeared to be corrupt in wind estimates. This data wasn't used. Instead, we used data from the closest point in the CCMP dataset.

We used several climate indices to represent climate drivers and large-scale relationships. Most of the indices are obtained from the National Ocean and Atmospheric Administration (NOAA)/Physical Sciences Division (PSD) Physical Sciences Division, such as the Oceanic Niño Index (ONI). Other related ENSO indices included Nino3.4 Index (NINO3.4), El-Niño Modoki index (MODOKI) (from Japan Agency for Marine-Earth Science and Technology (JAMSTEC)) and the Tripole Index for the Interdecadal Pacific Oscillation (IPO). We also add the climate indices of Dipole Mode Index of the Indian Ocean Dipole (DMI) and SAM, the latter provided by the British Antarctic Survey (BAS) (Marshall 2003).

As shown elsewhere (e.g., Cai et al. 2011) some of the climate indices are not independent, and the purpose of using several of them is to try to provide a standard index for future studies and to check if any other climate variability is coherent within the EGAB. For the GAB, the NINO3.4 was previously used to estimate ENSO effects (Li et al. 2004; Middleton et al. 2007a; Nieblas et al. 2009). As we will show, for our chosen time series and this study, the choice of compatible indices is not so important in general for detection of ENSO, given that

Table 6.2: Table of Tide Gauge station statistics between daily anomalies of sea level and mean sea level pressure. The sea level without the tidal signal (unadjusted) and adjusted (sub-surface pressure), the number of days, barometric factor and error (from the regression) and the overall correlation coefficient. All regressions are statistically significant ($p < 0.05$). Units are cm and hPa. Barometric factors are $cmhPa^{-1}$.

location	SL variance unadjusted	SL variance adjusted	days	JFM days	atmospheric pressure variance	barometric factor	stderr	R
Darwin	66.5392	47.1817	9360	2342	3.01852	-2.51888	0.0409584	-0.536496
Broome	72.0783	55.5109	9060	2240	4.72918	-1.86958	0.0360103	-0.478889
Hillarys	179.365	86.6064	9157	2257	25.9682	-1.88922	0.0190945	-0.718846
Esperance	171.345	91.4967	8880	2171	42.7816	-1.36592	0.0155233	-0.682525
Thevenard	335.802	230.747	8998	2179	33.0614	-1.78257	0.0278537	-0.559327
Portland	135.584	48.0464	9239	2219	55.0363	-1.26116	0.00972175	-0.803508
Burnie	79.9545	30.5458	8779	2166	66.6699	-0.860606	0.00722856	-0.785865

Table 6.3: As in Table 6.2, but for the monthly anomalies. All regressions are significant ($p < 0.05$).

location	SL variance unadjusted	SL variance adjusted	months	JFM months	atmospheric pressure variance	barometric factor	stderr	R
Darwin	54.5794	24.9004	309	78	1.12747	-5.07298	0.271764	-0.729123
Broome	51.4792	28.3632	302	75	1.60706	-3.78277	0.243062	-0.668361
Hillarys	53.7462	38.8196	302	75	3.44543	-2.07513	0.19402	-0.525404
Esperance	34.4161	20.3047	294	73	5.56542	-1.58897	0.111942	-0.638976
Thevenard	44.6926	22.1327	297	73	4.77101	-2.17446	0.125405	-0.710459
Portland	32.0933	11.2635	306	75	7.72766	-1.64168	0.069252	-0.805573
Burnie	20.2189	8.17151	292	72	9.6539	-1.11613	0.0540956	-0.771234

the different estimates lie within the confidence intervals of most linear regressions. However, we found the ONI as the easiest way to detect the influence of Pacific tropical variability in the data (this index had general higher significance).

For remote sensing SST, we use results from Jet Propulsion Laboratory (JPL)-MUR SST analysis from July 2002 to May 2016 and from the NOAA Optimum Interpolation Sea Surface Temperture (OISST) product (September 1981-May 2016), based on the Advanced Very High Resolution Radiometer (AVHRR) and Advanced Microwave Scanning Radiometer (AMSR) radiometers (OISSTv2), here defined simply as AVHRR. CHL-A satellite data from the JPL Moderate Resolution imaging spectro radiometer from the Aqua satellite (MODIS-A) is also used (January 2003 to March 2016). The CHL-A concentration is based on the merged version of the OCI algorithm (Hu et al. 2012).

Data from two IMOS moorings (*imos.org.au*) in the northern EGAB are used (marked as magenta squares in Fig. 6.3 and others), collected from February 2002 to May 2016. The variables in this study include barotropic components of velocities and bottom temperatures measured by an ADCP fixed at the bottom (Workhorse Sentinel—Teledyne Marine), between $90 - 110m$ isobaths and with a $20min$ sampling/average interval. For more details about the instruments, the reader is directed to the IMOS website and the metadata presented in the respective files for the Coffin Bay (*SAM5CB*) and Kangaroo Island (*NRSKAI*) moorings. We rely on the IMOS quality assurance and control (QA/QC) for most of the ADCP data, but excluding invalid surface values of velocity measurements and using linear interpolation between valid values in the same bin in the limit of a 1-hour window.

As in SL, the data was daily-averaged, de-seasonalised and detrended and then reduced to monthly values. We also used the daily bottom temperature data for the synoptic view (see the last section). After the processing, missing data in the current meters and bottom sensors were filled with linear interpolation values within a day if data during the day were longer than 12 hours, otherwise, they were marked as invalid. The ADCP barotropic velocities were computed by averaging all available observations in each bin in 2 valid days and integrating in the vertical by simple Riemann sums. The very few gaps in BT presented in the Kangaroo Island (KI) series were filled with the Coffin Bay (CB) data, with a simple linear correction based on the whole record. There were not many of these cases, given the already pre-processing efforts by IMOS.

Data from the HF-radar at the Bonney Coast (SeaSonde) is also used. The radar antennas are located south of Robe and north of Port Macdonnell with nominal ranges of $200km$. The period used is Jan-Mar of 2016 and data were provided in a $6km$ gridded resolution. We also follow IMOS quality control procedures but

enforced stronger criteria by removing data with less than 6 observations in the hour and with standard deviations larger than $3\,\mathrm{cm\,s^{-1}}$.

Lastly, observations from two glider missions during Feb-Mar of 2016 are used to show the synoptic nature of upwelling. These observations are the first of this kind during the summertime in the region and provide direct measurements of CHL-A (*Wetlabs* ECO-Puck), *TS* through a pumped SBE-GPCTD, and other variables not presented here. Sampling using the glider was performed in a ship-like, zig–zag pattern with some alongshore transects traversing the Bonney Coast. Data processing on each glider mission was limited to manual segment determination, cast classification, removal of upward cast observations, removal of invalid temperature and salinity pairs and isolating the dives into hierarchical and individual casts/dives per segment. Although the data is corrected by IMOS, we still found 'noise' at the Surface Mixed Layer (SML) transition (not shown). In this sense, only the downcast dives were selected, so as to provide a simple minimisation of the SML position mismatch and reduce noise by high-frequency motions. The data is presented in its full form (profiles), without any averaging or extrapolation, except for the density contours which were interpolated to vertical fixed levels and filtered for visualization purposes. For CHL-A we again relied on the IMOS quality control procedure, with only a simple masking threshold on values higher than the mean±3 standard deviations of each mission, as in Schaeffer et al. (2016). We also use the bathymetric charts from Geoscience Australia to estimate isobath locations of points and aid in data extraction along certain isobaths. We use linear interpolation to estimate these contour lines and also to sub-sample the reported surface values to 6-hour intervals (again to reduce noise and enhance visualization). For the alongshore and cross-shore estimates, the isobaths were shifted slightly downwards (-3m).

6.2.2 Methodology

To compute anomalies of SL, BT, SST, etc., we first construct a climatology. We compute the climatology in two steps. The first step involves averaging all respective data (e.g., coastal SL between $2002 - 2016$) for each day of the year (i.e. averaging data for all January 1, January 2, etc.). This results in a noisy climatology − see Fig. 6.2 (black lines). We low-pass filter this climatology using a $60day$ cut-off filter, yielding a temporally-smooth climatology (blue), that possess more energy than the monthly climatology (red line in Fig. 6.2). Anomalies are simply the difference between the data and this climatology and the linear trend, resulting in a zero-mean, de-seasonalised anomaly. This is similar to the methodology described in Banzon et al. (2014). Although the monthly and filtered climatology series are similar, the filtered climatology is more robust given the

reduced energy in the seasonal cycle in the resulting anomalies. This results in a more detailed map for remote sensing estimates, improving the contrast in regional features. An exception of the applied method above occurs with CHL-A anomalies, which were estimated using the canonical monthly mean values of the valid pixels, given missing values due to clouds. We also analyse the results in different scales; seasonal, semi-annual and interannual variability here defined as the monthly anomalies filtered with a $3mo$, $6mo$ and $12mo$ cut-off window, respectively.

Given that the extended upwelling season in the Southern Shelves is defined between November and April (Middleton et al. 2002; Nieblas et al. 2009), with reported minima in SST between January and early April, we defined our summer upwelling season between January and March (JFM). This is done mostly because the majority of our direct observations were in February and March, because the maxima (minima) in alongshore wind-stress (SL) seasonal cycle occurs within these months, and because the variability of the upwelling plume peaks between January and April (see Fig. 6.2 above and see the SST analysis in the following sections). Throughout the chapter, we also note that the stronger events of 2016 occurred in January and March, and as such, the choice of an upwelling season defined in JFM appears appropriate in this sense. While January/February are within the months of maximum shortwave radiation flux, damping the upwelling signal more strongly, March usually presents smaller net heat flux (not shown) and more upwelling favourable winds (see Fig. 6.2).

As an index for local upwelling/Ekman transport on the SL and SST, we used the daily mean of the alongshore surface wind-stress. This component is estimated from the daily alongshore component of wind stress, computed from 6-hourly 10-meter height wind speed, using the Large and Pond (1992) formulation. The component is projected in the mean coastline direction of the tide gauge station. Angles used for each TG are reported in Table 6.4 and the alongshore vectors are within the confidence interval of the maximum correlation with local sea level (not shown). The convention used is sea level related: a negative (positive) alongshore component generated negative (positive) SL, and indicates overall divergence (convergence) generated by the surface offshore (onshore) Ekman transport.

Regression analysis (correlation coefficients), as well as cross-correlations, are used to indicate relationships between the coastal TG stations and the existence of a waveguide connection between them. As well, correlations between pairs of seasonal variables are mostly done for summer (e.g., correlations between JFM seasons), or within lagged variables (ENSO indices mostly). Multi-linear/partial regression models are used to estimate different effects on the variable in question. The regression model used here can be expressed quite generally as (see also Davis

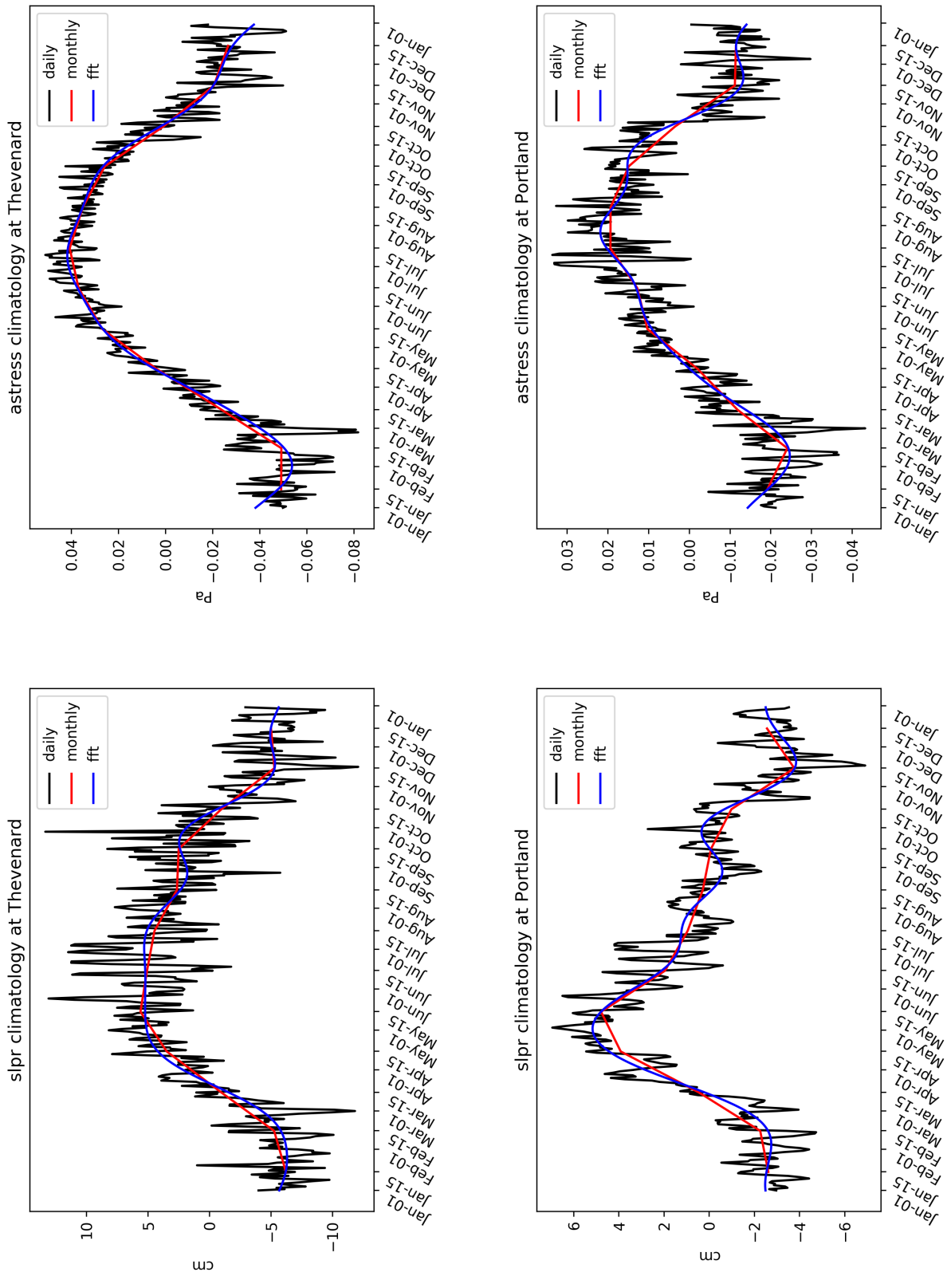

Figure 6.2: Left: The seasonal cycle of the de-tided, de-trended and adjusted Sea Level (SL_{adj}) at Thevenard and Portland. Right: same as left but for Alongshore wind stress (Pa). Daily estimates (black), monthly (red) and filtered (blue).

Table 6.4: Table of angles (°) used for the alongshore wind stress component computation for each of the TG stations. Angles are in meteorological convention (0° is North)

location	Azimuth
Darwin	120
Broome	50
Hillarys	350
Esperance	290
Thevenard	300
Portland	320
Burnie	10

1973):

$$y_m = \hat{y_m} + \epsilon \tag{6.1a}$$

$$\hat{y_m} = X\hat{\beta} \tag{6.1b}$$

$$X_{n\times m} = \begin{bmatrix} 1 & x_{n-q,t} & x_{n-q+1,t} & \dots & x_{n-2,t} & x_{n-1,t} \\ 1 & x_{n-q,t+1} & x_{n-q+1,t+1} & \dots & x_{n-2,t+1} & x_{n-1,t+1} \\ 1 & x_{n-q,t+2} & x_{n-q+1,t+2} & \dots & x_{n-2,t+2} & x_{n-1,t+2} \\ \dots & \dots & \dots & \dots & \dots & \\ 1 & x_{n-q,m} & x_{n-q+1,m} & \dots & x_{n-2,m} & x_{n-1,m} \end{bmatrix} \tag{6.1c}$$

$$\hat{\beta_{n\times 1}} = \begin{bmatrix} b_0 \\ b_1 \\ b_2 \\ \dots \\ b_n \end{bmatrix} \tag{6.1d}$$

Where y_m is a vector of data, $\hat{y_m}$ is the dependent (regressed) variable vector, i.e. the estimate of y_m, and ϵ is a residual vector (normally distributed with zero mean and fixed variance). The total number of observations is m, with t the individual index (e.g., time). X is the design matrix (mxn), with n as the number of regressors plus one. For simple univariate linear regression ($q = 1$), $n = 2$ and $\underset{t\times 2}{X}$, while for a three variable multi-linear regression, $q(i) = 1, 2, 3$ and $\underset{t\times 4}{X}$ follows. $x_{v,m}$ are the 'stacked' independent variable vectors (regressors with size m) and $\hat{\beta}$ is the estimated coefficients.

The solution of the problem is to find $\hat{\beta}$ that minimise the residual ϵ:

$$\hat{y_m} = b_0 + b_1 x_{n-q,m} + ... + b_q x_{n-1,m} \tag{6.2a}$$

$$y_m - \hat{y_m} = \epsilon \tag{6.2b}$$

Where b_o is the offset (intercept) and b_q the slope (correlation coefficient) for each individual(s) regressor(s) x. The solution here is via Ordinary Least Squares (OLS), i.e., by an unweighed minimisation of the Euclidean norm:

$$\sum_{t=1}^{m} (\epsilon_t)^2 = \sum_{t=1}^{m} (y_t - \hat{y}_t)^2 \tag{6.3a}$$

with solution:

$$\hat{y_m} = Hy = X_{n\times m}(X'_{m\times n} X_{n\times m})^{-1} X'_{m\times n} y = X\hat{\beta} \tag{6.3b}$$

Where H is the hat matrix — an individual entity for each design matrix X and the X' indicate transpose operation.

For the time series here we mostly use or simple linear regression ($q = 1$,$x = x_t$) or multi-linear ($q > 1$,$x = x_{v,t}$) regressions. We also used this method to fill some long-missing data in the weather station variables, mostly MSLP, by grouping variables per month and applying a regression of matched data to fill the missing dates (see also Middleton et al. 2012). As well, in the last section of this chapter, OLS is used to fit variables with $4th - order$ polynomials:

$$\hat{P_n} = b_0 x_n^4 + b_1 x_n^3 + b_2 x_n^2 + b_3 x_n + b_4 \tag{6.4}$$

With $\hat{P_n}$ being estimated with a single regressor (x_n) with n now as the number of observations. For example, a polynomial is fitted with x being depth, and P_n as temperature, generating a family of b coefficients that defined a smooth curve of temperature in the vertical.

Throughout the chapter and for most correlation coefficients, we use a 95% confidence interval based on an effective degrees of freedom (DOF), given that, although the time series have the same length, they can be filtered (such as interannual time-scales), and possess autocorrelations, decreasing the DOF. This effective DOF is calculated in the following manner: (a). We compute the length of the first zero crossing of the cross-correlation function between regressor and respective data; (b). We compute a new DOF with the actual length of the time series divided by (a). This way a strict criterion for the correlation coefficients

is adopted, compensating for the shorter independent values. In some gridded estimates we avoid this calculation but report the confidence limit assumed with a threshold in the correlation coefficient.

A non-parametric smoother (LOWESS) is also used to create a low-pass time series version of combined variables, such as the SL around Australia. The parameters used are reported accordingly.

As in the atmospheric and ocean heat waves analysis, we define extreme values based on the percentile range of the respective variable. The percentile used to define an extreme event is here defined by the $20th$ ($80th$) percentile of the anomalies.

Throughout the chapter, we mainly choose the ONI-ENSO index based on ERSSTv4 dataset (*https://www.esrl.noaa.gov/psd/data/climateindices/list/*), instead of the more commonly used NINO3.4. The choice appears to contradict previous studies, but the indices, as of today, are equivalent. These indices are statistically the same (r=0.97), even between different SST products (ERSSTv4 vs HadSSTi — not shown). They share the same units ($°C$) and are defined at the same region ($5°N - 5°S$,$170°W - 120°W$), but use slightly different running mean filters, $3mo$ vs $5mo$, for ONI and NINO3.4 respectively. The former is used for operational definition of ENSO given the smaller window filter. In a strict sense, direct comparisons with the NINO3.4 index, used in the studies of Middleton et al. (2007a) or Li et al. (2004), are less robust. This is because the former study used a further $3mo$ running average filter on top of the NINO3.4, while the latter used (an assumed) a non-filtered index. The SST products used to calculate the index have changed considerably in the last 10 years (Huang et al. 2015).

The ONI index based on ERSSTv4 data is available at *https://www.esrl.noaa.gov/psd/data/correlation/oni.data*. For the equivalence test, the reader can reach the HadSSTi NINO3.4 dataset at *https://www.esrl.noaa.gov/psd/gcos_wgsp/Timeseries/Data/nino34.long.data*.

Finally, the use of the NOAA Optimum Interpolation Sea Surface Temperature (OISST) version 2, as well as the ECMWF wind stress estimates, are consistent with the main products we used here and we limit the presentation of the latter most of the time. AVHRR is used for an extended time series analysis, but we focused our spatial analysis with the MUR SST product for the EGAB given the enhanced resolution. AVHRR is very crude for shelf regions and the SST indices in the BC region are not so well represented. In general, the results are consistent with the MUR dataset (see the SST sections).

Lastly, given that several observations are distributed in different time windows, correlations and analysis are provided with the respective window of data. For example, 1994–2016 is the period where all SL TG data match. As well, 2002–2016

is the available period for high-resolution SST (MUR) and data is cut to this period as required and in others (e.g., BT). All data presented in this chapter is publically available under the clauses of the respective providers.

6.3 Results

6.3.1 ENSO and SAM influence on sea-level and winds along the southern shelves

During late 2014, a significant El-Niño phase started, generating a strong signal throughout 2015 and 2016, as shown by the negative ENSO metric, ONI, in Figure 6.3 (green line/mid-upper panel). The relationship with adjusted SL (grey points) is clear, with strong visual correlation. Correlations between monthly SL and ENSO are ≈ -0.6 for the tropics and the western regions and maximum of ≈ -0.5 for the EGAB, all significant for all timescales selected (see Table 6.5). There is an expected increase in correlation for the interannual variability, mainly because the ONI predictor possess most variability below the seasonal frequencies (see the last column in Table 6.5). As a summary of the table, the sea level around Australia is represented in Fig. 6.3 as the LOWESS filter of all TG–SL data from 1992 to 2016 (red lines). The fraction parameter for the LOWESS fit is $frac = 0.05$ – equivalent to $\approx 12mo$.

It is important to note that the ONI index (and other ENSO indices) are not completely independent of other climate variability phenomena/indices. For example, it is known that the DMI, a proxy for Indian Ocean Dipole (IOD), is well correlated with Niño in spring (Cai et al. 2011). The IPO index is also coherent with ENSO, as well as the MODOKI, and this is manifested on the SL correlations (see for example Table 6.6)

Between 2015 and 2016, SL is low in the north, west and south of Australia (Figure 6.3, mid-lower panel), with values in the bottom $10th$ percentile. These extremes extend along the entire coastline between north-western Australia to Bass Strait. Also, the remarkable poleward coastal trapping of this signal is clear, particularly in the zonal shelves of the GAB. Boxplot's of observations at the TG stations on the EGAB (left and right panels in Figure 6.3), highlight that lower SL were one of the lowest on record since 1992. A fall in SL is also consistent between the northern limit (Thevenard) and the south (Portland) of the EGAB, with mean anomalies lower than $5cm$ (the same feature is found at Esperance – not shown). Thevenard variance is higher than off Portland (note the change in scale between the boxplot's) and anomaly amplitudes are mostly coherent. This indicates that the difference in variance is within the higher frequency band (weather band) and that anomalies share a common forcing (or damping) (see also Church et al. 1987).

Additionally, and consistent with ENSO time-scales, the SL signal occurs with distinct peaks and within a time-scale of $3 - 4$ years. The SL drop started in late autumn of 2015 (Fig. 6.3, mid-lower panel) and is coherent with the sea level inter-annual signature. Relative higher frequencies are also detected in the time

Table 6.5: Table of correlation coefficients for different time-scales between TG station variables and the ONI index. Time range is January 1994 to May 2016. Values are for the adjusted sea level corrected for isostatic effects at monthly timescales. Correlations for total sea level are higher (lower) for tropical (non-tropical) stations given the pressure effect. NS - not significant.

Station	Monthly	Seasonal	Monthly JFM	Interannual
Darwin	-0.601325	-0.643979	-0.517229	-0.74047
Darwin τ_a	NS	NS	NS	NS
Darwin P_{atm_a}	0.652655	0.731249	0.685157	0.853677
Broome	-0.596409	-0.65653	-0.517651	-0.773845
Broome τ_a	NS	NS	NS	NS
Broome P_{atm_a}	0.608257	0.687113	0.663031	0.828096
Hillarys	-0.618413	-0.654329	-0.651004	-0.741256
Hillarys τ_a	NS	NS	NS	NS
Hillarys P_{atm_a}	NS	0.416601	0.580886	0.613368
Esperance	-0.529925	-0.564591	-0.538951	-0.664795
Esperance τ_a	NS	NS	NS	NS
Esperance P_{atm_a}	NS	NS	NS	0.521015
Thevenard	-0.388744	-0.440138	-0.34821	-0.602988
Thevenard τ_a	NS	NS	NS	NS
Thevenard P_{atm_a}	NS	NS	0.531046	0.501668
Portland	-0.465279	-0.528244	-0.404606	-0.68708
Portland τ_a	NS	NS	NS	NS
Portland P_{atm_a}	NS	NS	0.286161	0.345731
Burnie	-0.534452	-0.572602	-0.428152	-0.685302
Burnie τ_a	NS	NS	NS	NS
Burnie P_{atm_a}	NS	NS	NS	NS

Table 6.6: As in Table 6.5, but for the IPO index

location	Monthly	Seasonal	JFM	Interannual
Darwin	-0.625792	-0.675295	-0.550142	-0.768967
Darwin τ_a	NS	NS	NS	NS
Darwin P_{atm_a}	0.632471	0.701536	0.677656	0.827279
Broome	-0.598882	-0.662591	-0.506914	-0.775147
Broome τ_a	NS	NS	NS	NS
Broome P_{atm_a}	0.581482	0.652857	0.642369	0.807804
Hillarys	-0.618136	-0.656616	-0.642769	-0.741185
Hillarys τ_a	NS	NS	NS	NS
Hillarys P_{atm_a}	NS	NS	0.603266	0.575643
Esperance	-0.518371	-0.552839	-0.509516	-0.660414
Esperance τ_a	NS	NS	NS	NS
Esperance P_{atm_a}	NS	NS	NS	0.482842
Thevenard	-0.40587	-0.456076	NS	-0.629883
Thevenard τ_a	NS	NS	NS	NS
Thevenard P_{atm_a}	NS	NS	0.541028	0.51566
Portland	-0.473935	-0.529094	-0.374683	-0.692815
Portland τ_a	NS	NS	NS	NS
Portland P_{atm_a}	NS	NS	NS	0.369408
Burnie	-0.53821	-0.576375	-0.436529	-0.700483
Burnie τ_a	NS	NS	NS	NS
Burnie P_{atm_a}	NS	NS	NS	NS

series, *e.g.* 2012 and 2013, where a La-Niña signal developed following an El-Niño (2010), with 2 clear peaks during 2011 and 2012. This indicates that not only larger and more prolonged ENSO events (3–4yr) propagate along the coast, but also relatively higher frequency ones. It is also clear from the time series that a decadal variability is present (IPO-like), but the time series here are too short to analyse such effects (see e.g., Kane et al. 2014; Henley et al. 2015).

Atmospheric variability was also in the extreme range throughout the 2016 summer, with alongshore wind stresses close to, or within, the 20th percentile range (light blue shading) and for both stations in the EGAB. The alongshore anomalies in wind stress in Portland were the highest of the southern stations, with upwelling favourable winds amplitude closer to the seasonal cycle amplitude in the region (Fig. 6.3 bottom right). In the North (Thevenard), values were more variable and smaller, probably by breeze effects and proximity of the land mass. At Esperance (west) values were also smaller, but with a more similar distribution to Portland (not shown – but see below).

Atmospheric pressure also reached the 80th percentile range (light red shading). By geostrophy, for an anomalous north-westward wind stress to develop, a stronger pressure gradient must exist over the GAB. This implies that the atmospheric pressure at mid-Bight (say 130°E-38°S, where the seasonal summer MSLP is maximum — not shown), was even higher than the coastal pressures presented in Figure 6.3, supporting a geostrophic upwelling favourable wind. It is also important to highlight that this relationship is not decoupled from the wind; e.g., for the summer of 1998 (middle left and right in Fig. 6.3), observations showed a positive anomaly (downwelling favourable) for winds and for pressure, which means that the pressure anomalies over the ocean in the GAB region were smaller than at the coast.

Results for the northern stations were also consistent with ENSO related surface pressures (Trenberth et al. 2000; Landerer et al. 2008); with positive (negative) anomalies in pressure during the El-Niño years (La-Niña) (see Table 6.5 and below). The serial correlations between the ONI and the TG station variables at the interannual timescales are shown in Fig. 6.4a (solid lines). Again, the reduction in poleward coherence is clear for both total SL (red), adjusted SL (blue) and MSLP (magenta). An Empirical Orthogonal Function (EOF) analysis was performed between the respective variables for all stations. The main principal components are presented as dashed lines in Fig 6.4a. This particular result is consistent with Li et al. (2004) (see their section 2.) in the sense that the first EOF mode is highly correlated with ENSO. We have about the same explained variance (blue dashed line), equivalent to their reported values. Note also the same conclusion of Li et al. (2004); although the EOF signal is correlated with ENSO, damping

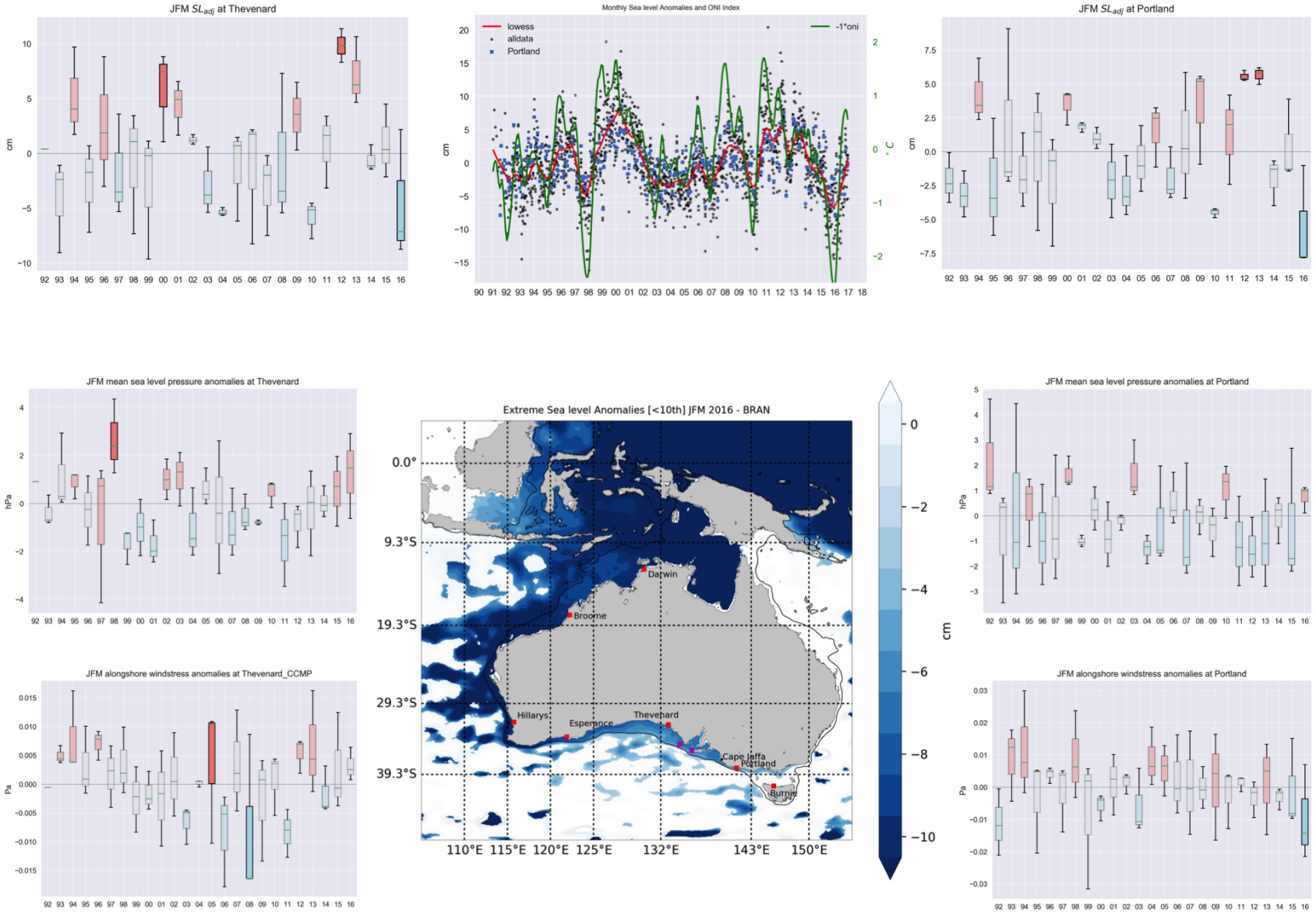

Figure 6.3: The extreme conditions of Sea Level during the upwelling season of 2016 and interannual observations from TG stations in the EGAB. From top to bottom: Box-plots of adjusted SL, atmospheric pressure anomalies and alongshore wind stress anomalies for Thevenard (left) and Portland (right). Blue and red opaque (semi-transparent) colours are the $10th$ ($20th$) and $90th$ ($80th$) percentiles. Top-mid panel: Time series of SL for all stations (grey), for Portland (blue squares), the negative of the ONI index (green) and a LOWESS filter of all TG–SL (red). The mid-bottom panel is the SL values in the extreme range (opaque-$10th$) around Australia in the BRAN reanalysis.

increases poleward (solid lines). The principal component of SL highlights the coastal waveguide effect and the leakage of energy towards the south, not only for ENSO but, for energy in sub-inertial scales as a whole. Hence, we confirm a strong interannual ENSO effect in SL along the southern shelves (Middleton et al. 2007a).

The ENSO effect on pressure is also clear when comparing the total SL and the residual (adjusted) SL: there is an overall decrease of $\approx 20\%$ in the ENSO amplitude when isostatic effects are ignored. The effect is more prominent in the tropics than in the south, with the latter isostatic effects more independent of ENSO (magenta lines). Despite the high ENSO correlations with MSLP in the tropics, there is also a marked poleward decay in correlation. Also, when local pressure variability is removed, there is a marginal improvement of ONI power (in an information sense) in the SL for Portland/Burnie; this indicates that the ENSO signal in total SL is 'hidden behind' a noisier time series. Nonetheless, the explained variances are still significant ($r \approx 0.5$) within the southern shelves. This is consistent with extra-tropical effects of ENSO and IOD reported elsewhere (e.g., Cai et al. 2011) as indicated by the isostatic ENSO effect on SL in the GAB. This was confirmed by a pattern correlation between monthly MSLP and ONI, with values of about $r = 0.23$ for the southern shelves, increasing to $r = 0.4$ for JFM (1994–2016 – not shown). Hence, as in SL, ENSO is more coherent with interannual MSLP. In other words, the ENSO effects on SL around Australia are largely steric, with a smaller isostatic contribution away from the tropics.

Another interesting result is that, for all stations, interannual surface Ekman transport at the coast appears not directly affected by ENSO at zero lag (cyan lines in Fig. 6.4a) with insignificant correlation values at the 95% significance level (see also Table 6.5). This appears to indicate that alongshore winds are a linear independent source for interannual SL variability and this relationship is consistent across the timescales. Middleton et al. (2007a) found the same result along the EGAB. A cross correlation between wind and ENSO index over the EGAB also indicates lower correlations/significances ($r < .5, p > 0.05$ with 15 DOF at interannual time-scales). This is consistent with the MSLP and wind pattern associated with ONI — they do not show favourable wind stress for upwelling in summer (JFM) (not shown). The alongshore series are also noisier and affected by the lateral and frictional atmospheric boundary layer, hence a long time series is required to confirm this.

As an illustration of the above SL results, the linear model between ONI and interannual total SL is presented in Fig. 6.4b. It is clear that the tropical effect projects above $13cm$ SL oscillations in the northern regions, while the anomaly is heavily damped poleward, reaching about $10cm$ ($5cm$) at the Thevenard (Portland).

During 1995–2016 there were at least eight ENSO episodes with significant negative SL values, with 2015–2016 a clear outstanding event along with 1998. Thus, 2015-2016 was an extreme year, with strong ENSO effects in SL.

More interesting perhaps, the residuals of the linear model are still highly correlated spatially, and heavily banded, with periods with higher variability mainly in the extra-tropical region (WA and GAB shelves). This indicates another source of interannual variability that is incoherent with ENSO but still coherent spatially. Use of adjusted monthly SL anomalies did not change the overall picture (not shown). Also, the peaks in the residuals occur in the WA region. This region has large variability in SL associated with strong ocean currents and local ocean-atmosphere coupled dynamics — the Leeuwin Current (LC) and Ningaloo Niño (Feng et al. 2013; Tozuka et al. 2014)). Note also that in the stronger El-Niño events (1998, 2016), the residuals are usually positive during summertime; this suggests that even though ENSO is reducing sea level, other effects are reinforcing it (amplitude of the effect is smaller than the signal). The Interannual residuals presented in Fig. 6.4b are close to $3cm$, while residuals after La-Niña events are usually higher in their amplitude.

In fact, for Portland, the total interannual SL series represents about 42% of the total monthly variance, with the linear ENSO model here representing close to 45% of this interannual variability (20% off the monthly SL — see Table 6.3). It is important to remember that the overall values of the coefficients in the interannual time-scales can change given different time series lengths, i.e. DOF, but would change less in the larger population of monthly values.

Finally, the correlations between SL monthly anomalies in BRAN and the ENSO index are presented in Fig. 6.4c and are consistent with the results above: tropical origin, poleward trapping, decreasing coherence poleward and away from the shelf/slope. Although the variances explained are significantly smaller, given the higher variability in the monthly estimates, a particular feature is found in the GAB: namely stronger correlations compared to the coast, following approximately the location of outer shelf/shelf-break current region (the Leeuwin Current system). There is a weak indication of interaction with the current system and some dispersion offshore/westward. This could be the outcome of higher friction or scattering into deep water of the ENSO slope wave — the angles of the coastline also changed to be more permissive to Rossby wave dispersion (see the Ocean currents section). Nonetheless, the results above confirm the nature of the internal Kelvin wave and the usability of the theoretical works of Clarke et al. (1991) and Clarke et al. (1994) to describe the SL interannual variability along the shelf.

This result also mimics the observational findings of Li et al. (2004): the strong coherence of SL in a cross-shelf sense over the shelf with an abrupt change at

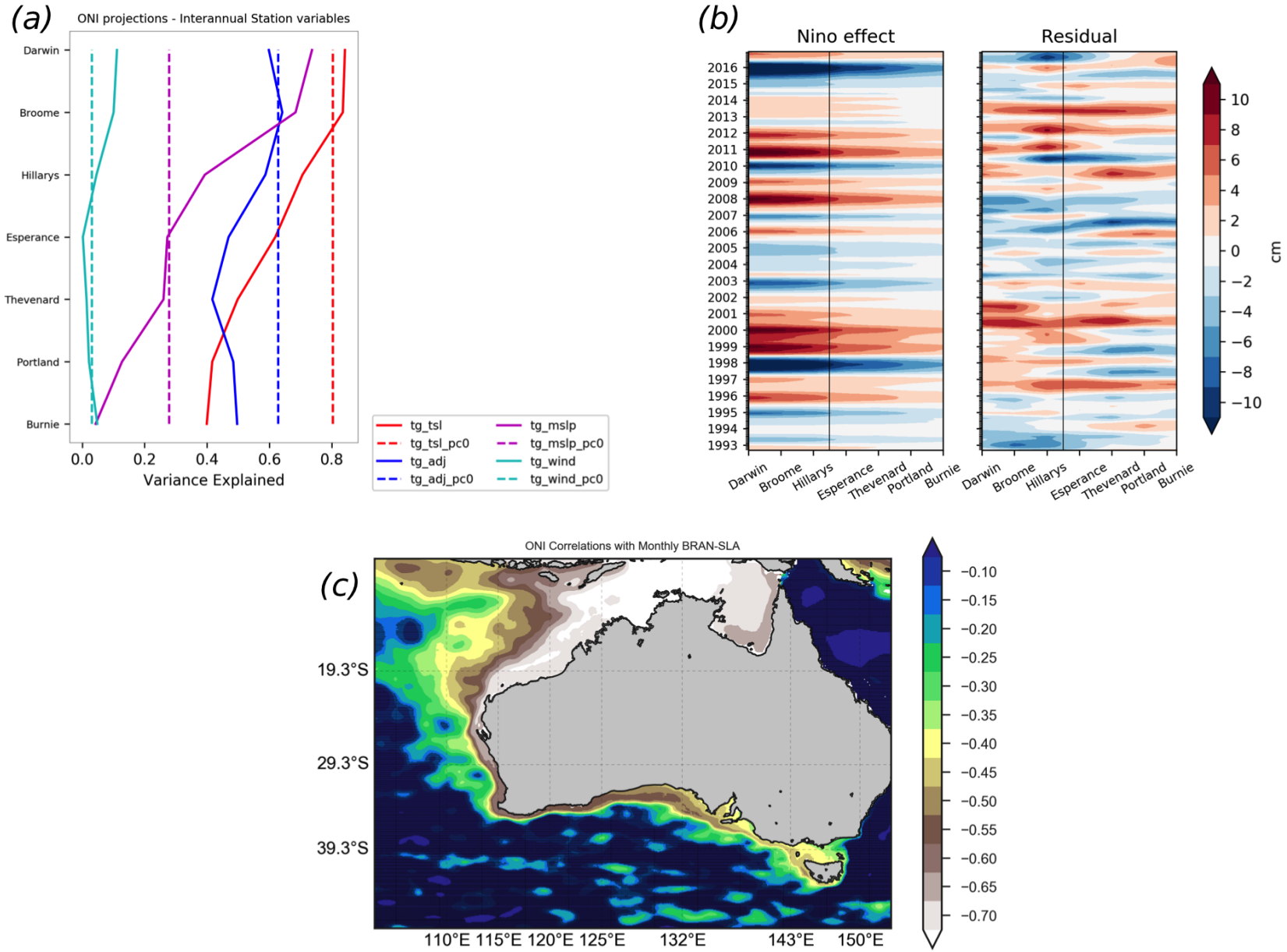

Figure 6.4: Projection of the ONI index into the station variables. (a) The variance explained by ONI in the interannual for each variable (solid) and the principal component of an EOF analysis of all stations (dashed). (b) The regression of Niño onto SL and its residuals. (c) correlation between BRAN reanalysis SL and the ONI index. Significant values ($p < 0.05$) are highlighted.

the shelf-edge — consistent with Kelvin wave dynamics. This would generate a coherent equatorward (poleward) current during El-Niño (La-Niña) events. During summer, Middleton et al. (2007a) could not detect ENSO related changes (in a global ocean model), however, they reported a reduced shelf-break currents during El-Niño winters.

Confidence on the coefficient for Fig. 6.4c is bounded to ≈ 0.33 (assuming a fixed value of 29 DOF for the region). However, the decay time-scales are indeed far from being homogeneous, with larger scales in the vicinity of the Spencer Gulf and Tasman outflow regions. A smaller offshore increase in coefficient occurs also at the BC region suggesting some extended offshore influence within the SAC system. In winter, downwelling, eddies, and offshore shelf water transports are dominant in these regions , particularly offshore of the Gulfs (Godfrey et al. 1986; Ridgway et al. 2004). This regions also share similarity with anomaly patterns within the seasonal cycle in Fig.3 of Ridgway et al. (2004). Hence, there is also some interaction between ENSO, onshore and offshore transports along the shelf-break currents.

Even though our series can be considered short for climate analysis, our interpretation of the waveguide is significant and consistent with previous results. The results presented above also imply that extreme sea levels reported in Fig 6.3 are largely from tropical/ENSO origin in the interannual band, particularly in the EGAB. However, the interannual variability only represents part of the total variances. The higher, intraseasonal frequencies are also important.

To search for other significant influences, a correlation matrix for several predictors at monthly scales and for summertime is presented in Figure 6.5. All series are detrended, then grouped and fit with a linear model with the intercept (the trend in summer is accounted for). As a reminder, because of our choice of independent estimates, the matrix is symmetric in power but not in significance, and Figure 6.5 should be read accordingly (x-axis are predictors).

Some predictors are heavily packed together; climate indices based on ENSO provide significant power to SL (ONI, IPO, MODOKI). They are also highly correlated among themselves, as is SL along the coast. This means that all ENSO metrics provide some information about SL, with the MODOKI index appearing as the less informative of the three considered here. Power between local alongshore winds against SL are also present in the southern shelves, but significance varies between stations with a poleward propagation — e.g. Darwin winds is coherent with Broome SL, as is Esperance winds with SL at Thevenard.

The new results presented here are related to correlations with wind predictors and non-ENSO indices. For example, the DMI index did not appear to be significant for SL. On the other hand, the SAM index appears to influence the EGAB alongshore wind anomalies during summer, particularly at Portland and

Esperance ($r \approx -0.27$). Although small, for the full yearly data, this is increased from Esperance to Portland ($r = -0.44$ in Esperance — not shown).

This is consistent with the role of SAM in the GAB region in general, where a positive SAM index indicates higher pressures within the southern Australia seas, with weaker westerlies, and as such, favourable for upwelling (Jones et al. 2009) (recall that negative alongshore wind stress is upwelling favourable in our convention). Although the composites for December, January and February (DJF) presented in Jones et al. (2009) do not show significant correlations of SAM and MSLP within the GAB during canonical summer (their figure 3), over winter the pattern is, on average, favourable for upwelling in the southern shelves (reducing downwelling). Nonetheless, the results indicate some rectification in wind direction and upwelling favourable winds with SAM. Particularly the SAM was positive since late spring of 2014 and was strongest in the summertime of 2015 and 2016 (not shown).

Another source of variability appears in the tropical winds, with the alongshore wind stress at the tropics (Broome most significant), explaining a small variance along the entire north-west-southern coastline in SL. Given the relative lower frequency variability of the tropics, this can be attributable to some anomalies locked to the long and strong seasonal cycle there. Although removed here, the mechanism of this transmission is possible to be trapped along the coastline such as the annual SL wave described in Domingues (2006) and Ridgway et al. (2015). For the yearly data, this coherence between tropical winds and SL along the coast shifts to Darwin, indicating that the source of variability is between these stations (not shown). Also, given that the distance between the tropics and Portland along the coastline is on the order of $6000 - 8000km$, a free barotropic shelf wave generated by winds, for example, would travel along the entire coastline in less than two weeks (the speed is in the range of $300 - 1600km/day$). The energy or period required for this forcing would be large, so as to the effect to be felt along the southern shelves. Hence, the leakage of energy is far from being exclusively related to ENSO.

Finally, the relationship between SL along the southern shelves and SST at the BC is also present, symmetric and significant (see SST section below for details). The relationship between winds and SST at the BC is also consistent with Ekman dynamics and the SL relationships, but suffer from insignificance and low correlations. The reason for this is explored in the SST section. Some of these influences, as reported above, shift during the yearly estimates, but since our focus is in the summertime we did not explore further (the overall picture still holds).

Since the SAM was strongly positive during 2016 and we found significance, we estimate a map correlation between anomalies in MSLP and winds for a group. The

group is defined jointly as the summer months (JFM) and when SAM was larger than the mean plus half of the total standard deviation of the series ($SAM > 0.9$) — i.e. above the $65th$ percentile. The correlations within this group are presented in Figure 6.6 and for the $1994 - 2016$ period, where conditions are met.

It is clear that when SAM is positive during summer, wind stress over the oceanic regions along the EGAB is upwelling favourable. The pattern is consistent with increasing MSLP and wind stress curl. The wind correlations are small between Esperance and Thevenard (and insignificant), but the high-pressure pattern and directions clearly provide wind direction anomalies favourable for upwelling. Hence, the mean wind circulation depicted in Fig. 6.1 is slightly changed to be more upwelling favourable during positive SAM. Furthermore, the mean value of the SAM was 2.3 during summer of 2016.

If using all data available, the MSLP pattern is a continuous positive zonal correlation (high-pressure) along $39°S$, with wind direction correlations with smaller significance but still westward (not shown). The pattern also moved to the east if only summer months are used (not shown). Thus, even though the general pattern of the SAM in canonical summer is weak, the effect can be detected in wind direction if more permissive limits are used (a 90% significance was used in wind vector direction).

In summary, Figures 6.5 and 6.6 indicate in general that the SAM index through local (remote) and winds (in the EGAB sense), tropical winds (also through the coastal waveguide), can indeed provide another source of information regarding SL in the EGAB and thus, to upwelling. The transmission of energy along the coast is foremost and should translate into variability over the BC, although the ENSO effect should dominate the longer time-scale response.

To highlight the sources and the transmission nature of the coast, the importance of locally generated variability in SL that leaks towards the BC is computed with a variogram for each station along the coastline (Figure 6.7a). In the variogram, the ONI index and each SL station is regressed against Portland SL (red lines — this is the Portland row in Fig. 6.5). The same is computed with ENSO regressed out (blue). Finally, a proxy for local (in the station sense) variability that reaches the BC is computed by stepwise variance difference of multi-linear regression models

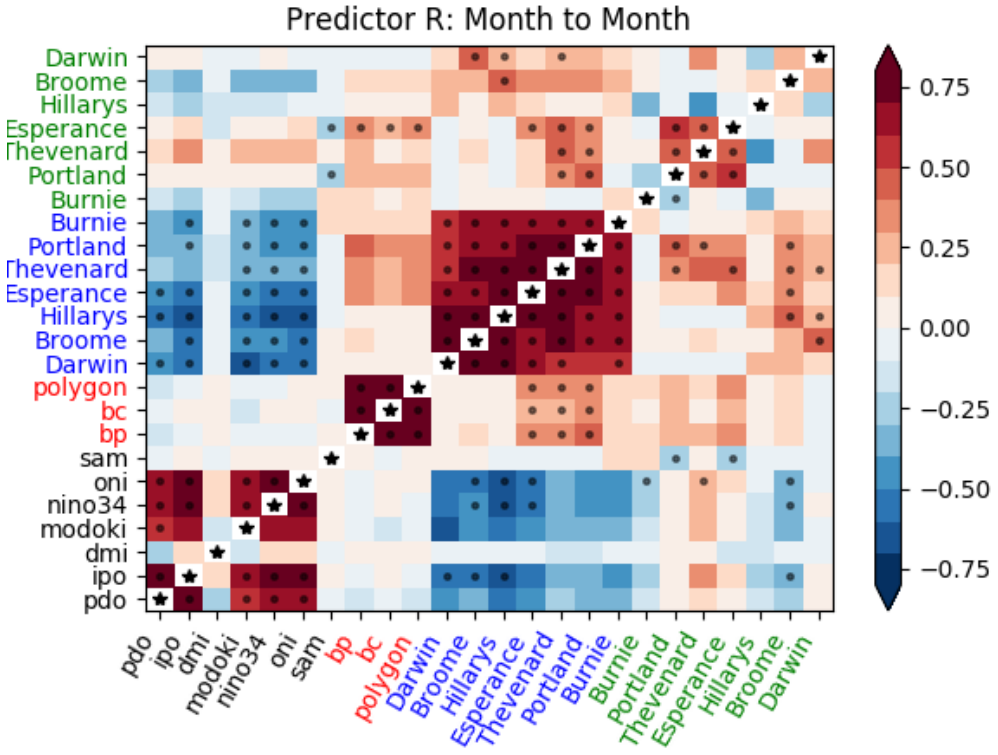

Figure 6.5: The summertime Correlation Matrix between monthly predictors (x) and monthly responses (y) for several climate indices and TG variables between 1994–2016 period (JFM months only). Climate indices (black), SST indices at the BC (red), adjusted SL (blue) and alongshore wind stress (green). Climate indices are detrended then grouped, while all other variables are anomalies from the detrended/de-seasonalised monthly time series. Black dots marks the significant predictors. Correlations (significances) are (not) symmetric. SST indices are based on the extended AVHRR-OISST product.

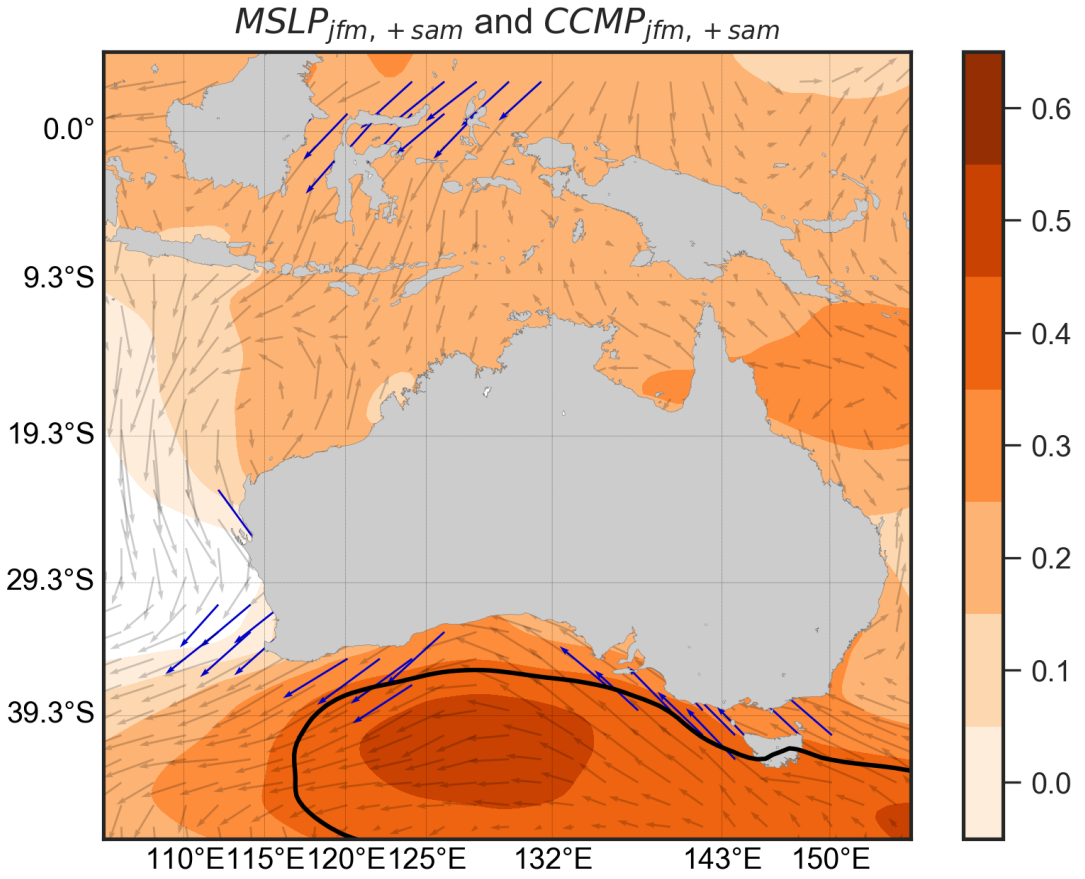

Figure 6.6: The correlation pattern between SAM and MSLP *anomalies* from ERA-I (shading) and the directional correlation (vector components are correlations) of wind stress *anomalies* from CCMP. Anomalies are monthly averages and grouping conditions are summertime months (JFM) and strong positive SAM ($SAM > 0.9$) and include 25 months from 1994-2016. The black contour delimits MSLP values within the significance bound ($r = 0.4$, at 95% level). Blue vectors also delimit direction components of wind stress ($r = 0.3$, at 90% level). Vectors are plotted every 2°. The summers of 2003,2010,2011 and 2014 are not included (non positive SAM).

between closest stations, viz.:

$$\hat{P_0} = b_0 + \alpha \text{ONI} \tag{6.5a}$$

$$\hat{P_1} = b_1 + \gamma \text{ONI} + \kappa \text{Darwin} \tag{6.5b}$$

$$\hat{D_{local}} = \Delta R^2 = Radj^2_{P_1} - Radj^2_{P_0} \tag{6.5c}$$

$$\tag{6.5d}$$

Where $Radj^2$ here is a function that computes the adjusted R^2, so as to take into account the number of regressors, while Greek letters are the respective correlation coefficients. The difference in variance explained at Portland between the model with *ONI* plus *Darwin* SL as regressors ($\hat{P_1}$), and another one with just *ONI* ($\hat{P_0}$), is regarded as the $Darwin_{local}$ variance that is coherent at Portland. This is done for all stations, using the previous stations correlations so as to isolate only the proportion of 'local' variability that can reach the BC. Here, local is defined in the sense that the series is *incoherent* with both previous stations equatorward and the ONI series. This locally generated and incoherent ENSO variability is shown as the magenta lines in Figure 6.7a, for the anomalies of all years (solid) and summertime months only (dashed lines).

The first thing to note is that, by removing the ENSO effects (blue lines), a 20% shift of variance is found — the previously reported variance related to ENSO at monthly scales. Note, too, that summertime explained variances (dash lines) within the GAB, are always larger than the annual (not grouped) estimates, particularly in the southern shelves. Hence, a less frictional pathway to the SL energy during summertime appears to hold. This appears to be consistent with the seasonal cycle during summer (negative SL along the coastline — see e.g., Fig.5 in Ridgway et al. 2015). A lower SL, divergence, stronger stratification and more frequent upwelling BBL would act to reduce damping by bottom friction if compared to wintertime where the shelf would be more homogeneous. For example, it's known by numerical experiments that upwelling jets under buoyancy shut-down adjustments lose less energy to bottom friction under stronger stratification (Chapman 2002). A stronger stratification also increases the speeds of Coastal Trapped Wave (CTW) (Middleton et al. 1990). So, in general, during summertime, there is an indication of faster and larger transmission of energy along the coastline of incoherent ENSO energy.

Although this intuition could lead to the idea that a stronger ENSO effect is expected during summer, the time-scales of the forcing are important. The ENSO signal is interannual and, on average should be sensitive only to a mean frictional

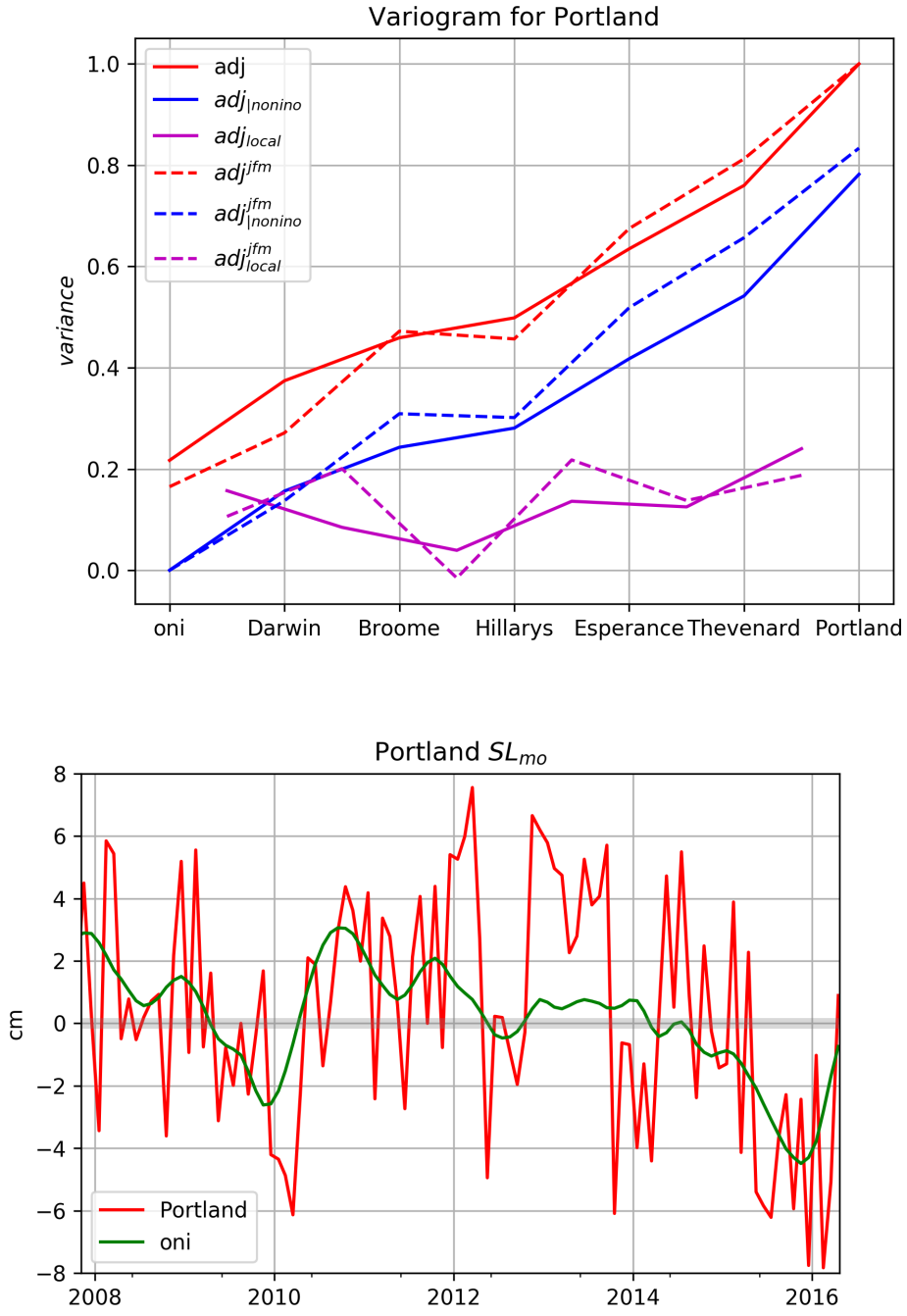

Figure 6.7: (a) Variogram of Portland monthly SL through a multilinear model using ENSO and the 5 TG stations along the coast. Red is total variance accumulated until the TG station, while blue is the total SL without ENSO effects. The magenta lines are the individual variance gains between stations. (b) The Portland monthly time series of adjusted SL (red) and the fitted ENSO linear model (green)

term. The ENSO signal is also bounded to the slope (Clarke et al. 1994), so although the stratification over the slope is changed in the same way, the role of background flow is important given ocean currents largely dictate the stratification there. Indeed, the shift in ENSO variance at summertime is not significantly different (the red line origin – Figure 6.7a). Note also that, despite the lower total variance in the monthly estimates, the interannual signature of the correlations with ENSO are very useful in estimating SL at the BC (Fig. 6.7b).

An almost constant linear increase in total variance also shows a significant, in the statistical sense, additive factor for almost all stations. Following the local (ENSO incoherent) variability sources, although the mean increase of variance appears to be 10% per station (the mean of the magenta solid lines), this *gain* in energy along the coastline is clearly not homogeneous or monotonic in summer. The summer gain between Broome and Hillarys is close to zero, with a marked decrease of variance and flattening of the accumulated variances. It is followed by an abrupt increase afterwards, in the proximity of the zonal shelves of the EGAB (magenta dashed lines). In wintertime, the effect appears nonexistent. Significance values here are about 4% (8%) for summer months (all years), and all stations, except the transition to Hillarys, provides useful gains in variance.

This result leads us to two hypotheses: 1. The northern narrow shelves of the WA region does not generate enough local variability in SL evident at Portland (at least at zero lag); 2. Particularly during summer, this region does not add any significant information towards the south. In other words, there is no significant energy origin between south of Broome and north of Hillarys that reaches Portland. This is expected for the narrow shelves there—small potential energy for CTW generation, and also for ocean currents—the LC and its eddies are stronger south of about $\approx 28^{\circ}S$ (Cresswell et al. 1993; Schiller et al. 2008; Feng et al. 2013).

The increasing gain in variability afterwards, in the southern regions where the LC is stronger and the shelf changes orientation, is dramatically higher during summer (21%). Values are larger than any of the previous locations, although the differences to the other values are not significant. This observation is a suggestion that one source of SL variability that reaches the BC is located close to Cape Leeuwin - the beginning of the zonal shelves of the GAB. This is consistent with the ocean circulation (stronger LC), the wind fetch and where coastal Ekman transport vanish during summer (a geographical origin).

However, for the full SL signal, we cannot ignore the tropical effects or ENSO effects. About 30% of the summer gain in monthly steric signal that reaches the BC is attributable to local variability of tropical stations (blue dashed lines), 50% with ENSO. This means that half the total variance of the BC can be related to tropical origin. This is also consistent with the wind correlations during summer. The

other half is divided into local variability between Cape Leeuwin and Thevenard (30%) and local variability in the vicinity of Portland (20%).

So, with the linearity assumed here, the local variability generated through the tropics is more important (in variance terms) than zero lag ENSO effects for the SL at the Bonney Coast. So, over the monthly timescales, the tropical and the western GAB regions provide most of the energy in SL that reach the BC. This is due to the leakage nature of the coastline and the interactions that could be generated along this long pathway.

Given that on *interannual* time-scales the ENSO linear model is very good and small residuals are generated for the EGAB (see Fig.6.4b), the indirect conclusion is that this local tropical energy is of higher frequency, i.e., on the weather-to-seasonal bands. Normalised cross spectral density estimates with the SL without ENSO, indicates that this is indeed the case, with most peaks in the seasonal band $(30 - 90d)$ significantly coherent with data at Portland (not shown). Estimates based on daily BRAN data at the station locations also hold significance at Broome in the $20d$ band for example, while more widespread coherences are found with stations to the south (not shown).

Some of these high-frequency peaks had almost the same amplitude as the ENSO effect, particularly during 2016. As will be shown in the last section, these signals, with periods less than 60 days were important. In the following section, we explore the variability in the EGAB related to SSTs.

6.3.2 The role of ENSO and the SAM on SST: Interannual variability, extremes and persistence effects

As already presented, the mean upwelling signal in the EGAB is a tongue of cold water with temperatures of about $18.5°C$ for the northern region, including the KI and Eyre Peninsula (EP) regions and about $17°C$ for the BC — see Fig. 6.1. The signal for the SAC, the shelf-break current that is part of the LC system (Cirano et al. 2004; Ridgway et al. 2004; Middleton et al. 2007b), is also clear in the bending of isotherms towards the south, being stronger in the northern sector of the EGAB and in Western Tasmania (WT), where it's referred to as the Zeehan Current (ZC). This cross-shore thermal gradient is usually maximum in the northern EGAB (about $1°C$ per $100km$), diminishing at the BC before increasing again in WT. The small zonal gradients in the BC region indicate stronger upwelling.

Indeed, the results in Fig. 6.1 are consistent with maps of regional anomalies presented in Ridgway et al. (2004), where a weaker SAC over the summertime months exists. Over the shelf, the BC plume is clear, but also another upwelling

plume is present in the north-western tip of Tasmania, where numerical modelling already indicated upwelling in this region (Evans et al. 1998). The shelf widths are also strongly variable along the coastline and have a clear effect on the distribution of the SST pattern; the wider (narrow) shelf in the GAB (BC) required longer (shorter) wind impulse functions for cold waters to reach the coast. Also, faster (slower) propagation of CTW (mode-1) in the northern (BC) regions is expected, which generates shut-down of interior upwelling, limiting the onshore transport to a thin BBL (see Chap. 5 and also Middleton et al. 2004).

The displacement of the plume westward of the BC coastline also shows the advective nature of the upwelling. Upwelled waters from the BC invade the Lacepede Shelf (LS) to the north, bifurcating in a westward flow, i.e. the outer coastal jet, and an inshore trapped transport along the coastline (inner jet). Although the inner jet is not clear in Figure 6.1, in the synoptic scales and SST anomalies this is evident (see below). The coastal jet location was also highlighted before and there is a clear effect of the phase lines of the mode-1 CTWs in this westward transport (see Figure 5.6 in Chapter 5).

The plume patch is evident in the standard deviations of the summer anomalies, Fig. 6.8 (a). Here the balance between the upwelling, advection of colder waters and maximum atmospheric heating during summer appears to explain the pattern at the BC. The northern shallow waters of the EGAB upwelling regions also highlight stronger SST variability, as well as the confined waters of the Gulfs and the oceanic and coastal waters off Western Tasmania. Lowest variability is found on the outer shelves of the northern sector of the EGAB and shallow waters south of Portland, such as in the Bass Strait. The band of low variability along the shelf break also appears to be related to the LC-SAC system, particularly in the Northern EGAB. Considering the lower variability in SST as a proxy for the SAC current, a weaker current is present towards the south in summer, again, consistent with the wind patterns of the region (Fig. 6.1, Fig. 6.2 (a,b)) and previous studies (e.g., the review of Middleton et al. 2007b).

There are also patches of SST variability in the oceanic regions, with scales of about $100km$, and a bigger patch of about 200–$400km$ southward of Portland ($141°E$). These active regions of eddy variability are under the influence of the boundary currents of the region (SAC and Flinders Current (FC)). These permanent features are also seen in the SL anomalies measured by altimetry (see Ridgway et al. 2004). Hence, these eddy locations could precondition the thermocline depth and upwelling in the shelf-break regions and could affect the shelf waters. This could be the case for the BC and its narrow shelves, where the shelf is more influenced by the oceanic features than the wider northern EGAB.

Given that our focus is within the upwelling region over the shelf, we construct

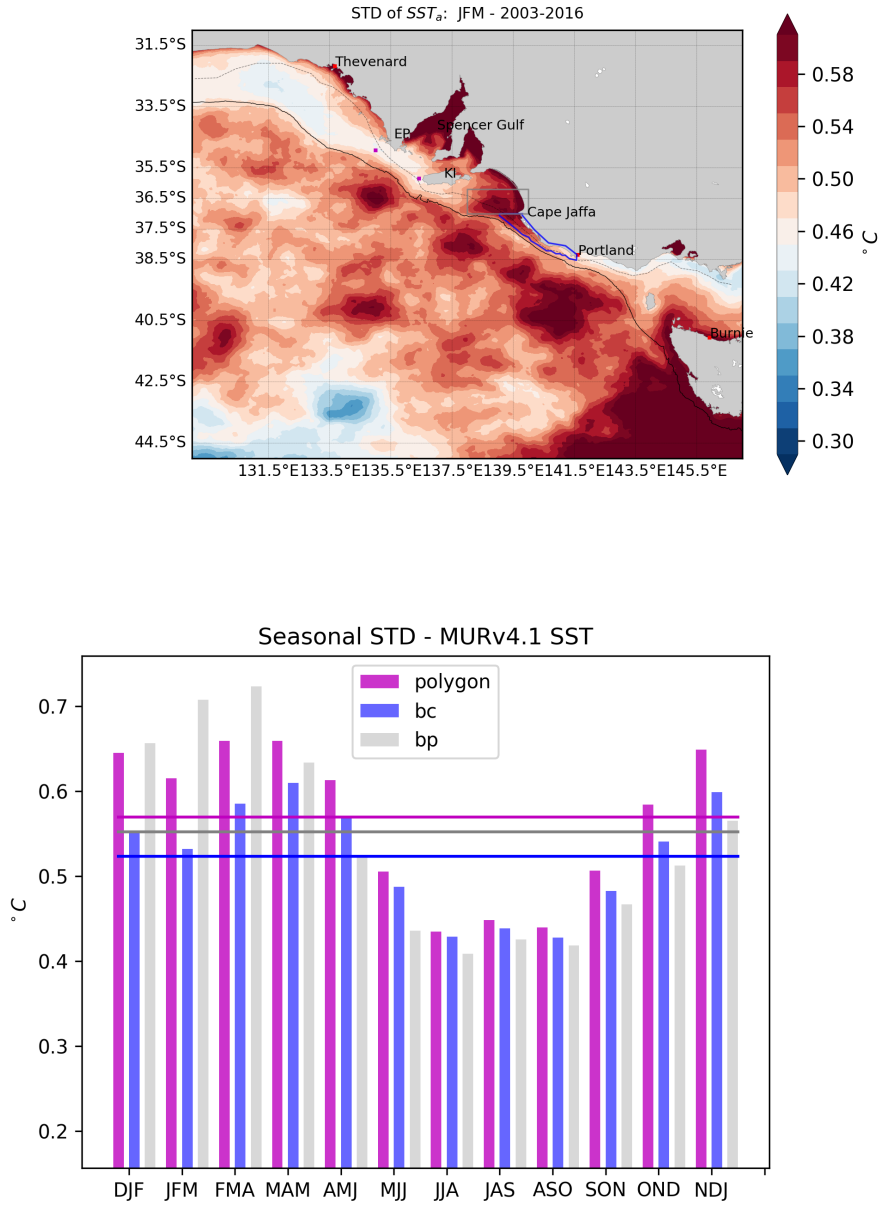

Figure 6.8: SST variability in the EGAB. (a) The standard deviation of the summertime (JFM). (b) The stratified standard deviation of the SST upwelling indices: *polygon* (magenta-see Fig. 6.1), *bc* (blue) and *bp* (grey). For reference of the areas used see the blue and grey polygons in (a). The horizontal lines in (b) are the variability of the entire dataset for each index/area. SST window is from 2002-2016 MURv4.1. Dashed grey line is the 60m isobath, while the solid black line is the 200m isobath.

several SST indices for the BC upwelling; one for just the plume region (*bp*), a second one comprising only the narrow shelf off the BC (*bc*) and a third (*polygon*) that is the sum of these two areas — see Fig.6.8a for the limits. Significant differences between these areas occur as shown by Figure 6.8b.

The plume-only region (Bonney Coast) has maximum (minimum) variability within summer, and differences of up to $0.2°C$ when upwelling is expected. This particular difference is large, since it's close to the range of the intraseasonal variability ($\approx 0.15°C$) off the BC (blue). The range of variability at the *bp* region is highest during summer and peaks between March and April. Again, this is consistent with a variability induced by the advective nature of the upwelling and damping of the signal by atmospheric heating.

More importantly though, is that the graph highlights that the plume is the most susceptible to extreme events. Indeed, mid-late canonical summer (two peaks at JFM and FMA) are the most likely months for extreme events to occur, while at the BC there is a tendency for extremes to occur early in summer or autumn. Results here are limited to a relatively short time series (2002–2016), but using the extended time series of the AVHRR (1994–2016), the picture did not change and the enhanced variability is also found to be between JFMA and over the plume region (not shown).

We choose to refer to the larger average area, the *polygon*, as the main index, and otherwise stated, we will call this the SST anomalies for the BC region. The polygon area is slightly skewed towards the plume given the number of pixels (area) is much larger than the narrow BC region. The outcome was, that over the year, this index has the highest variability of the SST records (magenta horizontal line in Fig. 6.8 (b)).

In summary, if an extreme event occurs within the BC region, the anomalies at the plume region are slightly amplified. The results above are also in agreement with the seasonal analysis presented in Nieblas et al. (2009) and the spatial variability is consistent with the lower resolution SST product (not shown).

6.3.2.1 Interannual variability of SST and the summertime of 2016

The JFM anomalies in the last decade for the BC region are presented in Figure 6.9 for two different products (top panels). Although variability between the two datasets used is expected, the results are, in general, consistent with each other. It's clear that 2014–2016 was extremely cold, with 2016 as the strongest negative anomaly of the last 15 years in the MUR product. Strong heating also occurred in 2013, while 2005 for example, was a normal year. These results are representative of all anomalies that affect SST – e.g., heat fluxes, wind-driven upwelling, vertical mixing, El-Niño – along the BC. Hence, the results indicate the net effect of coastal

upwelling — close to the coast, divergence and upward velocities should be large enough to reverse the high stratification and heating imposed by the atmosphere.

Nonetheless, of these other effects, a proxy estimate for anomalous heat content over the region is calculated: a horizontal average of SST anomalies for all coastal and oceanic waters ($z <= -5m$) within the regional bounding box ($31.5°S$–$45°S$ and $129°E$–$147°E$). This is exactly the horizontal limits in Fig. 6.8a.

This is presented for summer in Fig. 6.9 (bottom panels) and indicates that oceanic waters (given the predominant number of pixels) were indeed much warmer in 2013 and 2016 (and slightly colder in 2005). The heat content estimate above was normalised, with the region under anomalous warming during summertime in both products (not shown). Thus, the coastal upwelling signal in 2016 is hidden behind a positive heating anomaly trend in summer.

The spatial averaging along the BC with AVHRR data generate some deviations of the percentile range and amplitude in these estimates, but results are consistent in several years. For example, 2008 clearly stands out, with cold anomalies not presented in the MUR product. This relative uncertainty between the products affected the percentile difference between them in Fig. 6.9. Also, there were stronger correlations between the regional average SST and the BC SST indices in the AVHRR product than in the MUR product, given the low resolution of the former. This translates in the representation of the AVHRR data being more limited to detect coastal upwelling, while the MUR product developed larger minima within the SST index but limited to the last 15 years (not shown — but see below).

Given that the mean heat content in the region is positive, small or negative SST anomalies are obviously related to upwelling. The 2016 spatial SST anomalies within the BC are striking — see Figure 6.10a. While most of the oceanic waters experienced strong warming, particularly at the WT region, the shelf waters of the EGAB were cooler and below $1°C$ for the whole season. The pattern follows exactly the upwelling regions showed before, mainly north of the EP and the BC, where the Bonney Plume (BP) is present. It is clear that the northern half of the BC is affected by colder SSTs, while the other half of the region did not suffer such extremes. Again, this indicates the role of advection but also that the variability increases somewhat abruptly in the northern sector of the BC. This also suggests that upwelling is stronger in the north, and this region acts as the main source of the plume waters.

The bifurcation of colder waters is also clear with two different pathways; a deeper/outer jet transports waters to the west, while a narrow and shallow jet transports cold waters north of Cape Jaffa. South of Portland, the only persistent signal lies in the northern limits of Bass Strait, with a complete lack of anomalous upwelling in the WT region, where positive anomalies pertain. There, oceanic

SSTs appear strongly associated with the Sub Tropical Front (STF) region and the Tasman Outflow region, with apparently shallower mixed layers during the period. Moreover, the permanent eddy variability in the mean summertime anomalies presented before (Fig. 6.8a) is absent, with only a close to zonal band of positive oceanic anomalies west of Portland.

During summer of 2016, shortwave radiation anomalies in the EGAB were slightly negative, indicative of more clouds, and with positive net heat flux anomalies (stronger overall surface heating). This is consistent with a heavily damped upwelling signal which would cool the air above it. Although the ECMWF product resolution is relatively coarse, positive air temperature anomalies were negatively affected in the upwelling regions (reduced heating — not shown).

The wind seasonal anomalies are also consistent with the stronger upwelling picture, and differs significantly from the main direction for the season (Fig. 6.1). Values are up to $0.04Pa$, mostly directed alongshore — a factor of two from the expected value for the season (see Fig. 6.2c). Again, the SAM index was positive in general since spring of 2014 and during the summertime of 2016. The wind anomalies are reduced in magnitude in the north EGAB, increasing again only in the western GAB and WA (not shown). Within the vicinity of the upwelling plume, the wind anomalies are also reduced, indicating a possible strong feedback at the marine atmospheric boundary layer and wind drop-off, related to both SST and ocean-land gradients (Jin et al. 2009). Again, despite the stronger wind anomalies to the south, and favourable wind direction, a stronger upwelling signature is lacking south of Portland. Hence, the 2016 picture suggests that extreme SST signals were, on average, limited to the north of Portland.

The overall probability of the SST signal is of interest. The departures in SST anomalies from the median reach about 2 standard deviations ($<= 10th$ percentile). Again, a remarkable contrast, given that in the oceanic regions, the percentiles are in the opposite extreme $> 80th$ (Fig. 6.10b). If accounting for the heating, this is even more extreme in 2016. This clearly demonstrates the significance of this particular year and season. The percentiles also help to highlight that temperatures in the northern regions were much colder than first thought. For example, a surface signature of SST in the KI region is limited to stronger events, given that most upwelled waters remain close to the bottom (McClatchie et al. 2006; Ruth et al. 2010). The stronger cold waters in the northern EGAB also infer that a strong alongshore current persisted long enough to bring the anomalies at the coast to historic minimums. As we will show in the next section, BT were indeed very low in the 'cold pool' region off KI. The rather limited spatial bounds of the anomalies clearly indicate shelf processes and typical summer conditions — shallow mixed layers, strong heating, strong stratification and in the case of 2016, positive heat

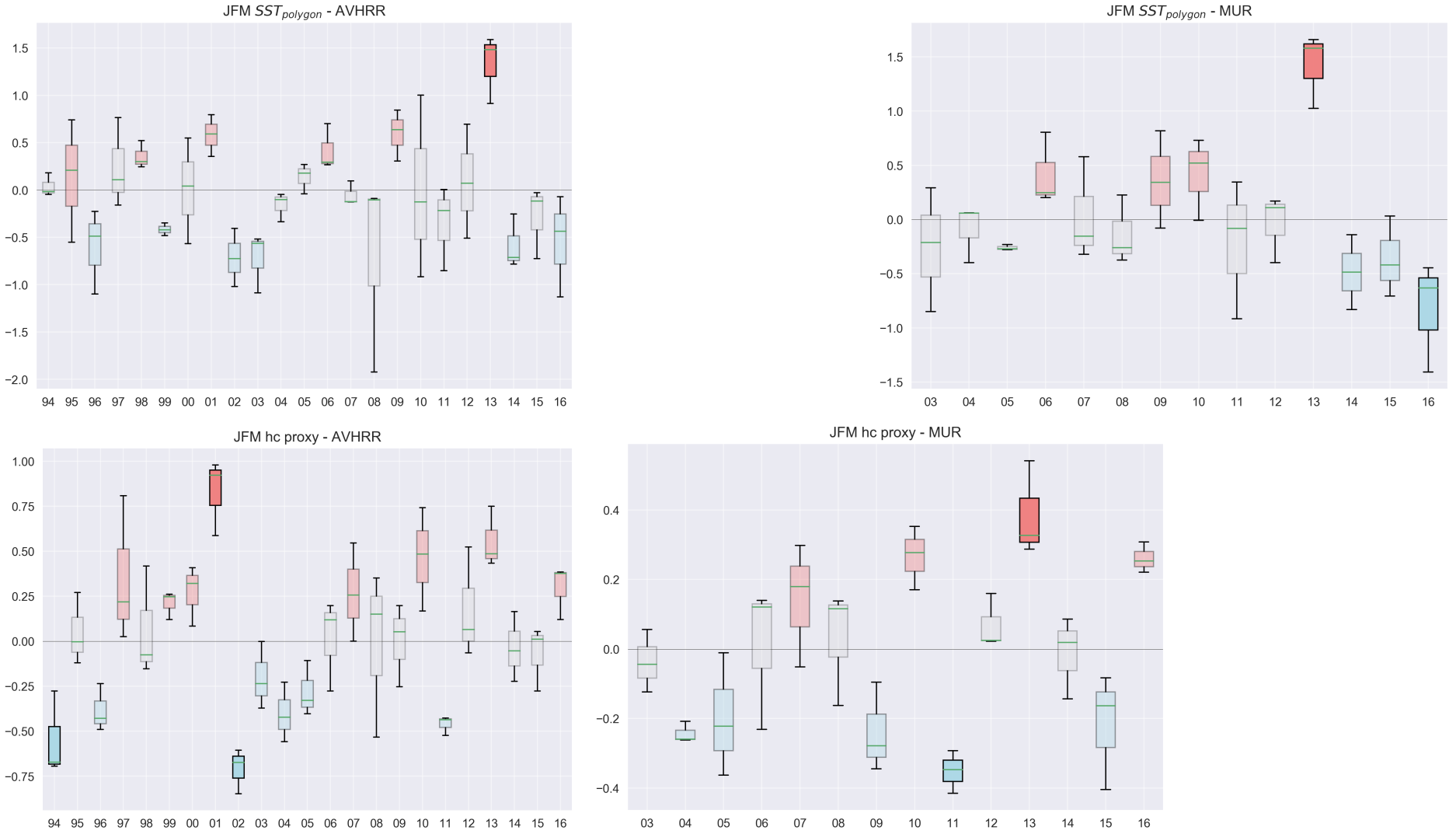

Figure 6.9: (Top) The Interannual variability of summertime SST in the BC region for the 1994-2016 period (AVHRR based - left) and for 2002-2016 (MUR based - right). (Bottom) The heat content proxy (regional average of SST) for the respective products. Blue and red opaque (semi-transparent) box colours are within the $10th$ ($20th$) and $90th$ ($80th$) anomaly percentiles.

content anomalies in the region.

It is useful to look at spatial patterns in other years that resembles 2016 in the SST anomalies. Such a year is 2005, which shows opposite values — Fig.6.10c. Note that 2005 was a year with previous neutral conditions and local sea level anomalies were also moderate (see mid and top-right panels in Fig. 6.3). A warmer EGAB shelf is present, but the seasonal cycle clearly dominates (the percentiles of these values are very close to the mean). Oceanic conditions were also colder than the average year. If the upwelling was driven solely by ENSO with close to zero lag, 2005 was supposed to at least provide some negative anomalies along the shelf or plume regions, which is not the case (wind anomalies were also small during this year). Note that this does not mean there was no upwelling — the BC plume signature is present, but it's slightly warmer.

A different picture also happened in 2013, when both SL and SST anomalies were positive. ENSO was again neutral at this time, with La-Niña conditions in the previous 2 years. Strong anomalies aligned with the shelf and downwelling favourable winds dominated the season, as shown by Fig. 6.10 (d) (see also Fig. 6.3 bottom left and right). Contrary to 2005, the heating is widespread, and the upwelling regions are much warmer; the BC plume is above the $90th$ percentile. The oceanic variability of this year also resembles the standard deviations of the whole $2003 - 2016$ period (Fig. 6.8 (a)). Thus, this particular year had one of the most significant EGAB positive SST anomalies in the last decade and as such, one of the most extremes SST signals. Indeed these warm conditions associated with La-Niña were very strong during 2011, with record rainfall in Australia and also strong SST anomalies in the tropical regions (Evans et al. 2012; Boening et al. 2012).

The differences between the extreme upwelling year of 2016, the normal year of 2005, and the reduced upwelling/heat wave season in 2013, indicate again that summertime extreme upwelling is related to ENSO but with some other influences or persistent effects. From the plots above, winds also appear in phase with ENSO. As shown before, this is in contrast with the insignificant relationship between coastal winds and the ENSO index as reported above and in Middleton et al. (2007a).

Moreover, serial correlations between the BC region SST anomalies and the ONI index are insignificant within the 1994-2016 period (AVHRR) (see Fig. 6.5). The values were also small in each pixel over the EGAB shelf and the BC region ($r \approx -0.18$), not significant in the longer AVHRR series (1982-2016), in the reduced series (1994-2016) or with the $MURv4.1$ product (2002-2016) (not shown). These regressions were also reportedly small for the shelf regions in Middleton et al. (2007a). The only regions that shown significance were the WA region (strong

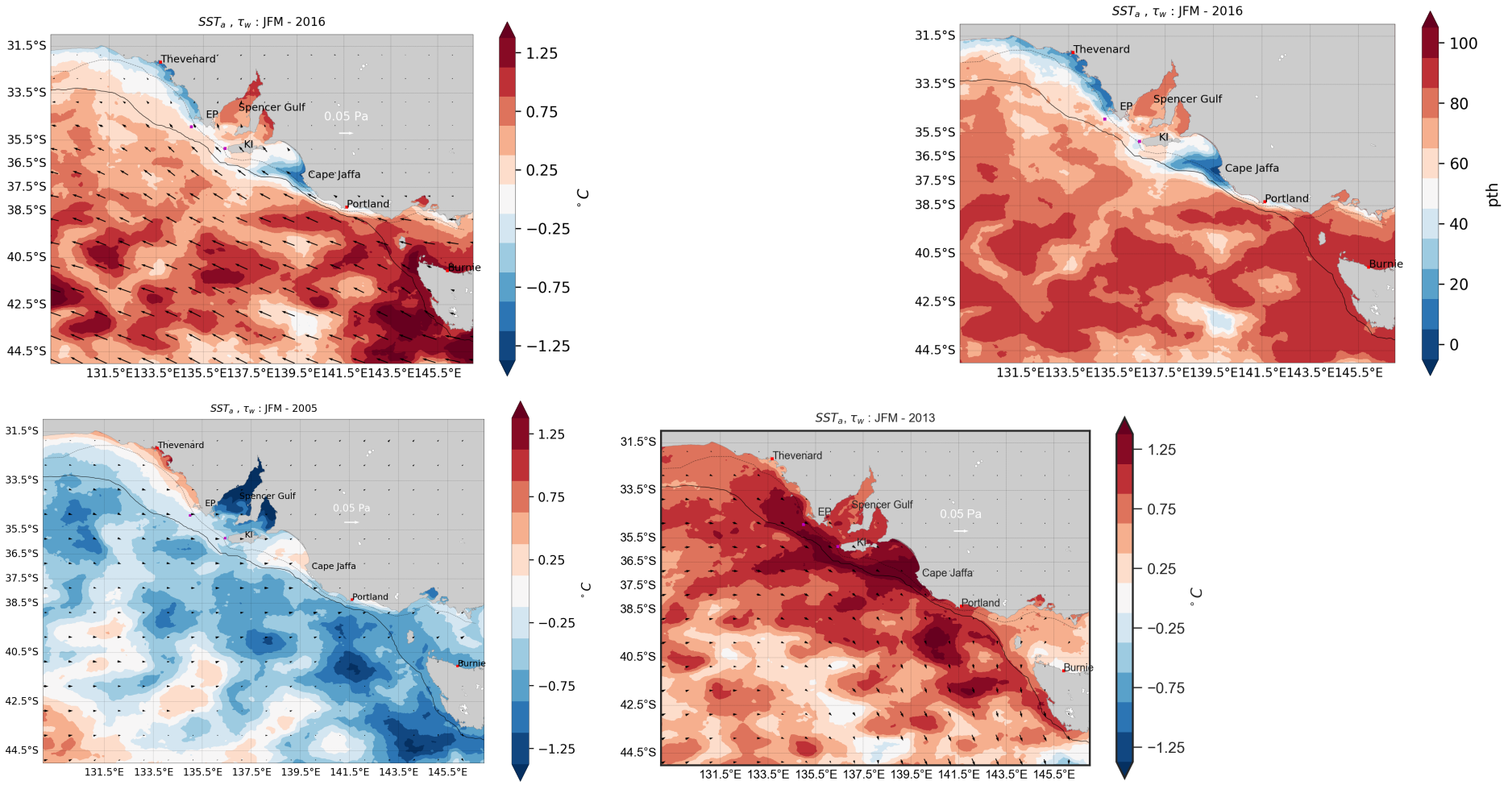

Figure 6.10: Remotely sensed SST anomalies (SST_a) for the JFM season. (a) SST and Winds anomalies for 2016. (b) Percentile range of the SST in 2016, (c) 2005 - mild El-Niño and mild negative SST and SL anomalies (see fig. 6.3). (d) mild La-Niña and strong positive SST and SL anomalies in 2013.

negative correlations within the LC system) and some oceanic regions, consistent with the overall summertime El-Niño pattern (not shown but similar to e.g., Fig.1 in Cai et al. 2013). Thus, even though the correlations indicate El-Niño provide colder temperatures, the signal is not clear.

However, *monthly* SL is also a good proxy for anomalous summertime SST (and upwelling), as shown by Fig.6.13a. The influence of Portland SL is bounded by the slope region and also significant only westward/equatorward, against the propagation of CTW, indicating a source from the north-west. Given the correlation presented is for all months, not only for summertime, the pattern is not locked to summer but a year-round feature. It's slightly magnified in summer in the upwelling regions while being weaker south of Portland (not shown). This suggests *both* CTW effects and ocean currents, given the SAC is weaker during summer. This thermosteric sea level influence has large spatial scales, particularly following the upwelling regions and the bottom cold water pathway modelled in Middleton et al. (2003) (Figures 12,13). Indeed, SL provides some skill in the estimates of the BT over the shelf in the EGAB (Middleton et al. 2007a).

Nevertheless, the relationship between SL and SST here is in relative contrast with Middleton et al. (2007a) results for the KI region. Their correlation with seasonal ($3mo$ running mean) SL was insignificant ($r < 0.25$) with their SST estimates. This appears to be related to a poor selection in the SST indices and the low resolution of their estimates — the KI region is not prone to large variability in SST as shown by Fig. 6.8. Their BC index is also poorly chosen; the estimate was done in the western flank of the plume (see their Fig.1). Here, our monthly results are able to detect significant relationships all along the EGAB, with higher correlations in the EP and BC for both winter and summer (summer is slightly higher — not shown).

Moreover, from Fig. 6.5 (low resolution AVHRR data) in the previous section, *monthly* summertime SL at Portland explains 15% of the SST variance in the BC region and slightly more for the plume region (bp). Figure 6.13a (from MUR) is consistent with the above and indicates that spatial correlation does vary — Portland can explain 35% of the plume signal during 2002-2016 (difference between summer and winter is negligible). As expected from Fig. 6.5, changing the regressors to Thevenard,Esperance or Broome provides very similar patterns as in Fig. 6.13a (not shown). Thus, the SST variability is tightly connected to SL, is bounded by the slope, has equator/westward origin and the signal is clearly hidden behind a heat flux anomaly.

Indeed, local winds and remote winds, by themselves, can explain some SL in Portland (refer back to Fig. 6.5). Their direct relationship with *monthly* SST was borderline significant, with $r \approx 0.2$ and low significance at the 95% level (see

Fig. 6.11a). This suggests alongshore wind anomalies are not a good information content to estimate SST in the EGAB, while SL being more representative. The presence of other processes appears to hide the wind-driven upwelling relationship. The wind-SST relationship is clearer when one takes into account the heat content. One way to accomplish this is to regress out the heat content proxy from the SST index at the BC, generating a coastal upwelling index based on SST (CUI_{sst}), and correlating this index with the local alongshore winds.

The relationship between this new estimate and winds is presented in Fig. 6.11(b). Clearly, the relationship is now stronger, a change to significance occurs and the coefficients had a 2-fold increase if compared with the non adjusted SST (from $13\,^{\circ}\mathrm{C\,Pa^{-1}}$ to $23\,^{\circ}\mathrm{C\,Pa^{-1}}$ – 1994-2016 AVHRR based). The same occurs using the MUR based product between 2002–2016 (not shown). Another way of achieving the same effect would be to obtained the CUI_{sst} index as the residual of a multilinear regression with winds and heat content. Thus, local winds are important, but the surface heating hides this relationship. Furthermore, this local wind effect is included when using SL — local winds did not provide extra information when it is one of the regressors along with SL (not shown). The reason why is that monthly SL contains information about the net wind impulse signal among other effects, while not being sensitive to surface heating in summer — the surface mixed layer is a very thin layer within the upper ocean thermal mass.

The results above also indirectly confirm that SAM effects are driving some of the upwelling in the EGAB through local winds. To directly confirm this, we use the SAM index against the CUI_{sst} above, and within the summertime and strong positive SAM group (as in Fig. 6.6). Not surprisingly, explained variances are high, significant and with coefficient $\kappa_{+sam} = -0.36°C$ — see Fig. 6.12a. Regressing positive SAM values against local winds at Portland (Fig. 6.12b) results in an insignificant coefficient, but still providing the same overall picture (other signals appear to affect the relationship). In conclusion, the independent CCMP analysis (Fig. 6.6) and the results above confirm that SAM is regulating the alongshore winds.

Therefore, the new result here is that we were able to detect relationships using monthly estimates of SL and SST, we showed explicitly how the Portland SL is useful in the BC SST estimates and that the SAM is affecting the local and remote (western GAB) winds.

This conclusion is even more clear in Figure 6.13b, which show that the autocorrelation between the SST anomalies at the BC is high within the EGAB. This fact also attests to the usability of the SST index as a proxy for the EGAB SST variability and to the usefulness of SL — their spatial correlations are very similar. The Autocorrelation function (ACF) is clearly bounded offshore by the

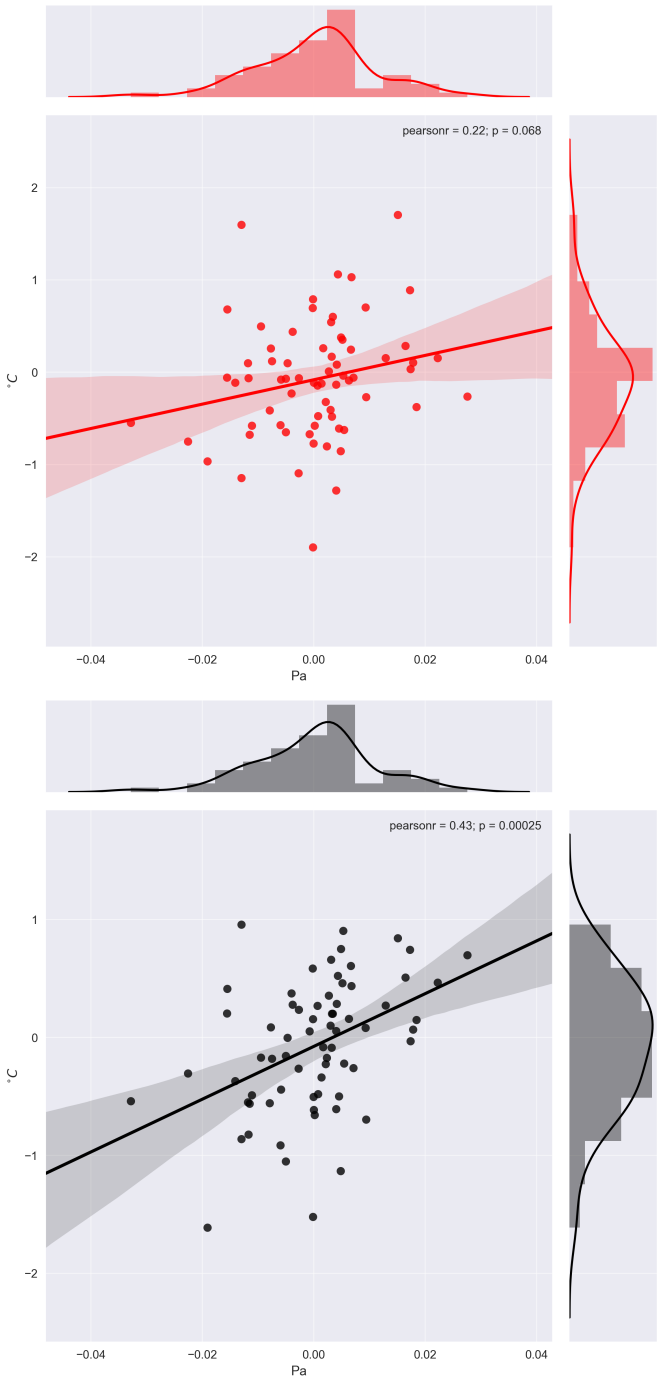

Figure 6.11: (a) The relationship between the summertime alongshore wind stress anomalies at Portland (x-axis) and the SST anomalies along the BC (y-axis). (b) Same as (a) but for the adjusted SST (CUI_{sst}). Both estimates are for JFM between 1994-2016 (AVHRR based). r and $p-values$ are based on the total number of observations (non significant cross correlations, and the shading area represent the 95% confidence interval.

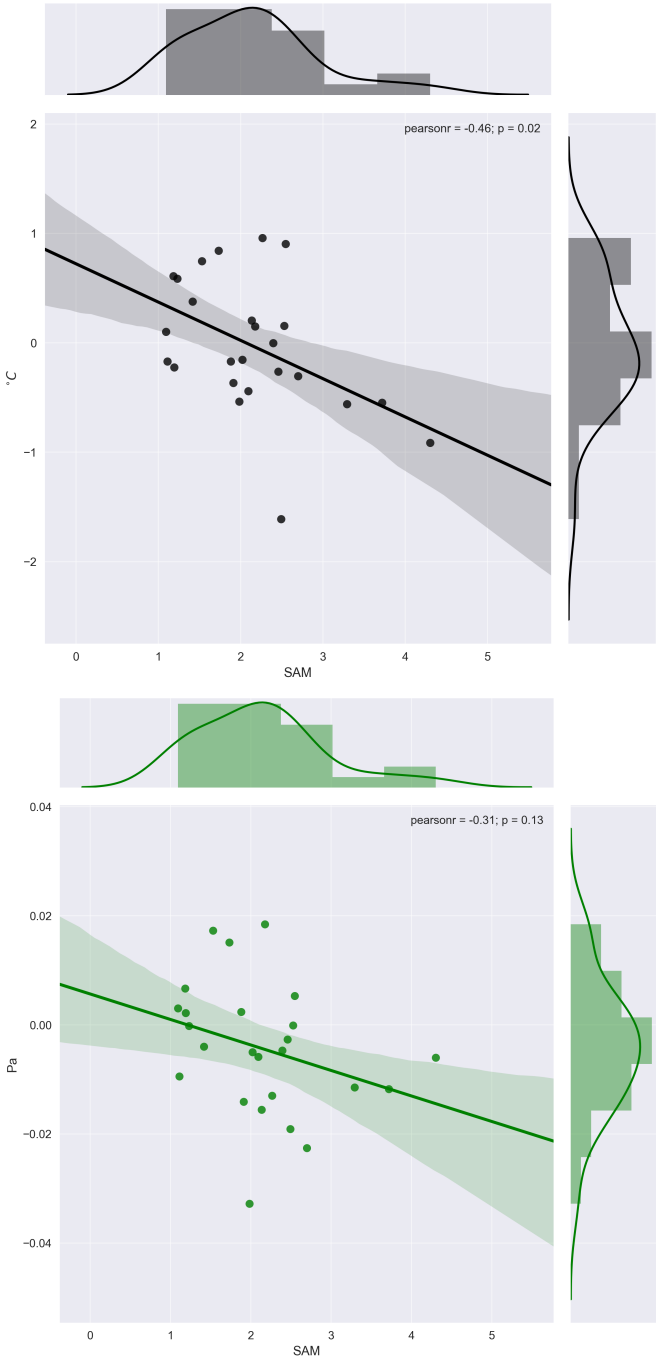

Figure 6.12: Similar to Fig. 6.11, but with the relationship between positive SAM during summer (x-axis) and the adjusted SST (CUI_{sst}). (b) same as (a) but between alongshore wind stress anomalies at Portland. Estimates are from JFM between 1994-2016 (AVHRR based) but with only months where SAM was positive.

shelf and onshore by the Gulfs, with some significant extension beyond the shelf break but still with maxima within the shelf. Again, this is a yearly pattern, and to the north (south) of Portland, over the shelf and slope, the correlation is increased (decreased) in summer. This is both consistent with the frictional decay of CTWs over the shelf and with the reduced extension of the SAC in summer. Over the shelf, CTWs can drive substantial currents and isotherm depth variability, particularly within the BC (see Chapter 5). Thus, the anisotropy in spread of the ACF north and south of the BC indicates a dynamical boundary for SST over the shelf.

6.3.2.2 The ENSO timing in the EGAB: persistence and detection

With general frequencies between $\frac{2\pi}{2yr}$ and $\frac{2\pi}{4yr}$, the general ENSO effects would persist for several seasons, and resonate in several different ways in the ocean and atmosphere along the Australian region (Feng et al. 2013; Kataoka et al. 2014; Middleton et al. 2007a). The EGAB extreme upwelling and preconditioning by ENSO (Li et al. 2004; Middleton et al. 2007a), is a type of resonance with the ENSO signal; after an idealised mode-1 internal Kelvin wave passed, deeper isotherms are displaced upwards, allowing favourable winds to permit a more efficient upwelling and negative SST anomalies to develop.

However, the ocean margins are not a vertical coastal wall, not void of friction or background flow. The signal suffers scattering to Rossby waves in tropical Australia and damping because of the shelf and slope (Clarke 1991; Li et al. 2004) as well as interactions with the LC (Clarke et al. 2004; Feng et al. 2013) and within the southern shelves (Middleton et al. 2007a). The timing of such interactions along the coastline is usually defined in a very wide frequency band — the same as the ENSO frequencies. The natural variability, the El-Niño/La-Niña asymmetry and other interactions also create uncertainty in the canonical expectation of ENSO events based on the simple correlation between ENSO and SL at zero lag (e.g. El-Niño – strong upwelling). For example, persistent colder waters are reported in some consecutive years after the onset of El-Niño (see e.g., section 3b in Middleton et al. 2007a).

To analyse if it is possible to achieve a better estimate of these persistent and resonant effects, a lagged regression analysis between the *monthly* BC SST index and ONI was performed. Given the interest in the upwelling timing, and that SST correlation with ENSO is close to zero, any increase in the cross-correlation function with SST could indicate secondary oscillations after the onset of ENSO conditions. This is presented in Figure 6.14a, for several lead-lag times, for both yearly (all months) and summer periods. Two high power peaks, close to $15mo$ and $40mo$, are found, although with significant changes in the time window selected.

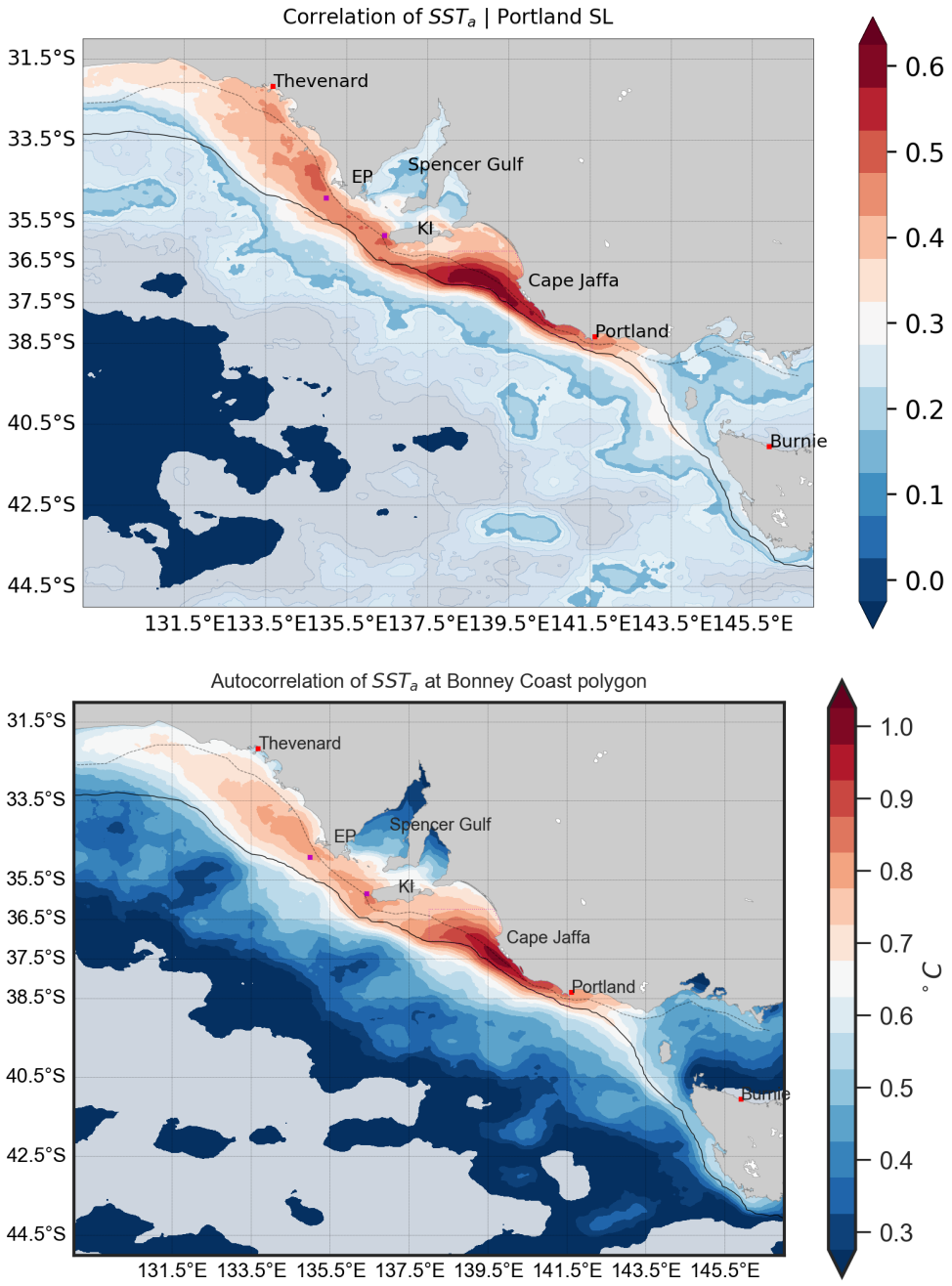

Figure 6.13: (a) Correlation between monthly SST and Portland SL at zero lag. (b) as in (a) but for the autocorrelation with the SST_a at BC.

Particularly during summertime and within the last two decades (yellow dashed lines), the detection of these effects is clearer. These lagged effects are within the ENSO timescales, have more coherence than ONI at zero lag and thus indicate a delayed effect in SST. Thus, the $15mo$ ($40mo$) effect appears a secondary (tertiary) timescale for stronger variability in SST related to ENSO in the BC. By the spatial autocorrelation function of the SST index, we can easily generalise that for the EGAB. A significance of 0.06 can serve as a soft limit bound for the summer grouping in the 1994–2016 period. A more strict bound value ,e.g. 0.13, would be adequate if considering each summertime year as an independent measurement. Nonetheless, within both limits, the peaks hold statistical significance.

Therefore, after $15mo$ and $40mo$ of an eastern Pacific SST oscillation, a coherent signal in SST appears to occur within the BC. To evaluate how well these effects are important in SST, we first evaluate their correspondence with SL and other stations along the eastern margins of Australia. Also, using the peaks of these two distinct lags in a 2-variable multilinear model:

$$\hat{y} = b + \alpha_{15} ONI_{15} + \alpha_{40} ONI_{40} \tag{6.6}$$

could indicate if they are independent in representing SST effects.

The linear model above is statistically significant and the regressors provide an additive variance for SST along the BC. When regressed independently against SST for summer, these regressors explain about the same amount of variance, 15%, while together they can explain 25% (AVHRR, 1994–2016). Additionally, the first lag (ONI_{15}) is anti-correlated with SST, while the longer period lag (ONI_{40}) possess a positive correlation. Using a three variables linear model $ONI_{0,15,40}$ against SST at the BC also indicates that these effects on SST are separated in time from the ENSO effects; the ONI_0 coefficient is still insignificant. Hence, these effects have opposite polarisation, present considerable information together and are separated from the onset of ENSO. The linear model (eq. 6.6) is also only significant in summer and autumn, suggesting a seasonal locking mechanism in SST along the EGAB. In that sense, these effects seem plausible if one takes into account the ENSO general characteristics; long timescales, propagation along the coastline, different timings of the El-Niño/La-Niña and the general strong (weak) amplitude and faster (slower) setup (decay) of El-Niño (La-Niña) (Jin 1997; Im et al. 2015). The existence of two different lags in the series appears to be related to this asymmetric nature of the ENSO periodicities.

In the context of previous results, the influence of the stronger La-Niña on the BC in 2013, presented in Figure 6.10c (last section), is consistent with lagged effects. The La-Niña developed in winter of 2010 appears to impact the 2013 warm

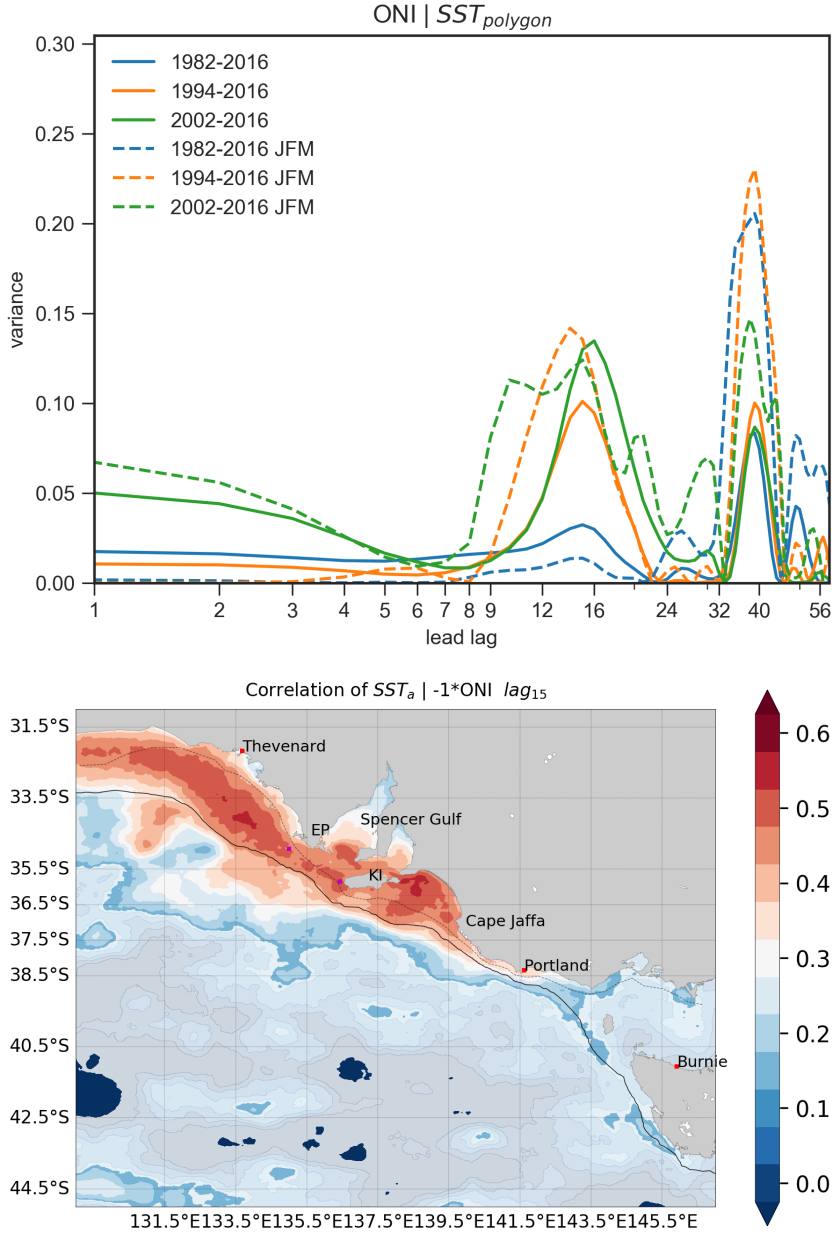

Figure 6.14: (a) The univariate signature of lagged ONI into the SST anomalies off the BC region (*polygon* index) for several lead lags (months). Dashed (solid) lines denote summertime only (year-round). The blue lines are the AVHRR extended index (1982–2016), the AVHRR during the same period as the modern TG data (1994–2016) and the MUR product (2002–2016) in the recent decade.(b) Correlation pattern in space with the **negative** of the ONI index in the EGAB. Opaque values are within the 95% significance level.

conditions — within the $32 - 42mo$ lag. Moreover, the same La-Niña conditions forced an unprecedented warming of the LC system during summer of 2011 (Feng et al. 2013). At the same time (summer of 2011), in the EGAB, SL had slightly higher values, slightly favourable wind stresses in the northern EGAB (see boxplots in Fig. 6.3) and some anomalous upwelling at the BC (see Fig. 6.9a). Over the 2011 winter, with a warmer LC over the western region, the southern shelves would then be affected throughout 2012-2013, and developed an extreme warm SST during summer of 2013 (see also the heat content proxy in Fig. 6.9). This lag appears to provide a simple explanation for this out-of-phase effect along the coastline, while the conditions at the same date in the central Pacific were nearly normal (2013 — see Fig. 6.3).

Moreover, based on the above, a speculation is possible regarding interactions along the coastline. The Ningaloo Niño event in WA is locked to the summer season, coherent with La-Niña conditions (increased SST anomalies) and influenced by local and remote atmospheric mass redistribution (Feng et al. 2013; Doi et al. 2013). It was also possible to predict two seasons ahead, given the strong relationship with La-Niña conditions (Doi et al. 2013). The above results raise a possibility that the Ningaloo Niño which developed in 2011 could have impacted the EGAB two years later. Animations of SST during summer for the WA region support long and sustained SST anomalies from one summer to the next that 'leak' towards the EGAB (not shown). Although this would require a different analysis that is out of scope here, these occurrences suggest interactions along the coastline.

The $15mo$ lag also helps explain what occurred in 2016. The onset of El-Niño ($ONI > 0.5°C$) occurred late in 2014, with strong upwelling occurring through the summer (JFM 2015), but with the most extreme signal one year later in 2016 (within the bounds of the $15mo$ peak lag). The same idea can be followed in other El-Niño years, like 1998-1999 and 2002–2003. Middleton et al. (2007a) suggested that previous ENSO conditions can influence the following summers. Their suggestion was drawn based on sequential findings of lower BT in the EGAB after El-Niño events (the peaks in NINO3.4). Despite some variation would exist, given both natural and ENSO asymmetry (e.g. stronger or weaker local winds), the $15mo$ lag appears to fit with that suggestion. Thus, if these effects are indeed the same one raised by Middleton et al. (2007a), then it needs to be consistent across SL and BT estimates. More evidence for this particular lag effect is presented below and in the BT section.

The correlation map of SST anomalies with the negative of ONI_{15} is presented in Figure 6.14b, and is very similar to the correlation with SL (Fig 6.13b), i.e., source is again attached to the shelf and slope, and origin si from the west of the EGAB (decreasing correlation poleward). Significance is attained at the shelf, but

with slightly larger cross-shore scales if compared to SL-SST effects presented in Fig. 6.13a. This suggests a broader influence on the slope. Thus, the effect appears from a remote origin off the EGAB, is within the SL and with the same signal as the canonical ENSO effect at zero lag. Hence, so far, with the same spatial relationship and polarisation, we could suggest this $15mo$ lag effect as a longer persistent effect, generated by the propagation pattern of the ENSO signal along the coastline.

In this context, Ridgway (2007b) also found a similar behaviour in the ENSO–SST relationship for the Maria Island region off the east coast of Tasmania. He attributed the origin of a positive sign correlation ($r = 0.17$) with a $9mo$ lag between ENSO and local SST to the SL–ENSO propagation along the southern shelves. Our results, on the other hand, indicate correlations within the EGAB that are later than that, negative (positive) with ENSO (SL) at similar lags, holding higher power and, as such, not consistent with his results. It appears that the only way to reconcile this information is that other processes shift this phase relationship or the correlation there is from another source.

As expected from the results above, using the $15mo$ lag effect to estimate the Portland summertime SL also provides significant power. For Portland, this effect alone represents close to 10% of the variance, and consistently, regressing this effect together with ONI_0 also provides additive variance (a 9% increase from the 15% with only ONI_0 – monthly values). Moreover, when inspecting the lagged regressions of SL at Portland and SST at BC during *summer* (not shown), the function peaks at $10mo$. An earlier shift in SL in relation to SST indicates that the $15mo$ lag effect is propagating from the tropics, through SL and affecting SST. This is also consistent with autumn to winter conditions in SL affecting the following summertime SSTs. Thus, we can now suggest that, despite being a long persistence effect of ENSO conditions, on average, $15mo$ after the onset of ENSO peaks, isotherm depths will peak during summer in the EGAB. Moreover, by the scale and timing, this would also have a clear effect on ocean current variability (see next section). This again appears to hold for 2016 — the onset of strong negative SL trends related to ENSO occurred at the BC in late 2014 (see Fig. 6.7b).

To further confirm the propagation nature of this effect, we perform the same lag analysis, using lead-lag SL stations west of the EGAB against the SST index of the BC — Figure 6.15. Again, the results indicate that peaks with lead-lag SL series occur to the left (red/green/purple), earlier than the ONI_{15} (blue). This confirms the propagation and clearly put the signal as an oscillation in the thermocline. This also suggests that a more complete setup of the thermocline is achieved later than the onset (ENSO at zero lag), as well as the peak in response on the ocean currents. Also, this secondary ENSO oscillation effect in SST could

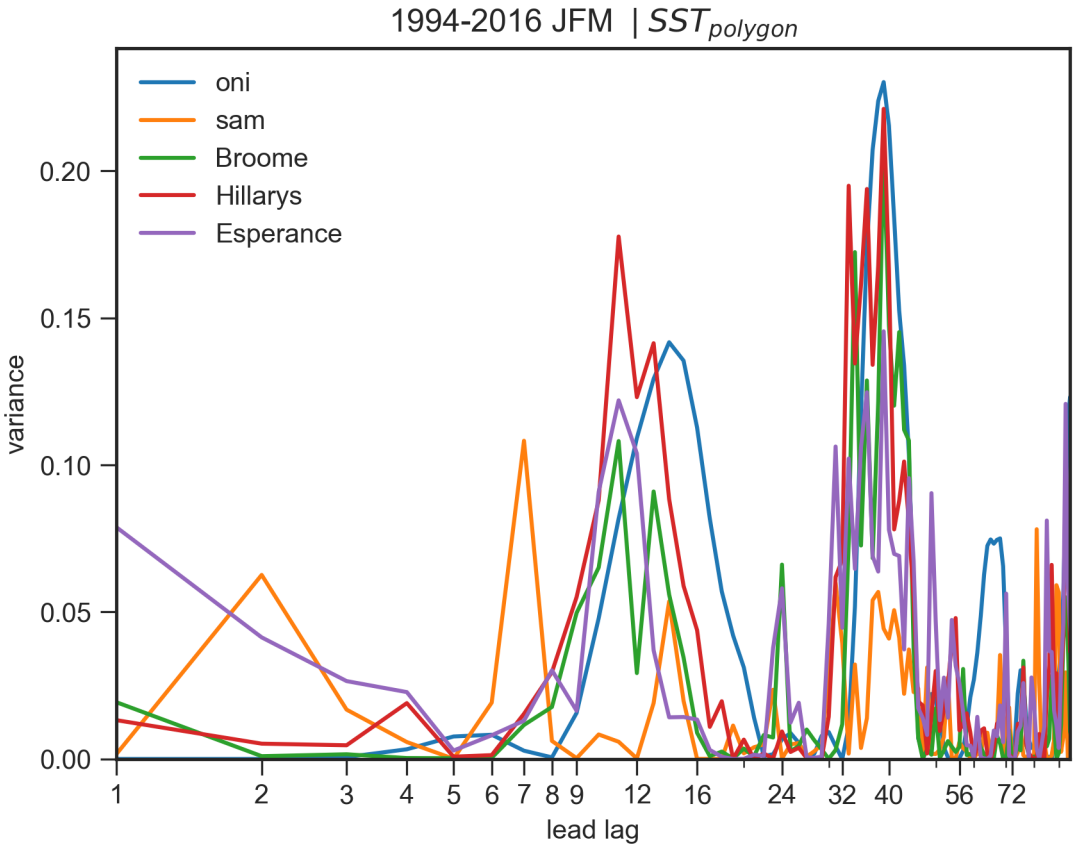

Figure 6.15: As in Fig. 6.14a but using TG SL stations and the SAM index against SST at the BC region

be loosely represented as a mode-2 internal Kelvin wave with much slower speeds than the first mode (i.e., ENSO at zero lag), since the arrival time is after the maximum in the correlations.

Moreover, lagged regressions between SL along the southern shelves using the model eq. 6.6, indicate Esperance at the best tide gauge for this effects; the variance explained with ONI_0 and ONI_{15} is 45% for this station. The fact that this is most detectable (and separable) in SL at the southern shelves corroborates the idea of this being an effect within the internal Kelvin wave envelope that propagates along the coast. This strongly suggests that effects over the LC-SAC current system would be stronger.

To complete the story, the peak of ONI_{40} also follows the same overall behaviour of ONI_{15} (see Fig. 6.15). The detection is even clearer than the $15mo$ effect in SST, peaks also slightly moved to the left (poleward propagation), but detection within SL was not so successful (not shown). Even at different lags ONI ($15 < l < 80mo$), peaks were not significant at Esperance SL for example, and using this lag to estimate SL variances was largely unfruitful. Thus, the lag is propagating in nature within SST, not detectable in SL, but SL still provides the same information as

ONI_{40} (still peak with SST). This suggests a more complicated pattern, with a possible connection to the atmosphere, but also a signal that could be out of phase with SL but still associated with the propagation along the coast (the series can be in quadrature). Also, the significance of this pattern in SST is only in summer, which suggests stronger interaction with the atmosphere. Given that the frequency spectrum of ENSO is complicated (non-linear), data is monthly and the interactions can change and lag in response, this separation in SST and SL is harder to infer just by this time series relationships.

Finally, large-scale pattern maps of pixel correlations of ONI_{15} and ONI_{40} with SST are presented in Figure 6.16a,b and highlight this hypothesis. For the ONI_{15}, the map is very similar to the one presented in Fig. 6.14b — the signal is locked to the shelf-slope. The result, however, indicates that the signal is continuous until Esperance, i.e. is not in phase along the entire coastline. This fact just proves the propagation pattern, the lagged response along the shelf and the effect in SST over the EGAB (correlations in Fig. 6.16a are significant in more than 30 years of summertime data). The propagation pattern is clear when regressing with other lags; for example, with ONI_9, the pattern is in the western GAB, while ONI_6 the maxima in SST correlations are close to Hillarys (not shown).

The same limit to the west occurs with the ONI_{40} in Fig. 6.16b, but with larger scales. Reversed responses and much broader scales pertain, significantly affecting the shelf-break and oceanic regions. At the same time, the pattern is larger in scale, it's also more correlated close to the shelf and slope — the effect appears a mix of *both* shelf-slope influence *and* atmospheric teleconnection. The previous lag maps also confirm the propagation nature and broader scales (not shown). Similar results (not shown) were also found in the spatial pattern for SL (with BRAN); negative correlations and high significance in the EGAB for the $15mo$ lag, and positive but insignificant correlations for the $40mo$ one (not shown).

Thus, throughout the above analysis, we can confirm the lagged effects are physical, with an ENSO origin, propagating in nature and that they provide independent information from the canonical ENSO effect estimated with zero lagged ENSO indices. The nature of the lag indicates that, on average, after $15mo$ of a positive anomaly in SST in the central Pacific, SST and SL anomalies at the southern shelves are still negative and under the El-Niño influence. Another tendency occurs after $40mo$ of the same onset of El-Niño, with warming over the southern shelves. However, in the ENSO timescales (2–$4yr$) this condition will be a single one — the mean conditions of ENSO. Clearly, in SL the onset conditions (ONI_0) would dominate the response (higher variances), but in SST, the response would not be in phase and dependent within a larger bandwidth in frequency. The effects above just highlight what are the key timings of the ENSO influence in

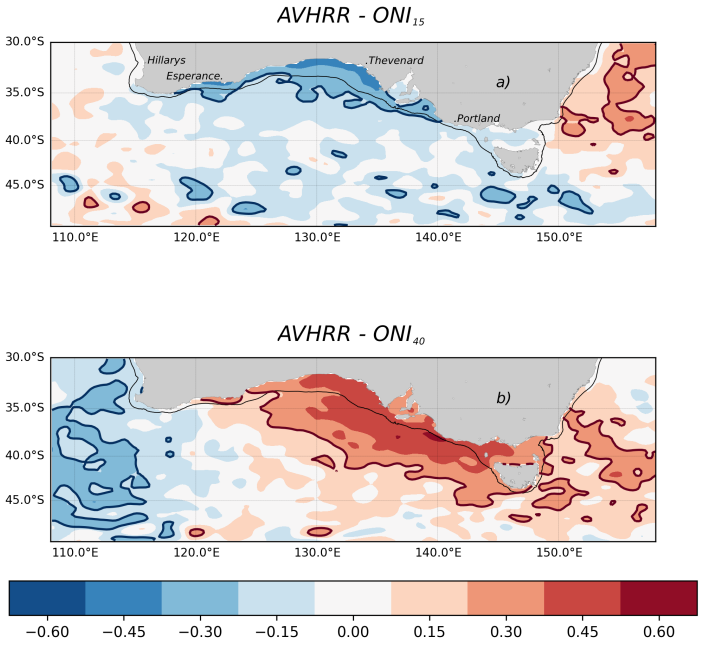

Figure 6.16: The large-scale correlation patterns of the lagged ENSO effects. (a) As in Fig. 6.13b but using the extended AVHRR anomaly time series (1982-2016) correlated with ONI_{15}. (b) As in (a) but for the ONI_{40}. Note the correlation is done with the standard value of the index (so as to mimic the response on SL). The solid contours delimit the significant values ($r = 0.21$).

SST. These relationships are also continuous, i.e. the current trends at any time can be represented as a combination of the current and previous conditions of the ENSO series.

We also found narrow peaks with lagged winds and SST in the tropical and western stations but they are statistically insignificant in the periods $1994-2016$ and/or $2002-2016$. They also did not match the same lag bounds within these periods (not shown). Some other climate indices also show significant effects; SAM index, with a peak at $7mo$ (yellow curve in fig. 6.15) and MODOKI, with peak at $15mo$ (but not independent from ONI_{15} in SST). The SAM $7mo$ peak appears consistent with the stronger winter pattern of SAM (Marshall 2003). It is no surprise that this can occurs — the SAM affects local winds. The search for all sources is beyond the scope of the study here, but it could be useful to disentangle the role of different interactions; for example, SAM also peaks at the same time as the ONI_{40}. The usefulness of these lags needs also to be confirmed in a statistical forecasting sense, e.g. under autoregressive models in different periods. The results above weakly support that these statistical models could provide some information into the future. In that sense, these results provide what are the first variables and lag ranges one should try to use in these models.

We now provide a glimpse of how useful these results are, highlighting the response of SST along the BC. Figure 6.17 presents several time series, including linear models with lagged effects and SL as regressors.

The models used are the following:

$$\widehat{\mathrm{ENSO}} = b_0 + \alpha ONI_{15} + \gamma ONI_{40} \tag{6.7a}$$

$$\widehat{ENSO_{jfm}} = b_1 + \alpha_{jfm} ONI_{15} + \gamma_{jfm} ONI_{40} \tag{6.7b}$$

$$\widehat{\mathrm{SL}} = b_2 + \xi ONI_{15} + \sigma ONI_{40} + \lambda SL_{portland} \tag{6.7c}$$

$$\widehat{SL_{jfm}} = b_3 + \xi_{jfm} ONI_{15} + \sigma_{jfm} ONI_{40} + \lambda_{jfm} SL_{portland} \tag{6.7d}$$

Where all estimates (hats) are related to *interannual* SST, and the subscript jfm is dropped (kept) for convenience in the regressor (coefficient) name. The ENSO indices are not filtered, but in eq. 6.7c,d we used interannual SL. The Interannual SST data used is the mean between the SST index from the AVHRR product and MUR, and such is limited to 2002-2016 (yellow line in Fig. 6.17). As a reference, the monthly data is in light grey, while the models above are in red ($\widehat{\mathrm{ENSO}}$), red stars ($\widehat{ENSO_{jfm}}$), blue ($\widehat{\mathrm{SL}}$) and blue stars ($\widehat{SL_{jfm}}$). Hence, we have constructed a model with yearly estimates based on lagged effects (eq. 6.7a), another with just summertime data (eq. 6.7b), and models that include local SL

variability (eq. 6.7c and 6.7d). The extension to models including winds are banal (SL carries this information), and using the lagged SAM did not provide more information in the interannual scales.

First, in Fig. 6.17, the grey lines are the monthly anomalies based on the MUR product. They reproduce the spatial results presented earlier, with 2005 having slightly positive anomalies, 2013 the strongest heatwave, while cold anomalies since winter of 2015. The estimates for 2003 also rivals with the strongest anomalies in 2016, but note that heat content anomalies were not positive at this year (see Fig. 6.9b). Despite the strong variability of the monthly data (see December/January in 2016), the interannual estimates usually fit well the time series (yellow lines and shading). The statistical significance for the interannual estimates based on the effective DOF can also be relaxed — we prove significance already in the noisier monthly series.

For 2002–2016 period, a considerable amount of information is obtained at interannual time-scales. In general, the lagged effects in summer usually fit well if one considers a categorical distribution of SST — when observations are warmer (colder) the fits are usually above (below) the zero (easily done when looking at red stars). The fits to summertime data only (stars) appear almost identical to the year-round fits (lines) — the wintertime conditions were harder to predict with lagged effects — consistent with the lack of significance for winter. The coefficients also did not provide useful information in some extreme upwelling years, particularly in 2015-2016, where the lagged model (red lines) missed completely the wintertime cold anomalies (see also 2007), but still picked up the sharp gradients associated with La-Niña conditions in 2012-2013 (although with a cold bias). The lagged model clearly misses the autumn-winter sharp cold anomalies that developed at the BC.

These errors are expected. The two lagged terms will clearly not provide all the information (‘forcing‘) to describe SST anomalies in the EGAB. For example, 2015–2016 would require another ‘forcing‘ term to reproduce the much colder and sharper drop in SST (see also 2006–2007). This is related to the local winds and other interactions. At the same time, newer term(s) in the equation would also need to correct the 2012-2013 bias — when stronger positive SST anomalies are required. Nonetheless, the results in Fig. 6.17 indicate that positive SST anomalies in the EGAB are somewhat more predictable.

The inclusion of zero lag interannual SL (blue lines) appears to provide the missing ‘forcing’. The improvement with SL in Fig. 6.17 is particularly visible both in 2015–2016 and in the La-Niña years. The biases during these years were largely reduced when including summer or yearly SL data — the differences in the seasonal grouping within the linear models also did not change the general

behaviour (stars and lines mismatch is negligible).

The inclusion of SL at zero lag, raises the variances to 65% in summer compared to 58% without SL for *interannual* estimates (all adjusted R^2). Although the increased was relatively small, it was key to represent the extreme upwelling. The use of SL alone was already enough to represent the 2016 summertime (not shown), with 25% of the interannual variance (refer back to Fig. 6.5 and Fig. 6.13a). Thus, in a sense, representing a quarter of the interannual SST variability during the 2002-2016 is already good in estimating the extreme upwelling interannual response. The reason why is clear — within the series, heating events are much stronger than cooling events.

Consistently similar increases and significant coefficients ($p < 0.05$) occurred for monthly estimates when adding SL as regressor (30% *vs* 46%), as well when using only the extended AVHRR product (23% *vs* 33%).

The high variability of the BC plume and the spatial pattern of the SST autocorrelation function permits the results above to be extrapolated to the north of Portland along the GAB. The results above also weakly suggest that positive anomalies in summertime would be easier to predict than upwelling. They also add more knowledge in the pre-conditioning of bottom waters in the EGAB, with other oceanic influences beyond ENSO at zero lag.

Hence, in the EGAB, a lingering/lagged signature of ENSO of about $15mo$ is present in both SST and SL, while an effect at $40mo$ was also found with connections to the atmosphere; these effects exists clearly within the interannual time-scales of ENSO and for the EGAB they are mostly locked to summertime. Some indication of lagged signatures for SAM also appear to exist.

The $15mo$ effect appears clearly as a persistent and propagating ENSO signal, locked to the shelf and slope, as the canonical ENSO effect in the southern shelves, but generating a peak in thermocline depth (and SST) depth later. The effect is coherent within the whole GAB, is more evident in the west and with the largest thermosteric variability of the region. By the timescale and influence in SL, this effect is clearly related to shelf-break dynamics and ocean currents. The $40mo$ effect also has a propagation pattern, but within much broader scales, clearly locked in summer to the EGAB and with an apparent stronger atmospheric/surface relationship. Given the long persistence of ENSO, the $15mo$ effect is suggested as being representative of the time-scale of the entire ENSO effects in the region and the time for a maximum influence in isotherm depth displacements.

We now explore Bottom temperatures and shelf currents from observations and reanalysis.

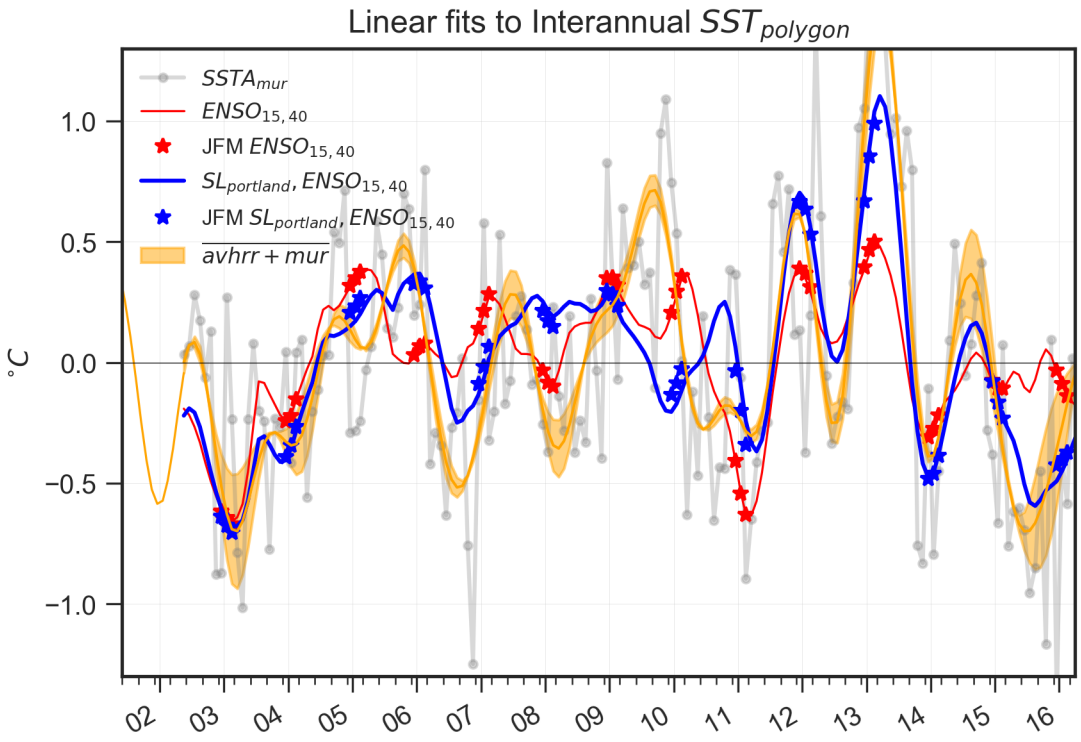

Figure 6.17: The Interannual SST upwelling Index for the Bonney Coast (orange), against the multilinear regression model with lagged ONI series (red) for all data, with summertime only (stars) and with added local interannual SL at zero lag (blue). The climate indices were not filtered. The yellow shading bound the range of interannual values between the MUR and AVHRR products within the 2002–2016 period. The multilinear fit was performed with the mean of the products (orange line).

6.3.3 ENSO influence in bottom shelf temperatures and ocean currents

Time series of bottom temperatures are rather limited in the Bonney Coast, while in the mid-GAB, west of the Kangaroo Island, two moorings at mid-shelf have being maintained since 2008 under IMOS (*NRSKAI* and *SAM5CB* - magenta squares in Figure 6.3). To estimate the thermosteric effect over the shelf, we analyse temperature measurements closest to the bottom, based on the ADCP sensor. These two locations are comparable; they lie within the $90-100m$ isobaths. We have already shown that SST variability is correlated along the shelf and we expect similar correlations should follow for BT. Moreover, at these depths, BT should provide a better partition of shelf-break processes, both by its location and by isolation from the surface; with longer time-scales. Our SL adjusted estimates are another proxy of the BT; but much more sensitive to shelf-processes and atmospheric forcing.

The seasonal cycle of BT in this region is strongly related to the cycle in SL — Figure 6.18a. As expected, the colder temperatures are found in late summer, between Feb-Mar, particularly at the KI mooring (blue lines), where a 'cold pool' is present during summertime (Middleton et al. 2003; McClatchie et al. 2006). Results here are consistent with CARS Atlas data (grey lines - see also Figure 3 in McClatchie et al. 2006), but with stronger minima in March and overall warmer waters in mid-spring, particularly for the northern mooring (CB location). The differences are attributable to the different resolution of the CARS atlas and the methods used here. Nonetheless, the cycle is similar, with the rapid heating over autumn, the late winter minimum and later spring heating in all estimates. The strong variability in BT anomalies are also locked to late summer, as in SST for the BC (magenta — right axis in Fig.6.18a). Extreme bottom uplift of isotherms is then more likely to occur within the end of summer, consistent with the SSTs in the region. The increase in variability occurs at late spring, while in winter, the bottom temperatures do not change much (about $0.5°C$).

Additionally, if one compares the seasonal cycle of BT with local seasonal SSTs (see Fig. 6.1), the vertical differences can reach up to $4°C$, or more, between surface and bottom temperatures in summer. Accounting for typical anomalies, the difference can be $7°C$ in March, and a remarkable thermosteric effect is implied with strong stratification. This is consistent with a shallow mixed layer in summer, usually less than $20m$ (see Schiller et al. 2013; de Boyer Montégut et al. 2004).

The seasonal cycle phase plot of mean barotropic currents, Figure 6.18(b,c) , is also consistent with the summer upwelling picture; they share mean upwelling favourable currents present in the first (second) quadrant, at KI (CB). The

consistency with wind, SL and BT peaks in Fig. 6.2, 6.18a is evident, with upwelling currents starting as early as November.

The shelf currents have two maximums in spring-summer conditions, with weaker currents in March compared to December/January. At KI, the currents are also strongly steered by the coastline/topography of the region (cyan vector in Fig. 6.18b), with a strong mean current offshore (south westward), close to $11cm/s$ (climatology based — $\approx 7y$ — 2008–2016). The currents at CB, however, show higher variability in direction, with a mean value close to zero ($\approx 3y$ — 2009—2016), but still heading eastward. The two clockwise motions, within the two summertime peaks, indicates that variability in direction occurs far more often in summer than in winter. This is consistent with the low-pressure systems that break through the GAB and change the wind regime as well as with the weather band CTWs (Church et al. 1987). The size of each dot in Figure 6.18(b,c) is also proportional to the standard deviations of the magnitude in the barotropic velocities (anomalies). They show the same feature as in the BT estimates — indicating that winter currents are generally more steady. So, despite the steering at KI, the phase plot of both stations is consistent within the seasons (Fig. 6.18); they show the same rapid changes from summer to autumn and late winter transitions.

The barotropic currents in the CB region ($\approx 8cm/s$), however, are double the strength of the corresponding upwelling favourable velocities in KI. This indicates that CB is a much better mooring site to monitor the shelf currents in the region; with greater variability (see also Oke et al. 2012). Indeed, the standard deviations of the major axis of barotropic velocities occur in different months; December (July) for the CB (KI). This is probably related to the low variances in KI and the Spencer Gulf Outflow that peaks at about June/July (Nunes Vaz et al. 1990). The proximity of KI to the coastline and the strong steering of the isobaths appears to be the cause for this behaviour. Because of this difference in variability, here and below we use the BT at KI as the BT index for the EGAB, while the major axis currents at CB are used as an alongshore current index for the 2015-2016 period — positive (negative) anomalies are north-westward in winter (summer).

6.3.3.1 ENSO effects in bottom temperatures

In Figure 6.19a, the $2008-2016$ bottom temperatures are highly correlated with SL and SST at the BC. BT is more coherent with SL than with SST, as expected, and also shows higher variances, whilst SST is more damped and with wider peaks. There are periods where the semi-annual BT (and SST) is slightly different from SL; such as wintertime of 2010 and 2015 and the 2011-2012 La-Niña events. So, there are events that affect the relationships of these variables for longer periods.

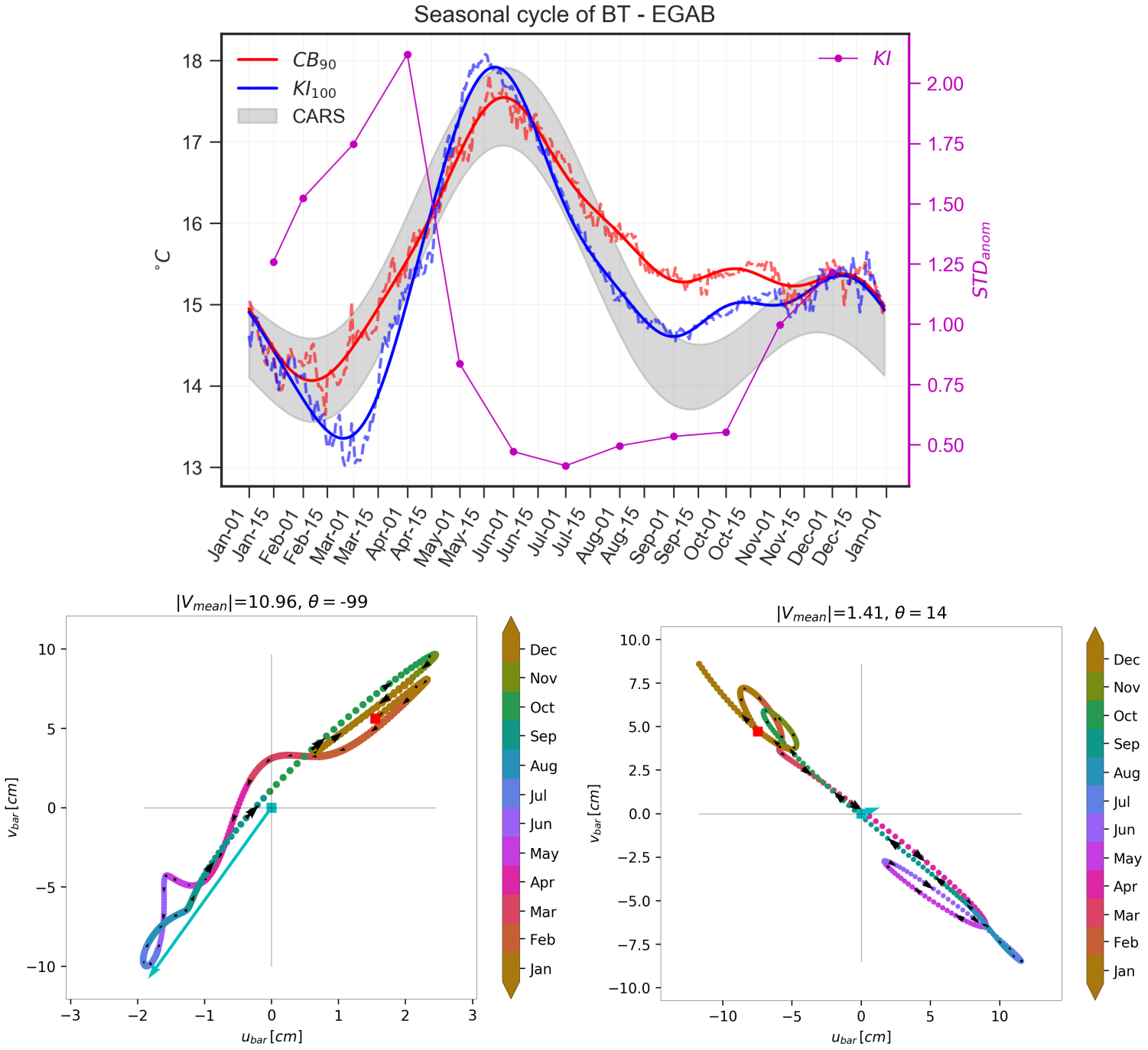

Figure 6.18: (a)The Seasonal cycle of ADCP Bottom Temperatures (solid lines) for the mid-EGAB and standard deviation of the anomalies (residuals - magenta) at Coffin Bay region (red—90m isobath—*SAM5CB*) and the western tip of the Kangaroo Island region (blue—100m isobath—*NRSKAI*). The grey shading is the range of CARS temperatures for the closest points. (b) Phase plot of the seasonal cycle for the barotropic currents at KI. (c) same as in (b) but for the CB station. The mean annual component of currents is indicated in cyan, red square indicates the start of the climatological year and the black arrow heads the phase direction. All seasonal estimates are from a daily filtered climatology as in Fig. 6.2

We now estimate and compare these SL–BT relationships with previous studies. Firstly, we define a general linear model with *monthly* data, viz:

$$\widehat{B_{temp}} = b_0 + \alpha SL_{portland} \tag{6.8}$$

and compare with the results of Middleton et al. (2007a) within all the available data and also only at summertime (as done in the previous sections). Linear regressions coefficients in this study, for *monthly* data during $2008 - 2016$, are $\alpha = 0.19 \pm 0.02°C\,cm^{-1}$ using SL at Portland as regressor (the largest correlations $r = 0.68$). For summertime only, the coefficient increases to $\alpha_{jfm} = 0.24 \pm 0.034$ ($r = 0.8$), all significant. With confidence intervals between $0.167 < \alpha_{jfm} < 0.319$, based on 22 DOF, these results are remarkably similar to Middleton et al. (2007a), who reported a coefficient of $0.22°C\,cm^{-1}$ for summer.

Apart from the coefficients here being slightly larger, indicating a stronger relationship, our results also indicate there was a stronger ENSO influence during the last decade. In Middleton et al. (2007a), the ENSO–BT relationship was not directly reported. They estimated the ENSO effect in BT by partial regression with the SL residuals (after regressing out ENSO).

Here, we directly account for ENSO effects. ONI at zero lag can explain almost 50% of the total summertime variance of BT (47% of the $1.10°C^2$). The coefficient is $\beta_{jfm} = -0.89 \pm 0.19$ (dimensionless); a relationship close to one-to-one for *monthly* estimates. This is considerably larger, more significant, and practical than previous findings. Verification of the previous coefficients is straightforward. For 2015-2016 for example, the ONI index indicates a maximum peak of $2.5°C$, and using the linear model, a BT drop of about $2.22°C$. This is in agreement with the semi-annual values shown in Fig. 6.19a. Results for the BT at CB were even higher (66% of the smaller total variance – $0.73°C^2$), but the time series are shorter and with more gaps. Additionally, the time series of BT considered here are slightly longer than in Middleton et al. (2007a), and with a larger population variance (about 45% more). Given the much larger coefficients in the presence of more variability, we conclude that previous estimates of the ENSO effect in BT for the region were underestimated, or the covariance has increased in the last decade. So, the source of the ENSO signal is within the shelf-break, given the largest coherence so far in the EGAB, and consistent with previous studies (Li et al. 2004; Clarke et al. 2004; Middleton et al. 2007a).

For winter months only, the variance explained between ONI and BT is less but still significant — 18% of the monthly data and with roughly 25% of the summer coefficients ($\delta_{jja} = -0.2591 \pm 0.11$). Taking this into account, it is clear that the linear coefficients are season dependent as is the response of BT to ENSO. This

is not surprising, given the ocean circulation in the region. During wintertime, the increase in vertical mixing, deeper mixed layers, and downwelling conditions shift the SL and shelf BT relationship, making it harder to detect ENSO over the shelf. Such conditions increase the coefficient. During summer, when the deep convection (mixed layer) reduces, strong stratification and the isotherms are raised, the relationship is stronger and clear, with decreased coefficients. The local seasonal cycle and incoherent anomalies with ENSO in this season act to hide the ENSO signal in winter from the shelf (less coherence), but allow it to appear clearly in summer (more coherence). Note that even with this seasonality in anomalies included, the ENSO signal is still detectable in the whole time series with linear regression (it is significant — 15% of the variance). In other words, this remarkable signal is obscured in the shelf BT during wintertime.

It is important to note that, because we matched the data to the BT observational window, our coefficients between ENSO and SL are generally greater than previous results based on $1994-2016$. Nonetheless, it is also interesting to show that the lagged effects found in SL and SST are also significant within BT. Using the ONI_{15} lagged effect *alone*, 18% of the variance could be represented ($\gamma_{ONI_{15}{}_{jfm}} = -0.66 \pm 0.26$ — dimensionless). Together with the ONI_0, the increase was small; towards 55% and statistically significant. The $40mo$ lag was not significant. Note that given the shorter series, we shift the ONI index in the longer time series first to avoid periodic effects. At the same time, BT is also positively correlated with SST, with 44% of variance (see Fig. 6.19a). Obviously, this is the best predictor of SST.

Our results confirm that El-Niño effects over the shelf are clearly evident in bottom temperatures, via positive isotherm displacements, reaching SST at zero lag and at $15mo$ lag. The presence of the lagged effects in BT also localises this effect along the shelf-break regions. Given this BT variability and coherence, as well as in other independent variables, we attribute that ENSO has a much larger significance than previously thought.

Given the above relationship, the results appear valid for the EGAB shelf-break region as a whole, even though our results here are based on a single mooring along the mid-shelf. The waveguide nature of the coast also supports this finding. Additionally, the results above indicate that autumn–winter and spring–summer transitions in BT are important, given that it is when the anomalies are damped and amplified, respectively. These standard deviations also help to explain why the ONI_{15} effect operates at this particular lag; it is within the bounds of the strongest BT anomalies of the previous year. This can be easily seen in Fig. 6.19a, where the trends of the previous year anomalies at the end of summer are in phase with the trend of the next year summer.

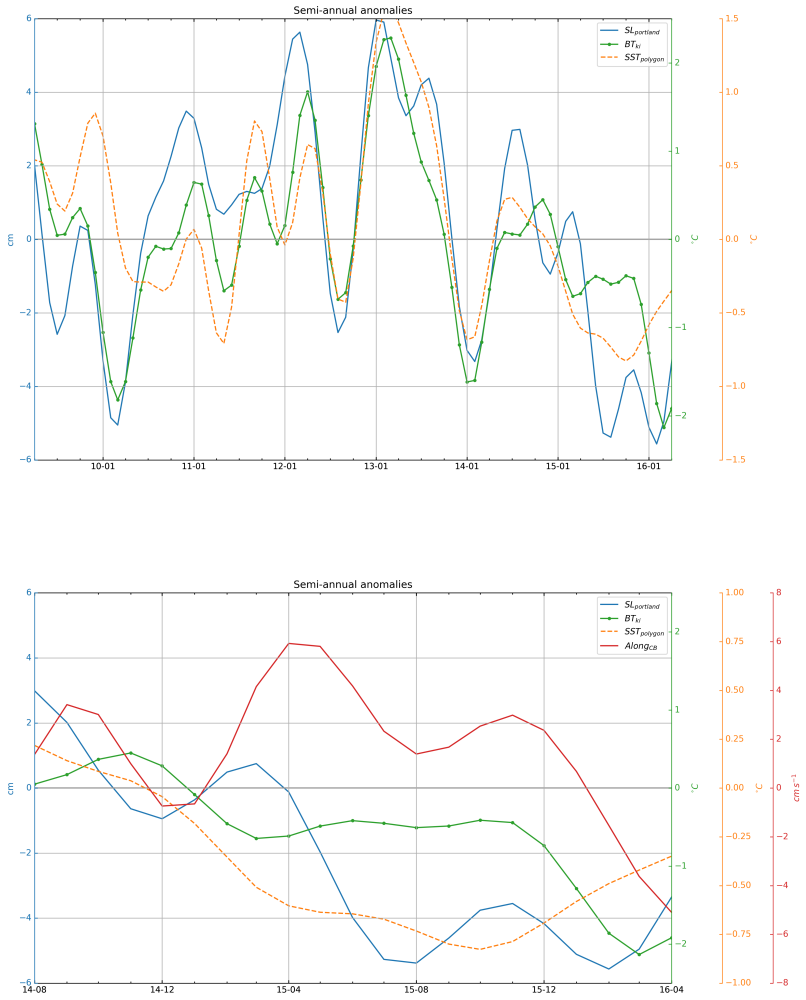

Figure 6.19: (a) Semi-annual anomalies of SL (blue), BT (green) and SST (yellow) in the EGAB. (b) as in (a) but with alongshore current (red) within the 2014-2016 period — semi-annual is the monthly data filtered with a $6mo$ cut-off frequency.

A more detailed picture of the $2015-2016$ period, together with the shelf major axis current anomalies, is presented in Figure 6.19b. First, during this period, the SL (blue) declined quickly from April to July, reaching extreme low values ($< 10pth$) and staying in the $-5cm$ range until the end of summer 2016. The SST response (yellow), also reached the lowest percentiles ($< 20pth$) at about the same time but decaying earlier (from autumn). The same occurred with BT (green), but the reduction in winter did not vary much from normal years. Note that, despite the different axis scales, BT and SST anomalies reach about the same value in winter ($-0.5°C$) with SST larger by a small margin. This correspondence between BT at the mid-GAB and SST at the BC, is again expected given the strong mixing and downwelling conditions of winter (Cresswell et al. 1993; Middleton et al. 2002).

Autumn-winter negative anomalies in SST can be indicative of a stronger heat loss to the atmosphere and/or a stronger mixed layer depth. A consistent positive anomaly in net heat flux ($20 W m^{-2}$) was found in the GAB throughout the year in the ECMWF dataset as well as anomalous high mean sea level pressures, particularly in winter. The net heat flux anomalies were widespread, following from tropical Australia, within the GAB, and along the Indian Ocean in the $48 - 52°S$ latitudinal band, while the MSLP signal was particularly strong in the STF region (not shown). Hence, the earlier drop in SST in winter had an atmospheric component generating colder than average surface waters.

The shelf current anomalies are positive during winter, indicating a weaker southward flow over the shelf (red line in Fig. 6.19b). The peaks are clearly associated with the SL, with maximum in April, and turning quickly to the strong negative anomalies during summertime. Although the reduction in summer is slightly exaggerated, given that monthly data peaked at April (about $18 cms^{-1}$), the shift in the major axis of the current is consistent with the monthly data during summer (a small positive anomaly occurred in Feb to Mar transition - not shown).

This positive/negative pattern in winter/summer is consistent with the wind and SL anomalies previously presented (see Fig. 6.3 wind panels and Fig. 6.17). Lower SL year-round, weaker southward currents in winter and stronger northward summer currents suggest that the SAC was weakened and shelf currents were more upwelling favourable during 2015—2016. The coherence of the alongshore shelf currents in the EGAB and BT after December is also very clear, with BT following up while SST at the BC were slightly shifted upwards during summer (heating).

6.3.3.2 Ocean currents at the Bonney Coast

Even though the shelf currents are indicative of the behaviour in the inner-shelf, they do not provide a complete picture of the oceanic circulation at the shelf break. To better understand what happened during the season along at the slope, we use results from BRAN along a zonal transect centred at $37.25°S$, south of Cape Jaffa, where the $200m$ isobath is almost zonal (Fig. 6.20). As with the shelf currents, we estimate the seasonal cycle (removing only a simple monthly climatology) and anomalies for each element and rotate the currents along the major axis of variability based on this climatological cycle. Overall, the mean axis of the currents was found to be south-eastward, with a strong eastward component (azimuth between 95° and 110°), given the shelf-break orientation at this location. The shelf flow had more influence from the meridional component and was slightly stronger and veered to the south (123° on average), while deeper flows followed the eastward direction (not shown).

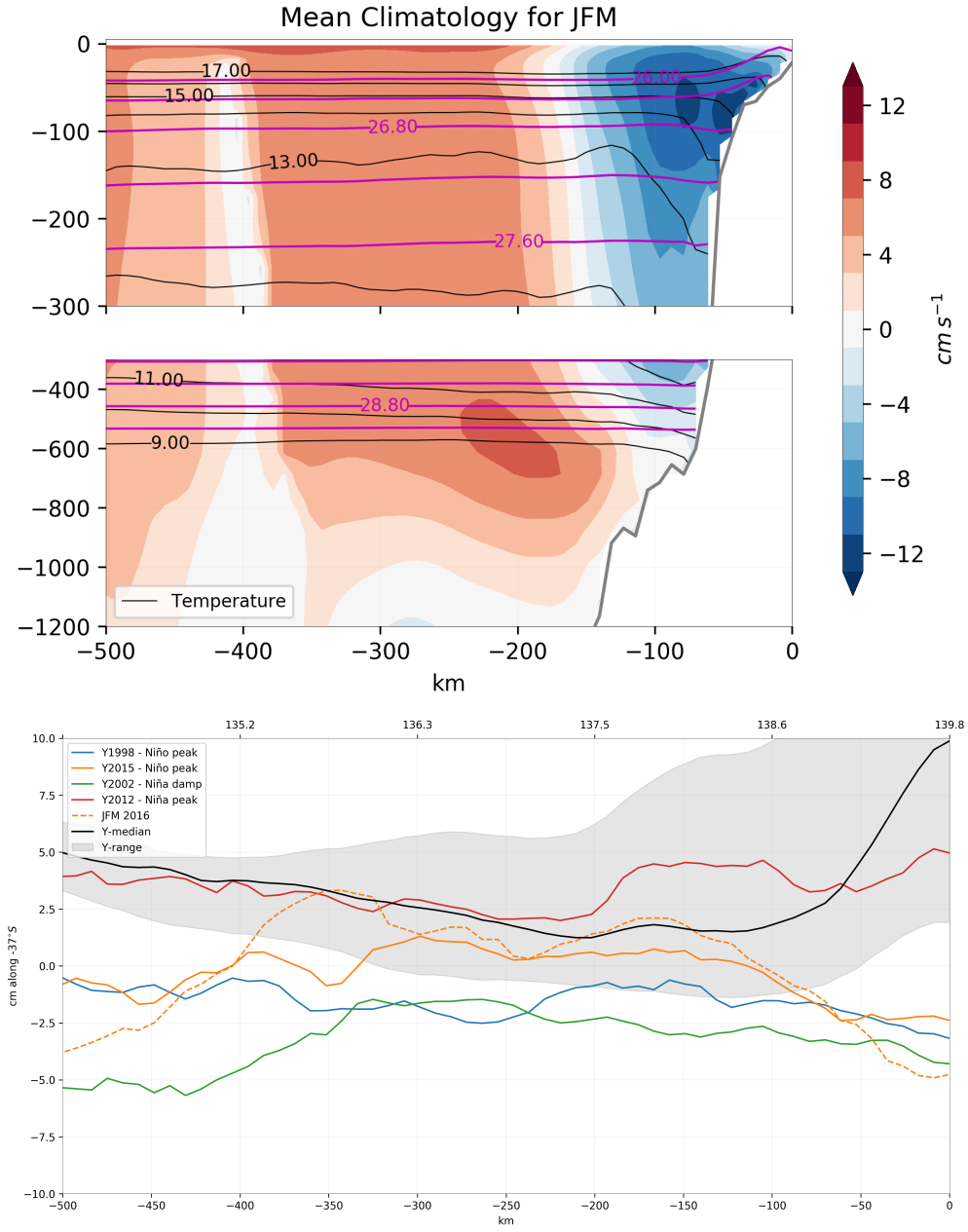

Figure 6.20: (a) The mean circulation in the BRAN reanalysis along the $37°S$ off the Bonney Coast for summertime (JFM). Shading (contours) are the major axis of the current (temperature). The magenta lines are the in-situ density anomalies (isopycnals) within interval of $0.4kgm^{-3}$, between 26 and 29.2. (b) The seasonal cycle in SL and selected anomalies in key ENSO events from the same zonal transect.

.

The mean climatology of temperature and the current major axis for summer (JFM) is presented in Fig. 6.20a. A clear south-eastward flow is found centred at $50m$ and about $100km$ away from the coast, with speeds of up to $10cm/s$ (south-eastward). The flow is a downwelling current, reaches $400m$ depth or so, and with an arm attached to the bottom over the shelf. The mean (seasonal) thermocline depth during this season is between 13–14$^\circ C$, with a clear sharp gradient at $100km$. Note that the core of the flow is localised above it, at the $\sigma_{26.4}$ isopycnal and speed exceeding $12cm/s$. Despite the overall downwelling conditions from $120km$ onshore, upwelling conditions prevail over the upper $50m$ in the shelf region, with a weakened southward flow and upwelling limited below the $\sigma_{26.4}/15.5^\circ C$ isopycnal/isotherm. The cross-shore extension of upwelling is also limited to about $90km$ off the coast, while above, a well-mixed layer is sustained (values less than σ_{26}). Also, the surface temperature distribution appears consistent with the mean SST presented earlier; note that the $\approx 17^\circ C$ mean value over the shelf is close to the estimates in Fig. 6.1. Finally, a wide north-westward flow is found offshore ($> 180km$ from the coast), with a deep core at $600m$, and speeds at about $8cm/s$. Offshore at about $400km$, this current variability is small and the major axis phase angle changes.

Given these mean characteristics, we will refer to this wide jet and with a deeper core as the Flinders Current (FC); The FC is at the expected location ($600 - 800m$ depth and $250 - 300km$ from the coast) and flows to the north-west (Middleton et al. 2002; Cirano et al. 2004; Middleton et al. 2007b; Schiller et al. 2008). The upper southward jet can be referred to as the SAC or as the Coastal Current of Cirano et al. (2004). It has a surface core with maxima at the shelf-break but still very close to the shelf. The mean summer conditions in BRAN suggest that the SAC is present year-round. While the picture above is a summertime mean picture, inspection of the yearly means did not change the picture much, with the core changing its size, increase of the magnitude of the flow while weakening the deep and offshore north-westward flow (not shown). Hence, the SAC is weaker during summertime.

The mean SL cycle and the anomalies along this transect are also presented in Fig. 6.20b. Note that here, we choose shifted yearly anomalies, centred at October, with the year in question starting in April — so as to include the summer upwelling season of the year ahead. Thus, by being centred at spring, the 2015 mean anomaly includes the 2016 upwelling season. The mean SL (black line) supports a southward current as seen above. The variability is stronger until about $200km$ from the coast, bounded by the shelf-break current while reducing towards the deeper ocean. As a reference, several yearly anomalies (centred in October) are indicated in colours (JFM of 2016 in dashed yellow lines). During La-Niña peaks (red) an overall positive mean SL in the region is present, particularly along the

shelf-break (60-200km). This value is still within the climatological bounds, even though this is a strong La-Niña year. El-Niño years, on the other hand, are clearly *out* of the climatological range, with strong negative SL anomalies over the whole region. Overall there are mean shifts of $2cm$ or more along this $37°S$ transect (1998 and 2002). In 2002, where an El-Niño developed followed by long La-Niña conditions, the region had a very strong mean drop of SL, with a minimum on the oceanic side of about $-5cm$. This year (2002) had the same pattern as in 2015/16; El-Niño and SL peaked during wintertime. At the end of 2002, summertime of 2003, low SL, and strong wind anomalies also occurred (see Fig. 6.3).

This picture was different from 1998/99, where the oceanic regions did not show this strong negative SL, while at the coastal ocean, divergence was still dominant. Apart from these differences in the open ocean, both curves show an accentuated decrease in SL towards the shelf, with the maximum gradient at about 75km off the coast. The 2015/16 results show a sharp gradient towards the coast, particularly in summer, where the SL anomalies presented in Fig. 6.3 are reached at the coast. The cross-shore gradients of the mean 2015/16 (yellow solid lines) were much higher than the other events ($0.2\,mm\,km^{-1}$ at $150km$–from the coast). At summertime it was indeed highest, clearly providing a favourable background state that enabled the extreme events to occur (dashed yellow lines).

So, these cross-shore gradients in SL lead us to two new conclusions and 2 verifications:

1. That a much larger scale process appears to be present in tandem with ENSO events, particularly in the deep ocean

2. That summertime of 2016 was indeed an extreme year, from the oceanic regions to the coastal ocean.

3. That El-Niño effects are evident in SL at the shelf-break also at the BC

4. El-Niño have a signature within the SAC at the BC

Thus, with the above anomalous sea level gradient, an anomalous northward geostrophic current is implied. Hence, the SL clearly suggests a weaker SAC current during summertime in El-Niño years. Results for both currents and temperature anomalies in the yearly means and during summertime confirm this in more detail, as shown in Figure 6.21.

The mean yearly anomaly between April–2015 and March–2016 (Fig. 6.21a) highlights that the largest anomalies were indeed at the shelf and shelf-break. Overall, the mean flow over the shelf was weakened by about $5cm/s$ — within the magnitude of the anomalous shelf flow north of the BC (mooring *SAM5CB*). As

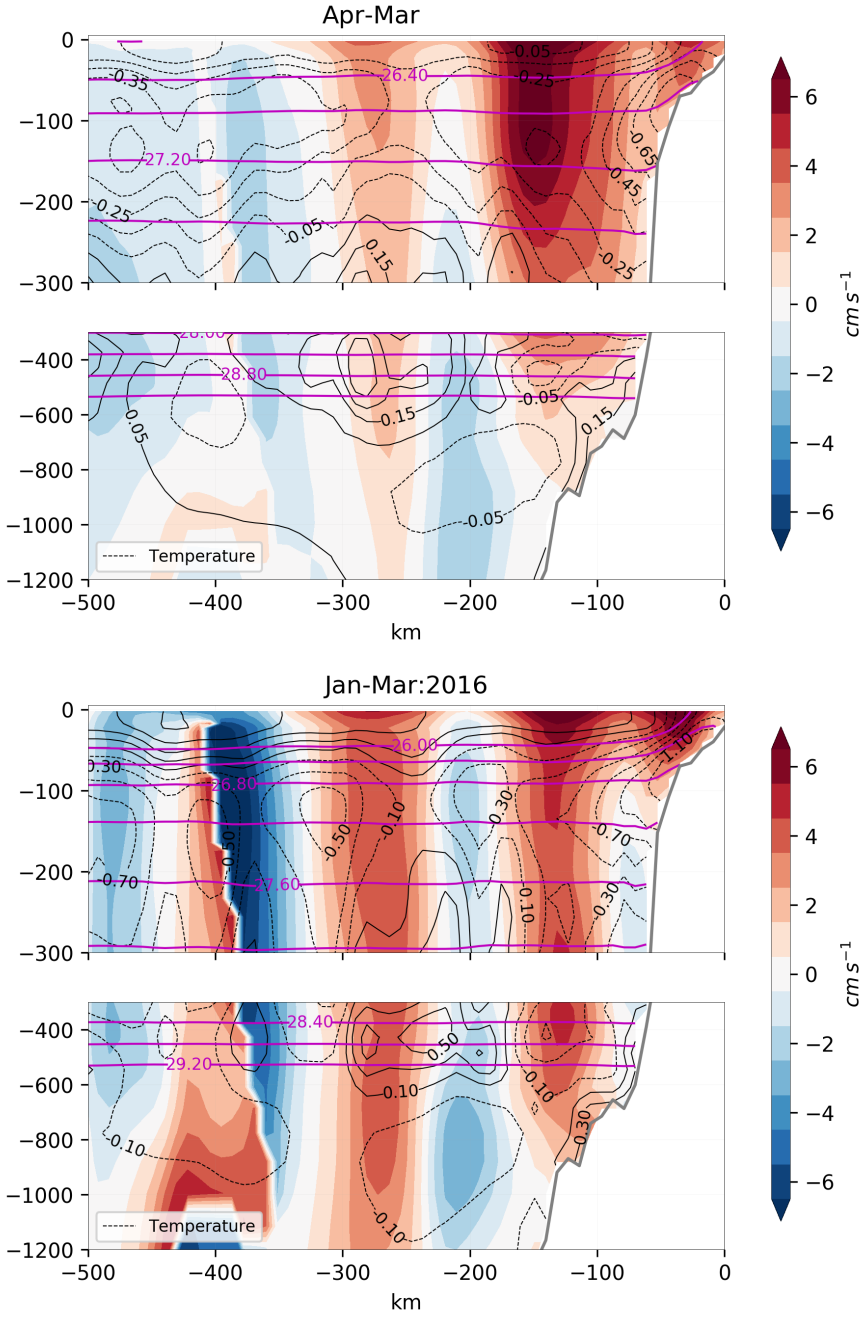

Figure 6.21: The mean anomalies of major currents (positive is north-westward) and temperatures (black contours) for the 2015–2016 year. (a) April 2015–March 2016 (b) Jan–Mar of 2016. Isopycnals (magenta) are calculated based on the mean absolute values of the respective months.

well, a very wide region under the SAC influence was slower (in excess of $6cm/s$ offshore). At the upper $200m$ depths a stronger northward anomaly dominated the outer section of the SAC jet. Note that, over the offshore side of this jet, the southward flow was more constrained over the whole water column. Towards the deeper ocean, lateral shear indicates eddy influence with smaller magnitude in the velocities (offshore of $200km$). Hence, the SAC current was more restrained, or that the northward FC current structure has moved onshore.

The wind stress curl in the region, which is one of the origins of the FC (Middleton et al. 2002), was above the average throughout the 2015-2016 period (not shown). This was consistent with the anomalously higher MSLP pressures found in the ECMWF dataset during the period, with the positive SAM and previous section results — the winds were stronger and upwelling favourable throughout the year in general. Thus, at the coastal ocean, with weaker (stronger) eastward (north-westward) winds during winter (summer), a reduced SAC is expected throughout the year. As well, north-westward upwelling favourable currents would be dominant over the shelf. The anomalies associated with the SAC were strongest in winter, with a much wider northward anomaly over the first $150km$ offshore than shown in Fig. 6.21b (not shown).

The temperature anomalies for this year, within the coastal ocean, follow the pattern in the velocities. It is no surprise that the weaker south-eastward currents lead to a considerable amount of colder water being attached to the coastal ocean and to the slope; the downwelling current has reduced. The strongest temperature anomalies are locked to the slope; $-0.85°C$ at the $100m$ isobath (black dashed thin contours). A weaker SAC appears to provide much of the colder waters at the shelf. However, the source of the cold anomalies in the upper $250m$ of the ocean did not appear uniquely related to this — colder anomalies are widespread in the upper ocean. In fact, the spread of negative temperature anomalies continues much farther than the $500km$ limit in Figs. 6.21. The source of this widespread cooling was, in part, generated by deep convection of anomalous colder surface waters in autumn–winter (not shown). Hence, if one considers a mean temperature anomaly value along the transect ($-0.35°C$) in the upper ocean, it's clear that the anomalies locked to the slope appear as a result of two different processes: one locked to the slope while the other a much larger scale cooling.

Consistently, the mean isopycnal depth of $\sigma_{27.6}$ for this *annual* mean along the transect is even sitting above the correspondingly *summer* mean depth (cf. Fig. 6.20a, 6.21a). Hence, the resemblance of the other isopycnals in this anomalous *year* was strikingly similar to *summertime* and the upwelling season — much weaker downwelling conditions. The pockets of anomalous warm waters at $300km$ off the coast at $\approx 400m$ can also be related to 'older' waters; they appear during

summer of 2015 at the surface, were downwelled during winter and transported offshore by eddies; they are consistent with results from previous seasons and also exhibit higher salinity anomalies (not shown). Hence, the presence of a cold signal throughout the first $300m$ in summer and with scales in excess of $1000km$ support a large-scale cooling with an atmospheric source and a coastal trapped signal.

These conditions were also present during JFM 2016, as shown in Fig. 6.21b. Despite the larger variability, given the shorter mean, colder temperature anomalies were also a permanent feature during summer. Moreover, closed and attached to the shelf and slope, a much colder anomaly of $1.1°C$ dominates the summer season at the shelf, with minima now much closer to the coastline. Hence, the anomalous temperature signal in the annual mean was enhanced and moved inshore. Additionally, given the localised and much stronger temperature anomalies in the first $200m$ at the slope, a more efficient interior Ekman upwelling is implied for the summer season. As we will show below (from the glider observations), the $\sigma_{26.4}$ isopycnal can be regarded as the limit of the SML during this summer. The reanalysis results above suggest that the SML was, on average, absent in the near-shore waters (first $30km$ from the coast) — i.e., stronger coastal upwelling. Favourable upwelling conditions also prevail at depth up to $\approx 400m$ and with a $150km$ offshore scale, but the largest changes relative to the yearly mean are locked to the slope. At the upper $20m$ of the ocean and away from the shelf ($90km$ off the coast), positive anomalies in SST are consistent with the previous results — the colder signal was trapped to the shelf, while SST were anomalously warm.

As in the annual mean, the north-westward velocity anomalies are the strongest close to the surface (in excess of $8cm/s$), within the shelf and in the offshore side of the mean SAC core. This is clearly associated with the stronger winds developed during the period (see also Fig. 6.10a). Within the offshore flank of the SAC, a stronger northward anomaly, from the surface of the ocean towards $200m$ depth, still dominates (cf. Fig. 6.21). In this region, at about $130km$ off the coast, the southward transport was reduced by about 50% or more. In comparison, the reduction in current strength reaches about the same amount over the shelf ($50km$ – above $100m$ depth).

The core of the SAC was less affected, but shifted in the vertical; by the anomaly patterns, the core moved to deeper isopycnals, given that at $100m$ and below a weak negative anomaly ($-1cm/s$ – southward flow) was in place throughout the bottom. This localised maintenance of the southward flow was stronger in summer than in the mean of this year (compare with Fig. 6.21a). This signal locked to the slope could be, in part, attributed to the winds and conditions in February (with reduced upwelling — see next section). So, the upper, coastal side and the outer side of the SAC was more affected, while the core of the current was shifted

downward in summer.

The net effect was a raised seasonal thermocline up to $100km$ from the coast. Again, the downwelling conditions offshore expected for a normal year were clearly reduced as seen by the flattening and upward displacement of the isotherms close to the slope (cf. Fig. 6.20a). For example, consider the climatological $13°C$ isotherm; it's clear that in JFM 2016, the $13°C$ isotherm upwelled from $240m$ to $150m$, sitting slightly above where the $14°C$ isotherm should be — representing a large and the strongest uplift of the seasonal thermocline in the whole transect. So, in a very thin band of the slope, waters below the seasonal thermocline were lying over the shelf in summer 2016. As well, all upper isopycnals along the transect were also slightly shifted upwards (note how the $\sigma_{27.6}$ is shifted towards $200m$ – Fig. 6.20). Finally, the eddy-like structure and its pockets of warm and salty waters ($400m$ depth) still persisted in the outer regions.

Hence, upwelling favourable anomalies were more locked to the upper slope ($200m$ onshore), and also below the SML offshore. Within the first $100km$ of the coast, and below $80m$, downwelling was reduced not only close to the bottom but also in the interior of the ocean, as cold anomalies were also found offshore in a much larger scale. In other words, and comparing with the mean annual picture, the anomalous upwelling winds constricted even more the core of the SAC, pushing it downwards, offshore and reducing its influence on the shelf. On the outer side of the SAC, the north-westward flow associated with the FC appears to have shifted upward and onshore, given the stronger north-westward anomaly sitting at $150km$ between 400–$800m$. (Fig. 6.21b). The south-eastward coastal current was more reduced in summer.

Let's now consider the ENSO effects. In the idealised study of Clarke et al. (1994), where tropical variability propagates along a coastline, the velocity field (ENSO jet) is trapped at the slope, centred at about $1500m$ depth and with cross-shore scales of the internal equatorial deformation radius (dependent on the β parameter and mode number — see below). While the bottom relief and friction are the core of the ENSO jet dynamics, there is no coastal or shelf velocity signal because of friction. Also, the ENSO currents would peak in the subtropical transition, deepening and weakening poleward, with strong scattering along the coastal waveguide and reducing the cross-shore scales towards the pole. The trapping conditions for long and free waves along the coast are also dependent on the angle of the coastline as well as the latitude (Clarke 1991). The detection of these waves was mostly focused on the pressure (SL) fields, where the mode-1 signal is much clearer (see Fig.15 in Clarke et al. 1994).

In an idealised setting, the condition for trapping of a first vertical mode, i.e.

for Kelvin wave dynamics to dominate, is (Clarke 1991; Li et al. 2004):

$$\omega > \beta c \frac{cos(\theta)}{(2|f|)} \tag{6.9}$$

Where ω is the frequency of the motion, β is the planetary gradient of the Coriolis parameter (f), c is the wave speed and θ is the angle of the abyssal ocean wall ('coastline') with North (anti-clockwise).

Our transect here is very far from the Equator ($\approx 8000km$), so a weaker ENSO jet is expected. Given the highly variable shelf (and friction), higher modes and scattering are also expected. Also, the theoretical conditions for trapping of mode–1 waves along the EGAB are not met (eq. 6.9). The angle of the coastline relative to the north can be estimated from the wind angles used in Table 6.4. Between Thevenard and Portland, this angle is approximately 40°. (about the same at the slope edge). Using the same general parameters as in Li et al. 2004 ($\omega = 6.64 \times 10^{-8}\,\mathrm{s}^{-1}$, $f = 8 \times 10^{-5}\,\mathrm{s}^{-1}$, $\beta = 2 \times 10^{-11}\,\mathrm{m}^{-1}\,\mathrm{s}^{-1}$) and $c = 2.7\,\mathrm{m\,s}^{-1}$ (first mode), the critical period is reached, curvature is large and the motion is not completely trapped to the coast. Although these conditions provide a mixed environment, higher modes would also be less affected by the coastline angles and still be trapped (c will reduce and critical periods are much larger). Moreover, the trapping theory did not consider the effect of shelf-break currents — the monochromatic ENSO wave in Clarke et al. (1994) is not alone in its poleward pathway. As shown in Clarke et al. (2004) for the western Australia region and in Li et al. (2004) for the southern shelves, the SL *is* trapped to the coastal ocean and influences the ocean currents. Our results from Fig. 6.4c also indicates trapping, but with some extended cross-shore scale correlations away from the slope if compared to the mostly zonal shelves in the western GAB. Thus, a mixed case scenario is expected for the EGAB, particularly in the BC.

The time window in the results presented above is too short — a mean over 2-4y would be more representative of ENSO effects. But the transect suggests a peak in anomalies within the slope regions in both temperature and velocities (until $200km$ off the coast). In general, the results also show that the maximum isotherm (and density) displacements are in the upper $200m$, locked to the coast/slope and reduces offshore at the surface (in both annual and summer estimates). Hence, a consistent El-Niño effect in the SAC appears to exist at the BC, as in Li et al. (2004) and with some trapping conditions over the slope. The extended limit of colder anomalies beyond $500km$ suggests that another large-scale variability also occurred in 2015-2016 that is correlated to ENSO.

Indeed, the correlation with ONI_0 at this transect is significant and broad, as shown in Figure 6.22. We detrended all anomalies between $1994 - 2016$ for JFM

and assume an effective 24 observations, with a corresponding correlation of ± 0.40 as the significance bound — everything within this contour strictly did not occur by chance. Significant correlations are located for the major axis currents in the exact locations of the offshore limits of the SAC, as in summertime of 2016. An overall weak (strong) SAC is then present during El-Niño (La-Niña); consistent with the SL gradients, previous studies and the results above (see also Fig.9,10 in Li et al. 2004). However, the effect is not clear within the core of the current and attached to the coast, but within the offshore flank of the jet. It's important to note that we use monthly values, unfiltered and as such the correlations are not in the interannual timescales of ocean currents, but within the monthly time-scales (winds would also have a role in the upper ocean variances and close to the slope). Also, the offshore influence appears slightly barotropic here, at $150km$ or so off the coastline (and what would be seen by the altimeter), with correlation increasing toward the interior and below the mean seasonal thermocline. There, it is centred at the $12°C$ isotherm, below the $\sigma_{27.2}$ isopycnal (compare with Fig. 6.20a). No significant values were found away from the offshore flank of the SAC — over the shelf, the coherence in currents is not significant and is consistent with the lack of correlation between ENSO and alongshore winds. The same can be said about the deeper flow in the FC region (the offshore significance at $400km$ is not relevant here and is close to the phase angle shift).

The temperature anomalies over the upper ocean and close to the shelf-break also provide a different view from the velocities (black contours in Fig. 6.22). Offshore and in the upper $20m$, SST is positively correlated (heating) but not significant. As well, zero correlations are found at the SST over the shelf — all consistent with the previous results that ONI_0 is not well correlated with SST.

Bottom temperatures over the shelf, which are related to ENSO at zero lag, also have negative tendencies with ENSO, attached to the slope, but not significant in this period (only 10% of the variance). This appears to contradict the observational results in the KI region bottom temperatures, which are related to ENSO at zero lag in the northern region at about $z = 100m$. By the spatial autocorrelations between SL and SST observations, the results over the BC should be similar to the upwelling tendency in the north, but here this is not as clear as in the observations. But the datasets, periods and locations are different. Reducing the reanalysis period to 2008-2016 and using BT as regressor ruled out this insignificance. The model shows positive (negative) significant correlations with BT (SAC flow), i.e., the waters at the BC were in-phase with KI and within a weaker SAC flow (not shown). Thus, local and shorter timescale variability are changing the ENSO effects (or masking it).

In the same way, the seasonal thermocline depth appears to be weakly related to

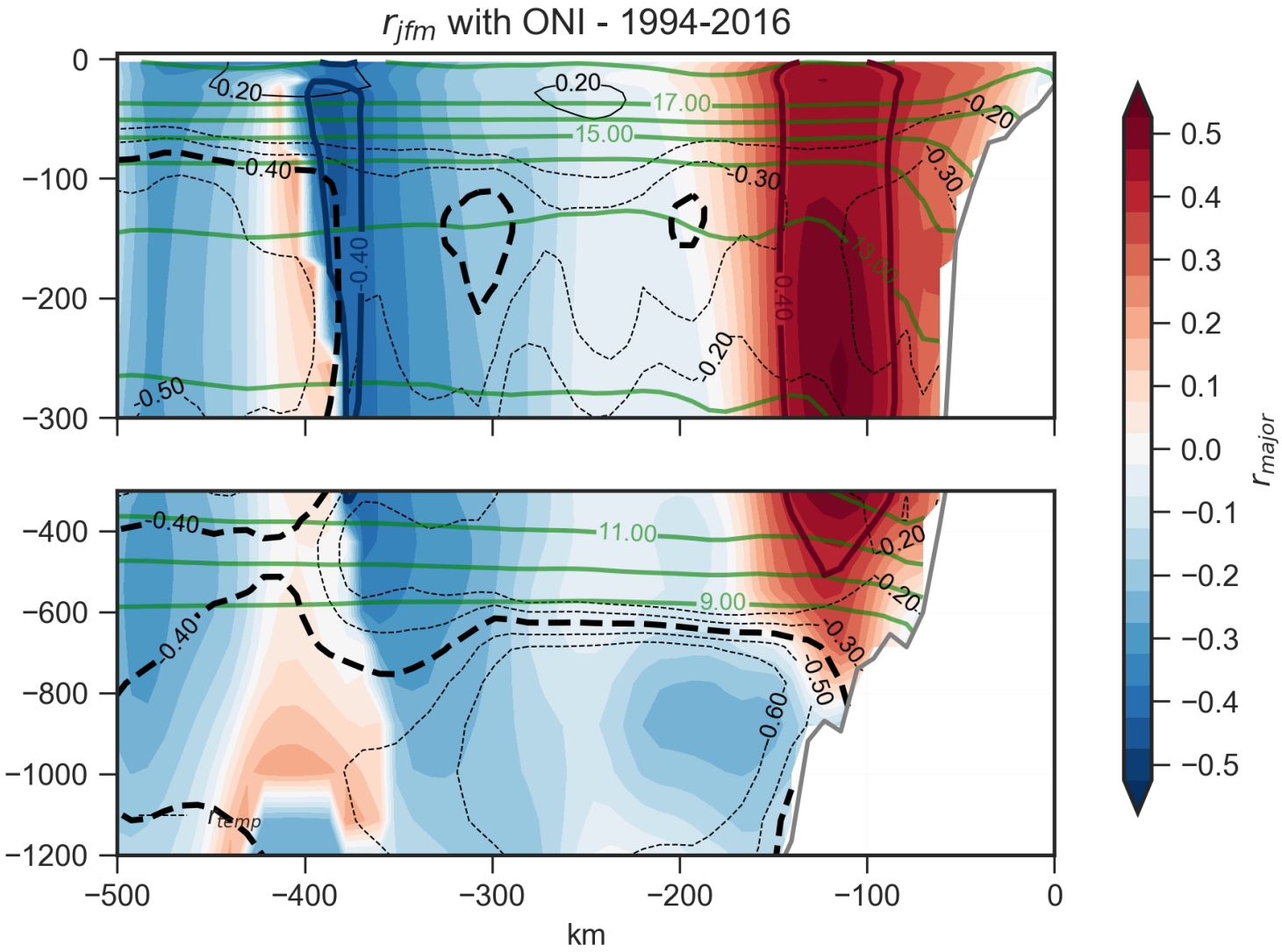

Figure 6.22: The correlation of the ONI index with the major currents (shading) and temperature (black contour) anomalies along the $37.25°S$ transect. Summer only (JFM 1994–2016). The green lines indicates the mean isotherm depths. Significant values are within the thick colour and black contour lines of $r = 0.40$ (significance bound). Note that the blue and red thick contours refer to major axis velocities, while dashed black contours refer to negative temperature anomalies. Temperature contour range is 0.6, with $r = 0.1$ step with values below ± 0.1 ignored for clarity.

ENSO at zero lag, with insignificant values in the upper ocean in the vicinity of the jet. The presence of cold offshore significant correlations at $450km$ (and patches) in the upper $300m$ put more weight to the suggestion that previous autumn-winter cooling is related to ENSO. Again, these correlations extended beyond the axis limits (at least $1000km$ offshore). Given that, if one considers the mean signal of the temperature correlations, a cooling of the entire $1000m$ of the ocean appears in phase with ENSO. Away from the influence of the upper ocean and the coast, in the deeper limits of the transect (below $9°C$), temperature correlations are strongly significant at the base of the permanent thermocline ($1000m$). The core of this feature is associated with the FC core location and spreads laterally over the entire $500km$, in a similar way as the mean velocities in Fig. 6.20a.

The temperature variability in the deeper regions is small, timescales are much longer and a correlation with ENSO indicates an ENSO effect in the permanent thermocline. The location is consistent with a mode-1 internal Kelvin wave effect, but the horizontal scales are not. This could be a longer (e.g. IPO) manifestation in the correlations regulating the FC flow, the result of scattering into Rossby waves (large horizontal scales) and the internal Kelvin/slope wave together. As well, the large-scale cooling in the surface could be related to teleconnections.

So, it appears that the ENSO effect is far from being in the mode-1 only internal Kelvin wave and that interaction with the background flow and the atmosphere generates much larger scales coherent with ENSO. Both correlations in currents and temperatures presented are just too big and far apart from the slope to be regarded as just an internal Kelvin wave. However, these correlations include several processes and the interesting coherences found here are more related to the permanent thermocline displacement and large-scale cooling — not so directly related to the shelf upwelling signal. The deeper ocean variability in the region is also not so well understood and not the focus here. The result above, however, still supports strong upwelling in ENSO years, both through the interior Ekman upwelling and through the BBL.

Consistent with the wind results for summer and winter, major axis velocities were also upwelling favourable at the shelf if correlated with SAM, and significance was found in the same offshore location of the SAC (not shown — nothing in temperatures). On the other hand, currents were borderline significant, while temperature fields were very significant using the $15mo$ and $40mo$ lagged effects of ENSO — Figure 6.23 (top). The $15mo$ lag effects in BRAN are consistent with previous findings; it is affecting bottom temperatures at the slope (and SL) and a strong tendency above the seasonal thermocline. The signal is clearly related to the uplift of isotherms from the seasonal thermocline — affecting interior, BBL upwelling, BT, SSTs and SL here and in observations (previous sections —

Fig. 6.16a). The current pattern is consistent and borderline significant; a narrow pattern, close to the slope and upwelling favourable (north-westward anomaly). The $40mo$ signal also shares similarities with the previous results, with warming in the upper $50m$, large horizontal scales and a borderline correlation at the slope in the velocity field. From the point of view of broad scales and surface signature, it's clearly the same pattern as in Fig. 6.16b (positive correlations in the upper ocean). Thus, this appears to be oscillations components of ENSO that add information (trends) in different variables, but clearly most important for SST.

Finally, the results of correlations between major axis currents and SL at Portland (summer months) is presented at the bottom of Fig. 6.23. This is useful because it represents several things; includes ocean currents, winds, and ENSO information, match seasonal thermocline anomalies that are setup later ($15mo$ effect), it is $20y$ long, is significantly correlated with SST (after BT) and representative of the mean 2016 conditions.

The result is not surprising; The SAC is weak, the shelf currents strong, the coastal ocean is significantly colder up to $z = 300m$ and the upwelling is extended to $100km$ offshore, with significant cold anomalies up to $200km$ offshore. The correlations are at the shelf, slope, SAC and seasonal thermocline, while some correlation is also found within the permanent thermocline. As we will see in the next section, this maximum depth over the slope related to SL is within the source water depths found over the shelf (see next section).

Thus, we suggest that the maximum speeds offshore of the SAC are clearly related to ENSO but onshore reductions are related to the overlap of other effects (with positive feedbacks). Winds (SAM) through anomalous shelf flow over the GAB and persistent ENSO effects create an overlap of conditions that help the upwelling in 2016 be an extreme event. The attachment to the slope of the seasonal and permanent thermocline shifts are clearly long and related to the setup and adjustment of interannual waves along the shelf as in Clarke et al. (2004).

So, all the findings in the previous sections are supported in a range of different observations and reanalysis, indicating that the long waves propagating from the tropics and extreme winds within the GAB are the main drivers of the upwelling. ENSO and SAM have intimate relationships in relation to the setup of upwelling, as such the mean conditions of 2016 were largely influenced by them acting together. The timing for perfect conditions in upwelling is clearly not instantaneous but can be attributed to the onset of different processes; arrival of internal waves, deceleration of SAC, slow uplift of the thermocline over several seasons followed by strong winds. This result clearly explains the 'asymmetric' response between central Pacific SST and the BC upwelling, implying a long persistence of conditions that can be useful to predict upwelling seasons ahead. The results above show how

ENSO, on average, is related to the onset and persistence of colder temperatures in the BC within its main time-scale of 2 to 4 years.

Following the El-Niño development throughout 2016, results here indicate that both enhanced wind stress curl, westward winds and positive MSLP developed within the GAB in winter. This would generate colder temperature anomalies in the deep oceanic regions (winter *positive* net heat flux anomalies), while a coastal ENSO signal was already at the shelf-break, within the upper ocean. With the intense loss of heat to the atmosphere in wintertime, it is likely that an atmospheric anomaly/teleconnection is acting at the same time as the Kelvin/slope wave. The follow-up summer wind anomalies and the interactions of the Kelvin wave with the background flow then lead to an overall reduced SAC, lifting of the isotherms close to the slope in the upper $300m$, providing colder waters for both BBL upwelling and interior Ekman upwelling. Thus, if one considers the general upper ocean cooling and the trapped effect of the ENSO wave, two direct ENSO mechanisms, one persistence effect and a SAM effect to active help in the development of a strong upwelling season. Nonetheless, this is not the complete picture and still, a lot of the variance is still left to be explained — like the role of tropical winds and the weather band forcing. The above analysis puts more weight in the weakening of the SAC than in the FC, mostly because the dynamics of the latter at this location are largely uncertain. For example, the FC was defined in Middleton et al. (2002) in the northern GAB only (from about $126°E$ see their Fig.1b). The strengthening and surfacing of the FC core could affect canyon upwelling, however, the deep canyons at the BC are not completely connected to the shelf (Huang et al. 2014).

The ENSO signal via the shelf-waveguide is ubiquitous. We have shown, exhaustively, that this signal is very clear within the GAB and that it has particular characteristics regarding the local variability. Although we did not track the wave along the Australia coastline in detail, we found that this signal is persistent with positive feedback and capable of different effects than previously explored in the context of upwelling. The role of ocean currents and their pathway from Western Australia is also foremost, with the highlighted importance of seasonal persistence. The strong correlation (Fig. 6.22) below the SAC core suggests that interaction between internal dynamics and boundary currents is at play during ENSO events and more studies are required, particularly with the SAC and FC interannual variability.

We now explore a synoptic view along the Bonney Coast as measured by two glider missions. The focus is shifted towards a smaller spatial and temporal period, within the weather band variability. As we will show, at these sampling periods, other factors also play an important role in making the summertime of 2016 an

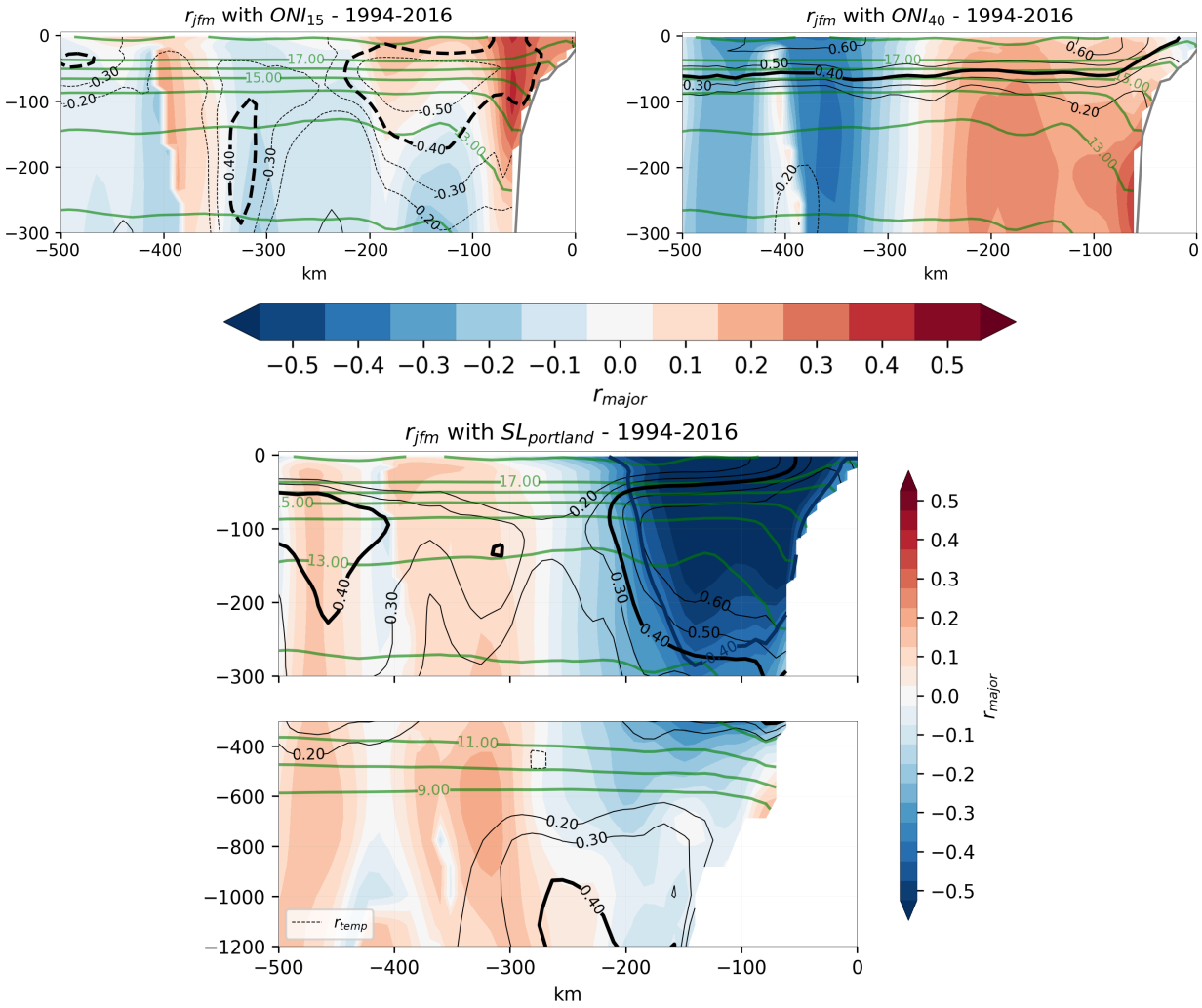

Figure 6.23: (Top) as in Fig. 6.22, but for the upper ocean and with the ONI_{15} (left) and ONI_{40} (right). (Bottom) as above but with SL at Portland

extremely cold one.

6.3.4 Glider observations of extreme upwelling: The joint effect of ENSO,SAM and local topography

We focus now on the synoptic features at the Bonney Coast, in particular to the events that set-up the extreme anomalies of the season. Observational efforts off the BC include remotely sensed measurements, surface velocities from HF radar and in situ observations from two glider missions. These missions were almost contiguous, from 27 January to 26 February, and from 28 February to 30 March of 2016 — see Figure 6.24a,b.

The aim of the glider mission was to investigate the BC upwelling circulation. The deployment, operation, and recovery of the glider were performed under IMOS. A zig–zag pattern was chosen to optimise coverage and provide transects along the shelf (Fig. 6.24c,d). Here and below, we restrict our vertical view to the main slab-like segments that matched upwelling events and particular features; cross-shore segment M1–S6 (mission 1, segment 6) and alongshore M2–S4, M2–S13 and M2–S18. The cross-shore segment M1–S6 reached the deeper waters off the BC, while the other two were the longest quasi-linear segments, following approximately the $110m$ and $130m$ isobaths. Between M2–S4 and M2–S18, the minimum bottom temperatures in the observations were found (M2–S13).

Although the glider did not sample the northern region of the BC and the plume, the volume of observations was unprecedented for this region. Figure 6.25a is a TS diagram of the two glider missions (grey lines and orange shading), together with several historical observations (cyan lines) from a bounding box in the region extracted from the CARS-Extended dataset — see methods section. We use historical data from spring–summer, with close to 1200 points in the first $400m$ depth of water, 80% of these data in JFM (i.e., representative of summertime — not shown). Because of the focus of this study, the TS diagram is clipped at the top limit of typical oceanic values, being limited below by the $T = 10°C$ and $S_A = 34.8\,\mathrm{g\,kg^{-1}}$ values (max. depth is about $200m$).

We see that the glider observations have significantly more resolution than historical observations, with considerably larger range (grey dots). The fresher and colder observations in the TS diagram, within the $\approx \sigma_{26.6}$ isopycnal (referenced to $0dbar$ in black lines) and spiciness $\mathcal{T} < 1.8\,\mathrm{kg\,m^{-3}}$ (red lines), were largely sampled by the two missions — they are the most frequent (orange shading). The lower spiciness waters in the TS diagram has a clear linear characteristic; it's bounded by a narrow density range in the majority of the observations (orange shading). The presence of observations parallel to the spiciness curves (low spice - cool and fresh waters) also indicates internal wave activity in the waters colder than $13°C$ or so (Warren et al. 1980; Flament 2002). On the other hand, large

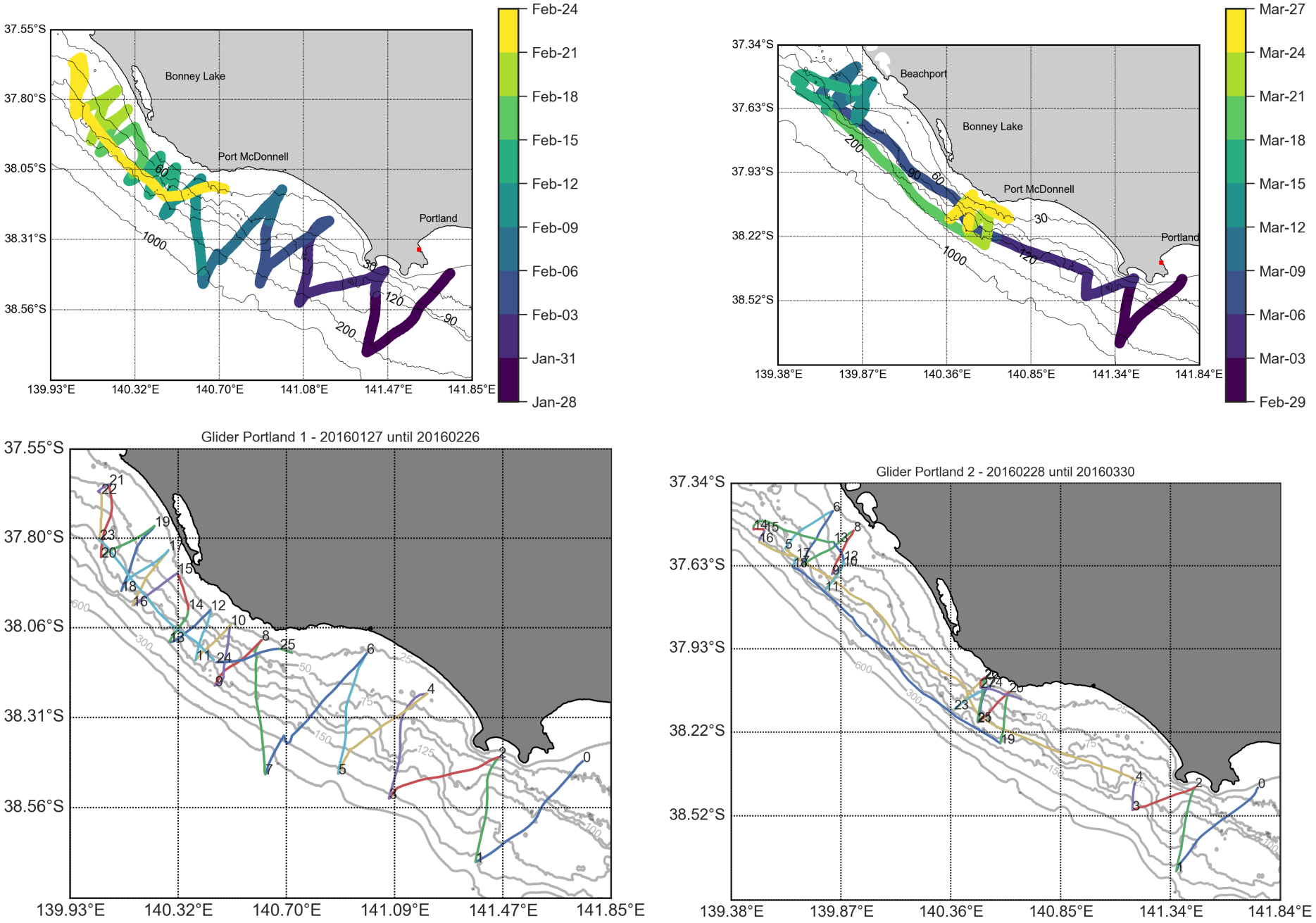

Figure 6.24: Top: Glider mission tracks and corresponding dates for mission 1 (left) and mission (2) right. Bottom: the numbering used for each segment in the missions. Grey contours are the isobaths in meters. The small red square close to the beginning of each mission marks the Portland TG. The coastal lake at $140.36°E$ is the Bonney Lake while at $38.05°S$, where the shelf become wider (Discovery Bay), is Port Macdonnell

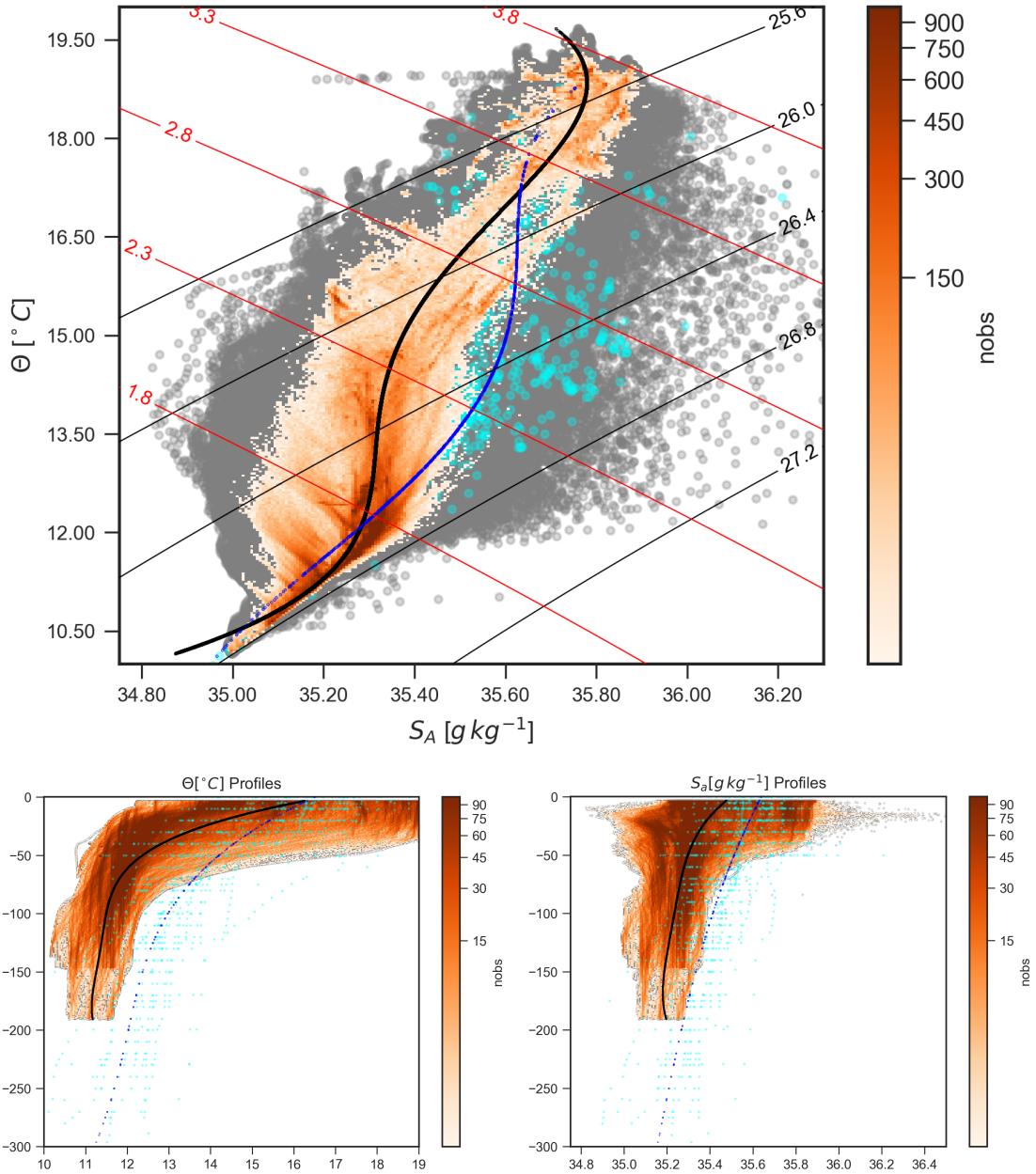

Figure 6.25: (a) The TS diagram for the two glider missions (downcast only). (b) Vertical Conservative Temperature profile. (c) as in (b) but for Absolute Salinity. The black-dot line is a fourth-order polynomial fit to the glider TS points, while the blue-dot line is the fit for summer and spring historical data (Oct-Mar). The grey dots represent all glider observations, while the orange shading represents the number of observations for each (0.01 bin resolution in Θ,$\S_A$). Cyan dots represents the historical observations from the CARS-extended dataset (spring-summer only). In (a), density contours referenced at $0dbar$ are in black thin contour, while spiciness contours are in red.

horizontal variations along isopycnals indicate horizontal mixing and the SML appears between $\sigma_{25.8}$–$\sigma_{26.4}$. Given the upper ocean characteristics of our sampling, low spiciness can be approximately considered a passive tracer for upwelling as well as CHL-A (clear waters). We will use the CHL-A in conjunction with T,S by convenience and robustness; it is an extra independent variable/sensor on the glider and in conjunction with low salinity and temperatures indicate 'new' waters from below.

Using the bounded values in temperature and salinity in the above region, the most frequent observations can be linked to thermocline waters of the STF region, defined as Indian Central Water (ICW) (Tomczak et al. 2004). On the other hand, using information of the regional oceanography of the GAB, this could also be regarded as the FC water following Richardson et al. (2009) (with $T < 15°C, S_A < 35.66\,\mathrm{g\,kg^{-1}}$). The number of observations (orange shading) is highest within or lower than the FC water mass range — the most frequent observations were between $T < 15°C$,$S < 35.4\,\mathrm{g\,kg^{-1}}$). Hence, FC waters were found over the BC shelf region, with even fresher signatures.

Looking at a mean mixing curve (black), here defined as an ordinary least squares fit with a $4th$ order polynomial between S_A and Θ, we see that strong diapycnal mixing occurs when the curve crosses the $\mathcal{T}_{1.8}$ curve, at about $\sigma_{26.6}$. This mixing line is considerably different from the same curve computed with the climatology for the extended upwelling season (light blue dot-curve). The climatology curve reaches a maximum mixing at $S_A = 35.6$, $\mathcal{T} > 2.3$, while in our observations at colder and fresher waters (centred at $S_A = 35.3$). Hence, the climatological curve is shifted to the bottom and to the left in the 2016 summertime. This indicates strong diapycnal mixing of low spiciness waters; the pathway of strong heating with small evaporation — a strong upwelling. The fact that the mixing curve regains some linearity at the top of the diagram also implies strong lateral mixing, typical of warm surface mixed layers. Additionally, high spicy waters (warmer and salty) were more frequent in 2016 than in previous upwelling seasons.

Individually, the first glider mission provided the largest variability in Fig. 6.25 (the wider grey spread), while for the second mission the values were more compact and constrained to the waters with $\mathcal{T} < 2.8$ (not shown). This is because the first mission sampled remnants of strong upwelling and heating events, while the second mission sampled an extreme upwelling event (see below).

The vertical TS profiles in Figure 6.25b,c also highlight the strong upwelling characteristics of the observations. Again, both variables (Θ,S_A) are clearly skewed to the left, if compared to the historical observations. Temperature profiles show maximum variance at the mixed layer depth (about $40m$), while the seasonal

thermocline occurred at depths as shallow as $90m$. Using the mean profiles (black - polynomial fit) as a reference, we see that stratified waters were dominant over the shelf, and much fresher salinities were present at the surface. Again, despite some profiles matching the vertical distribution of our sampling, the 2016 summer was much colder and fresher (black-dot *vs* blue-dot curves). It's clear they came from populations of different variance — a Levene test statistic (Brown et al. 1974) also supports this ($p - value << 0.05$). The thermocline uplift is also clear in the profiles; at $z = 200m$, waters were on average colder by $\Theta = -1.°C$ and $S_A = -0.1\,\mathrm{g\,kg^{-1}}$ — an $\approx 100m$ uplift if referenced to the historical data. Given the previous definitions and bound limits of water masses in this area, the profiles indicate that FC/ICW waters are often found at the surface. If one compares these figures with previous results (e.g., figure 7. in Richardson et al. 2009), the waters have source depths up to $350m$ or so, consistent with the limits of historical observations presented here, and with a raised thermocline (blue and cyan points in Fig. 6.25b,c). Overall, the extreme upwelling nature of the observations is very clear, as well as the strong heating at the surface mixed layer (note the warmer values are also slightly skewed to the right in Fig. 6.25b,c). The time series in Fig. 6.26 displays the extended upwelling season of 2015-2016 (Nov-Mar), with several variables from independent sources. The variables were filtered with a cut-off period of $5d$ to reduce sub-weather scales. In the upper panel, alongshore wind anomalies show a larger variance in the northern EGAB (Thevenard - red), with peaks between 5-12 days and a clear maxima during early January and March — the red curve (shading) is the mean (range) between the weather station and the CCMP reanalysis estimate. At Portland (blue - weather station), the winds are less variable and weaker, is correlated with Thevenard (maximum coherence between $5 - 7$ and at 20 days - not shown). We can also already note that the strongest anomalies in the weather band for alongshore winds started at the end of December. An approximate $8d$ wind burst in early January was clearly extreme, reaching almost an 8-fold (3) increase over the mean climatological values of $0.015Pa$ ($0.04Pa$) at Portland (Thevenard) — compare this with Fig. 6.2, top-right panel.

Estimates of the wind stress curl (green - CCMP based) over the entire BC (*polygon*) were also in tandem with the strong alongshore winds and were upwelling favourable. A negative wind stress curl will generate an extra source of upwelling through Ekman pumping. The mean pumping velocity of this curl along the BC ($Ek_{pump} = \frac{1}{\rho f}\nabla \times \tau_w$) is small; $1.5m/day$ in the strongest events (with $f = 8.8 \times 10^{-5}\,\mathrm{s^{-1}}$ and $\rho = 1024\,\mathrm{kg\,m^{-3}}$). However, despite being small, this means that favourable winds were coherent with favourable wind stress curls. This indicates a coastal origin for the curl; the drop-off effect caused by the lateral and

frictional boundary layer between the atmosphere and the land (Pickett 2003; Capet et al. 2004; Renault et al. 2016). In the previous sections, we already detected some coherent wind stress anomalies associated with the thermal structure of the upwelling plume; such a (thermal) vertical marine boundary layer would also change the curl (O'Neill et al. 2003; Jin et al. 2009). We did not attempt to separate these effects, but we noted that the negative curl was very attached to the coast, while in the oceanic regions a positive curl prevails (not shown).

Nonetheless the effect here is small if compared to the idealised vertical velocity induced by the Ekman Transport ($EkT_w = \frac{\tau_a}{\rho f R_i}$). Accounting for the seasonal cycle in the January wind burst, with $\tau_a = 0.12Pa$ and an internal Rossby radius of $R_i = 10km$, the induced vertical velocity at the coast is about $12m/day$ within the region. The curl will be an important effect at monthly and seasonal scales, as well as changing the interior and BBL partition (Song et al. 2011; Jacox et al. 2012). We don't investigate this further, given the relatively small value of the curl during the wind events.

Following Fig. 6.26, the SL anomalies (second panel from top to bottom) show that long wave activity in Thevenard is, not surprisingly, higher than Portland. This is again consistent with Church et al. (1987) results and the variance ratio between the stations reported in Table 6.2. Spectral analysis of SL anomalies indeed indicates largest amplitudes between $8-12d$ for these CTWs, while primary oscillations were between $50-70d$ during summer (not shown). A lag close to $2d$ exists between the two stations in SL. The signal also is damped in its southward propagation and slows down — note the widening of the peaks at Portland. This suggests frictional decay of the CTW and reduced speeds with the shelf width variability, as shown by the idealised model results in Chapter 5. The lag estimate in the last chapter was also very similar to the observations here - slightly more than $\approx 2d$ for a $10d$ periodic signal, if one shift the results to Thevenard instead of the western boundary in Fig. 5.6.

Additionally, in January 2016, the peak in winds coincides with the low frequency and lowest SL anomalies. This was responsible for a strong upwelling (SST) at the beginning of the season (between 31–Dec 2015 and 15-Jan 2016 — third panel — brown line). In February, on the other hand, two strong positive SL peaks ($15cm$) occurred with $8d$ periods, accompanied by positive and short periods of southward winds ($3d$ or so). These peaks lead the warmer SSTs anomalies that occurred at the end of February.

The SST anomaly, within the third panel, suffered a sudden drop along the BC region (brown curve) within the January event. Note that this event was fast in driving the SST down, given that variability in the whole region was almost zero; the range of SST along the $BC_{polygon}$ region (brown shading) contracted towards

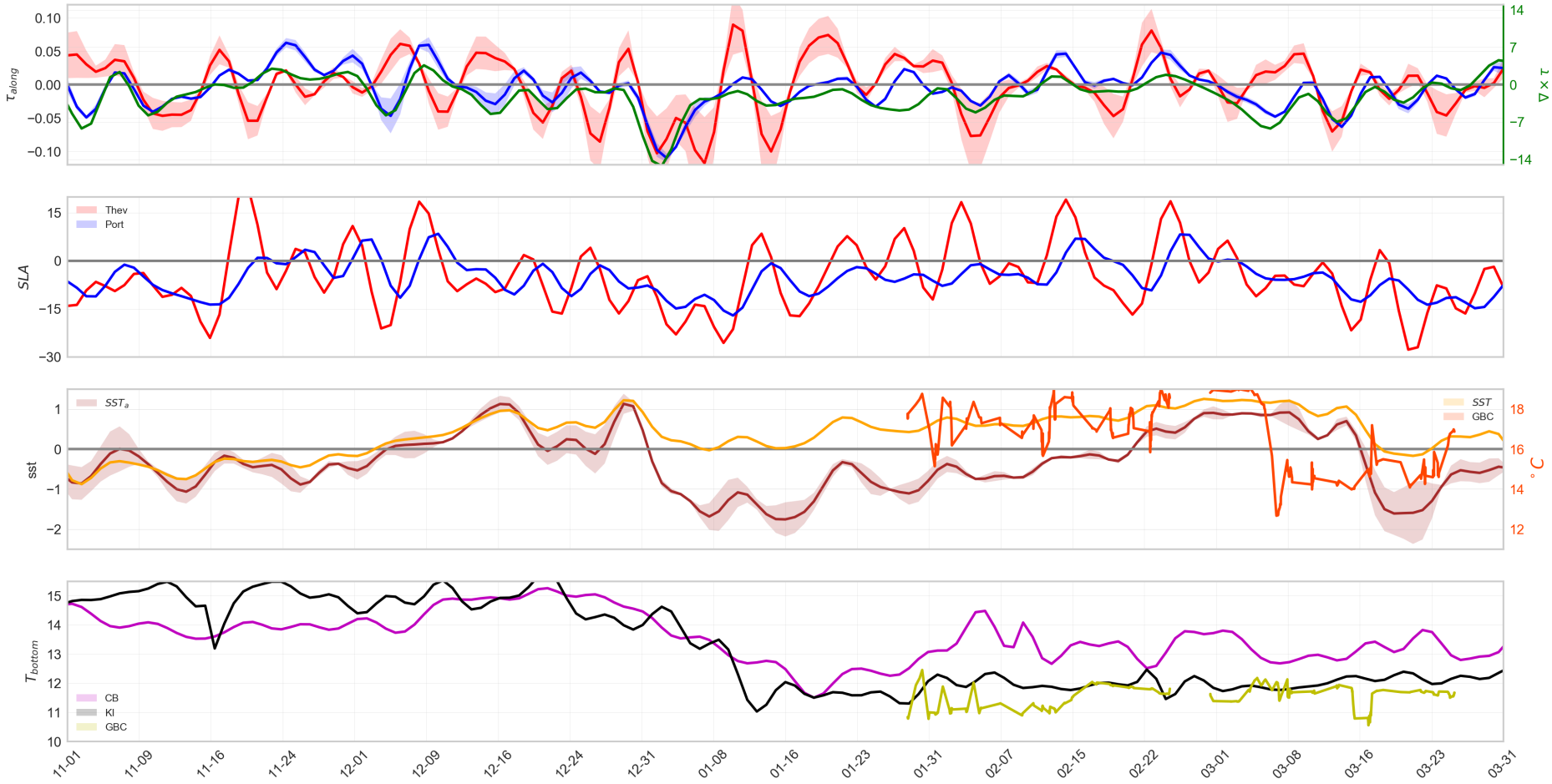

Figure 6.26: Time series during the summertime of 2016. (a) Top panel: anomaly of the alongshore wind stress (Pa - left axis) for Portland (blue) and Thevenard (red shading). The red shading represents variability between the weather station and the CCMP estimate at Thevenard only. Right axis (green) represents the mean wind stress curl in the BC region ($10^{-7} N\, m^{-3}$).(b) Second panel from top: The SL_{adj} anomalies for Portland (blue) and Thevenard(red). (c) Third panel from top: The SST anomalies for the BC region (*polygon*) $°C$ - left axis - brown shading. Right axis: The raw MUR SST for the BC region (yellow) and in situ SST close to the $100m$ isobath from the two glider missions (orange). (d) The bottom temperatures at CB (magenta), KI (black), and close to the $100m$ isobath measured by the gliders along the BC.

the mean (brown line). During this event, anomalies reached $-2°C$ (below the $5pth$ percentile of the season in MUR estimates – see Fig. 6.10b). The winds and SL were favourable for these cold anomalies to be maintained for up to $15d$, with stronger variability at heating events (positive trends) and cooling events (negative trends) that followed. This contraction and expansion of SST variability along the region are consistent with the SST anomaly differences between the plume region and the BC found in the SST analysis section. As a reference, we indicate in yellow at the right axis, the actual mean value of SST iin the region during this period (about $16°C$ — MUR).

After the extreme January 2016 event, and shorter upwelling events that followed, the upwelling in general relaxed, and SST started to heat up throughout February. Before the end of the month ($\approx$ 22 Feb), it broke the normal year values and developed $1°C$ positive anomalies (above $18°C$) for most of February and early March. These strong, warm anomalies were above the $90pth$ of the season (using the independent MUR estimates) and persisted for another $15d$ before the second extreme upwelling event started. So, the upwelling largely ceased during this month, as did the shelf northward currents (not shown but note the positive trend in alongshore winds). The first glider mission at the BC was $15d$ before the extreme warm anomalies developed (M1–S6 is at Feb–7th). Here, the glider SST (orange line) is defined as the mean daily values above $4m$ along the $95 - 105m$ isobath range. As expected, given the zig–zag pattern and the uneven spacing of the data, the variability of the signal is high, but the SST values on these isobaths still follow the mean value along the BC region (yellow). This spatial anomaly appears as strong and short-lived peaks with SSTs less than $16°C$.

The glider sampled the start of the third and last extreme event of the season. Just a week after the second mission resumed, on Mar 7, the glider measured a strong peak in SST when it was crossing the BC along the $100m$ isobath ($M2 - S4$ — see 6.24 bottom right panel). The peak occurred $10d$ earlier than over the SST index indicated. The sharp drop resulted in $13°C$ SST at the BC. This means that the upwelling setup at the BC can be very fast and responds to the winds much quicker, given the narrow shelf width. Over the next days, the development of the strong negative anomalies afterwards was highly variable (note the spread in the shading), particularly after the mean anomaly reached the minimum. This event was shorter than in January but had slightly colder values (below $-2°C$.) Hence, at this time, relaxation after upwelling was quicker than in January. This is expected given that favourable SL and wind weather band signals were much reduced in the following days.

Finally, the BT index in the mid-EGAB are also consistent with the BC upwelling picture, with lower BT invading the shelf during the January 2016 event.

The BT at KI (black), the "cold pool" region, was kept anomalously cool for the whole of the season after the January event. The behaviour was followed similarly by the ADCP sensor within the CB region, with a mean shift to positive values. Of interest to note is that the SST at the BC appears to lead the BT in the mid-EGAB (faster response at BC — see the January event), as well as some of the peaks at KI appear to lead those at CB. This suggests the KI region as being the source of the cold waters at CB, as proposed in Middleton et al. (2003) and McClatchie et al. (2006).

Also, for the following months, the northern mid-GAB shelf appeared to not have suffered any stronger/deeper upwelling in the same way as in January. For example, the BT in these areas did not change much beyond the weather band scale after the January event — a long and persistent preconditioning.

These observations explain why March was preconditioned for strong upwelling; That is, the bottom waters were uplifted by previous events. However, the mean winds and SL also shift at March, limiting the duration of the anomalies. Lastly, the BT from the glider also highlighted that the BC indeed had much colder waters sitting at the bottom than at the mid-GAB. The values observed when crossing the $100m$ isobath reached $11°C$, and during March-17th a minimum value of $10.7°C$ was sampled by the glider.

At this maximum drop in temperature, the glider was performing the M2–S18 segment and crossing the northern region of the BC in the vicinity of Beachport (see below). The much smaller variance of BT in the glider measurements also indicates that during this season, strong bottom upwelling and persistence/preconditioning was in place. Hence, El-Niño was indeed a player in the availability of colder waters (an overall mean) but the strongest setup occurred within the weather band and intra-month timescales.

A spatial view of the extreme events previously highlighted can be evaluated within the weekly means of SST and Chl-A anomalies, presented in Figures 6.27, 6.28. On the top diagonals, the weekly means of January 2016 are presented, while bottom diagonals pertain to the March weeks. The January event had an unusually large and strong plume which occupied most of the LS. The wind stress was stronger for the whole EGAB, and with stronger SST signals also at the northern regions (Eyre Peninsula and north of CB mooring). Again, in the western and southern regions off Portland, the SSTs did not develop such extremes. Over the KI region, the SST signature was not as strong as in the BC, even with the stronger winds. A weaker anomalous plume was formed, which followed the isobaths. A bulge of cold waters ($SST < -2°C$) is present in the following weeks, as the wind relaxed toward weaker north-westward anomalies. After almost a month of anomalous upwelling winds, the plume is fully developed

and even starts to meander, with filaments extending from its boundaries. Note how this particular scenario is very similar to the idealised experiment in chapter 4 for the entire region.

In the CHL-A anomaly maps, Fig. 6.28, the primary production estimates were also unusually high, particularly in the early weeks, decaying towards normal conditions at the end of the January. As a reference, monthly remotely sensed CHL-A values in the area are stronger in March than in January, and values are close to $1\,\mathrm{mg\,m^{-3}}$ and $0.7\,\mathrm{mg\,m^{-3}}$ respectively (not shown). Some care here is required, given that cloud cover affects the estimates of the weekly CHL-A anomalies, particularly for 1–12 of January (not shown). Nonetheless and overall, the difference between the northern and southern BC regions is absent in Fig. 6.28 — the CHL-A is a continuous signal from Portland to the plume region. Hence, the remotely sensed CHL-A alongshore variability did not follow exactly the SST anomalies — the euphotic zone and nutrient availability is not solely correlated with SST anomalies. The estimated values for mid-late January are very high. As we show below, the increase in primary production at the BC in March is consistent with the glider measurements. The transition to normal CHL-A concentrations towards the end of January appears to be related to a lack of extreme upwelling to sustain the higher than average primary production — mean SST anomalies in the region reached normal values at this month.

The alongshore surface velocities in January are also consistent with the stronger winds that were present during this period, with magnitudes up to $0.3\,\mathrm{m\,s^{-1}}$. As the winds reduced, the velocities were modulated and changed direction, particularly in the outer shelves and in the vicinity of the coastline. Note that the surface velocity is strong up to the $200m$ isobath; its curl onshore (offshore) of the jet is then favourable to upwelling (downwelling).

On the other hand, March was also a strong event, but with a different development. First, the SST did not propagate as strongly and far into the LS. The surface signal reached extreme lower values ($-2°C$) within a much smaller wind impulse function — see Fig. 6.27 bottom panels and the Fig. 6.26 top panel. The core of the anomalies remained between Cape Jaffa and Port McDonnell, at the BeachPort region. The plume also developed the same type of meandering in the same locations. Hence, this confirms that surface waters that reach the LS are largely from north of Port Macdonnell.

CHL-A was more confined onshore and to the BC instead of following the outer plume jet towards the west in the LS. A small-scale signal, with strong negative CHL-A values (much clearer waters than the mean) also appears in the vicinity of BeachPort and the Bonney Lake (first bottom panel in Fig. 6.28). It's important to note that this clear water signal was in tandem with the stronger bottom signal

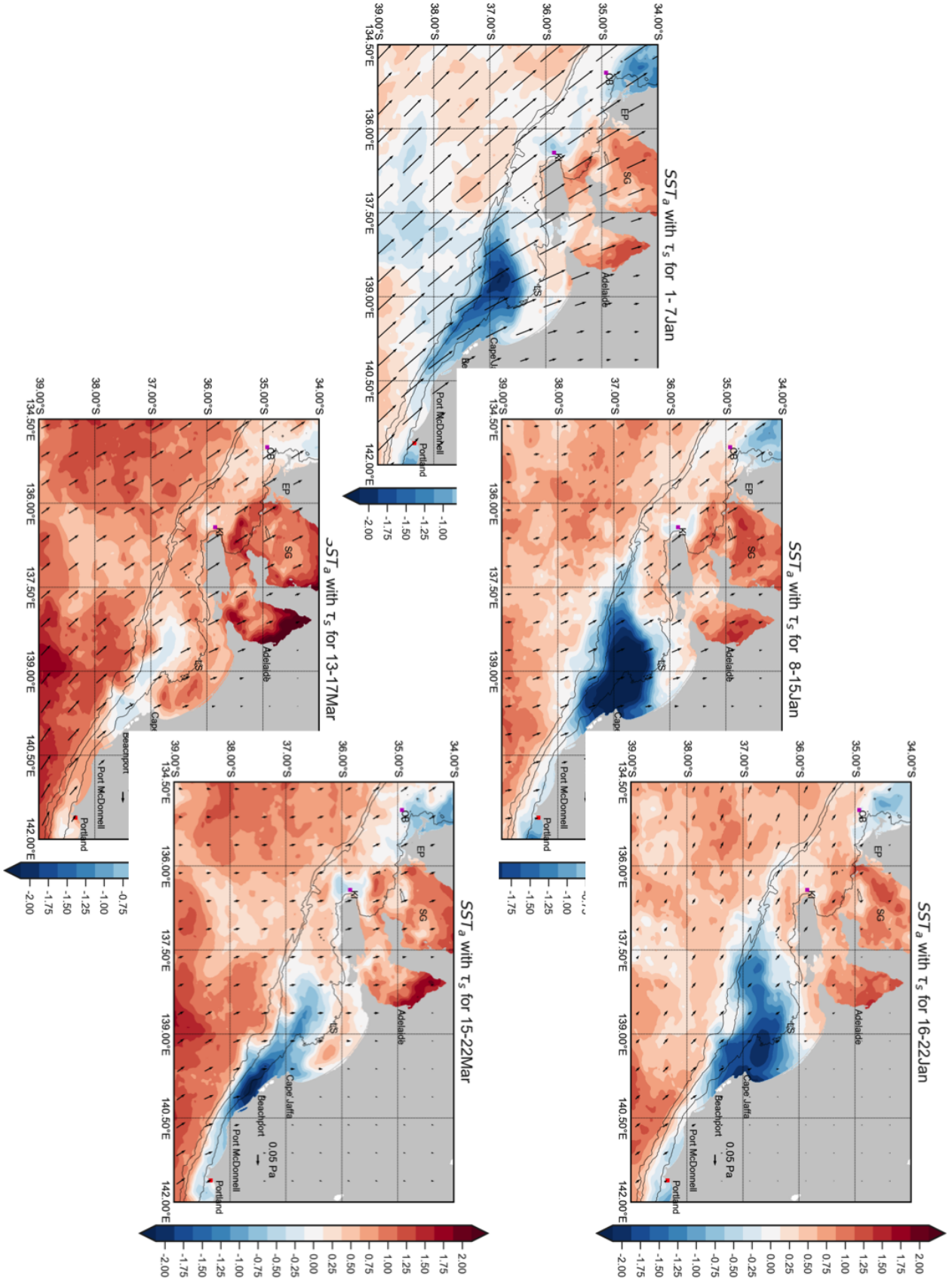

Figure 6.27: The SST anomalies (MUR, $^{\circ}C$) and wind stress (CCMP, Pa) during the extreme events in summer 2016. Top diagonal: Weekly means during the January event. Bottom diagonal: Weekly means during the March event. Thin black lines delimit the 50, 200 and 1000m isobaths.

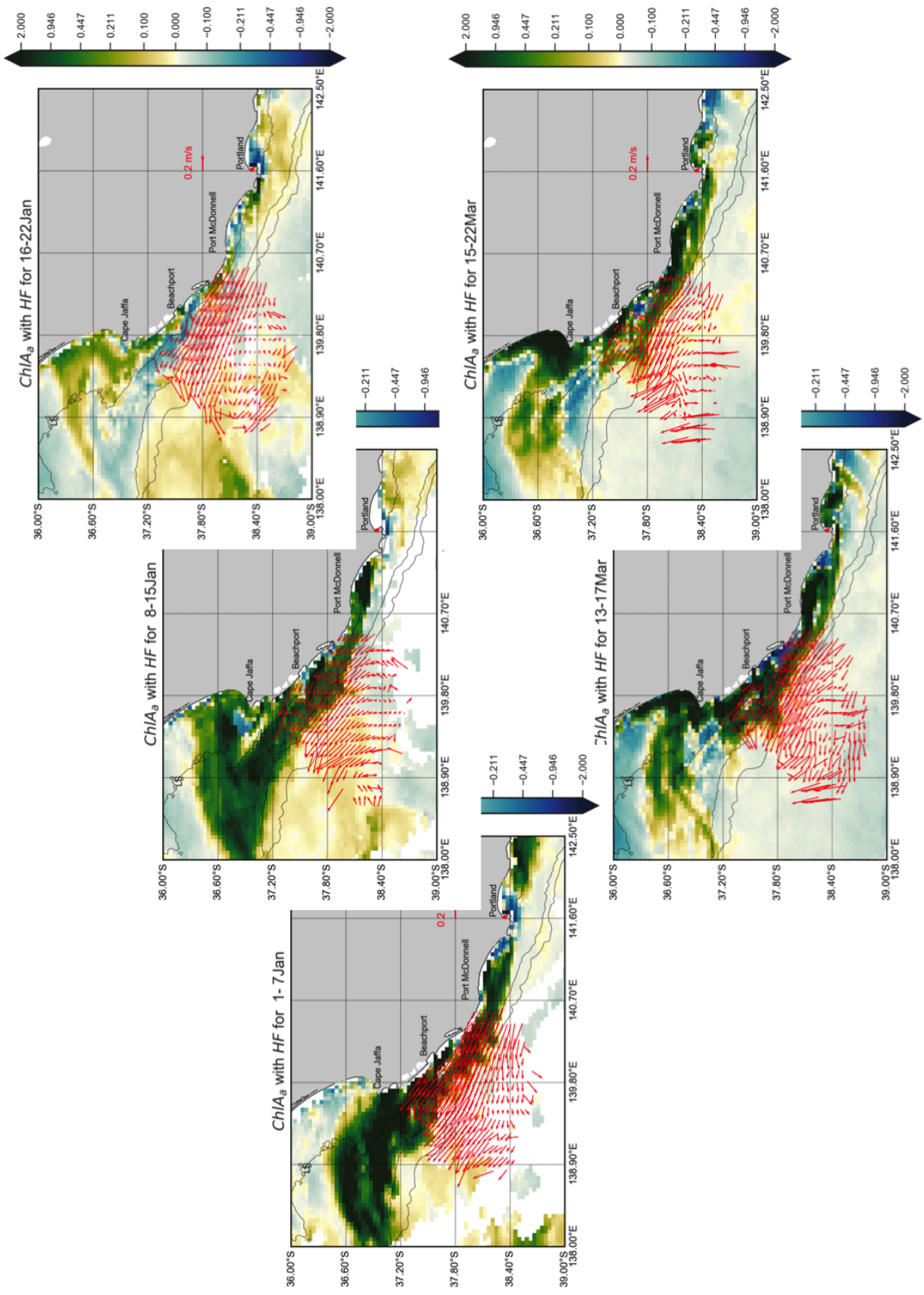

Figure 6.28: Same as in Fig. 6.27 but for CHL-A anomalies (MODIS-OCI, mg/m^3) and mean HF-Radar surface velocities (m/s). Coverage is limited between 12–15 Jan 2016 for both CHL-A and HF radar estimates.

found at the $100m$ isobath at March 16 (third panel in Fig. 6.26).

Although the surface velocities were still north-westward, they appear weaker at the inner-shelf and also more steered by the small topographic features. In the same regions of the small-scale CHL-A signal, the flow is more offshore than alongshore, indicating a stronger upwelling in the BeachPort region. Offshore, the SAC surface signal was indeed absent during the upwelling events, consistent with the BRAN mean results for the region.

So, both upwelling events were related to strong winds, but the stronger wind impulse in January and SL anomalies provided a larger plume in January than in March. Although we don't have continuous measurements at the BC during January, the stronger anomaly developed in March with a weaker wind impulse function suggests the first event could have preconditioned the entire season in the EGAB (it certainly preconditioned the KI region).

The cross-shore hydrographic fields during mission 1 and over the southern sector at the BC are shown in Fig. 6.29. Note first that distances (bottom x–axis), are measured from the start of the segment, the dates of the measurements are presented at the top x–axis, with this transect corresponding to two days of measurements (7–8 Feb, time in UTC).

This transect was obtained before the anomalous warmer conditions took place along the region and just after a strong negative anomaly peak in winds, but with moderate SL anomalies (see Fig. 6.26). The overall slope of isotherms and isopycnals clearly reflects upwelling conditions. From the ocean, a warm and salty surface mixed layer is found within the upper $50m$, reducing to $25m$ at $8km$ from north-east, which is $\approx 15km$ off the coast — see bottom right in Fig. 6.29).

Strong upwelling is found onshore, with $13°C$ waters present at the coast. Note the strong cross-shore density gradient at the surface; $d\sigma/dx \approx 0.8\,\mathrm{kg\,m^{-1}}$. Also, the distance from the coast to the upwelling front at the surface is of the order of the R_i defined above.

If one considers a piece-wise linear function, the slope of isopycnals has two positive slopes; 1. An inner-outer shelf one (at $3 - 30km$), 2. an oceanic one ($30 - 50km$). An upwelling front is clear in the salinity picture as well as in the clear waters (low CHL-A) offshore of the $75m$ isobath. The fresher waters onshore of that isobath below the SML can be related to the $z = 150m$ depth. The minimum salinities during these two days were indeed very low, reaching close to the minimums of the observational record ($\sigma_{37.1}$) and close to the surface ($z \approx 25m$) — the upper left arm in Fig. 6.25 bottom right.

Maximum and vertically homogeneous values of CHL-A were present close to the coast and followed the $\sigma_{26.4}$ offshore (red line). Values were in excess of $1mg/m^3$ for both the coast and in the Deep Chlorophyll Maximum (DCM). Clearly, the

CHL-A sensors were unbiased during this segment (zero values at $z > 100m$ in the outer shelf). There is no coverage for remotely sensed CHL-A in this period (high occurrence of clouds from 6-12 of Feb — not shown).

In the northward alongshore transect that occurred in March (Fig. 6.30), we also synoptically capture an upwelling event. When the glider started to move towards the northern region of the BC, following the $120m$ isobath, a relatively deeper SML/DCM was present (until 6 March). As the glider moved to shallow isobaths ($80m$) it encountered an upwelling circulation ($75km$ from the start of the segment), with increased noise in the measurements, also seen by the filtered isopycnals.

One day later, after reaching the BeachPort Valley ($110km$ and $z \approx 90m$ — see Fig. 6.30 bottom right panel), a complete upwelling has taken place, with a lack of both SML and DCM, and the appearance of cold, fresh and clear waters at the bottom. At this particular day, intense solar heating, low clouds and both wind curl and alongshore winds peaks occurred, followed by the first strong variability in the SST anomalies for the mean region (see Fig. 6.26 first and third panels). The surface signature of this upwelling event was very localised in both time and space. Taking into account the local wind conditions at that time ($0.07Pa$ — accounting for the seasonal cycle), the idealised Ekman transport is not enough to provide such a strong value alone ($EkT_{w_{T4}} = 8m/day$).

The effect over the bottom waters also appears more long-lived, given that low CHL-A waters are more frequent close to the upwelling event and below the SML. As the glider moved northward and over the BeachPort bank ($140km$ from the south), downwelling is evident, with a thick DCM reaching close to the bottom (as such the SST jumped slightly closer to $16°C$). Slightly to the north, below the SML, the pattern reverses again and we observe isotherm uplift, fresh and clearer waters on the equatorward side of the BeachPort bank/headland. It is important to note that overall, S_A values here were not so low as in the first mission at the cross-shore transect. This is expected given the previous warmer conditions and weaker upwelling winds.

The overall upwelling velocities during the event between 6–8 March can be considered larger than $25m/day$. For example, at $z \approx 30m$ at 7 March ($90km$ from the south-east), there are $14°C$ waters along the $90m$ isobath (white colour). One day later, in the same isobaths, these waters were at the surface — an implied $30m/day$ as the glider moves towards the BeachPort valley region. Indeed, after crossing the rim of the shallow valley, upwelling conditions prevail.

The same can be found in salinity and chlorophyll values after crossing the BeachPort Bank. There, the isopycnal of $\sigma_{26.8}$ slopes upwards after leaving the bank – $\approx 20m/day$ isopycnal displacement. Hence, lateral density gradients in

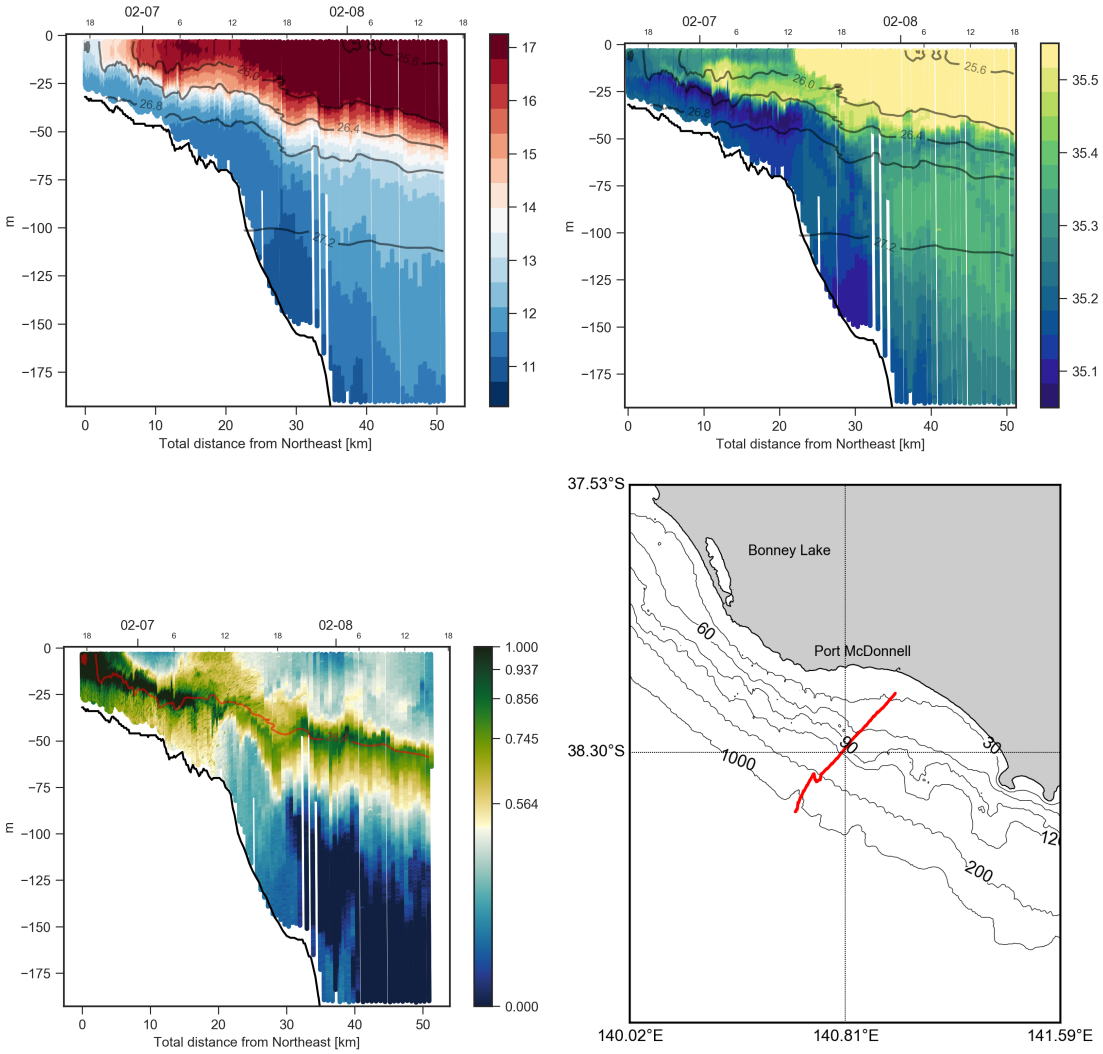

Figure 6.29: The M1-S6 hydrography Transect. (a) Potential Temperature ($°C$), (b) Absolute Salinity (g/kg), (c) CHL-A (mg/m^3) and (d) location of the segment. Isopycnals (in-situ density) are contoured in grey, while the red line in (c) is the $\sigma_{26.4}$. Distances are cumulative from the start of the segment and the in-situ density contours were filtered with a Gaussian filter (std= 0.9) to improve visualization. The upper x-axis denotes the February 2016 date in UTC. Local Time is $2hr$ earlier. Bottom relief is estimated from the Geoscience Australia Bathymetric chart and slightly shifted downward as a reference

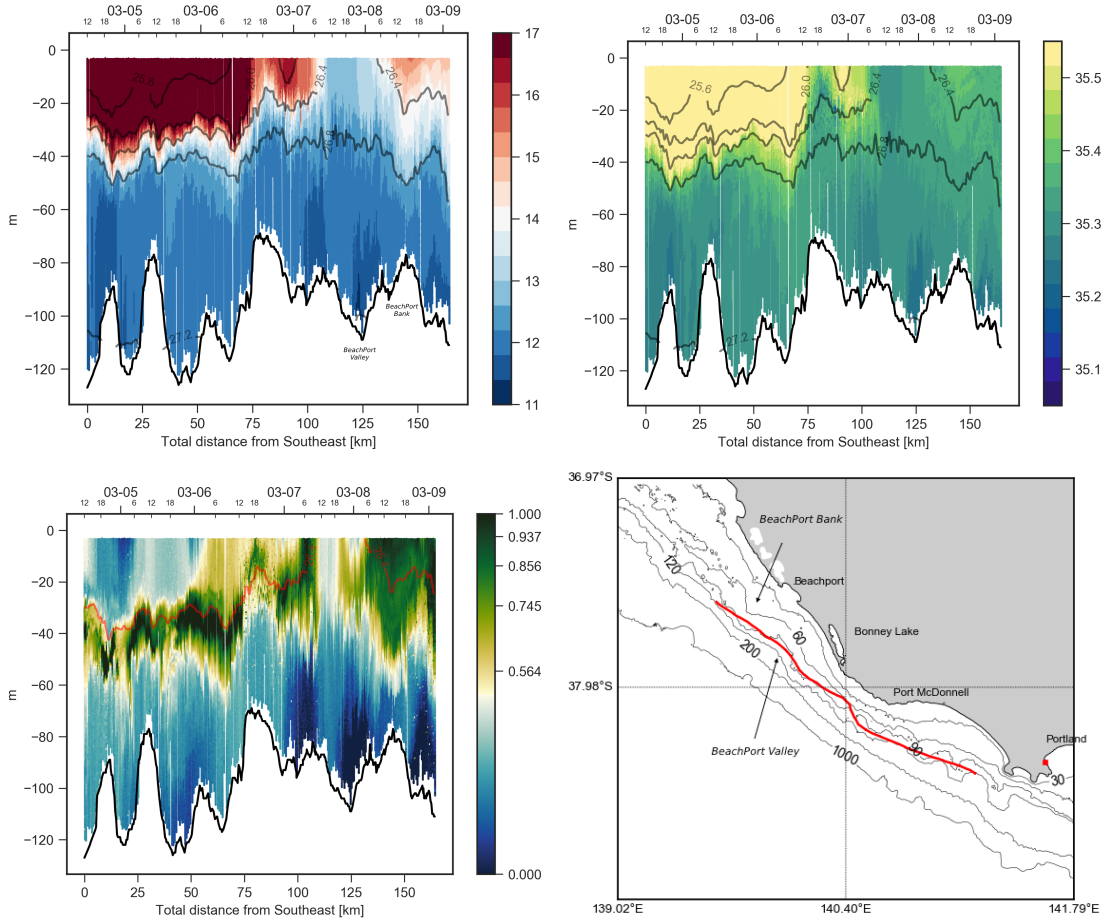

Figure 6.30: Same as fig. 6.29, but for the M2-S4 segment.

these regions were indeed large.

After the BeachPort Bank, the BT minimums at the $100m$ isobath of the entire sampling was found (Fig. 6.31). The previous $T < 14°C$ waters are now at the surface over $30km$ offshore, and indeed bottom temperatures are coldest in the locations noted above. The source waters are clearly from below $150m$ and salinities were also at minimum values, as well as low CHL-A values (not shown). This was the northernmost segment; after that, the glider turned southward, while the SST and plume anomalies were developing and wind was mainly north-westward.

Another alongshore transect, Fig. 6.32, in the southward motion, sampled at approximately the same positions, but slightly offshore. Between 120–$130m$, in the alongshore direction, upwelling was again associated with the bottom relief.

The alongshore transect was within the March extreme upwelling week $18 - 21$, which was exactly when the plume was prominent (see Fig. 6.27). Hence, through most of the sampling, the flow was strongly northward — SL anomalies were much lower. The glider passed through the same bottom features: first the BeachPort headland/bank ($15km$ from north-west), followed by the Valley (30-$40km$) and into deeper isobaths (after $\approx 60km$). Equatorward of these two features, cold and

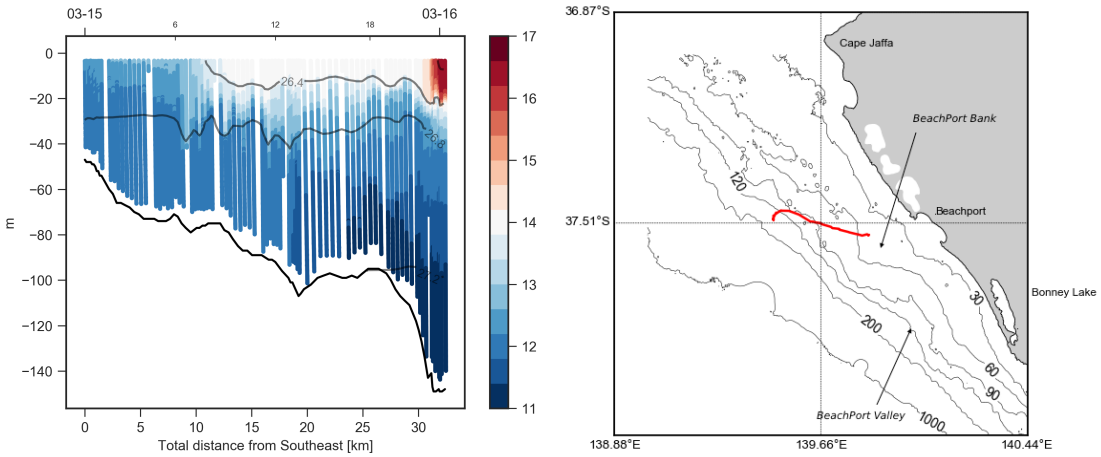

Figure 6.31: Same as fig. 6.29, but only for Conservative Temperature to the north of the BeachPort Bank — where the minimum temperature of the missions is located (M2–S13 segment)

fresh waters were found close to the bottom. Below the SML, values are much lower if compared to the M2–S4 transect. The surface signature is also smaller, the $14°C$ waters occur at $z = 25m$ — this segment was performed in deeper waters ($> 140m$) than the others described above.

Note also the strongest signal in salinity, north of the BeachPort Bank is consistent with the glider profile taken 2 days earlier in Fig. 6.31. The upper isopycnals (e.g., $\sigma_{26.8}$) highlight that upwelling was strongest earlier (Mar-18) while toward the south it was diminishing — note how the anomalous winds were also reducing at this same time (Fig. 6.26 top panel).

The overall downward displacement of the isopycnals only changes sign again close to the BeachPort Valley, where the $\sigma_{26.8}$ shifted upward. There, internal wave activity seems to be present, with wavelengths between $10km < \lambda < 30km$ and located northward of the southern rim of the BeachPort Valley. The associated vertical velocities within this location are $w_{\sigma_{26.8}} = 40m/day$ at the base of the SML $z = 50m$ at the $40km$ from Northwest (19 March). The horizontal scales are the same or less than the topographic features, and the time-scales are at or below the local inertial period.

Upwelling favourable winds were acting during the whole duration of the segment, but after 20 March the winds weakened. This explains why the SST were slightly increasing towards the end of this segment (see also Fig. 6.26). The CHL-A sensor appeared to be more contaminated with noise than in the previous results, particularly during the strong upwelling. The DCM is also above the SML. Below, vertical mixing and bottom attached values are present, particularly close to the bank and valley rims. At this time and locations, high CHL-A values are associated with the fresher and colder waters, indicating alongshore transports, intrusion of nutrient- rich waters and strong vertical mixing. The remotely sensed estimates at

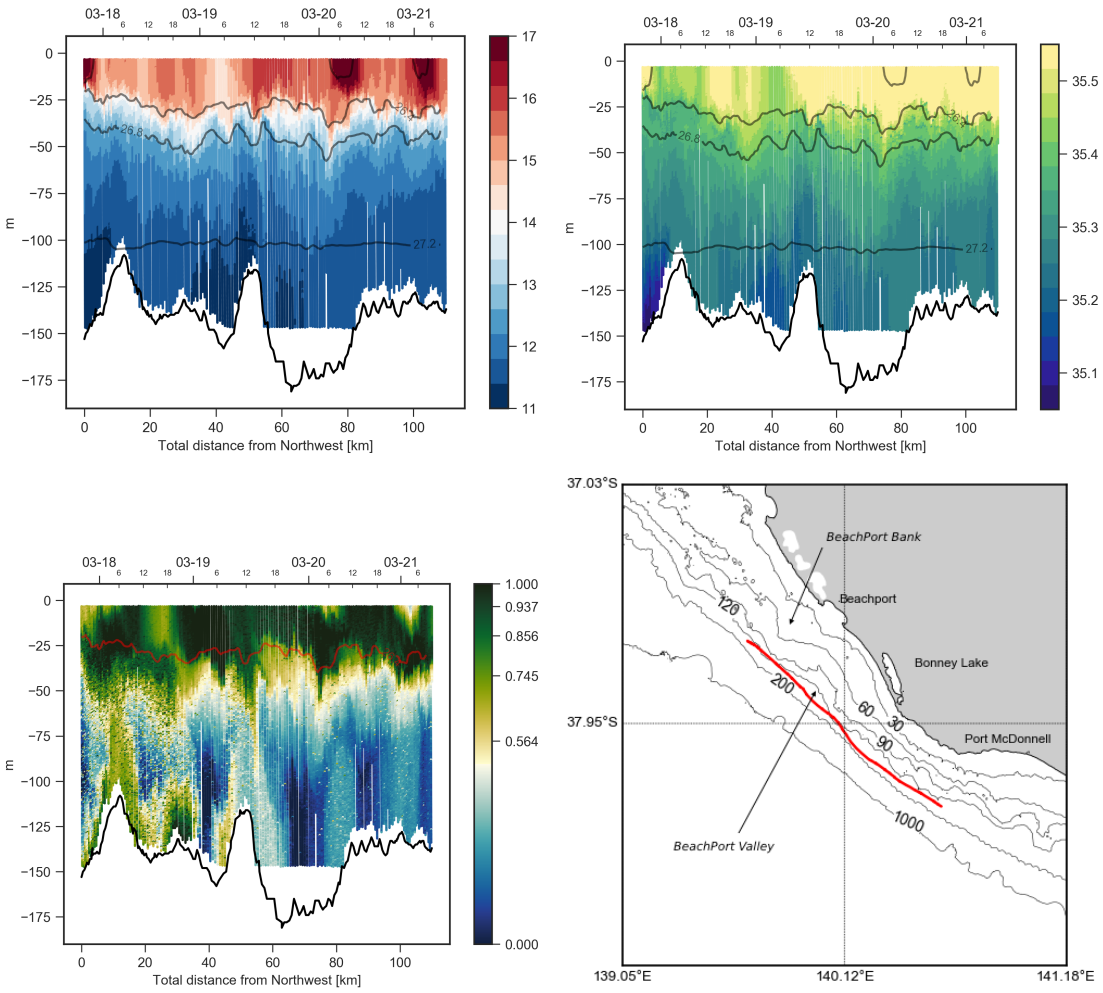

Figure 6.32: Same as fig. 6.30, but for the M2-T18 segment

the exact dates above were also mostly absent in the satellite data, but before and after this segment, CHL-A values were in excess of $1mg/m^3$, consistent with the results in Fig. 6.28.

The colder signatures at the bottom highlight the bottom upwelling similarities with the idealised experiments in Chapter 4. Despite the highly idealised stratification, constant winds, and lack of surface thermal forcing, the similarities between the above results and Figs. 4.7 for example are striking. The relatively small topographic features are then clearly affecting the BC upwelling, along with the alongshore gradients.

6.4 Conclusions

In this research, through an extensive collection of observations and models, we analysed, verified, explained, and extended the role of several oceanographic and atmospheric influences in the EGAB upwelling system and their relationship with extreme events.

Consistent with previous studies, we found that the ENSO effect is indeed a large component in the SL extremes along the Australian eastern boundary (Clarke et al. 2004; Li et al. 2004; Middleton 2006). Although its effects can be related to an excess of $10cm$ in SL amplitude in the year-to-year variations along the north-eastern margins of Australia, the direct effect is reduced towards the EGAB given the frictional decay of long waves. Moreover, taking into account a larger portion of the spectrum (monthly estimates), the partition of the energy along the coastline varies and a considerable amount of energy, incoherent with ENSO, helps to explain about half of the total month to month variability in the EGAB. The EGAB region can be considered as a highly sensitive region to remote forcing, with an important origin of variability located in the western GAB.

In that sense, our results mimicked several previous results (mostly Li et al. 2004; Middleton et al. 2007a) off the southern shelves:

- ENSO is direct correlated with extremes in SL, BT and thermocline depth;
- Summer coastal winds and SST are not directly correlated with ENSO; and
- The coastal waveguide clearly provides ENSO related signals to travel towards the EGAB shelf and slope;

On the other hand, we also extend the understanding of other aspects in the atmosphere and in the ocean that affect upwelling in the EGAB, including:

- Anomalous tropical winds contribute to monthly SL anomalies in the EGAB during summer;
- The western GAB also contributes with a significant variance to anomalous SL at the BC at monthly timescales;
- Up to 50% of the anomalous sea level variance along the BC can be directly related to tropical and ENSO origins;
- Summertime upwelling favourable winds and high atmospheric pressure within the GAB are related to positive states of the SAM index; and
- There are seasonal lagged effects of ENSO in SST, and a delay in the onset of the thermocline that explains the SST response during ENSO events.

Of these findings, the confirmation of influences of SAM in the upwelling through winds is relatively new. A strong positive SAM was found to be correlated with stronger alongshore winds anomalies over the GAB in the last 25 years — the western GAB (Esperance) appears a good gauge for this influence. The large-scale influence of SAM in MSLP in the region is not new, but we showed that when the SAM is highly positive, the wind direction and alongshore magnitudes are more upwelling favourable than in normal years. A direct effect in SST, however, was not found as in Middleton et al. 2007a; the definitions of a categorical Antarctic influence index and different areas, products, and methods appear the cause of this discrepancy. Moreover, we found that the 2016 extreme upwelling season was particular in the sense that it occurred when both SAM and ENSO had strong and positive values.

Above-average values of SAM were present from winter of 2015 to 2016, together with high MSLP, positive wind stress curls, eastward wind anomalies, and ENSO coherent widespread cooling in winter (summer) at the surface (sub-surface). The role of this large-scale, oceanic wintertime conditions affecting the SAC and the FC was not explored, but these conditions affected the summer of 2016, where at the coast, significant uplift of the thermocline associated with ENSO and the strong summertime winds permitted the upwelling season to be one of the strongest over the last 15 years. Clearly, several effects acted together, but ENSO effects were particularly important, influencing the onset of colder temperatures over the shelf.

Although a more careful statistical treatment is required, results here appear to support three hypotheses:

- That when SAM is positive and beyond the normal conditions, extreme upwelling is more likely;
- That if the above occurs, with positive ENSO phases (El-Niño), extreme upwelling is even more likely;and
- That the lack of direct ENSO-alongshore wind correlation is related to SAM.

Additionally, we provide an ad-hoc fix to the last hypothesis of Middleton et al. (2007a); El-Niño events can substantially reduce wintertime **and** summertime shelf-edge currents. Several observations here support a statistically significant weakening (enhancement) of the south-eastward SAC flow at the BC during summertime under El-Niño (La-Niña) conditions. The reason why this hypothesis was incomplete in the Middleton et al. (2007a) study lies within the limited model results and the methods used. Their time series used for the transport calculations was too short and they didn't remove the seasonality of the series; with their $\approx 10y$

of data, the effective sample size is very small. Only a remarkable correlation, larger than their ENSO-SL correlations would be statistically significant. Indeed, even the wintertime conclusions based on the global model are not robust, but fortuitously correct as we point out in this study — the ocean reanalysis, SL, and BT are coherent with ENSO year-round in *monthly* estimates.

Their results for the relationship between SL,BT and ENSO were also confirmed, but we found a much stronger and more useful relationship; within the last decade, there is an almost one–to–one relationship between BT in the EGAB and SST in the Pacific (ONI index). Also, the ENSO effects, through shelf BT, are seasonally locked to summer, while in winter they are less coherent. This should provide useful information, as well as the SL and SST relationships found here and elsewhere, for management of fisheries (recruitment) and statistical prediction (Clarke et al. 2004).

The SST interannual variability also clearly indicates the strong and expected relationship with the atmosphere and how ENSO persistence can affect SST. The persistence appears to affect the EGAB, on average, over the following summer after significant trends in the central Pacific SST anomalies develop ($15mo$). These persistence effects occur at large lags, provide significant information and were related to both the propagation along the coast and interactions within the ocean and atmosphere. The propagation pattern of the lagged effects was clearly found in SL as part of the tropical persistence of the ENSO signal and to a slower and later onset of the seasonal thermocline peak along the BC. Another lag relationship ($40mo$) was found to also be bounded to broader scales and with atmospheric connections. The detection of these effects appears to provide an explanation of why there can be a delay in the occurrence of extremes in the EGAB during ENSO events. Particularly, the suggestion of the Ningaloo Niño energy affecting the EGAB upwelling appears another hypothesis that worth further analysis. These effects provide useful information for SST, particularly for warm conditions, and could be explored within statistical seasonal prediction. A successful prediction for upwelling appears to be more bounded in time, with the spring-summer transition important, given the seasonal locking of ENSO effects and BT in summer and the role of summertime winds.

The BC region is considered to be the best location for monitoring the summertime shelf SST variability for the EGAB; the region is highly sensitive to extreme events, it is well correlated to SL and provides a good pattern correlation up to the northern limit of the EGAB. The spatial autocorrelations with SL also point to a different regime south of Portland that appears related to both shelf-break currents and CTW dynamics. This dynamical boundary also appears related to the atmospheric influence within the Tasman Outflow region. The coastal anomalies

in these areas are much higher and with a different magnitude, both at the shelf and in the open ocean. This suggests that, although they share similar alongshore favourable upwelling winds in summer, their interannual variability are markedly different.

Finally, we explored with more detail the onset of extreme conditions during the 2015-2016 period. Apart from the influence from previous autumn-winter conditions with colder waters in the oceanic regions, coastal observations of SST and BT were the first to reach colder anomalies in autumn, together with anomalous north-westward shelf-currents within the EGAB. The coastal SL signal followed these anomalies in winter, clearly showing that away from the shelf, thermocline uplift was already in place. During summer, the sub-surface low temperature values were amplified over the shelf; (a) by the normal mean winds of the season, (b) by the anomalous summertime northward winds, and (c) by further ENSO persistent effects along the shelf and slope. SST was also damped at the thin SML by strong air temperature anomalies that affect the region as a whole. Accounting for the anomalous heat flux in 2016, the 2015/2016 upwelling was one of the strongest on record.

The ENSO effects were maximum over the outer-shelf, and with a weaker SAC. Even though the linear wave theory and the internal Kelvin wave paradigm are not entirely valid in the region, it's still useful given that wave modes are trapped, propagating and interacting with the background flow along the southern shelves. The SAC was clearly reduced in 2016, at the surface and in its flanks; a lateral 'squeeze' that shifted the core of the jet towards slightly deeper levels in 2016. The mean outcome was a strong reduction of the downwelling conditions imposed at the slope and more upwelling — through the interior and the BBL. For the upwelling over the shelf, the anomalous conditions during summer permit upwelling waters from up to $200km$ offshore and $350m$ depth along the slope to change vertical positions and to be located over the shelf. The ENSO persistence effects were explicitly used in showing the onset of the thermocline depth anomalies, as well as the weakening of the SAC as a whole. Clearly, the deeper FC dynamics and the CTWs in several frequencies had a role in the circulation over the slope region; whereas both are related to ENSO and with spatial scales not previously detected. Hence, more studies for the current response is warranted.

We found that the match between monthly to weather band frequencies is critical in the setup of extreme upwelling events. Strong monthly SL anomalies *matched* with strong northward winds were the key ingredient to the extreme events during JFM of 2016. The season exhibits opposite extremes, going from an extreme upwelling from Dec-Jan, relaxing towards extreme warmer conditions in February, before suffering a much shorter but still extreme upwelling condition in

March. Our glider sampling was fortuitous in the sense that we could measure the BC upwelling during such a unique event with high fidelity. Several independent observations and sensors confirmed the extreme upwelling of the season. Extreme cold, fresh and clear waters intruded over the shelf resulting in: (a) highly skewed sampling populations; (b) FC water masses present both at the surface and over the shelf, and (c) strong diapycnal mixing along a pathway of rapid heating and small evaporation.

The upwelling circulation, bottom uplift, and the upwelling plume were also far from being homogeneous, with high spatial variability and different responses in time regarding wind impulses. Remote sensing estimates and glider observations indicate that alongshore variability in source waters and upwelling also occurs within the BC; the Northern regions are much more prone to extreme events. This spatial variability is also found to be particularly related to the bottom relief in the vicinity of the Beachport. There, the BC responded much quicker to the winds, with stronger bottom upwelling related to the valleys and banks/headlands presented at relatively shallow isobaths (50-150m). On the equatorward side of the valleys and banks, stronger bottom upwelling was found, on several occasions. Although the sampling here was done in an extreme scenario case, as discussed, the topographic upwelling mechanism would pertain all the time, even in the barotropic limit, as shown in Chapter 4. The intensification on the equatorward side, generated by the density field in conjunction with advection should also always occur; ocean heat flux response, advection, mixing and vertical density would always be dependent on the topography. The scales of vertical velocity estimated above are in the same position and within the same order of magnitude as the alongshore transects presented in Chapter 4. The presence of internal waves in higher frequencies attest to what we would expect in reality; noisier harmonics are also present but are related to the bottom relief. Thus, previous numerical idealised results of upwelling in the BC coast region are indeed 'confirmed' by our synoptic observations. The increased primary production in the region appears unique, and the impact of this type of extreme upwelling extreme event has on the ecosystem remains uncertain. Although far from addressing all the physical mechanisms that are affecting upwelling, this study suggests that some important insights have been gained in relation to the role of ocean current interactions with ENSO and the role of SAM. Previous studies indicate that the SAM is weakly but **negatively** related to ENSO at interannual scales while being correlated with tropical convection at intraseasonal scales (Pohl et al. 2010). This opposite relationship appeared to have changed with global warming, and under increasing global mean temperatures, models and observations indicate a flip to a positive relationship (Wang et al. 2013). This suggests that long-term changes in the BC

upwelling are already happening.

Chapter 7

Summary, Conclusions and Recommendations

This thesis investigates the dynamics and the variability of the summertime upwelling circulation along the Eastern Great Australian Bight (EGAB). This region is important because it supports roughly 1/5 of the total Australian fisheries value (Savage 2015). The Bonney Coast (BC), in the mid-south EGAB, is Australia's strongest upwelling region. Some studies have examined the impacts of wind-driven upwelling along the BC (e.g., Cai 1992; Middleton et al. 2003; Nieblas et al. 2009). Since the initial observations of Rochford (1977) and Lewis (1981) and Schahinger (1987), however, no study has examined the circulation or dynamics of the BC upwelling in detail. As a result, this region is regarded as a classic case of two-dimensional wind-driven upwelling (Middleton et al. 2003; Nieblas et al. 2009) with little regard for the role of topography, the role of Coastal Trapped Waves (CTWs), and with little attention given to its interannual variability and the climatological influences.

The primary objective of this thesis is to better understand the dominant physical drivers of the summertime shelf circulation of the EGAB using a numerical model and observations. I configured a regional, numerical ocean model, based on a widely-used Ocean General Circulation Model (OGCM), with realistic topography and coastal geometry; and with an idealised initial, surface, and boundary conditions. The observations used are from a wide range of different platforms, including satellites, moorings, HF radar, and tide gauges. Measurements analysed here are from long time series (tide gauges and satellite data) and an intensive observation program during the 2015/16 upwelling season. These observations are supplemented with climate indices and ocean reanalysis used to understand the interannual variability, the climatological influences on the BC upwelling, and to describe the 2016 season.

The key findings of this thesis include the first demonstration of the role of submerged headlands and valleys along the BC (Chapter 4); and the role of CTWs

in shutting down the upwelling circulation, including an explanation for why, how, when and where the CTW forcing is important in the GAB as a whole (Chapter 5). The analysis in Chapter 6 represents the most comprehensive observational study of the EGAB and the BC upwelling on record – with unprecedented observational coverage, from more observational platforms than ever before. Together with large-scale datasets (satellite and global reanalyses), we explain how and why the 2015/16 upwelling season was one of the most extreme seasons in the last 15 years.

In the high-resolution numerical experiments of Chapter 4, upwelling and downwelling circulations were found in different locations, with dependency on shelf-width and associated with the bottom relief. Along the BC, several submerged headlands and valleys with scales between 20–40km abound, and results with a $0.05Pa$ alongshore wind exhibited strong topographic locking and remarkable upwelling, exceeding $30m/day$ and bottom onshore velocities between $4-8km/day$. Upwelling was found generally confined to the valleys and downwelling on top of the submerged headlands.

The circulation was shown to be qualitatively consistent with barotropic vorticity dynamics, where bottom velocity is inferred from the acquisition of anti-cyclonic (cyclonic) vorticity as a fluid column moves equatorward across the headlands (valleys). Upwelling was also found most intense on the equatorward side of the submerged headlands; a fact long known from other upwelling regions in both observations and modelling studies (e.g., Arthur 1965; Peffley et al. 1976; Barth et al. 2005; Gan et al. 2002b; Whitney et al. 2009a). An explanation for this preferential upwelling is given by baroclinic pressure gradients, setup by the density field that generates onshore geostrophic flow — a positive feedback mechanism. This intensification pattern result is robust in several aspects; it explains the upwelling in different regions of the EGAB, was not sensitive to sign changes in the Coriolis parameter, developed markedly under stratified conditions, and glider observations in Chapter 5 supported its existence.

In Chapter 5, we investigated the time scales of the upwelling circulation, the shut-down of interior upwelling flow in response to the passage of CTWs, and role of remote forcing. The shut-down by CTWs is a time-dependent adjustment to the simplified shut-down time scales, given the existence of a shelf and propagating wave solutions from an origin. A geographical origin of the CTW front lies in the west of the Great Australian Bight (GAB). The results are consistent with theory, with the weakest (largest) upwelling closer (farther) to the CTW origin. Our periodic experiment highlights the role of remote forcing in driving strong bottom flow and deep canyon upwelling in the Kangaroo Island (KI) region. The phase lines of the CTW propagation highlight onshore-offshore phase differences, and a stronger flow developed in the northern sector of the BC. Not surprisingly,

the bottom flow is intensified in the same locations as those in the wind-forced experiments (Chapter 4). Clearly, a deeper verification of the geographical origin in the west appears important, as well as the lack of surface signature of strong upwelling there, even within the narrow shelf sectors.

Although our modelling study only explicitly assessed the impact of 10-day period CTWs, our numerical results provide strong intuition about the role of winds and the remote forcing in general. For example, in strong El-Niño years, Thevenard would have a surge amplitude of about $-5cm$ (see Chapter 6), that would last for many seasons. The propagation of this signal as a mode-1 CTW, for example, will have a similar effect – with an equivalent long surge of low Sea Level (SL) and shelf alongshore pressure gradients associated with the wave solution. Linearly superimposed with a seasonal and/or anomalous wind field (high amplitude weather band CTW and local wind-stress forcing), this will clearly help in precondition shelf bottom waters for extreme upwelling. Idealised experiments with a much longer periodic paddle, with and without winds, and with more frequency components (e.g., a SL paddle with data from the Thevenard station), also strongly support this, but are not presented in this work. Thus, remote forcing is a very important component in the EGAB.

Previous studies have identified that climatological factors with tropical origin – namely El-Niño-Southern Oscillation (ENSO) – influence coastal sea-level off Southern Australia, via the coastal waveguide (Pariwono et al. 1986; Li et al. 2004; Clarke et al. 2004; Middleton et al. 2007a). However, there is a large knowledge-gap in relation to the BC upwelling interannual variability. The analyses in Chapter 6 address this gap, and confirms and extends previous results on the influence of ENSO in the region. Specifically, we examine the correlations between climatological indices and the EGAB upwelling. We show that more upwelling favourable winds occur during summertime when a strong and positive Southern Annular Mode (SAM) phase develops. Also, the coastal waveguide effect enables the ENSO signals (a coastal/slope trapped wave) to reach the BC and affect upwelling through a delayed uplift of the summer thermocline, lowering of the SL, and setting up strong Bottom temperature (BT) anomalies. A close to one-to-one linear relationship between Sea Surface Temperature (SST) anomalies in the central Pacific and BT in the EGAB was found. The long propagation nature of ENSO generates delayed effects along Australian eastern margins. For the EGAB this appears to explain the onset timing for maximum upwelling, and a more efficient interior and bottom boundary layer (BBL) flow in El-Niño events. We conclude that several climatological factors "pre-conditioned" the EGAB to extreme upwelling in 2016. Extreme SST anomalies, stronger weather band winds, low SL, highly skewed waters, high Chlorophyll-A (Chl-A) values, and cold

and fresh water distribution over the shelf created the unique event. The high fidelity glider observations indicated deeper water sources — Flinders Current (FC) waters — that were vertically mixed and reached the photic zone. Observational results were consistent with our previous idealised model experiments, showing the same alongshore variability of upwelling with colder and fresher waters on the equatorward side of the submerged headlands.

The analysis of climatological factors that influence the BC upwelling lead us to speculate about the possible development of a predictive tool for the BC. Specifically, results in Chapter 6 show that several climate indices are statistically correlated with the circulation in the EGAB with lead/lag times. This is an area of potential future work. Another area that warrants further development, involves the addition of data assimilation to the regional model used here under realistic conditions. The 2015/16 upwelling season included unprecedented observational coverage. A comprehensive reanalysis of the shelf circulation during this period – generated through a data-assimilating model - would undoubtedly shed even more light on the subtleties of this important upwelling region.

The numerical results and the observational analysis also provide guidance that could benefit future observational efforts. Over the shelf, the lack of high-quality, continuous and fixed measurements over the BC is surprising. This important upwelling region, with a large coastal plume, is not monitored consistently beyond satellite measurements and some temperature loggers in lobsters pots! At the same time, we expect that direct monitoring of the plume would be a useful metric.

Direct observations and dynamics of the South Australia Current (SAC)/FC and its seasonal to interannual variability also needs to be addressed in more detail. While the global reanalysis is useful, modern and direct observations are necessary. Given the correlation with ENSO and the importance in the shelf source waters, the lack of shelf-break current observations is a 'blind spot' in the regional oceanography of the southern shelves.

Thus, the results in this thesis go some way towards filling the key knowledge-gaps of the oceanography of this region. Many aspects of the EGAB upwelling still remain open. This mainly includes the role of the deep ocean in promoting or suppressing upwelling and the potential predictability of the region. These topics will no doubt be addressed in future studies of the region, building on previous findings and results presented in this thesis.

Bibliography

[1] JS Allen, PA Newberger, and J Federiu. "Upwelling circulation on the Oregon Continental Shelf. Part I: Response to Idealized Forcing". In: *Journal of Physical Oceanography* (1995). DOI: *10.1175/1520-0485(1995)025<1843:UCOTOC>2.0.CO;2*.

[2] S. E. Allen and B. M. Hickey. "Dynamics of advection-driven upwelling over a shelf break submarine canyon". In: *Journal of Geophysical Research* (Aug. 2010), p. C08018. DOI: *10.1029/2009JC005731*.

[3] R. S. Arthur. "On the calculation of vertical motion in eastern boundary currents from determinations of horizontal motion". In: *Journal of Geophysical Research* (June 1965), pp. 2799–2803. DOI: *10.1029/JZ070i012p02799*.

[4] R. Atlas, R. N. Hoffman, J. Ardizzone, S. M. Leidner, J. C. Jusem, D. K. Smith, and D. Gombos. "A cross-calibrated, multiplatform ocean surface wind velocity product for meteorological and oceanographic applications". In: *Bulletin of the American Meteorological Society* (Feb. 2011), pp. 157–174. DOI: *10.1175/2010BAMS2946.1*.

[5] J. A. Austin and S. J. Lentz. "The Inner Shelf Response to Wind-Driven Upwelling and Downwelling*". In: *Journal of Physical Oceanography* (2002), pp. 2171–2193. DOI: *10.1175/1520-0485(2002)032<2171:TISRTW>2.0.CO;2*.

[6] V. F. Banzon, R. W. Reynolds, Diane Stokes, and Yan Xue. "A 1/4-Spatial-Resolution Daily Sea Surface Temperature Climatology Based on a Blended Satellite and in situ Analysis". In: *Journal of Climate* (2014), pp. 8221–8228. DOI: *10.1175/JCLI-D-14-00293.1*.

[7] J. A. Barth, S. D. Pierce, and R. M. Castelao. "Time-dependent, wind-driven flow over a shallow midshelf submarine bank". In: *Journal of Geophysical Research C: Oceans* (2005), pp. 1–20. DOI: *10.1029/2004JC002761*.

[8] Aike Beckmann and Dale B. Haidvogel. "Numerical Simulation of Flow around a Tall Isolated Seamount. Part I: Problem Formulation and Model Accuracy". In: *Journal of Physical Oceanography* (1993), pp. 1736–1753. DOI: *10.1175/1520-0485(1993)023<1736:NSOFAA>2.0.CO;2*.

[9] T. H. Bell. "Lee Waves in Stratified Flows with Simple Harmonic Time-Dependence". In: *Journal of Fluid Mechanics* (1975), pp. 705–722. DOI: *10.1017/S0022112075000560*.

[10] C. Boening, J. K. Willis, F. W. Landerer, R. S. Nerem, and J. Fasullo. "The 2011 La Niña: So strong, the oceans fell". In: *Geophysical Research Letters* (Oct. 2012), n/a–n/a. DOI: *10.1029/2012GL053055*.

[11] K. H. Brink. *A Comparison of Long Coastal Trapped Wave Theory with Observations off Peru*. 1982. DOI: *10.1175/1520-0485(1982)012<0897:ACOLCT>2.0.CO;2*.

[12] K. H. Brink and J. S. Allen. "On the Effect of Bottom Friction on Barotropic Motion Over the Continental Shelf". In: *Journal of Physical Oceanography* (Sept. 1978), pp. 919–922. DOI: *10.1175/1520-0485(1978)008<0919:OTEOBF>2.0.CO;2*.

[13] K. H. Brink and D. C. Chapman. *Programs for computing properties of coastal-trapped waves and wind-driven motions over the continental shelf and slope*. Tech. rep. Massachusetts: Woods Hole Oceanographic Institution, 1987, p. 46.

[14] Morton B. Brown and Alan B. Forsythe. "Robust tests for the equality of variances". In: *Journal of the American Statistical Association* (1974), pp. 364–367. DOI: *10.1080/01621459.1974.10482955*.

[15] J. A. T. Bye. "Oceanic circulation south of Australia". In: *Antartica Oceanology II: The Australian-New Zealand Sector* (1972), pp. 95–105. DOI: *10.1029/AR019P0095*.

[16] J. A. T. Bye. "The general circulation in a dissipative ocean basin with longshore wind stresses". In: *Journal of physical oceanography* (1983), pp. 1553–1563. DOI: *http://dx.doi.org/10.1175/1520-0485(1983)013%3C1553:TGCIAD%3E2.0.CO;2*.

[17] W. Cai. "A revised Layered Model - Application to the Bonney Coast Upwelling". In: *Estuarine, Coastal and Shelf Science* (1992), pp. 235–252.

[18] W. Cai, P. van Rensch, T. Cowan, and H. H. Hendon. "Teleconnection pathways of ENSO and the IOD and the mechanisms for impacts on Australian rainfall". In: *Journal of Climate* (2011), pp. 3910–3923. DOI: *10.1175/2011JCLI4129.1*.

[19] W. Cai, G. Shi, T. Cowan, D. Bi, and J. Ribbe. "The response of the Southern Annular Mode, the East Australian Current, and the southern mid-latitude ocean circulation to global warming". In: *Geophysical Research Letters* (2005), p. L23706. DOI: *10.1029/2005GL024701*.

[20] Wenju Cai and Peter van Rensch. "Austral summer teleconnections of indo-pacific variability: Their nonlinearity and impacts on australian climate". In: *Journal of Climate* (2013), pp. 2796–2810. DOI: *10.1175/JCLI-D-12-00458.1*.

[21] X. J. Capet, P. Marchesiello, and J. C. McWilliams. "Upwelling response to coastal wind profiles". In: *Geophysical Research Letters* (July 2004), p. L13311. DOI: *10.1029/2004GL020123*.

[22] David C. Chapman. "Deceleration of a Finite-Width, Stratified Current over a Sloping Bottom: Frictional Spindown or Buoyancy Shutdown?*". In: *Journal of Physical Oceanography* (2002), pp. 336–352. DOI: *10.1175/1520-0485(2002)032<0336:DOAFWS>2.0.CO;2*.

[23] David C. Chapman. "Numerical Treatment of Cross-Shelf Open Boundaries in a Barotropic Coastal Ocean Model". In: *Journal of Physical Oceanography* (1985), pp. 1060–1075. DOI: *10.1175/1520-0485(1985)015<1060:NTOCSO>2.0.CO;2*.

[24] J. A. Church and H. J. Freeland. *The Energy Source for the Coastal-Trapped Waves in the Australian Coastal Experiment Region*. 1987. DOI: *10.1175/1520-0485(1987)017<0289:TESFTC>2.0.CO;2*.

[25] M. Cirano and J. F. Middleton. "Aspects of the Mean Wintertime Circulation along Australia's Southern Shelves: Numerical Studies". In: *Journal of Physical Oceanography* (Mar. 2004), pp. 668–684. DOI: *10.1175/2509.1*.

[26] A. J. Clarke. "On the reflection and transmission of low-frequency energy at the irregular western Pacific Ocean boundary". In: *Journal of Geophysical Research* (1991), p. 3289. DOI: *10.1029/90JC00985*.

[27] A. J. Clarke and K. H. Brink. *The Response of Stratified, Frictional Flow of Shelf and Slope Waters to Fluctuating Large-Scale, Low-Frequency Wind Forcing*. 1985. DOI: *10.1175/1520-0485(1985)015<0439:TROSFF>2.0.CO;2*.

[28] A. J. Clarke and J. Li. "El Niño/La Niña shelf edge flow and Australian western rock lobsters". In: *Geophysical Research Letters* (June 2004), n/a–n/a. DOI: *10.1029/2003GL018900*.

[29] A. J. Clarke and C. Shi. "Critical frequencies at ocean boundaries". In: *Journal of Geophysical Research* (1991), p. 10731. DOI: *10.1029/91JC00933*.

[30] A. J. Clarke and S. Van Gorder. "On ENSO Coastal Currents and Sea Levels". In: *Journal of Physical Oceanography* (Mar. 1994), pp. 661–680. DOI: *10.1175/1520-0485(1994)024<0661:OECCAS>2.0.CO;2*.

[31] Thomas P. Connolly and Barbara M. Hickey. "Regional impact of submarine canyons during seasonal upwelling". In: *Journal of Geophysical Research: Oceans* (Feb. 2014), pp. 953–975. DOI: *10.1002/2013JC009452*.

[32] M. Crépon and C. Richez. "Transient upwelling generated by two-dimensional atmospheric forcing and variability in the coastline". In: *Journal of Physical Oceanography* (1982), pp. 1437–1457. DOI: *10.1175/1520-0485(1982)012<1437:TUGBTD>2.0.CO;2*.

[33] G. R. Cresswell and J. L. Peterson. "The Leeuwin Current south of Western Australia". In: *Australian Journal of Marine Freshwater Research*. 1993, pp. 285–303. DOI: *10.1071/MF9930285*.

[34] G. T. Csanady. "The Arrested Topographic Wave". In: *Journal of Physical Oceanography* (1978), pp. 47–62. DOI: *10.1175/1520-0485(1978)008<0047:TATW>2.0.CO;2*.

[35] J. C. Davis. *Statistics and Data Analysis in Gelology*. Wiley, 1973, p. 550.

[36] C. de Boyer Montégut, G. Madec, A. S. Fischer, A. Lazar, and D. Iudicone. "Mixed layer depth over the global ocean: An examination of profile data and a profile-based climatology". In: *Journal of Geophysical Research C: Oceans* (2004), pp. 1–20. DOI: *10.1029/2004JC002378*.

[37] D. P. Dee, S. M. Uppala, a. J. Simmons, P. Berrisford, P. Poli, S. Kobayashi, U. Andrae, M. a. Balmaseda, G. Balsamo, P. Bauer, P. Bechtold, a. C. M. Beljaars, L. van de Berg, J. Bidlot, N. Bormann, C. Delsol, R. Dragani, M. Fuentes, a. J. Geer, L. Haimberger, S. B. Healy, H. Hersbach, E. V. Hólm, L. Isaksen, P. Kållberg, M. Köhler, M. Matricardi, A. P. Mcnally, B. M. Monge-Sanz, J. J. Morcrette, B. K. Park, C. Peubey, P. de Rosnay, C. Tavolato, J. N. Thépaut, and F. Vitart. "The ERA-Interim reanalysis: Configuration and performance of the data assimilation system". In: *Quarterly Journal of the Royal Meteorological Society* (Apr. 2011), pp. 553–597. DOI: *10.1002/qj.828*.

[38] T. Doi, S. K. Behera, and T. Yamagata. "Predictability of the Ningaloo Niño/Niña." In: *Scientific reports* (2013), p. 2892. DOI: *10.1038/srep02892*.

[39] C.M. Domingues. "Kinematics and Heat budget of the Leeuwin Current". PhD thesis. Flinders University, 2006, p. 156.

[40] J. P. Evans and I. Boyer-Souchet. "Local sea surface temperatures add to extreme precipitation in northeast Australia during La Niña". In: *Geophysical Research Letters* (May 2012), n/a–n/a. DOI: *10.1029/2012GL052014*.

[41] S. R. Evans and J. F. Middleton. "A regional model of shelf circulation near Bass Strait: a new upwelling mechanism". In: *Journal of Physical Oceanography* (1998), pp. 1439–1457. DOI: *10.1175/1520-0485(1998)028<1439:ARMOSC>2.0.CO;2*.

[42] M. Feng, M. J. McPhaden, S. Xie, and J. Hafner. "La Niña forces unprecedented Leeuwin Current warming in 2011." In: *Scientific reports* (Jan. 2013), p. 1277. DOI: *10.1038/srep01277*.

[43] Ming Feng. "Annual and interannual variations of the Leeuwin Current at 32°S". In: *Journal of Geophysical Research* (2003), p. 3355. DOI: *10.1029/2002JC001763*.

[44] Ming Feng, Harry H Hendon, Shang-ping Xie, Andrew G Marshall, Andreas Schiller, Yu Kosaka, Nick Caputi, and Alan Pearce. "Decadal increase in Ningaloo Niño since the late 1990s". In: (2014), pp. 104–112. DOI: *10.1002/2014GL062509.Received*.

[45] P. Flament. "A state variable for characterizing water masses and their diffusive stability: Spiciness". In: *Progress in Oceanography* (2002), pp. 493–501. DOI: *10.1016/S0079-6611(02)00065-4*.

[46] R. A. Flather. "A Tidal Model of the North-West European Continental Shelf". In: *Memoires Societe Royale des Sciences de Liege* (1976), pp. 141–164.

[47] S. D. Foster, D. A. Griffin, and P. K. Dunstan. "Twenty Years of High-Resolution Sea Surface Temperature Imagery around Australia: Inter-Annual and Annual Variability". In: *PLoS ONE* (July 2014). Ed. by Inés Álvarez, e100762. DOI: *10.1371/journal.pone.0100762*.

[48] J. Gan and J. S. Allen. "A modeling study of shelf circulation off northern California in the region of the Coastal Ocean Dynamics Experiment 2. Simulations and comparisons with observations". In: *Journal of Geophysical Research* (2002), p. 3184. DOI: *10.1029/2001JC001190*.

[49] J. Gan and J. S. Allen. "A modeling study of shelf circulation off northern California in the region of the Coastal Ocean Dynamics Experiment: Response to relaxation of upwelling winds". In: *Journal of Geophysical Research* (2002), p. 3123. DOI: *10.1029/2000JC000768*.

[50] Jianping Gan, Anson Cheung, Xiaogang Guo, and Li Li. "Intensified upwelling over a widened shelf in the northeastern South China Sea". In: *Journal of Geophysical Research* (2009), p. C09019. DOI: *10.1029/2007JC004660*.

[51] Guy H. Gersbach, Charitha B. Pattiaratchi, Gregory N. Ivey, and George R. Cresswell. "Upwelling on the south-west coast of Australia—source of the Capes Current?" In: *Continental Shelf Research* (Mar. 1999), pp. 363–400. DOI: *http://dx.doi.org/10.1016/S0278-4343(98)00088-0*.

[52] A. E. Gill. *Atmosphere-Ocean Dynamics*. 1st ed. Academic Press, 1982, p. 662.

[53] A. E. Gill and E. H. Schumann. "The Generation of Long Shelf Waves by the Wind". In: *Journal of Physical Oceanography* (Jan. 1974), pp. 83–90. DOI: *10.1175/1520-0485(1974)004<0083:TGOLSW>2.0.CO;2*.

[54] P. C. Gill. "A blue whale (Balaenoptera musculus) feeding ground in a southern Australian coastal upwelling zone". In: *Journal of Cetacean Research and Management* (2002), pp. 179–184.

[55] J. S. Godfrey, D. J. Vaudrey, and S. D. Hahn. "Observations of the Shelf-Edge Current South of Australia, Winter 1982". In: *Journal of Physical Oceanography* (Apr. 1986), pp. 668–679. DOI: *10.1175/1520-0485(1986)016<0668:OOTSEC>2.0.CO;2*.

[56] S. D. Hahn. *Physical structure of the waters of the South Australian continental shelf*. Tech. rep. Adelaide: Flinders University, 1986, p. 284.

[57] RL Haney. "On the pressure gradient force over steep topography in sigma coordinate ocean models". In: *Journal of Physical Oceanography* (1991), pp. 610–619. DOI: *http://dx.doi.org/10.1175/1520-0485(1991)021%3C0610:OTPGFO%3E2.0.CO;2*.

[58] Katherine S Hedström. *Technical Manual for a Coupled Sea-Ice / Ocean Circulation Model (V3)*. Tech. rep. Alaska: University of Alaska Fairbanks, 2009, p. 168.

[59] B. J. Henley, J. Gergis, D. J. Karoly, S. Power, J. Kennedy, and C. K. Folland. "A Tripole Index for the Interdecadal Pacific Oscillation". In: *Climate Dynamics* (2015), pp. 3077–3090. DOI: *10.1007/s00382-015-2525-1*.

[60] Chuanmin Hu, Zhongping Lee, and Bryan Franz. "Chlorophyll a algorithms for oligotrophic oceans: A novel approach based on three-band reflectance difference". In: *Journal of Geophysical Research: Oceans* (2012), pp. 1–25. DOI: *10.1029/2011JC007395*.

[61] B. Huang, V. F. Banzon, E. Freeman, J. Lawrimore, W. Liu, T. C. Peterson, T. M. Smith, P. W. Thorne, S. D. Woodruff, and H. Zhang. "Extended Reconstructed Sea Surface Temperature Version 4 (ERSST.v4). Part I: Upgrades and Intercomparisons". In: *Journal of Climate* (Feb. 2015), pp. 911–930. DOI: *10.1175/JCLI-D-14-00006.1*.

[62] Zhi Huang, Scott L Nichol, Peter T Harris, and M Julian Caley. "Classification of submarine canyons of the Australian continental margin". In: *Marine Geology* (2014), pp. 362–383. DOI: *10.1016/j.margeo.2014.07.007*.

[63] Adriana Huyer, Robert L Smith, and Theresa Paluszkiewicz. "Coastal upwelling off Peru during normal and El Niño times, 1981–1984". In: *Journal of Geophysical Research* (1987), p. 14297. DOI: *10.1029/JC092iC13p14297*.

[64] S. Im, S. An, S. T. Kim, and F. Jin. "Feedback processes responsible for El Niño-La Niña amplitude asymmetry". In: *Geophysical Research Letters* (July 2015), pp. 5556–5563. DOI: *10.1002/2015GL064853*.

[65] David R. Jackett and Trevor J. Mcdougall. "Minimal Adjustment of Hydrographic Profiles to Achieve Static Stability". In: *Journal of Atmospheric and Oceanic Technology* (1995), pp. 381–389. DOI: *10.1175/1520-0426(1995)012<0381:MAOHPT>2.0.CO;2*.

[66] M. G. Jacox and C. a. Edwards. "Upwelling source depth in the presence of nearshore wind stress curl". In: *Journal of Geophysical Research: Oceans* (May 2012), p. C05008. DOI: *10.1029/2011JC007856*.

[67] M G Jacox, A M Moore, C A Edwards, and J Fiechter. "Spatially resolved upwelling in the California Current System and its connections to climate variability". In: *Geophysical Research Letters* (May 2014), n/a–n/a. DOI: *10.1002/2014GL059589*.

[68] Michael G. Jacox, Jerome Fiechter, Andrew M. Moore, and Christopher A. Edwards. "ENSO and the California Current coastal upwelling response". In: *Journal of Geophysical Research: Oceans* (Mar. 2015), pp. 1691–1702. DOI: *10.1002/2014JC010650*.

[69] Fei-Fei Jin. "An Equatorial Ocean Recharge Paradigm for ENSO. Part II: A Stripped-Down Coupled Model". In: *Journal of the Atmospheric Sciences* (1997), pp. 830–847. DOI: *10.1175/1520-0469(1997)054<0830:AEORPF>2.0.CO;2*.

[70] X. Jin, C. Dong, J. Kurian, J. C. McWilliams, D. B. Chelton, and Z. Li. "SST–Wind Interaction in Coastal Upwelling: Oceanic Simulation with Empirical Coupling". In: *Journal of Physical Oceanography* (Nov. 2009), pp. 2957–2970. DOI: *10.1175/2009JPO4205.1*.

[71] J. M. Jones, R. L. Fogt, M. Widmann, G. J. Marshall, P. D. Jones, and M. Visbeck. "Historical SAM Variability . Part I : Century-Length Seasonal Reconstructions". In: *Journal of Climate* (2009), pp. 5319–5345. DOI: *10.1175/2009JCLI2785.1*.

[72] J. Kämpf. "On preconditioning of coastal upwelling in the eastern Great Australian Bight". In: *Journal of Geophysical Research: Oceans* (Dec. 2010), pp. 1–11. DOI: *10.1029/2010JC006294*.

[73] J. Kämpf. "Phytoplankton blooms on the western shelf of Tasmania: Evidence of a highly productive ecosystem". In: *Ocean Science* (2015), pp. 1–11. DOI: *10.5194/os-11-1-2015*.

[74] J. Kämpf. "Transient wind-driven upwelling in a submarine canyon: A process-oriented modeling study". In: *Journal of Geophysical Research: Oceans* (Nov. 2006), p. C11011. DOI: *10.1029/2006JC003497*.

[75] J. Kämpf, M. Doubell, D. Griffin, R. L. Matthews, and T. M. Ward. "Evidence of a large seasonal coastal upwelling system along the southern shelf of Australia". In: *Geophysical Research Letters* (May 2004), n/a–n/a. DOI: *10.1029/2003GL019221*.

[76] T. J. O. Kane, R. J. Matear, M. A. Chamberlain, and P. R. Oke. "ENSO regimes and the late 1970 ' s climate shift : The role of synoptic weather and South Pacific ocean spiciness". In: *Journal of Computational Physics* (2014), pp. 19–38. DOI: *10.1016/j.jcp.2013.10.058*.

[77] T. Kataoka, T. Tozuka, S. Behera, and T. Yamagata. "On the Ningaloo Niño/Niña". In: *Climate Dynamics* (2014), pp. 1463–1482. DOI: *10.1007/s00382-013-1961-z*.

[78] F. W. Landerer, J. H. Jungclaus, and J. Marotzke. "El Niño–Southern Oscillation signals in sea level, surface mass redistribution, and degree-two geoid coefficients". In: *Journal of Geophysical Research* (Aug. 2008), p. C08014. DOI: *10.1029/2008JC004767*.

[79] SJ Lentz and DC Chapman. "The Importance of Nonlinear Cross-Shelf Momentum Flux during Wind-Driven Coastal Upwelling*". In: *Journal of Physical Oceanography* (2004), pp. 2444–2457.

[80] R. K. Lewis. "Seasonal upwelling along the south-eastern coastline of South Australia". In: *Marine and Freshwater Research* (1981), pp. 843–854.

[81] J. K. Li and A. J. Clarke. "Coastline direction, interannual flow, and the strong El nino currents along Australia's nearly zonal southern coast". In: *Journal of Physical Oceanography* (2004), pp. 2373–2381. DOI: *http://dx.doi.org/10.1175/JPO2645.1*.

[82] A. Linnane, W. Dimmlich, and T. Ward. "Movement patterns of the southern rock lobster, Jasus edwardsii, off South Australia". In: *New Zealand Journal of Marine and Freshwater Research* (2005), pp. 335–346. DOI: *10.1080/00288330.2005.9517314*.

[83] Adrian Linnane, Caleb Gardner, David Hobday, André Punt, Richard McGarvey, John Feenstra, Janet Matthews, and Bridget Green. "Evidence of large-scale spatial declines in recruitment patterns of southern rock lobster Jasus edwardsii, across south-eastern Australia". In: *Fisheries Research* (2010), pp. 163–171. DOI: *10.1016/j.fishres.2010.04.001*.

[84] Zhiqiang Liu and Jianping Gan. "Modeling Study of Variable Upwelling Circulation in the East China Sea: Response to a Coastal Promontory". In: *Journal of Physical Oceanography* (2014), pp. 1078–1094. DOI: *10.1175/JPO-D-13-0170.1*.

[85] Zhiqiang Liu and Jianping Gan. "Upwelling induced by the frictional stress curl and vertical squeezing of the vortex tube over a submerged valley in the East China Sea". In: *Journal of Geophysical Research: Oceans* (Apr. 2015), pp. 2571–2587. DOI: *10.1002/2015JC010715*.

[86] Kazuyuki Maiwa, Yukio Masumoto, and Toshio Yamagata. "Characteristics of coastal trapped waves along the southern and eastern coasts of Australia". In: *Journal of Oceanography* (2010), pp. 243–258. DOI: *10.1007/s10872-010-0022-z*.

[87] P. Marchesiello and P. Estrade. "Upwelling limitation by onshore geostrophic flow". In: *Journal of Marine Research* (Jan. 2010), pp. 37–62. DOI: *10.1357/002224010793079004*.

[88] G. J. Marshall. "Trends in the Southern Annular Mode from observations and reanalyses". In: *Journal of Climate* (2003), pp. 4134–4143. DOI: *10.1175/1520-0442(2003)016<4134:TITSAM>2.0.CO;2*.

[89] Evan Mason, Jeroen Molemaker, Alexander F. Shchepetkin, Francois Colas, James C. McWilliams, and Pablo Sangrà. "Procedures for offline grid nesting in regional ocean models". In: *Ocean Modelling* (Jan. 2010), pp. 1–15. DOI: *10.1016/j.ocemod.2010.05.007*.

[90] Ricardo P. Matano and Elbio D. Palma. "On the Upwelling of Downwelling Currents". In: *Journal of Physical Oceanography* (Nov. 2008), pp. 2482–2500. DOI: *10.1175/2008JPO3783.1*.

[91] E. L. Mathers and P. L. Woodworth. "A study of departures from the inverse-barometer response of sea level to air-pressure forcing at a period of 5 days". In: *Quarterly Journal of the Royal Meteorological Society* (Jan. 2004), pp. 725–738. DOI: *10.1256/qj.03.46*.

[92] S. McClatchie, J. F. Middleton, and T. M. Ward. "Water mass analysis and alongshore variation in upwelling intensity in the eastern Great Australian Bight". In: *Journal of Geophysical Research: Oceans* (2006), p. C08007. DOI: *10.1029/2004JC002699*.

[93] S. McClatchie, P. J. Rogers, and L. McLeay. "Importance of scale to the relationship between abundance of sardine larvae, stability, and food". In: *Limnology and Oceanography* (2007), pp. 1570–1579. DOI: *10.4319/lo.2007.52.4.1570*.

[94] G. Meyers. "Variation of Indonesian throughflow and the El Niño-Southern Oscillation". In: *Journal of Geophysical Research: Oceans* (May 1996), pp. 12255–12263. DOI: *10.1029/95JC03729*.

[95] J. F. Middleton. "The coastal-trapped wave paddle and open boundary conditions". In: *Ocean Modelling* (Jan. 2006), pp. 224–236. DOI: *10.1016/j.ocemod.2005.09.001*.

[96] J. F. Middleton. "Wind-Forced Upwelling: The Role of the Surface Mixed Layer". In: *Journal of Physical Oceanography* (May 2000), pp. 745–763. DOI: *10.1175/1520-0485(2000)030<0745:WFUTRO>2.0.CO;2*.

[97] J. F. Middleton, C. Arthur, P. Van Ruth, T. M. Ward, J. L. McClean, M. E. Maltrud, P. Gill, A. Levings, and S. Middleton. "El Niño effects and upwelling off south Australia". In: *Journal of Physical Oceanography* (Oct. 2007), pp. 2458–2477. DOI: *10.1175/JPO3119.1*.

[98] J. F. Middleton and K. P. Black. "The low frequency circulation in and around Bass Strait: a numerical study". In: *Continental Shelf Research* (1994), pp. 1495–1521. DOI: *10.1016/0278-4343(94)90087-6*.

[99] J. F. Middleton and J. A. T. Bye. "A review of the shelf-slope circulation along Australia's southern shelves: Cape Leeuwin to Portland". In: *Progress in Oceanography* (Oct. 2007), pp. 1–41. DOI: *10.1016/j.pocean.2007.07.001*.

[100] J. F. Middleton and M. Cirano. "A northern boundary current along Australia's southern shelves: The Flinders Current". In: *Journal of Geophysical Research* (2002), pp. 1–11. DOI: *10.1029/2000JC000701*.

[101] J. F. Middleton, N. P. James, C. James, and Y. Bone. "Cross-shelf seawater exchange controls the distribution of temperature, salinity, and neritic carbonate sediments in the Great Australian Bight". In: *Journal of Geophysical Research: Oceans* (Apr. 2014), pp. 2539–2549. DOI: *10.1002/2013JC009420*.

[102] J. F. Middleton and O. K. Leth. "Wind-forced setup of upwelling, geographical origins, and numerical models: The role of bottom drag". In: *Journal of Geophysical Research C: Oceans* (2004), pp. 1–12. DOI: *10.1029/2003JC002126*.

[103] J. F. Middleton, R. McGarvey, A. Linnane, S. M. Middleton, C. E.P. Teixeira, and P. Hawthorne. "Using observations of bottom temperature to calibrate the output of an ocean model". In: *Journal of Marine Systems* (Mar. 2012), pp. 34–40. DOI: *10.1016/j.jmarsys.2011.09.006*.

[104] J. F. Middleton and G. Platov. "The Mean Summertime Circulation along Australia's Southern Shelves: A Numerical Study". In: *Journal of Physical Oceanography* (Nov. 2003), pp. 2270–2287. DOI: *10.1175/1520-0485(2003)033<2270:TMSCAA>2.0.CO;2*.

[105] J. F. Middleton and D. Ramsden. "The evolution of the bottom boundary layer on the sloping continental shelf: A numerical study". In: *Journal of Geophysical Research: Oceans (1978–2012)* (1996), pp. 18061–18077.

[106] J. F. Middleton and D. G. Wright. "Coastally Trapped Waves in a Stratified Ocean". In: *Journal of Physical Oceanography* (1990), pp. 1521–1527.

[107] A. Nieblas, B. M. Sloyan, A. J. Hobday, R. Coleman, and A. Richardson. "Variability of biological production in low wind-forced regional upwelling systems : A case study off southeastern Australia". In: *Limnology and Oceanography* (2009), pp. 1548–1558. DOI: *10.4319/lo.2009.54.5.1548*.

[108] R. A. Nunes Vaz, G. W. Lennon, and D. G. Bowers. "Physical behaviour of a large, negative or inverse estuary". In: *Continental Shelf Research* (1990), pp. 277–304. DOI: *10.1016/0278-4343(90)90023-F*.

[109] P. R. Oke, G. B. Brassington, D. A. Griffin, and A. Schiller. "The Bluelink ocean data assimilation system (BODAS)". In: *Ocean Modelling* (Jan. 2008), pp. 46–70. DOI: *10.1016/j.ocemod.2007.11.002*.

[110] P. R. Oke and P. Sakov. "Assessing the footprint of a regional ocean observing system". In: *Journal of Marine Systems* (Dec. 2012), pp. 30–51. DOI: *10.1016/j.jmarsys.2012.05.009*.

[111] P. R. Oke, P. Sakov, M. L. Cahill, J. R. Dunn, R. Fiedler, D. A. Griffin, J. V. Mansbridge, K. R. Ridgway, and A. Schiller. "Towards a dynamically balanced eddy-resolving ocean reanalysis: BRAN3". In: *Ocean Modelling* (July 2013), pp. 52–70. DOI: *10.1016/j.ocemod.2013.03.008*.

[112] Larry W. O'Neill, Dudley B. Chelton, and Steven K. Esbensen. "Observations of SST-induced perturbations of the wind stress field over the Southern Ocean on seasonal timescales". In: *Journal of Climate* (2003), pp. 2340–2354. DOI: *10.1175/2780.1*.

[113] ED Palma and RP Matano. "On the implementation of open boundary conditions for a general circulation model: The three-dimensional case". In: *Journal of Geophysical Research: ...* (2000), pp. 8605–8627.

[114] E.D. Palma and R.P. Matano. "On the implementation of passive open boundary conditions for a general circulation model: the barotropic mode". In: *Journal of Geophysical Research* (1998), pp. 1319–1341. DOI: *10.1029/97JC02721*.

[115] J. I. Pariwono, J. A. T. Bye, and G. W. Lennon. "Long-period variations of sea-level in Australasia". In: *Geophysical Journal International* (Oct. 1986), pp. 43–54. DOI: *10.1111/j.1365-246X.1986.tb04545.x*.

[116] J. S. Paterson, S. Nayar, J. G. Mitchell, and L. Seuront. "A local upwelling controls viral and microbial community structure in South Australian continental shelf waters". In: *Estuarine, Coastal and Shelf Science* (Jan. 2012), pp. 197–208. DOI: *10.1016/j.ecss.2011.11.009*.

[117] Alan Pearce and Charitha Pattiaratchi. "The Capes Current: a summer countercurrent flowing past Cape Leeuwin and Cape Naturaliste, Western Australia". In: *Continental Shelf Research* (Mar. 1999), pp. 401–420. DOI: *10.1016/S0278-4343(98)00089-2*.

[118] M. B. Peffley and J. J. O'Brien. "A three-dimensional simulation of coastal upwelling off Oregon". In: *Journal of Physical Oceanography* (1976), pp. 164–180. DOI: *10.1175/1520-0485(1976)006<0164:ATDSOC>2.0.CO;2*.

[119] S. G. H. Philander and J-H. Yoon. "Eastern Boundary Currents and Coastal Upwelling". In: *Journal of Physical Oceanography* (1982), pp. 862–879. DOI: *10.1175/1520-0485(1982)012<0862:EBCACU>2.0.CO;2*.

[120] M. H. Pickett. "Ekman transport and pumping in the California Current based on the U.S. Navy's high-resolution atmospheric model (COAMPS)". In: *Journal of Geophysical Research* (2003), p. 3327. DOI: *10.1029/2003JC001902*.

[121] B. Pohl, N. Fauchereau, C. J.C. Reason, and M. Rouault. "Relationships between the Antarctic oscillation, the Madden-Julian oscillation, and ENSO, and consequences for rainfall analysis". In: *Journal of Climate* (2010), pp. 238–254. DOI: *10.1175/2009JCLI2443.1*.

[122] R. M. Ponte. "Understanding the relation between wind-and pressure-driven sea level variability". In: *J. Geophys. Res.* (1994), pp. 8033–8039.

[123] James M Pringle. "Enhancement of Wind-Driven Upwelling and Downwelling by Alongshore Bathymetric Variability*". In: *Journal of Physical Oceanography* (2002), pp. 3101–3112. DOI: *10.1175/1520-0485(2002)032<3101:EOWDUA>2.0.CO;2*.

[124] J. L. Reid, G. I. Roden, and J. G. Wyllie. *Studies of The California Current System*. Tech. rep. Scripps Institution of Oceanography, 1958, p. 30.

[125] L. Renault, A. Hall, and J. C. McWilliams. "Orographic shaping of US West Coast wind profiles during the upwelling season". In: *Climate Dynamics* (Jan. 2016), pp. 273–289. DOI: *10.1007/s00382-015-2583-4*.

[126] Francis A. Richards. *Coastal Upwelling*. Ed. by Francis A. Richards. Coastal and Estuarine Sciences. Washington, D. C.: American Geophysical Union, 1981, pp. ix–ix. DOI: *10.1029/CO001*.

[127] L. E. Richardson, T. K. Kyser, N. P. James, and Y. Bone. "Analysis of hydrographie and stable isotope data to determine water masses, circulation, and mixing in the eastern Great Australian Bight". In: *Journal of Geophysical Research: Oceans* (Oct. 2009), p. C10016. DOI: *10.1029/2009JC005407*.

[128] K. R. Ridgway. "Seasonal circulation around Tasmania: An interface between eastern and western boundary dynamics". In: *Journal of Geophysical Research* (Oct. 2007), p. C10016. DOI: *10.1029/2006JC003898*.

[129] K. R. Ridgway and S. A. Condie. "The 5500-km-long boundary flow off western and southern Australia". In: *Journal of Geophysical Research C: Oceans* (2004), p. C04017. DOI: *10.1029/2003JC001921*.

[130] K. R. Ridgway, J. R. Dunn, and J. L. Wilkin. "Ocean Interpolation by Four-Dimensional Weighted Least Squares—Application to the Waters around Australasia". In: *Journal of Atmospheric and Oceanic Technology* (Sept. 2002), pp. 1357–1375. DOI: *10.1175/1520-0426(2002)019<1357:OIBFDW>2.0.CO;2*.

[131] K. R. Ridgway and J. S. Godfrey. "The source of the Leeuwin Current seasonality". In: *Journal of Geophysical Research: Oceans* (Oct. 2015), pp. 6843–6864. DOI: *10.1002/2015JC011049*.

[132] Ken R. Ridgway. "Long-term trend and decadal variability of the southward penetration of the East Australian Current". In: *Geophysical Research Letters* (July 2007), n/a–n/a. DOI: *10.1029/2007GL030393*.

[133] Craig M. Risien and Dudley B. Chelton. "A Global Climatology of Surface Wind and Wind Stress Fields from Eight Years of QuikSCAT Scatterometer Data". In: *Journal of Physical Oceanography* (Nov. 2008), pp. 2379–2413. DOI: *10.1175/2008JPO3881.1*.

[134] D. J. Rochford. *A review of possible upwelling situation off Port Macdonnell SA [South Australia]*. Tech. rep. Cronulla: CSIRO, 1977, p. 15.

[135] Vincent Rossi, Ming Feng, Charitha Pattiaratchi, Moninya Roughan, and Anya M. Waite. "On the factors influencing the development of sporadic upwelling in the Leeuwin Current system". In: *Journal of Geophysical Research: Oceans* (July 2013), pp. 3608–3621. DOI: *10.1002/jgrc.20242*.

[136] P. D. van Ruth, G. G. Ganf, and T. M. Ward. "Hot-spots of primary productivity: An Alternative interpretation to Conventional upwelling models". In: *Estuarine, Coastal and Shelf Science* (Dec. 2010), pp. 142–158. DOI: *10.1016/j.ecss.2010.08.009*.

[137] J Savage. "Australian fisheries and aquaculture statistics 2015". In: *Fisheries Research and Development Corporation project 2016-246.* (2015), p. 160.

[138] A. Schaeffer, M. Roughan, T. Austin, J. D. Everett, D. Griffin, B. Hollings, E. King, A. Mantovanelli, S. Milburn, B. Pasquer, C. Pattiaratchi, R. Robertson, D. Stanley, I. Suthers, and D. White. "Mean hydrography on the continental shelf from 26 repeat glider deployments along Southeastern Australia". In: *Scientific Data* (Aug. 2016), p. 160070. DOI: *10.1038/sdata.2016.70*.

[139] R. B. Schahinger. "Structure of coastal upwelling events observed off the south-east coast of South Australia during February 1983–April 1984". In: *Marine and Freshwater Research* (1987), p. 439. DOI: *10.1071/MF9870439*.

[140] A. Schiller, P. R. Oke, G. Brassington, M. Entel, R. Fiedler, D. A. Griffin, and J. V. Mansbridge. "Eddy-resolving ocean circulation in the Asian-Australian region inferred from an ocean reanalysis effort". In: *Progress in Oceanography* (Mar. 2008), pp. 334–365. DOI: *10.1016/j.pocean.2008.01.003*.

[141] A. Schiller and K. R. Ridgway. "Seasonal mixed-layer dynamics in an eddy-resolving ocean circulation model". In: *Journal of Geophysical Research: Oceans* (July 2013), pp. 3387–3405. DOI: *10.1002/jgrc.20250*.

[142] Gary Shaffer, Oscar Pizarro, Leif Djurfeldt, Sergio Salinas, and José a Rutllant. "Circulation and Low-Frequency Variability near the Chilean Coast: Remotely Forced Fluctuations during the 1991–92 El Niño". In: *Journal of Physical Oceanography* (1997), pp. 217–235. DOI: *10.1175/1520-0485(1997)027<0217:CALFVN>2.0.CO;2*.

[143] A. F. Shchepetkin and J. C. McWilliams. "The regional oceanic modeling system (ROMS): A split-explicit, free-surface, topography-following-coordinate oceanic model". In: *Ocean Modelling* (Jan. 2005), pp. 347–404. DOI: *10.1016/j.ocemod.2004.08.002*.

[144] Alexander F. Shchepetkin. "A method for computing horizontal pressure-gradient force in an oceanic model with a nonaligned vertical coordinate". In: *Journal of Geophysical Research* (2003), pp. 1–34. DOI: *10.1029/2001JC001047*.

[145] M. D. Sikirić, I. Janeković, and M. Kuzmić. "A new approach to bathymetry smoothing in sigma-coordinate ocean models". In: *Ocean Modelling* (2009), pp. 128–136. DOI: *10.1016/j.ocemod.2009.03.009*.

[146] Piotr K. Smolarkiewicz and Len G. Margolin. "MPDATA: A Finite-Difference Solver for Geophysical Flows". In: *Journal of Computational Physics* (Mar. 1998), pp. 459–480. DOI: *10.1006/jcph.1998.5901*.

[147] Hajoon Song, Arthur J. Miller, Bruce D. Cornuelle, and Emanuele Di Lorenzo. "Changes in upwelling and its water sources in the California Current System driven by different wind forcing". In: *Dynamics of Atmospheres and Oceans* (Sept. 2011), pp. 170–191. DOI: *10.1016/j.dynatmoce.2011.03.001*.

[148] Nobuo Suginohara. *Coastal upwelling: onshore-offshore circulation, equatorward coastal jet and poleward undercurrent over a continental shelf*. 1982. DOI: *10.1175/1520-0485(1982)012<0272:CUOCEC>2.0.CO;2*.

[149] M. Tomczak, L. Pender, and S. Liefrink. "Variability of the subtropical front in the Indian Ocean south of Australia". In: *Ocean Dynamics* (2004), pp. 506–519. DOI: *10.1007/s10236-004-0095-6*.

[150] T. Tozuka, T. Kataoka, and T. Yamagata. "Locally and remotely forced atmospheric circulation anomalies of Ningaloo Niño/Niña". In: *Climate Dynamics* (2014), pp. 1–9. DOI: *10.1007/s00382-013-2044-x*.

[151] K. E. Trenberth and J. M. Caron. "The Southern Oscillation Revisited: Sea Level Pressures, Surface Temperatures, and Precipitation". In: *Journal of Climate* (Dec. 2000), pp. 4358–4365. DOI: *10.1175/1520-0442(2000)013<4358:TSORSL>2.0.CO;2*.

[152] J. H. Trowbridge and S. J. Lentz. *Asymmetric Behavior of an Oceanic Boundary Layer above a Sloping Bottom*. 1991. DOI: *10.1175/1520-0485(1991)021<1171:ABOAOB>2.0.CO;2*.

[153] Lars Umlauf and Hans Burchard. "A generic length-scale equation for geophysical turbulence models". In: *Journal of Marine Research* (Mar. 2003), pp. 235–265. DOI: *10.1357/002224003322005087*.

[154] M. A. Verschell, J. C. Kindle, and J. J. O'Brien. "Effects of Indo-Pacific throughflow on the upper tropical Pacific and Indian Oceans". In: *Journal of Geophysical Research* (1995), p. 18409. DOI: *10.1029/95JC02075*.

[155] Guojian Wang and Wenju Cai. "Climate-change impact on the 20th-century relationship between the Southern Annular Mode and global mean temperature". In: *Scientific Reports* (2013), p. 2039. DOI: *10.1038/srep02039*.

[156] T. M. Ward, L. J. McLeay, W. F. Dimmlich, P. J. Rogers, S. McClatchie, R. Matthews, J. Kämpf, and P. D. Van Ruth. "Pelagic ecology of a northern boundary current system: Effects of upwelling on the production and distribution of sardine (Sardinops sagax), anchovy (Engraulis australis) and southern bluefin tuna (Thunnus maccoyii) in the Great Australian Bight". In: *Fisheries Oceanography* (May 2006), pp. 191–207. DOI: *10.1111/j.1365-2419.2006.00353.x*.

[157] John C. Warner, W. Rockwell Geyer, and James A. Lerczak. "Numerical modeling of an estuary: A comprehensive skill assessment". In: *Journal of Geophysical Research C: Oceans* (2005), pp. 1–13. DOI: *10.1029/2004JC002691*.

[158] B. A. Warren and C. Wunsch. *Evolution of Physical Oceanography: Scientific Surveys in Honor of Henry Stommel*. MIT Press, 1980, p. 664.

[159] M. M. Whitney and J. S. Allen. "Coastal Wind-Driven Circulation in the Vicinity of a Bank. Part I: Modeling Flow over Idealized Symmetric Banks". In: *Journal of Physical Oceanography* (June 2009), pp. 1273–1297. DOI: *10.1175/2008JPO3966.1*.

[160] M. M. Whitney and J. S. Allen. "Coastal Wind-Driven Circulation in the Vicinity of a Bank. Part II: Modeling Flow over the Heceta Bank Complex on the Oregon Coast". In: *Journal of Physical Oceanography* (June 2009), pp. 1298–1316. DOI: *10.1175/2008JPO3967.1*.

[161] Weifeng (Gordon) Zhang and Steven J. Lentz. "Wind-driven circulation in a shelf valley. Part I: Mechanism of the asymmetrical response to along-shelf winds in opposite directions". In: *Journal of Physical Oceanography* (2017), JPO–D–17–0083.1. DOI: *10.1175/JPO-D-17-0083.1*.